Design of a 0.3-12 GHz Ground-Penetrating Radar Underground Imaging System

By

SAMUEL WAGNER
DISSERTATION

Submitted in partial satisfaction of the requirements for the degree of

DOCTOR OF PHILOSOPHY

in

Electrical and Computer Engineering

in the

OFFICE OF GRADUATE STUDIES

of the

UNIVERSITY OF CALIFORNIA

DAVIS

Approved:

_____

Anh-Vu Pham, Chair

_____

Omeed Momeni

_____

J. Sebastian Gomez-Diaz

Committee in Charge

2022

Abstract

We develop the theory behind and a prototype of a 0.3-12 GHz ground-penetrating radar (GPR) system for use in imaging the subsurface environment. Experimental results show that the prototype GPR system is likely able to perform in field applications including buried utility detection and humanitarian demining operations. First, we present two antenna designs – the resistively loaded vee dipole (RLVD) and elliptical RLVD based on a Guanella balun structure. However, we found a disconnect between the performance of these antennas in simulation and the real-world system performance. Therefore, we have developed a theory of how the less-often-considered aspects of antennas including coupling, distortion, beamwidth, and radar-cross section dramatically affect the overall imaging performance. We perform a deep-dive into the causes, solutions, and design decisions that each aspect of the antenna requires in order to make it more likely that an antenna will perform well in the niche application of GPR. In order to validate and apply these principles in the real world, we present the creation of a 0.3-12 GHz GPR system in both the lab and outside environments. We show the entire build of the custom FPGA-based sampling receiver, examine the VHDL backend for data offloading, and describe the real-time visualization system. Next, we show in depth the signal-processing pipeline required to take raw data to a pre-processed image: de-glitching, de-jittering, and background removal algorithms, among others. The Kirchhoff-Migration imaging algorithms used to transform the pre-processed data into human-readable images are presented in detail. Finally, lab-based and real-world underground imaging results are presented as validation of the operation of the GPR system. We demonstrate the detection of steel rebar in a laboratory sandbox imaging test and portions of the underground structure around Kemper Hall at UC Davis.

Acknowledgement

I would like to express my gratitude toward my Ph.D. advisor Professor Anh-Vu Pham for his close support, encouragement, and belief in my ability to conduct research over the past several years. I would also like to thank my committee members Professor Omeed Momeni and Professor J. Sebastian Gomez-Diaz for their time and flexibility.

I am grateful to my peers who have worked with me on this and other related projects: Stephen Pancrazio, Ababil Hossain, Ahmad Alkasimi, Nhat Tran, Tyler Kelley, and Tyler Shepard for both invaluable comments on my research and the collaboration required to bring a fully operational radar system to life.

For their valuable technical discussions and general brightening of lab life, I would like to thank Dr. Nguyen Nguyen, Dr. Matthew Clements, Phat Tan Nguyen, and Juan Manuel Romero.

I am grateful to my parents Susanne and Mike Wagner for their unconditional support and love, my sister Natalie Killeen for helping to guide me to be the person I am today, and Soren Lipman for keeping me sane the past several years.

This project is sponsored by the Department of the Navy, Office of Naval Research under award N00014-17-1-2488. Any opinions, findings, and conclusions or recommendations expressed in this material are those of the author(s) and do not necessarily reflect the views of the Office of Naval Research.

works for resale or redistribution, please go to http://www.ieee.org/publications_standards/publications/rights/rights_link.html to learn how to obtain a License from RightsLink. If applicable, University Microfilms and/or ProQuest Library, or the Archives of Canada may supply single copies of the dissertation.

Table of Contents

Abstract ii
Acknowledgement iii
Table of Contents v
Table of Figures vi
List of Publications ix
Introduction 1
1. Ground-Penetrating Radar Antennas 4
A. Resistively-Loaded Vee Dipole 4
B. ERLVD & Guanella Balun 10
C. Guanella Balun 32
2. GPR System-Level Effects and Specifications 39
A. Jitter 39
B. Added Distortion and Clutter from Surrounding Structures 58
C. System-Based Antenna Specifications 62
3. DC-12 GHz, 100 GS/s Equivalent-Sampling Receiver 97
A. Overview/Block Diagram 97
B. Equivalent Sampling & Hardware 99
C. FPGA-Based Data Offloading 105
D. Real-time Visualization and Data Storage 109
4. GPR Scanning Systems (2D and 3D) 111
A. 2D System Diagram 111
B. 3D System Diagram 112
C. Sandbox System 115
D. Outside GPR Cart System 118
5. GPR Processing Pipeline 123
A. Preprocessing 123
B. Imaging 145
6. 2D GPR Scan and Image Results 149
A. Buried Wire 149
B. Sandbox GPR Scans - Rebar 154
C. Outside GPR Scans 163
Conclusion 175

References 176

Table of Figures

Fig. 1: HFSS model of RLVD with sizing information 5
Fig. 2: Circuit schematic diagram of even-mode matched balun 6
Fig. 3: Photograph of balun feeding RLVD without connector 7
Fig. 4: Photograph of the fabricated RLVD with even-mode matched balun 8
Fig. 5: Return loss simulations and measurements of the RLVD 8
Fig. 6: Radiation patterns of the designed RLVD 9
Fig. 7: S_{21} measurement of two prototyped RLVDs with 10 cm board-to-board separation. 10
Fig. 8: Transmit measurement between two RLVDs with 1m separation 10
Fig. 9: Diagrams of ERLVDs with different geometries 13
Fig. 10: Direction and magnitude of surface current flow at 1 GHz on elliptical sub-elements 16
Fig. 11: Images of ERLVDs with different growth rates. 19
Fig. 12: Simulated usable bandwidths of all ERLVDs with growth rate greater than 1 19
Fig. 13: Simulated comparison of boresight gains for ERLVDs 21
Fig. 14: Simulated ERLVD lower cutoff frequencies directivities versus inner arm angle 22
Fig. 15: Photograph of fabricated RLVD and ERLVDs. 23
Fig. 16: Simulated and measured VSWR response of unity growth-rate ERLVD$_{\Gamma=1}$. 24
Fig. 17: Simulated and measured VSWR response of high growth-rate ERLVD$_{\Gamma=2.6}$ 25
Fig. 18: Measured transient response of pair of identical antennas sighted boresight at 1 meter apart 27
Fig. 19: Calculated power spectral densities (PSDs) in dB/Hz for the received signals at 1 meter 28
Fig. 20: Measured and simulated gains of ERLVDs 29
Fig. 21: Measured radiation patterns of the prototyped ERLVD and RLVD at selected frequencies 31
Fig. 22: Schematic diagram of 1:4 classic Guanella balun with single-ended terminations. 33
Fig. 23: HFSS model of Guanella balun 34
Fig. 24: Photograph of the manufactured balun 35
Fig. 25: Simulated versus measured differential transmission and input return loss 36
Fig. 26: Measured amplitude and phase imbalances of the Guanella balun 37
Fig. 27: Simulated Ricker wavelet response using measured vector S-parameters 38
Fig. 28. Measured example of sampling jitter in a GPR waveform 42
Fig. 29. Experimental setup used to simulate jitter. 43
Fig. 30: Jittered GPR B-scans and images 48
Fig. 31: Power spectral densities of the measured GPR signal versus jitter 50
Fig. 32: Filtering background-removal jitter residue 50
Fig. 33: Linear slope calculated from measured GPR coupling signal 53
Fig. 34: Probability distribution of absolute value of migrated noise image 55
Fig. 35: Probability that migrated noise magnitude is greater than half of the expected target strength 56
Fig. 36: Additional clutter generated from inclusion of a supporting structure 59
Fig. 37: GPR B-scans with various backing structures 61

Fig. 38: GPR A-scans with various backign structures 62
Fig. 39. Diagram showing an example GPR B-scan using real data with adverse effects labelled 64
Fig. 40. Diagram showing coupling setup 69
Fig. 41: Potential sources of distortion in an antenna.....73
Fig. 42: Effects of poor pulse transmission on the quality of a GPR B-Scan.....74
Fig. 43. Example showing three different values of pulse integrity 75
Fig. 44. Example residual ringing of a 0.5-3 GHz Ricker pulse.....77
Fig. 45. Diagram showing the geometrical maximum view angle.. 78
Fig. 46. Example beamwidth-resolution curves for various GPR systems.....81
Fig. 47: Example of increased antenna RCS creating false targets. 83
Fig. 48. Two-layer simulated maximum tolerable antenna RCS versus operating height 87
Fig. 49: Diagram showin high-FBR and low-FBR antennas in an enclosure.....88
Fig. 50: Equivalent-sampling receiver block diagram showing hardware, FPGA, and software.98
Fig. 51. Concept of equivalent-time sampling.....100
Fig. 52: Detailed sampling of a 1 GHz sine wave 102
Fig. 53: Photograph of custom-build receiver 104
Fig. 54: Block diagram with more detail of FPGA program 106
Fig. 55: Inner structure of each transmitted 32-bit word 107
Fig. 56: Switching sequence for 3-D imaging. 108
Fig. 57: Internal program structure of Rust-based real-time visualizer. 109
Fig. 58: Desktop screenshot of running the real-time radar visualization program.....110
Fig. 59: System block diagram of the 2D GPR sensing system. 111
Fig. 60: System block diagram of the 3D GPR sensing system. 113
Fig. 61: Overall fast-time axis for GPR system with relevant windows and events indicated...114
Fig. 62. Photograph of sandbox GPR system. 115
Fig. 63: Benchtop layout of radar circuitry.....117
Fig. 64. Photograph of cart operating on dirt track (2D scan). 118
Fig. 65. Closeup zoom of cart circuitry 119
Fig. 66. 8x8 (Tx x Rx) antenna array of Vivaldi-type antennas 119
Fig. 67. Cart calibration configuration.....122
Fig. 68: Sandbox with half-buried rebar targets 124
Fig. 69: Dimensions of buried rebar targets in sandbox. 124
Fig. 70: Example GPR A-scan with coupling, ground reflection, and targets highlighted. 125
Fig. 71. Example GPR B-scan with coupling, ground, and targets highlighted. 126
Fig. 72: Example of an edge glitch. 128
Fig. 73. Code to remove edge glitches.....128
Fig. 74: A-scan glitch (energy-based detection method).....129
Fig. 75: Code to remove A-scan energy-based glitches. 130
Fig. 76: Example time-of-arrival jitter in GPR A-scans. 131
Fig. 77: Code to remove time-of-arrival jitter. 132
Fig. 78: Performance of de-jittering on a worst-case time-of-arrival jitter GPR B-scan.....133
Fig. 79: Code to perform windowed moving average. 135
Fig. 80: Code to automatically correct t=0 errors in a GPR B-scan. 137
Fig. 81: Example time-zeroed A-scan. 138
Fig. 82: Code to perform B-scan background removal with PCA.....139

Fig. 83: Comparison of raw and background-removed GPR B-scan data. 140
Fig. 84: Code to filter B-scans in frequency and space. 141
Fig. 85: Comparison of filtered and un-filtered GPR B-scans 142
Fig. 86: Code to perform a matched filter on a GPR B-scan. 143
Fig. 87: Comparison of filtered and matched-filtered GPR B-scans. 144
Fig. 88: Comparison of BKGR GPR B-scan and migrated 2D image 147
Fig. 89: Annotated 2-D GPR image. 148
Fig. 90: System and experimental diagram for detecting sub-surface wires 150
Fig. 91: 2D GPR B-Scan data for wires of varying diameter 152
Fig. 92: RCS of a 60-cm cylindrical wire versus diameter and frequency 153
Fig. 93: GPR B-scans of three rebar targets using pulses of different bandwidths. 156
Fig. 94. Migrated images of Fig. 93 157
Fig. 95: SNR and target horizontal/vertical resolutions versus pulse bandwidth. 159
Fig. 96: Photograph of sidewalk scan south of Kemper Hall. 163
Fig. 97: 2D GPR scan of sidewalk south of Kemper Hall 164
Fig. 98: Photograph of sidewalk scan to the east of Kemper Hall. 165
Fig. 99: 2D GPR scan of sidewalk east of Kemper Hall. 166
Fig. 100: Photograph of dirt scan to the west of Kemper Hall. 168
Fig. 101: 2D GPR scan of dirt section 1 west of Kemper Hall 169
Fig. 102: 2D GPR scan of dirt section 2 west of Kemper Hall 170
Fig. 103: 2D GPR scan of dirt section 3 west of Kemper Hall 171
Fig. 104: 2D GPR scan of dirt section 4 west of Kemper Hall 172

List of Publications

* - covered in this work

Journal Papers

1. ***S. Wagner** and A. Pham, "The Ultrawideband Elliptical Resistively-Loaded Vee Dipole," in IEEE Transactions on Antennas and Propagation. doi: 10.1109/TAP.2019.2949680

2. ***S. Wagner**, B. M. Worthmann and A. Pham, "Minimizing Timing Jitter's Impact on Ground-Penetrating Radar Array Coupling Signals," in IEEE Transactions on Geoscience and Remote Sensing. doi: 10.1109/TGRS.2020.3019976

3. **S. Wagner**, A. Alkasimi, and A.-V. Pham, "Detecting the Presence of Intrusive Drilling in Secure Transport Containers Using Non-Contact Millimeter-Wave Radar," *Sensors*, vol. 22, no. 7, p. 2718, Apr. 2022, doi: 10.3390/s22072718.

4. ***S. Wagner**, S. Pancrazio, A. Hossain, A. Pham, "System-Based Design Specifications for Better Design of Ground-Penetrating Radar Antennas," (Submitted, Under Review)

Conference Papers

1. A. Hossain, **S. Wagner**, S. Pancrazio and A. -V. Pham, "An Electrically Smaller Ultra-Wideband Monopole Antenna for Ground Penetrating Radar Application," *2021 IEEE International Symposium on Antennas and Propagation and USNC-URSI Radio Science Meeting (APS/URSI)*, Singapore, Singapore, 2021, pp. 485-486.

2. A. Hossain, **S. Wagner**, S. Pancrazio and A. -V. Pham, "A Compact Low-Cost and Lightweight 3-D Printed Horn Antenna for UWB Systems," *2021 IEEE International Symposium on Antennas and Propagation and USNC-URSI Radio Science Meeting (APS/URSI)*, Singapore, Singapore, 2021, pp. 51-52. doi: 10.1109/APS/URSI47566.2021.9704737

3. S. Pancrazio, P. Nguyen, **S. Wagner**, A. Hossain and A. -V. Pham, "Digital Pre-Distortion to Correct UWB Pulses in a Boresight Test," *2021 IEEE International Symposium on Antennas and Propagation and USNC-URSI Radio Science Meeting (APS/URSI)*, Singapore, Singapore, 2021, pp. 525-526. doi: 10.1109/APS/URSI47566.2021.9704281S.

4. ***Wagner, S**. Pancrazio, A. Hossain and A. -V. Pham, "Experimental Detection of Buried Sub-mm Diameter Wires Using Microwave Ground-Penetrating Radar," *2021 IEEE USNC-URSI Radio Science Meeting (Joint with AP-S Symposium)*, Singapore, Singapore, 2021, pp. 37-38. doi: 10.23919/USNC-URSI51813.2021.9703496

5. **S. Wagner**, A. V. Pham, "Standoff Non-Line-of-Sight Vibration Sensing Using Millimeter- Wave Radar," *2020 17th European Radar Conference (EuRAD)*, Utrecht, Netherlands, 2021, pp. 82-85.

6. ***S. Wagner** and A. Pham, "Structural Effect on Image Quality Degradation in Ground-Penetrating Radar Array," *2019 IEEE International Symposium on Antennas and Propagation and USNC-URSI Radio Science Meeting*, Atlanta, GA, USA, 2019, pp. 1631-1632.

7. ***S. Wagner**, G. Le and A. Pham, "Ultrawideband Compact 50:200 Ohm Guanella Balun Using Asymmetric Broadside-Coupled Lines," *2018 Asia-Pacific Microwave Conference (APMC)*, Kyoto, 2018, pp. 485-487.

8. ***S. Wagner**, A. Pham, S. Bond and J. Jeon, "Design of a Wideband Resistively Loaded Vee Dipole Fed by an Even-Mode Matched Marchand Balun," *2018 IEEE International Symposium on Antennas and Propagation USNC/URSI National Radio Science Meeting*, Boston, MA, 2018, pp. 1353-1354.

9. G. Le, **S. Wagner**, C. Pham, J. S. Gomez-Diaz, A.V. Pham, "Inverted-F Antenna Radiation Efficiency Enhancement Based on a Slotted Ground", *IEEE Antennas and Propagation, URSI Conference 2018*. Boston, MA

Introduction

Ground-penetrating radar (GPR) is an electromagnetic sensing modality used to image the sub-surface environment. The operating principle of GPR relies on the reflection of emitted electromagnetic waves by buried targets which, when received, can be processed and interpreted as the distribution of reflective objects below ground. Typical uses of GPR include humanitarian de-mining [1, 2], buried utility location in construction sites [3-5], and archaeological dig-sites [6, 7]. Though GPR has existed for many years [8], development of new UWB components, GPR signal and image processing pipelines, and overall GPR systems has not slowed down. The main areas of improvement in literature have been in increasing the bandwidth, transmitted power, and detection quality of GPR systems and sub-components. Depending on the application, GPR systems operate in the MHz-to-low GHz range. Deep-looking ground penetrating radars operate in the tens of MHz [9, 10], while shallower GPRs can extend into the low GHz range [11]. In this work, we focus on shallow-looking GPRs. The best operating frequency and bandwidth of a GPR is determined by its operating conditions. Because the reflected electromagnetic wave will travel through the soil twice – once down, once up – the soil's electromagnetic attenuation will limit the GPR system's high operating frequency by decimating high frequencies. High frequencies are the most attenuated because the attenuation of soil is dominated by water, which has increasing attenuation with respect to frequency [12]. The GPR system's lower operating frequency is realistically limited by the antenna size – critically, in order to obtain non-distorted targets, the antenna's group delay profile must be flat, its input impedance well-matched, and its overall transfer function (antenna-to-antenna) relatively flat. At low frequencies, a typical antenna may have a large negatively-sloped group delay, high input impedance, and low gain. Therefore, a system which uses these low frequencies with such an antenna will encounter undesired distortion.

It is critical to know beforehand the full performance of the antenna in the operating band before deployment. However, there seems to be a gap in literature where many antennas are designed with the major specifications in mind – gain, bandwidth, and group delay – but without reference to the still important but harder-to-quantify tertiary specifications that still impact the radar scan. In this work, we tackle this question of what are the remaining issues for ground-penetrating radar design.

There are three main types of ground-penetrating radar system. First, an impulse-GPR works in the time domain by generating, transmitting, and receiving a single pulse with a large instantaneous bandwidth such as in [13-15]. This work focuses on impulse-GPR. Impulse-GPR offers a lower SNR compared to the other types of GPR, but fast digitization times per unit of bandwidth (on the order of tens of μs/GHz) make impulse-GPR the most practical technology for fast-scanning GPR. The second type of GPR is Stepped-Frequency Continuous Wave (SFCW)-GPR as in [16-18]. SFCW-GPR works by transmitting and digitizing a narrowband signal and scanning that frequency across an entire bandwidth. A majority of SFCW implementations actually use a vector network analyzer (VNA) for transmission and receiving, which causes long scan times (on the order of ms/GHz) which reduces practicality at the benefit of increased SNR. Several SFCW-GPR implementations improve acquisition time by transmitting several frequencies simultaneously and exploiting orthogonality at the cost of increased complexity. Lastly, frequency-modulated continuous wave (FMCW)-GPR is the implementation of the commonly-used FMCW radar method which measures the distance of objects by measuring the beat frequency between transmitted and received chirps. While FMCW radar is a very popular option for most radar applications, FMCW-GPR has seen less adoption in GPR literature, likely due to the difficulty of creating high-precision FMCW components with the ultra-wide bandwidth

ratios seen in GPR. Still, FMCW-GPR has seen success in [19-21]. In terms of practicality, a typical FMCW-GPR occupies a mid-space between impulse-GPR and SFCW-GPR in terms of both SNR and acquisition time (practicality).

In this dissertation, we answer the question of: what are the secondary phenomena which affect impulse-GPR imaging quality, and how do we fix them? To answer these questions, we build the widest-bandwidth time-domain GPR system presented in literature, and design equipment to test the quality of these GPR scans. In the first chapter, we focus on the GPR antenna with designs of two versions of RLVDs (resistively loaded vee-dipoles) designed to radiate pulses faithfully over a wide bandwidth. In the second chapter, we a set of general specifications for GPR antennas and a deep-dive into how system jitter affects antenna design. In the third chapter, we describe the 0.3 – 12 GHz receiver build with a deep-dive into the designed 12 GHz 100 GS/s equivalent-time sampling FPGA-based receiver. In the fourth chapter, we provide system block diagrams, explanations, and photographs of the developed GPR systems. In the fifth chapter, we present the processing pipeline with data preconditioning, imaging algorithms, and imaging statistics/detection with useful code. In the sixth and final chapter, we present results of 2D GPR scans around Kemper Hall at UC Davis.

1. Ground-Penetrating Radar Antennas

In a ground-penetrating radar (GPR) system, antennas are the interface between the transmitter and receiver's guided signal and the ground-penetrating electromagnetic wave. Due to their ultrawideband and complex nature, antennas used in GPR are the source of many unwanted effects. In addition, the niche application of GPR means that an antenna, though it may work well in another application, may perform poorly when pointed towards the ground for imaging. In this chapter, we present two antenna designs – the Marchand-balun fed Resistively Loaded Vee Dipole (RLVD) and its wider-shaped cousin the Elliptical RLVD (ERLVD) designed to mitigate some of the unwanted effects of antennas in GPR.

A. Resistively-Loaded Vee Dipole

This section contains significant portions from [22] reprinted with permission. The designed RLVD operates in a multi-static ground-penetrating radar (GPR) with close proximity to receiving antennas. A major performance limitation of this system is low-frequency out-of-band coupling saturating the receiver. The objective is to redesign the RLVD to have higher out-of-band rejection and longer arms for better low-frequency directivity.

The RLVD achieves non-reflectivity through resistive loading following the Wu-King profile [23]. Kim [24] modified the loading profile to reduce input reflections:

$$\frac{1}{R(s)} = \frac{1 - \frac{s}{h}}{R_0} + \frac{\left(1 - \frac{s}{h}\right)^2}{mR_0} \tag{1}$$

where $R(s)$ is resistance along the arm, s is position, h is total arm length, R_0 is a resistance in Ohms, and m is a modifier.

The input impedance of a RLVD is determined by the spacing at the feed point that forms a coplanar stripline (CPS) transmission line structure. Previous work on RLVDs uses a double-Y balun to transform a 50 Ω input to a 200 Ω RLVD [24, 25]. There are two downsides to using the double-Y balun structure for band-limited pulsed radar – it has poor out-of-band rejection and a large footprint on the antenna board. In this paper we have developed a bandpass Marchand balun for the RLVD. The Marchand balun occupies a 50 mm x 54 mm area, 50 mm smaller compared to the double-Y balun. Design procedures of both the RLVD and the even-mode matched Marchand balun are presented and results are shown.

i. Design of a Resistively-Loaded Vee Dipole

The RLVD and balun sit on a 1.524 mm thick 4-layer Rogers RO4003C substrate. The RLVD impedance characteristic resembles a small capacitor at low frequencies [25] but converges at high frequencies to the CPS input impedance. The broadside Marchand balun naturally transforms to 50 Ω but even-mode matching techniques can increase that output impedance [26].

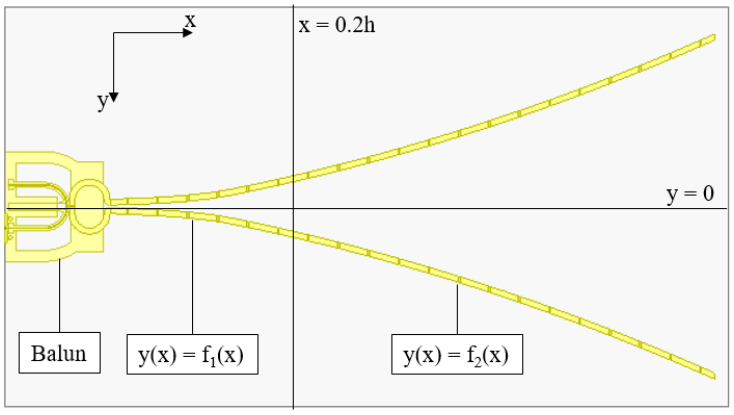

Fig. 1: ANSYS HFSS model of RLVD with sizing information

We choose an arm length *h* large enough to be directive at low frequencies. The final parameters are chosen such that the antenna is both directive at low frequencies but also matches the even-mode matched balun well.

ii. Even-Mode Matched Marchand Balun

The Marchand balun consists of two asymmetric broadside-coupled lines over a defected ground structure (DGS) as in [27]. The broadside-coupled lines without a ground plane naturally transform a 50 Ω impedance to a 50 Ω differential impedance. To achieve impedance transformation from 50 Ω to the RLVD input impedance, two transmission lines at the balanced port of the balun add even-mode impedance transformation [26].

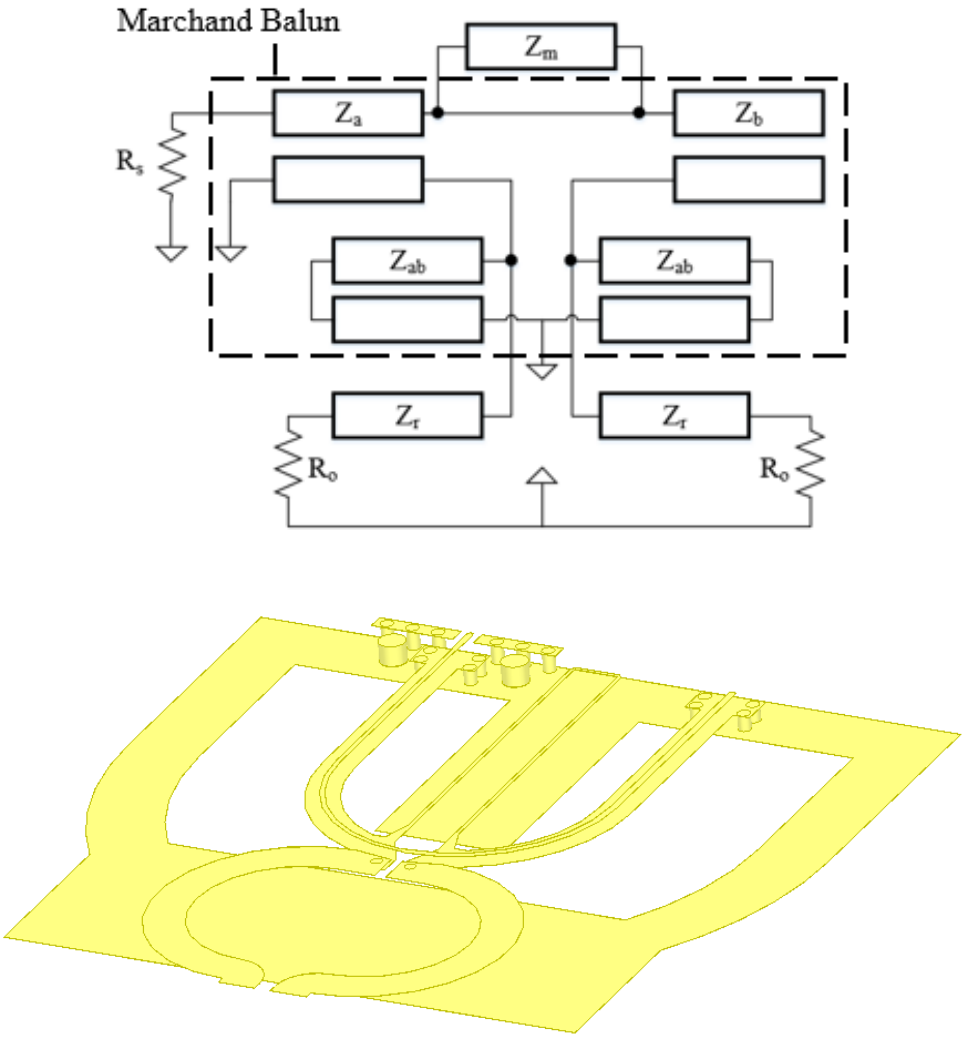

Fig. 2: (top) Circuit schematic diagram of even-mode matched balun. (bottom). HFSS 3-D model of completed balun.

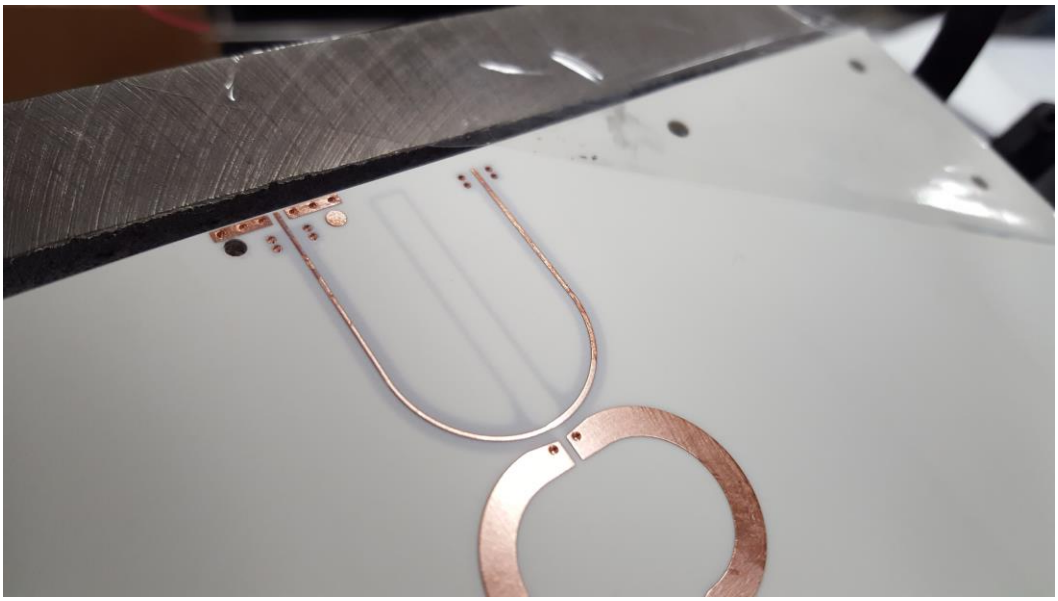

Fig. 3: Photograph of balun feeding RLVD without connector.

The balun is realized on the same 4-layer Rogers RO4003C substrate as the RLVD as shown in Figs. 2 and 3. The broadside-coupled lines are spaced on the first two layers. Lines Z_a, Z_b, and Z_r sit on the top layer while lines Z_m and Z_{ab} sit on the first inner metal layer. The DGS is interrupted to provide a ground plane for lines Z_m and Z_r. The impedances chosen for the proper balun performance are determined by the RLVD input impedance. Z_{ab} is defined by the defected ground structure and varies from approximately 150 Ω to 100 Ω along the line due to varying distances from the ground plane. Z_{ab} is ideally as high as possible to extend bandwidth [27], but the application bandwidth from 0.5 – 1.5 GHz does not require high Z_{ab}.

iii. Prototype and Measurement

The RLVD with an even-mode matching Marchand balun is prototyped and measured, below in Fig. 4.

Fig. 4: Photograph of the fabricated RLVD with even-mode matched balun

Below in Fig. 5 is the return loss measurement of the RLVD with even-mode matched balun.

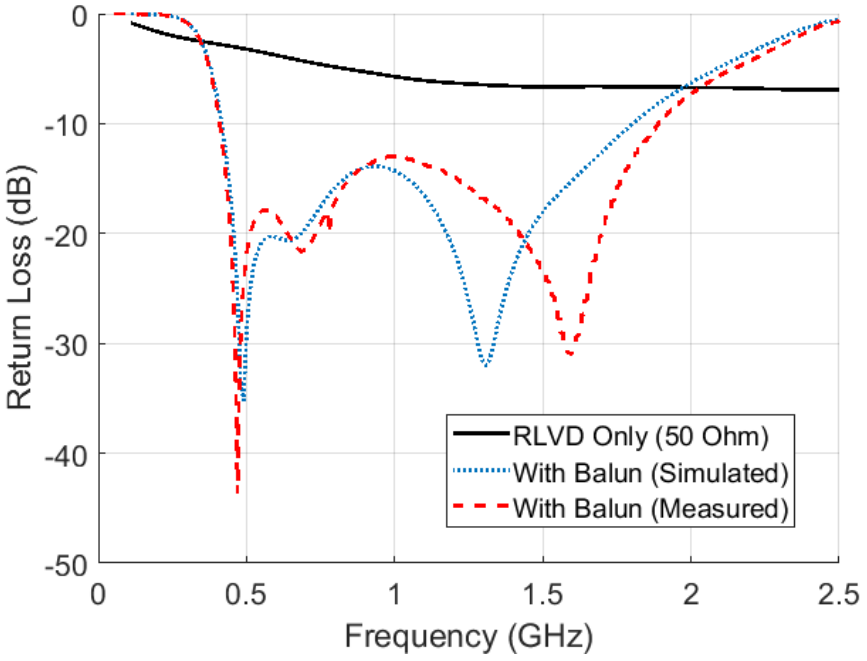

Fig. 5: Return loss simulations and measurements of the RLVD. RLVD only is matched differentially to 50 Ohms between the two arms.

From Fig. 5, measurement matches the simulation well at low frequencies, but has its second resonance peak shifted in frequency. The even-mode matched balun coupled with a larger antenna maintains a return loss greater than 1 dB for frequencies less than 300 MHz. Fig. 6 shows the measured radiation patterns, which are typical for an end-launch RLVD. Fig. 7 is a measurement

of the monostatic coupling between two antennas in the same plane, spaced with 10 cm from board to board.

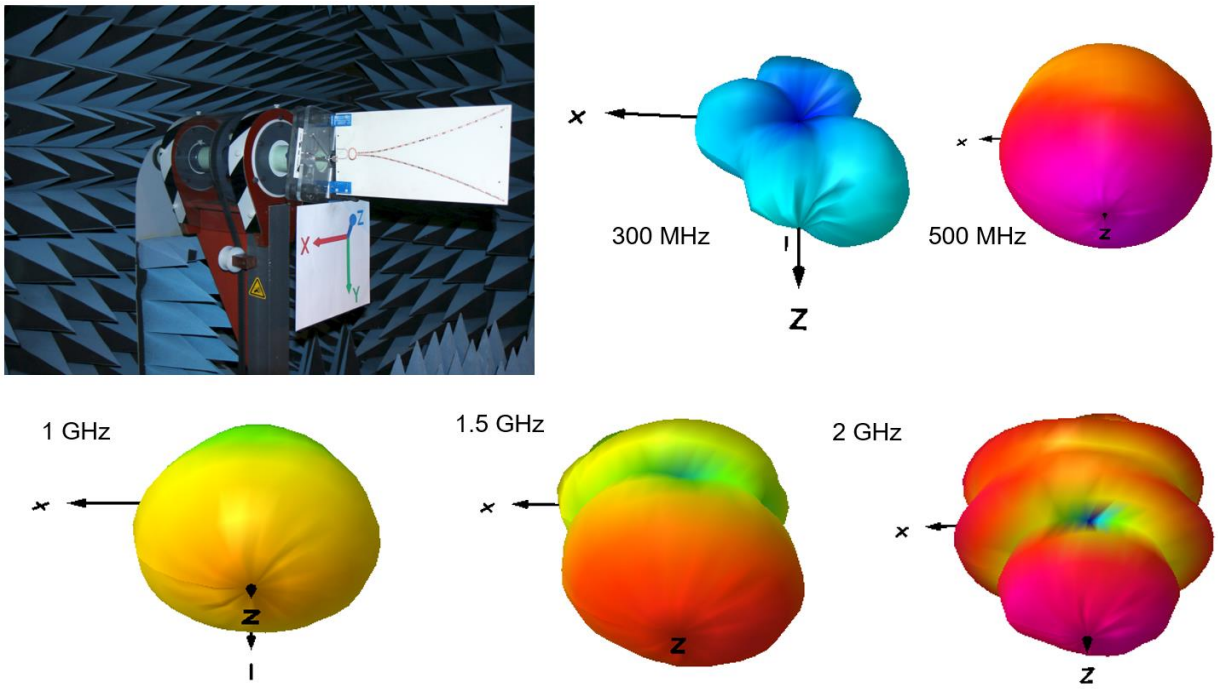

Fig. 6: Radiation patterns at 300 MHz, 500 MHz, 1 GHz, 1.5 GHz, and 2 GHz of the designed RLVD. Coordinate axes indicated in photograph.

A measurement similar to Fig. 7 for an RLVD with a double-Y balun [24] or another kind of high-pass transformer would have a nearly flat line extending into low frequency. Using this extrapolation, the band-pass characteristic of the even-mode matched balun provides an approximately 30 dB reduction in monostatic coupling at frequencies less than 300 MHz. This reduction in out-of-band low frequency energy also has a significant reduction on the length of the pulse ringing in a transmit conFiguration.

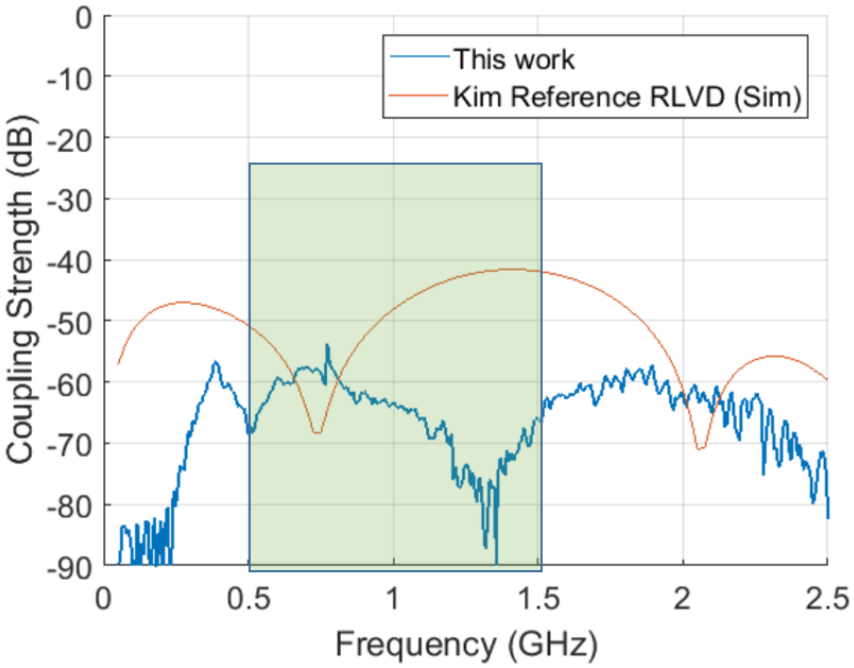

Fig. 7: S_{21} measurement of two prototyped RLVDs in the same plane (monostatic case) with 10 cm board-to-board separation.

In Fig. 8, the ringing after the main pulse shape only lasts for 2.5 ns. Additional returns at 20 ns and 30 ns are from cable reflections.

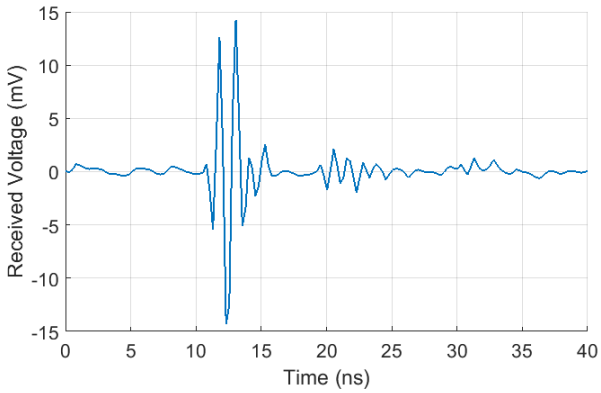

Fig. 8: Transmit measurement. Input pulse is a Mexican-hat pulse. Distance between antennas is 1 meter.

B. ERLVD & Guanella Balun

This section contains significant portions from [28], reprinted with permission. The resistively-loaded vee dipole (RLVD) has been explored as an excellent directional travelling-wave antenna

for ground penetrating radar (GPR) applications. However, its usage is often limited by its extreme negative gain, often less than -10 to -15 dB near its low operating frequency as well as its large size. Kim developed a version of the RLVD by modifying the arm shape and loading profile, improving gain from approximately -10 dB to -7 dB and achieving an operating frequency of 1.5 GHz for a length of 171 mm [29]. Yang used passive L-section filters to achieve a lower frequency of 500 MHz for a length of 150 mm, but gain is not explicitly mentioned [25]. Other modifications have also shown desirable performance enhancements [22, 24, 25, 30]. In this paper, we consider a novel concept of modification to the RLVD by changing the sub-element shape and size and explore increased flexibility in gain and bandwidth tradeoffs.

Planar realizations of the RLVD use surface-mount chip resistors to realize the Wu-King profile [23]. The geometry leads to a significant current crowding effect at the corners near the transition between printed strip and resistor. Additionally, a thin strip does not fill the space of the board that the RLVD is printed on effectively, which goes against wideband design principles. We instead substitute a printed elliptical element in place of the wire or printed strip in an RLVD. The elliptical sub-element fills more space of the antenna as well as creates smoother current transitions between sub-elements.

We propose a new elliptical resistively loaded vee dipole antenna (ERLVD). By simply replacing the rectangular printed strip with elliptical sub-elements, we can achieve much lower frequency and much higher gain. We show that there is increased flexibility in design of an ERLVD compared to an RLVD. We create prototypes of two versions of ERLVD and compare their performance to a classical RLVD of the same length. The first ERLVD prototype with no growth rate parameter has a bandwidth from 0.49 – 6.41 GHz at an arm length of 104 mm. This prototype is shown to have a 2 to 3 dB gain increase over a similarly sized RLVD prototype. The

second ERLVD prototype with a high growth rate attains a low operating frequency of 290 MHz with a relative gain increase of up to 8.5 dB. The ERLVD can be a potential replacement for RLVDs in a ground penetration radar application [31]. This paper is organized as follows: Section II covers the structure and theory of the ERLVD, Section III contains a parametric study of the growth rate parameter, and Section IV details the measurements of two ERLVD prototypes.

i. Development of Antenna Structure

Physical Shape of the ERLVD

The ERLVD with an axial ratio and growth rate can be divided into three main subcategories, all pictured in Figures 9a-9c. First, we define the growth rate as:

$$\Gamma(n) = \frac{L_{n+1}}{L_n}. \tag{2}$$

where L_n is the length of the n^{th} elliptical sub-element's major axis.

With a constraint of growth rate Γ=1 in Figs. 9a and 9b, we can have axial ratio $\alpha < 1$ and $\alpha > 1$, respectively. The ERLVD should also have a cut plane on its first sub-element passing through its center to form the correct input impedance. The cut plane may be relaxed for very high growth rate ERLVDs (approximately $\Gamma > 2$), where a wideband high impedance match is difficult to achieve. The three main subcategories of ERLVDs are pictured in Figs. 9a to 9c.

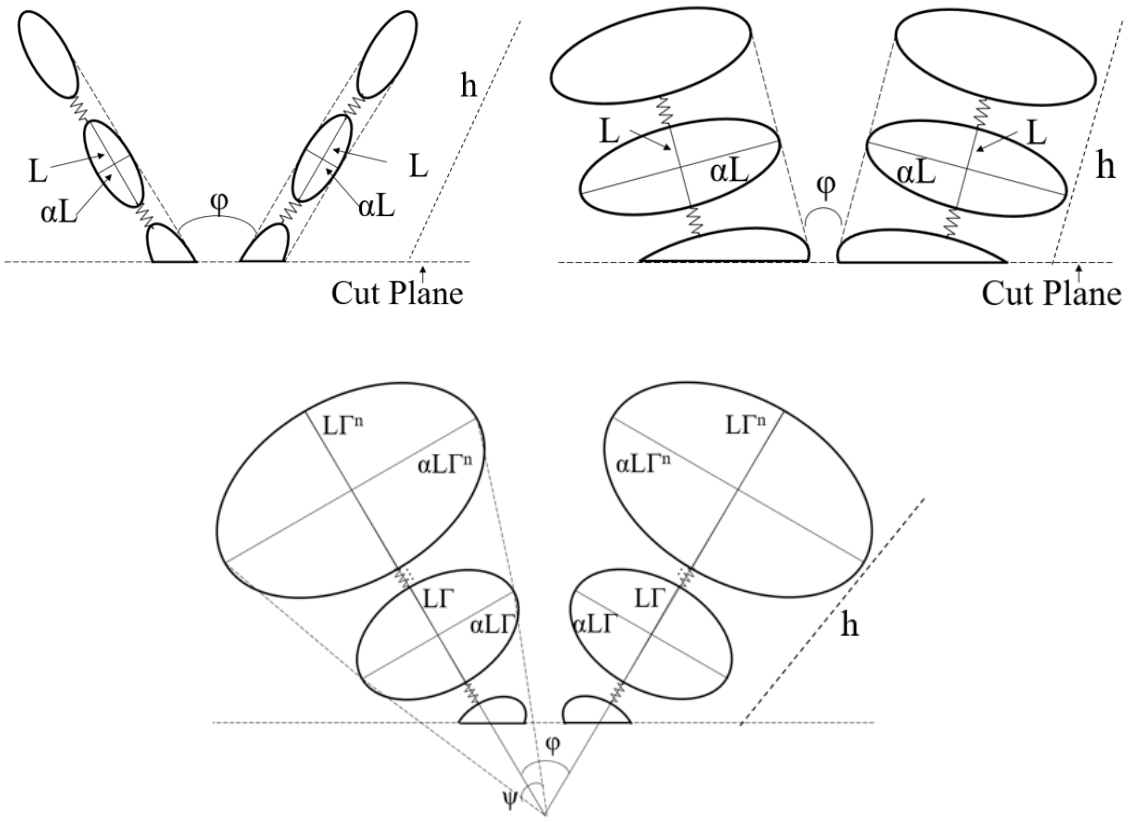

Fig. 9: (a) - ERLVD with $\alpha < 1$ and $\Gamma = 1$, b) ERLVD with $\alpha > 1$ and $\Gamma = 1$, and c) ERLVD with $\Gamma > 1$

Design Variables of the ERLVD

By including a non-rectangular sub-element, we add three design variables to the traditional straight-armed RLVD: an outer arm angle, an axial ratio (sub-element shape), and a growth rate. The design variables are listed in Table 1 with their description and are illustrated in Fig. 9c. The values of three variables are heavily interdependent and design equations are derived in this section. We can develop simple inter-relations based only on the geometry of the ERLVD.

Table 1: List of ERLVD Design Variables

Variable	Origin	Significance
ϕ	Inner Arm Angle	Determines maximum directivity [32]
ψ	Outer Arm Angle	Determined by growth rate Γ, indirectly affects bandwidth and directivity
α	Axial Ratio	Design choice, affects lower cutoff frequency and gain
h	Total Length of Arm	Affects lower cutoff frequency and maximum directivity [32]
L	Sub-element length	Determines N
Γ	Growth Rate	Integer numbers of growth rates are realizable with a constrained N. Deviation from unity implies higher gain, but worse bandwidth.
s	Sub-element separation	Spacing s is determined by the chip resistor dimensions
R_0	Wu-king resistive profile constant	Determined by shape of ERLVD [23]
N	Number of chip resistors	Higher N creates bandwidth better transient damping, due to better discretization of the Wu-King profile.

Next, we derive the design equations for the ERLVD. Using the geometry described in Fig. 9, we can derive the inter-relation for the height *h*, sub-element length *L*, resistor quantity *N*, spacing *s*, and growth rate Γ as:

$$h = \begin{cases} L\left(N + \frac{1}{2}\right) + Ns, & \text{if } \Gamma = 1 \\ L\left(\frac{1}{2} + \frac{\Gamma - \Gamma^{N+1}}{1-\Gamma}\right) + Ns, & \text{if } \Gamma \neq 1 \end{cases} \tag{3}$$

Next, we can define an external angle ψ by connecting the external points on the minor axis of the two extreme sub-elements.

$$\tan\frac{\psi}{2} = \left| \frac{L\alpha(\Gamma^N - 1)}{L\left[1 + 2\frac{\Gamma - \Gamma^N}{1-\Gamma} + \Gamma^N\right] + 2Ns} \right|, (\Gamma \neq 1) \tag{4}$$

It must be noted that (4) is only derived for ERLVDs with growth rate not equal to unity. With growth rate equal to unity, the external angle is defined to be equal to zero. If we set the inner angle $\varphi = 180^{o}$, then the outer arm angle ψ describes a flare angle similar to that of a bowtie antenna that can be optimized for bandwidth. It must be noted that the outer arm angle is defined between the first and last elements, and the actual angle varies with sub-element number.

In order to design an ERLVD, we follow the steps:

1. Choose $h = \lambda_{low}/4$
2. Choose s based on the dimensions of the lumped resistors. Calculate R_0, the Wu-King resistive profile constant [23]. R_0 may also be optimized using a genetic algorithm as shown in [33].
3. Select axial ratio α – increased α implies higher gain and bandwidth, but larger arm width
4. Choose a sub-element length L to be used in (5) to derive L_{eff}. Substitute L_{eff} in (3) to generate pairs of Γ and N that satisfy h.
5. Select inner arm angle ϕ. Based on the choice for α, ϕ may have to be changed to fit the elliptical arms.
6. For each pair generated in Step 4, simulate the antennas and choose the version of (Γ, N) with desired antenna parameters.

Current Flow on Elliptical Sub-Elements

Now, we look at the effect on the effective total length of the antenna from using elliptical sub-elements. Using the ANSYS High Frequency Structure Simulator (HFSS), we plot the 1 GHz

vector surface current on sub-elements with α = 0.5 and 1.5 versus a rectangular sub-element in Fig. 10.

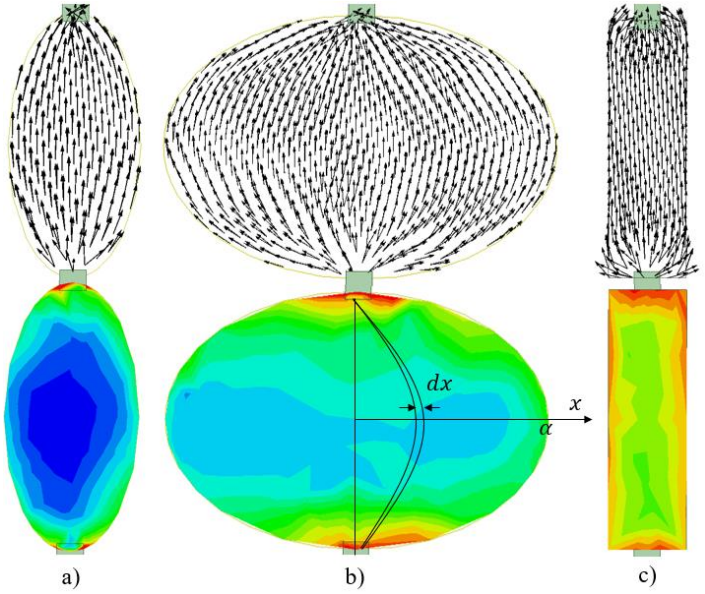

Fig. 10: Direction and magnitude of surface current flow at 1 GHz on elliptical sub-elements with a) α = 0.5, b) α = 1.5 compared to c) rectangular elements.

The current vectors flow smoothly along the metallized surface. In contrast, the current on a rectangular sub-element experiences a sharp direction change at the corners of the rectangle. As current does flow along a longer path, it effectively creates a meandering structure to form a longer antenna based on the length of the path. This effective sub-element length depends on the approximate magnitude of current filament flowing through each infinitesimally-thin elliptical path dx as indicated in Fig. 10 and its corresponding elliptical integral according to (5):

$$L_{eff} \approx -\frac{1}{\beta}\tan^{-1}\left[\frac{\mathrm{Im}\left(\int_0^{\alpha} J_x(x,\omega)e^{-j\beta L_x}dx\ \right)}{\mathrm{Re}\left(\int_0^{\alpha} J_x(x,\omega)e^{-j\beta L_x}dx\ \right)}\right] \tag{5}$$

where L_{eff} is the effective sub-element length with axial ratio α, β is the lossless propagation constant, $J_s(x, \omega)$ is the magnitude of the surface current at axial ratio x and frequency ω, and L_x is the effective length of the current's path at axial ratio x. The complete derivation of (5) is included in the appendix. Equation (5) can simply be extended for ERLVDs with non-unity growth rate by summing N+1 integrals, substituting $L = L_k = L\Gamma^k$ where $k \in [0, N]$.

While (5) tells us about the effective length of each particular sub-element, the actual value L_{eff} is problematic to calculate in practice. Specifically, the distribution of the surface current $J_s(\alpha, \omega)$ over the sub-element varies with sub-element number. For example, the first two sub-elements from the feedpoint have a current distribution weighted towards the inside of the antenna due to the differential excitation, while sub-elements near the end of the antenna have a surface current distribution that is well-balanced over the middle axis. Thus, (5) does not take these effects into account. However, (5) is still useful to calculate approximate length of the ERLVD sub-element.

Additionally, as current distribution varies with frequency, (5) implies that there is increased variation in the group delay of the ERLVD with nonzero α. This variation in the group delay, however, tends to have insignificant magnitude with respect to other causes such as the low-frequency end of the impedance bandwidth.

To provide an example, we choose to analyze the effective length of an ERLVD with elliptical sub-element axial ratio α = 1.0 and $\Gamma = 1$ compared to an otherwise identical RLVD. For the x-dependence of our surface current distribution, we model $J_s \propto x^2$. This is found from HFSS simulation to have reasonable accuracy for an approximation. By neglecting variations in the x-dependence of J_s with respect to frequency (i.e., assuming that J_s can be separated into two separate

functions $J_s \propto W(\omega)X(x)$), the frequency dependence of the integrals in (5) drops out. Choosing $\beta = {}^{\omega}/_{c}$ in air, we calculate that an elliptical sub-element length of L = 10 mm results in an effective sub-element length L_{eff}= 13.69 mm. This is a 36.9% increase in sub-element length. Taking parameters N = 9 and s = 1 mm, (5) results in an effective antenna arm length h of 139 mm instead of 104 mm. For reference, the total length increase of 35 mm reduces the $\lambda/4$ frequency from 720 MHz to 539 MHz. In the following sections, we consider full-wave simulations to better understand the effect of the elliptical sub-elements.

ii. Parametric Study of ERLVD Variables With Constant Non-Unity Growth Rate

In this section, we explore the bandwidth and gain of ERLVDs of the type in Fig. 9c. To provide a fair comparison, the antennas in this parametric study are kept at a constant length of 104 mm. With an integer N and constant total length h, we are constrained to a finite number of ERLVDs for comparison. We set design variables to be constant in Table 2. The resulting geometric shapes are shown in Fig 11. We iterate over all possible N with $\Gamma \geq 1$ for a single sub-element length L using (3). Each iteration is then simulated with HFSS for comparison of impedance bandwidths and gains.

Table 2: Γ > 1 Parametric Study Design Variables

Variable	Value (If not swept)	Variable	Value (If not Swept)
ϕ	60º	s	1 mm
α	0.75	R_0	33 Ω
h	104 mm		
L	10 mm		

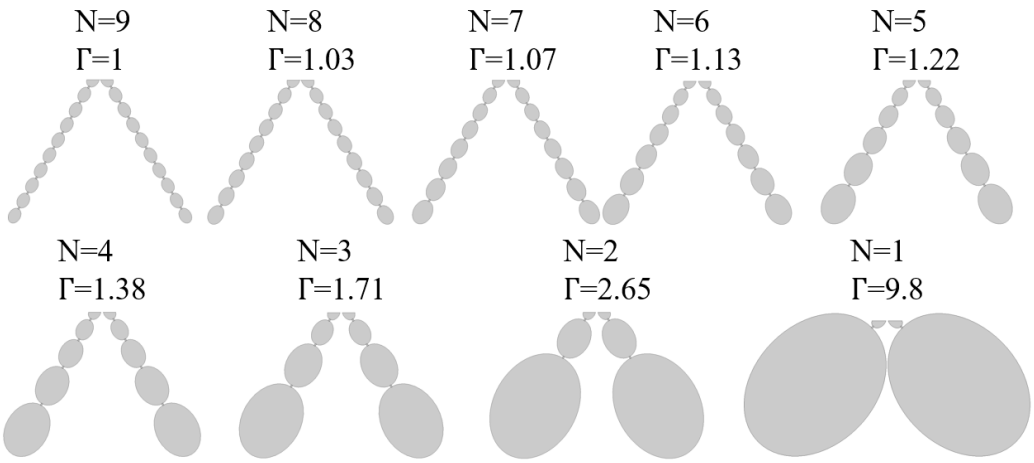

Fig. 11: Images of ERLVDs with properties given in Table 2. Numbers above each ERLVD indicate number of resistors and per arm growth rates.

Below in Fig. 12, we plot the bandwidth of all iterations of ERLVDs, starting from unity growth rate at N=9 up to N=1. A black bar indicates that the VSWR of the ERLVD is less than 2.0.

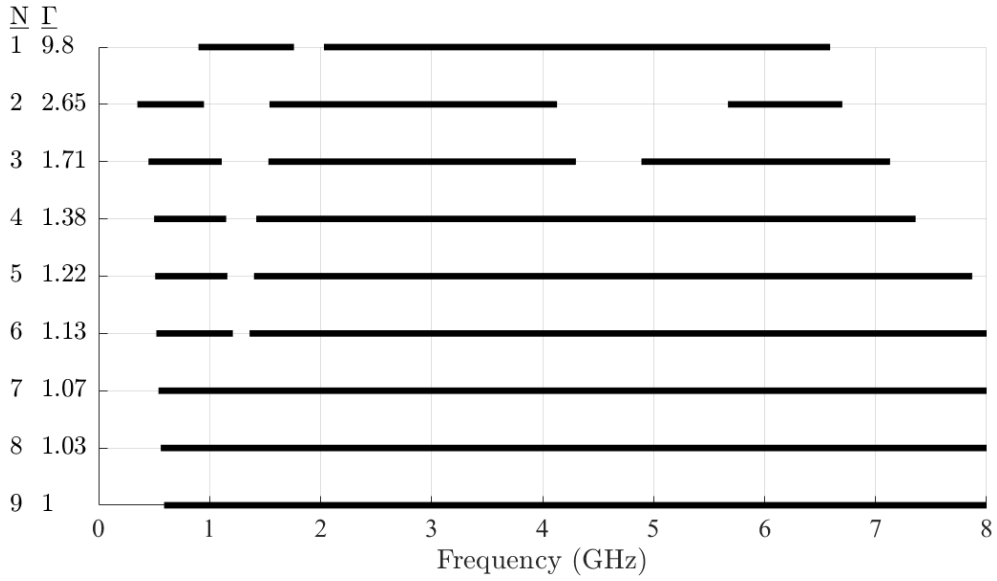

Fig. 12: Simulated usable bandwidths of all ERLVDs with growth rate greater than 1. Black line indicates VSWR < 2.0.

The cutoff frequency of unity growth rate ERLVD (N=9) is 550 MHz. The lowest cutoff frequency is 292 MHz at N = 2. A reference 104-mm long RLVD with strip width of 3 mm has a

simulated VSWR<2.0 lower cutoff frequency of 768 MHz. Thus, for the same length, the ERLVD can achieve a lower operating frequency decrease by 476 MHz.

There are several patterns visible in the bandwidth plot of Fig. 12. First, lower operating frequency generally tends to decrease with N, with exception of N=1. Note that for N is less than 9, Γ will not be equal to 1. The decrease in minimum operating frequency can be attributed to the effective increase in length mentioned previously. Second, bands where VSWR > 2 open up as we decrease N. These bands occur because of two phenomena: first, using a low N to discretely model the Wu-King profile leads to the creation of standing waves. Second, each sub-element along the length of the antenna arm has a resonant frequency determined by its electrical size. For Γ not equal to 1, the progressively larger sub-elements have staggered sub-element resonant frequencies, and large sub-elements have resonant frequencies entering the band of interest. These two phenomena lead to deviation from the flat impedance profile and create a poor match. Next, Fig. 13 shows the boresight gains of all ERLVDs with $\Gamma \geq 1$.

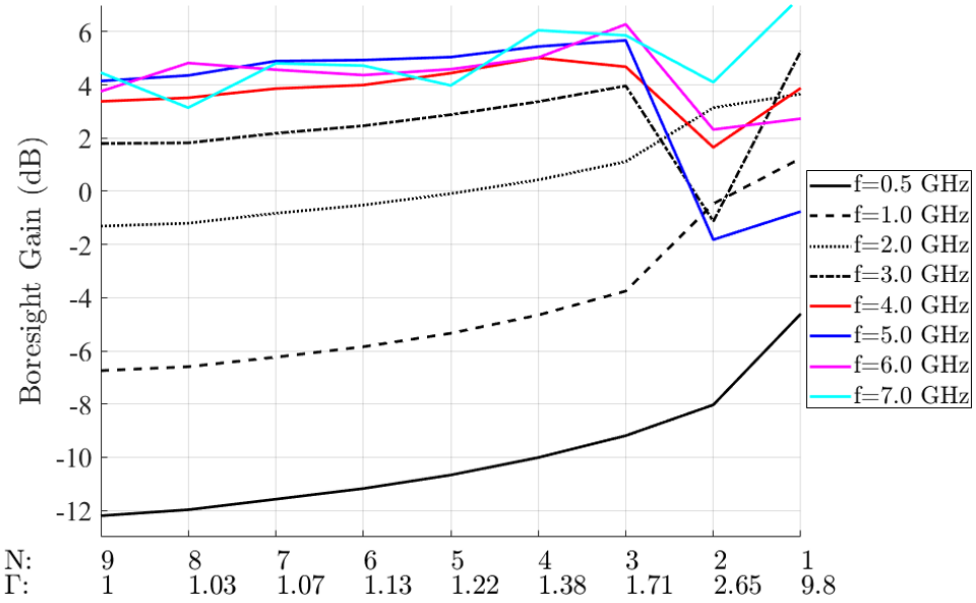

Fig. 13: Simulated comparison of boresight gains for ERLVDs with properties detailed in Table 2. All ERLVDs have a physical arm length of 104 mm.

In the boresight gain plot in Fig. 13, we can see the effect of increasing sub-element size. As N decreases, the ERLVD has higher average boresight gain. However, directivity decreases with fewer sub-elements or lower N. Hence, the dominant factor that improves gain is less dissipated power in resistors for lower N. Additionally, VSWR degrades when N is lower than 3 due to poor realization of the Wu-King profile. As seen from Fig. 13, gain is degraded at high frequency when N is less than 3. N = 3 provides an excellent tradeoff point of gain and bandwidth.

Along with Γ, we have conducted parametric simulations sweeping the inner arm angle ϕ using an ERLVD with Γ=1.71, α=0.75, N=3, and h=104 mm to analyze the sensitivity. Fig. 14 shows the simulated directivity and lower cut-off frequency with respect to inner arm angle ϕ. The boresight directivity is very dependent on the inner arm angle. The relationship between inner arm angle and directivity changes with frequency as is known from [32]. An optimization for directivity at 3 GHz would dictate an inner angle of 90°, while a design for 5 GHz would dictate a smaller inner angle of 60°. For broadband design, a compromise on either the upper or lower frequency

band's directivity must be made. From Fig. 14, we can also conclude that the increase of inner arm angle decreases the lower operating frequency. Sweeping the entire range of ϕ from 30° to 120° changes the lower operating frequency from 0.59 GHz to 0.46 GHz. The changes of directivity and lower cut-off frequencies with respect to inner arm angle ϕ are due to the control over the direction of current and over the coupling strength at the feed-port, respectively.

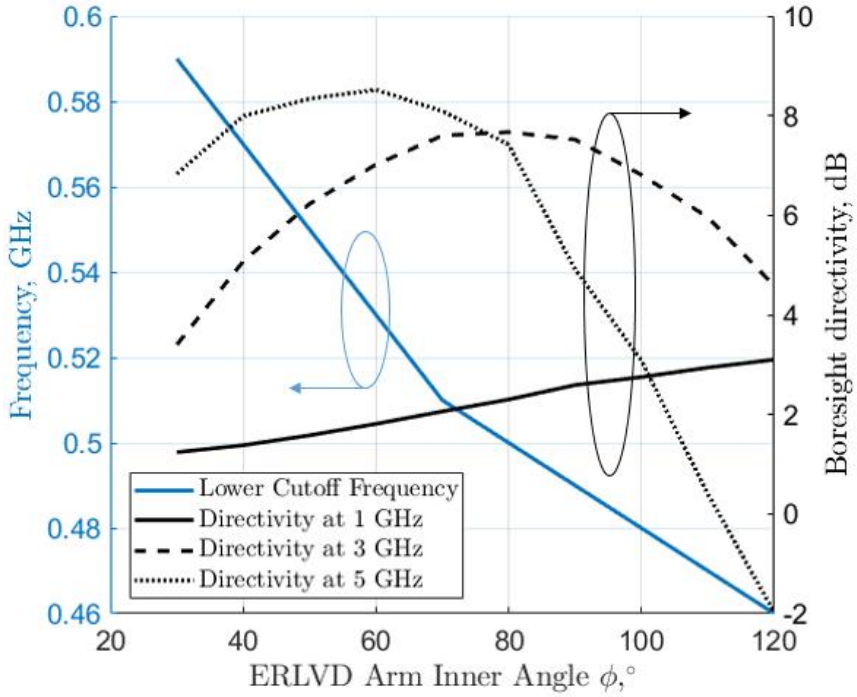

Fig. 14: Simulated lower cutoff frequencies and boresight directivities versus inner arm angle for an ERLVD with Γ=1.71, $\alpha = 0.75$, N=3, and h=104 mm.

iii. Design and test of Select ERLVDs

To validate our proposed designs, we have designed and prototyped an ERLVD with Γ=1, α=1.5, N=9, and an ERLVD with Γ=2.654, α=0.5, and N=2. We choose these antennas to represent the two sides of the spectrum with respect to growth rate. We choose N=2 instead of N=1 because of its favorable bandwidth. Additionally, we prototype an RLVD of the same length of 104 mm to compare our measured results. These antennas are fed by a Guanella balun that transforms from

50-200 Ohms over a wide bandwidth [34]. The antenna and balun are realized on the same board made of 10-mil (0.254 mm) thick Taconic TLY-5 with relative permittivity 2.2. For clarity and brevity, we denote these antennas as: Fig. 15a) RLVD, Fig. 15b) ERLVD$_{\Gamma=1}$, and Fig. 15c) ERLVD$_{\Gamma=2.6}$.

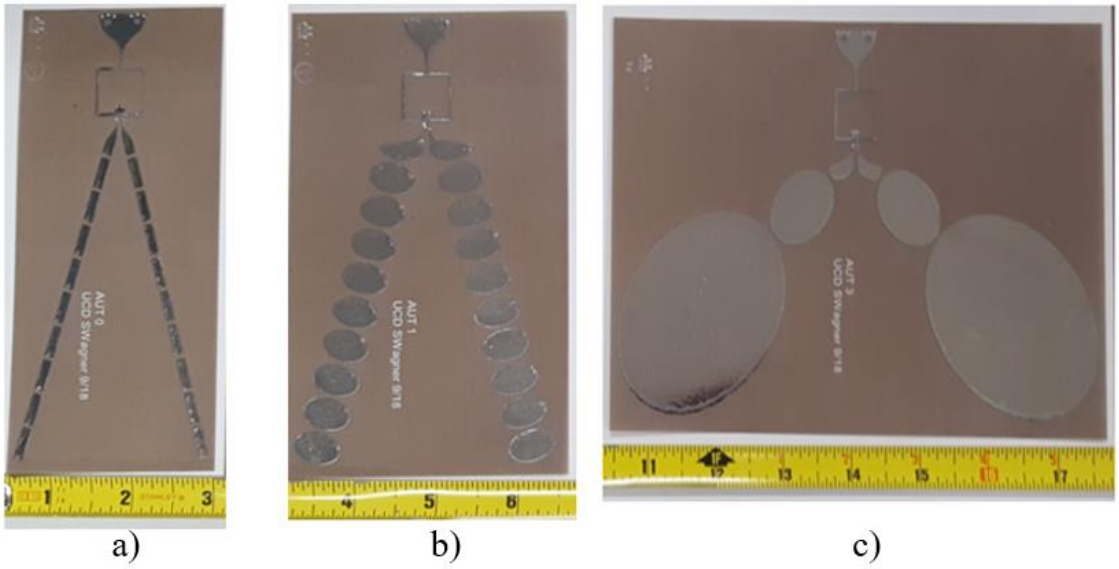

Fig. 15: Photograph of fabricated RLVD and ERLVDs. a) Base RLVD for comparison, called "RLVD", b) ERLVD with unity growth rate and axial ratio 1.5, called "ERLVD$_{\Gamma=1}$" and c) ERLVD with high growth rate and N=2, called "ERLVD$_{\Gamma=2.6}$"

The antennas are measured using an Agilent E8358A PNA (Performance Network Analyzer) over frequencies from 10 MHz to 8 GHz. One-port calibration is performed to set the measurement reference at the coaxial connector. To provide mechanical support for testing, a thin plastic backing plate is 3-D printed and mounted on the ERLVD. The plastic structure is experimentally found to have no dramatic effect on the antenna performance.

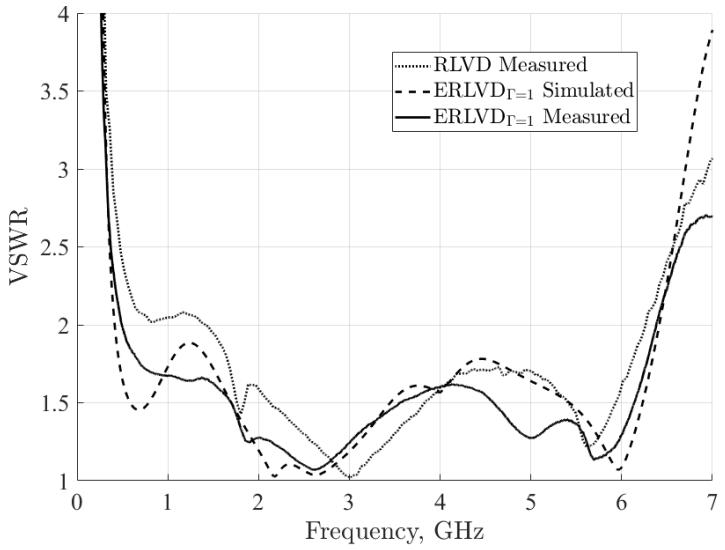

Fig. 16: Simulated and measured VSWR response of unity growth-rate ERLVD$_{\Gamma=1}$ in Fig. 15b compared to base RLVD in Fig 15a.

Figs. 16 and 17 show the measured VSWR of the two prototyped ERLVDs compared to their HFSS simulation results. The measured results correlate well with the simulated data from HFSS. The prototyped ERLVD$_{\Gamma=1}$ (Fig. 16) has a VSWR < 2.0 bandwidth from 490 MHz – 6.41 GHz, a bandwidth ratio of 13:1. The high growth rate ERLVD$_{\Gamma=2.6}$ (Fig. 17) has a VSWR < 2.0 bandwidth from 290 MHz – 940 MHz, 1.57 GHz – 4.12 GHz, and 5.66 GHz – 6.63 GHz. The in-band VSWR ripples never increase above 4.0 VSWR. It must also be noted that the in-band VSWR peak of approximately 3 at 7 GHz is due to an innate response of the ultrawideband Guanella balun used to feed these antennas [34].

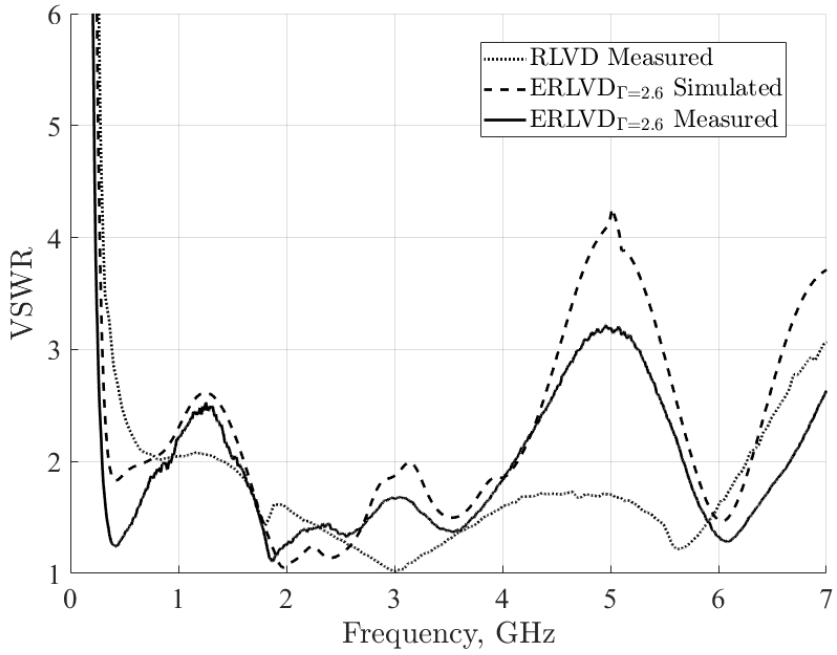

Fig. 17: Simulated and measured VSWR response of high growth-rate ERLVD$_{\Gamma=2.6}$ in Fig. 15c compared to base RLVD in Fig 15a.

Next, we examine the transient response of 3 pairs of identical antennas, specifically RLVD to RLVD, ERLVD$_{\Gamma=1}$ to ERLVD$_{\Gamma=1}$ and ERLVD$_{\Gamma=2.6}$ to ERLVD$_{\Gamma=2.6}$. For each experiment, the two antennas are placed one meter apart in an anechoic chamber facing each other. The input pulse (Fig. 18a) is generated by an arbitrary waveform generator (AWG) based on the AD9162 ADC from Analog Devices and is centered around 1 GHz with -10 dB bandwidth from 300 MHz – 2.5 GHz. This input pulse is fed into the transmitting antenna. The receiving antenna is directly connected to an 8 GS/s real-time oscilloscope to measure the waveform.

In Figs. 18b, 18c, and 18d, we compare the measured pulse voltage received from a normal (rectangular) RLVD, an ERLVD$_{\Gamma=1}$, and an ERLVD$_{\Gamma=2.6}$. First, we can note the absolute peak voltage received for each pair of antennas. The RLVD, ERLVD$_{\Gamma=1}$, and ERLVD$_{\Gamma=2.6}$ have peak voltages of 4.93 mV, 8.01 mV, and of 63.7 mV, respectively. These peak voltages correspond to

a 4.2 dB and 22.2 dB increase in peak voltage for the unity growth rate $ERLVD_{\Gamma=1}$ and the high growth rate $ERLVD_{\Gamma=2.6}$ compared to the RLVD. The higher signal response is as predicted from the simulated gain in Fig. 13, where the high growth rate $ERLVD_{\Gamma=2.6}$ has significantly higher gain than other antennas. We can see that the $ERLVD_{\Gamma=2.6}$ has higher gain at lower frequency.

We calculate the fidelities of Figs. 18b, 18c, and 18d using a normalized cross-correlation with the input. The base RLVD has a pulse fidelity of 0.712. The $ERLVD_{\Gamma=1}$ and $ERLVD_{\Gamma=2.6}$ have pulse fidelities of 0.835 and 0.883, respectively. Both ERLVDs transmit the given pulse more faithfully.

We used MATLAB to transform the measured time-domain data into power spectral density (PSD) in Fig. 19. Compared to the RLVD, the $ERLVD_{\Gamma=1}$ and $ERLVD_{\Gamma=2.6}$ have approximately 5 dB and 18 dB increases in PSD over the pulse bandwidth in Fig. 18, respectively.

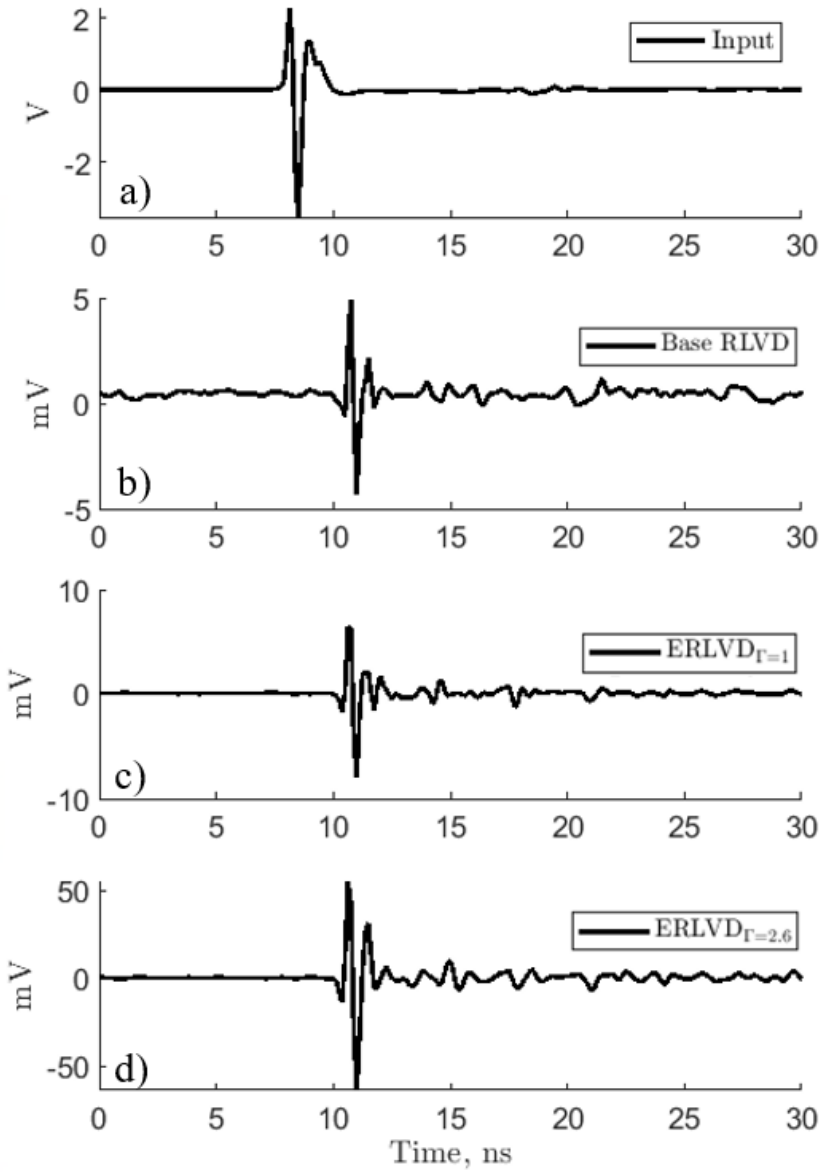

Fig. 18: Measured transient response of pair of identical antennas sighted boresight at 1 meter apart. a) Pulse input into the respective antenna, b) Pulse received by the pair of RLVDs, and c) Pulse received by the pair of ERLVD$_{\Gamma=1}$'s, d) Pulse received by the pair of ERLVD$_{\Gamma=2.6}$'s.

Additionally, the in-band VSWR of the high growth rate ERLVD$_{\Gamma=2.6}$ from 940 MHz – 1.57 GHz does not present a significant distortion in the radiated pulse PSD. It is clear that at higher frequencies greater than 3 GHz, the ERLVD$_{\Gamma=2.6}$ begins to lose its gain advantage. Overall, we can tell that the ERLVDs offer improved received pulse magnitudes without the tradeoff of pulse fidelity.

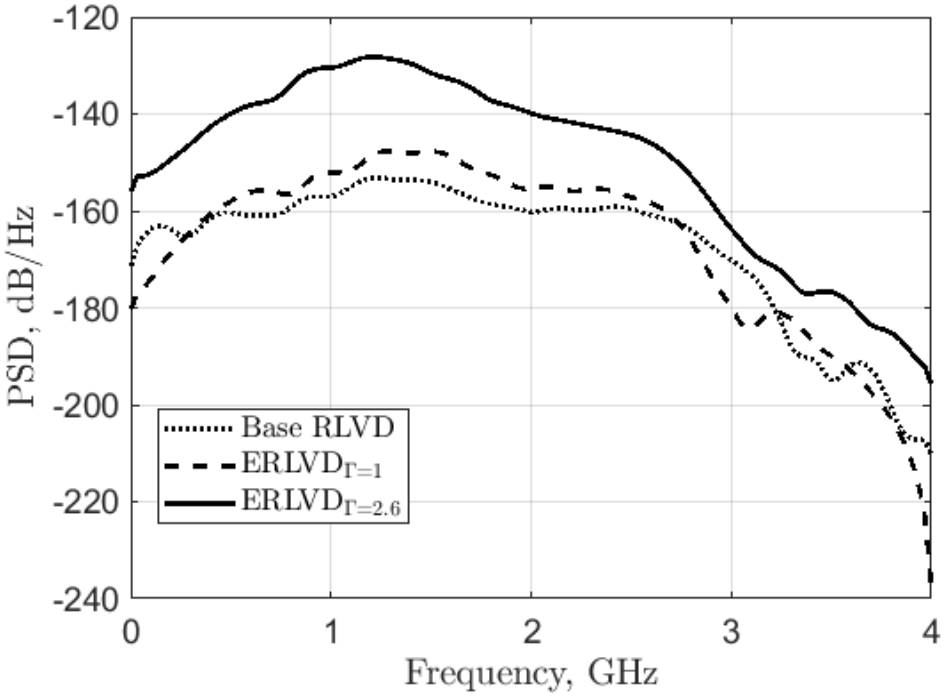

Fig. 19: Calculated power spectral densities (PSDs) in dB/Hz for the received signals at 1 meter in Fig. 18.

Finally, we examine the boresight gains of these prototyped antennas. The boresight gains are measured in an anechoic chamber using a reference antenna over the frequencies 300 MHz – 6 GHz. The measured data is compared to the simulated value in Fig 20.

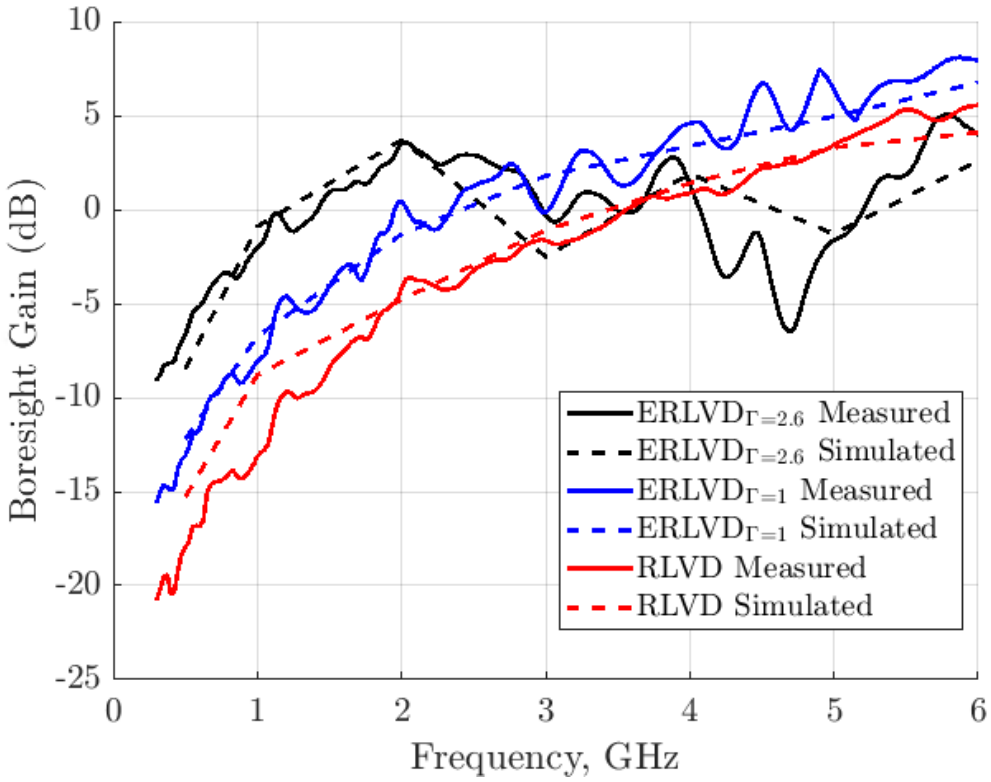

Fig. 20: Measured and simulated gains for the unity growth rate and high growth rate ERLVDs versus simulated RLVD for comparison.

There is a good agreement between the simulated and measured values. For GPR applications, lower frequency boresight gain (f < 500 MHz) is of special interest. At 500 MHz, the high growth rate ERLVD$_{\Gamma=2.6}$ has -7.52 dB of boresight gain. The gain of the unity growth rate ERLVD$_{\Gamma=1}$ is -12.1 dB and the simulated RLVD is -15.3 dB. Thus, there is a 7.6 dB measured increase in gain at 500 MHz for the ERLVD$_{\Gamma=2.6}$ compared to an RLVD of the same size. There is a peak difference between the high growth rate ERLVD$_{\Gamma=2.6}$ and base RLVD of 8.5 dB at 2 GHz. For higher frequencies, we can see that the unity growth rate overtakes the high growth rate ERLVD in gain at approximately 3 GHz. This is primarily due to the decrease in directionality with fewer rectangular sub-elements. Finally, the unity growth rate ERLVD$_{\Gamma=1}$ shows a 2 to 3 dB gain increase with respect to the RLVD over the bandwidth due only to the effective increase in sub-element length as derived previously.

In addition to the boresight gain, we show the measured radiation patterns at 1.5 GHz and 5 GHz in Fig. 21. The Guanella balun used to feed all three antennas has up to 1 dB of amplitude imbalance and 8 degrees of phase imbalance which creates imperfectly-centered patterns. Again, we see that the ERLVD$_{\Gamma=2.6}$ has lower gain than both the RLVD and ERLVD$_{\Gamma=1}$ at higher frequencies. One conclusion visible in Fig. 21 is that each pattern is "wider" in terms of the off-boresight radiation due to the inclusion of elliptical sub-elements. This phenomenon is due to the different direction of currents along the antenna arms. With a thin-wire RLVD, the current generally only travels in one direction. Conversely, currents in ERLVDs travel along curved elliptical paths to increase off-boresight radiation.

Additionally, we can calculate the efficiencies of these antennas. The RLVD, ERLVD$_{\Gamma=1,}$ and ERLVD$_{\Gamma=2.6}$ have efficiencies of approximately -10 dB, -8 dB, and -5 dB, respectively over their bands. The increase in antenna efficiency corresponds directly to the gain increase previously examined.

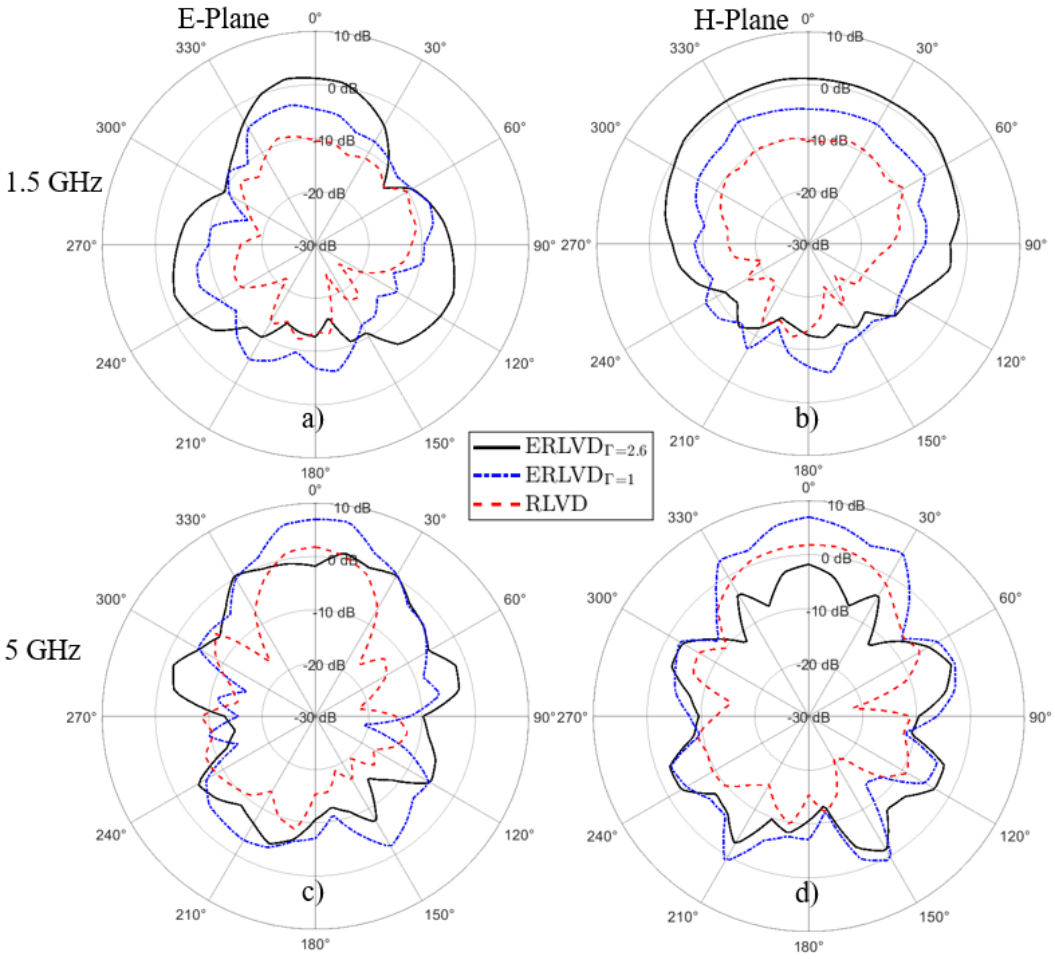

Fig. 21: Measured radiation patterns of the prototyped ERLVD and RLVD at selected frequencies. a) E-plane pattern at 1.5 GHz b) H-plane pattern at 1.5 GHz c) E-plane pattern at 5 GHz d) H-plane pattern at 5 GHz

In Table 3, we compare this antenna to similar antennas developed in literature. It must be noted that bandwidth ratio of the RLVD is often determined by the feeding balun for each case in Table 3.

Table 3: Comparison to Similar RLVD Designs

Ref.	500 MHz Gain	2 GHz Gain	Bandwidth ($f_{low} - f_{high}$), GHz	Arm Size
[29]	-15 dB	-2.5 dB	1.5 – 7 GHz (4.6:1)	171.5 mm ($1.16\lambda_{low}$)
[25]	N/A	N/A	0.5 – 3 GHz (6:1)	150 mm ($0.25\lambda_{low}$)
[22]	-15.1 dB	-7.2 dB	0.49-1.96 GHz (4:1)	300 mm ($0.49\lambda_{low}$)
ERLVD Γ=1	-12.1 dB	-0.5 dB	0.49–6.41 GHz (13:1)	104 mm ($0.17\lambda_{low}$)
ERLVD Γ=2.6	-7.52 dB	3.5 dB	0.29–0.94, 1.57-4.12, 5.66-6.63 GHz	104 mm ($0.1\lambda_{low}$)

C. Guanella Balun

This section contains significant portions from [34], reprinted with permission. With the development of ultrawideband (UWB) radar systems, balanced UWB antennas require a single-ended to differential conversion typically provided by a balun. UWB baluns using the Marchand topology have been proposed [27, 35], but Marchand baluns typically provide 1:1 impedance transformation. Many UWB antennas including the spiral antenna and Resistively Loaded Vee Dipole (RLVD) [22] have an input resistance of ~200 Ω, rendering the Marchand balun inadequate. This creates a need for compact, UWB, impedance transforming baluns at microwave frequencies. The Guanella balun [36-39] is a class of microwave circuit that can provide an impedance transformation from 50:200 Ω.

Classical Guanella balun implementations use bifilar wire-wrapped toroids to provide the 1:4 impedance transformation. Toroid implementations are not planar and have poor efficiency at frequencies above 50 MHz. Planar PCB implementations use broadside-coupled lines . In order to achieve constant coupling with broadside lines, the substrate must be very thin. The most successful implementation to date [39] uses a thin film structure, which is often expensive and not easily integrated into a planar system.

In this paper, we present the design of a planar UWB Guanella balun for feeding an UWB antenna such as a spiral or RLVD. The Guanella balun operates over a 0.35-3.4 GHz bandwidth with less

than 1 dB insertion loss. The Guanella balun is designed using defected ground techniques in thin substrates available through standard PCB fabrication. Our Guanella balun has the largest impedance bandwidth reported to date. In addition, to the best our knowledge, we report the first PCB Guanella balun that can transform 50 to 200 Ω.

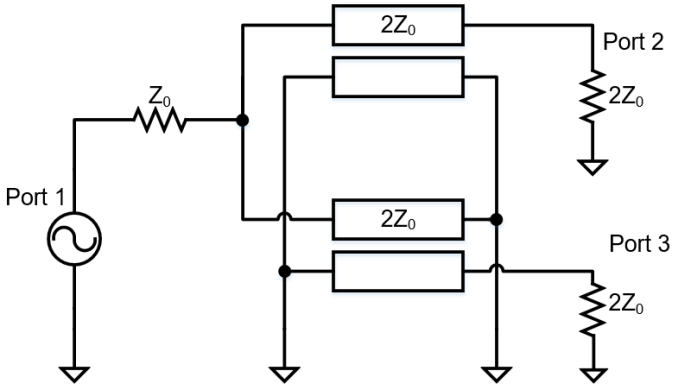

Fig. 22: Schematic diagram of 1:4 classic Guanella balun with single-ended terminations.

To achieve a 50-200 Ω impedance transformation, the conventional Guanella balun calls for use of two parallel 100 Ω coupled transmission lines as in Fig. 22. However, there are competing design factors:

1. The upper operating frequency is limited by the coupling strength of the 100 Ω lines. As we implement the 100 Ω lines with broadside-coupled lines, the substrate should be as thin as possible to maintain 3 dB coupling over a large bandwidth.
2. With decreasing substrate thickness, the 100 Ω trace width becomes small and unrealizable with common PCB manufacturing technology (trace width less than 6 mil). For high dielectric constant substrates, the line width is even smaller for 100 Ω. The smaller trace width also increases conductor loss.

The best PCB implementation would be on a thin substrate with a low dielectric constant. For this application, a substrate with $\varepsilon_r = 2.2$ and $h = 0.254$ mm fits these criteria and is commonly available.

The Guanella balun's upper bandwidth relies significantly on a high even-mode impedance for its 100 Ω coupled lines. Therefore asymmetric broadside-coupled lines with a defected ground structure (DGS) are chosen to serve as the main 100 Ω lines. This simplifies the design significantly, as we enlarge the "ground" line to 3 times the width of the "signal" line, effectively making the signal line follow microstrip impedance formulas.

The Guanella balun schematic diagram (Fig. 22) calls for the join of the bottom two transmission lines at the balanced port, forming an odd-mode ground. In the case of a differential load this is sufficient. In the single-ended case, the join of the two transmission lines should also be physically grounded for common-mode rejection. The grounding is visible in Fig. 23.

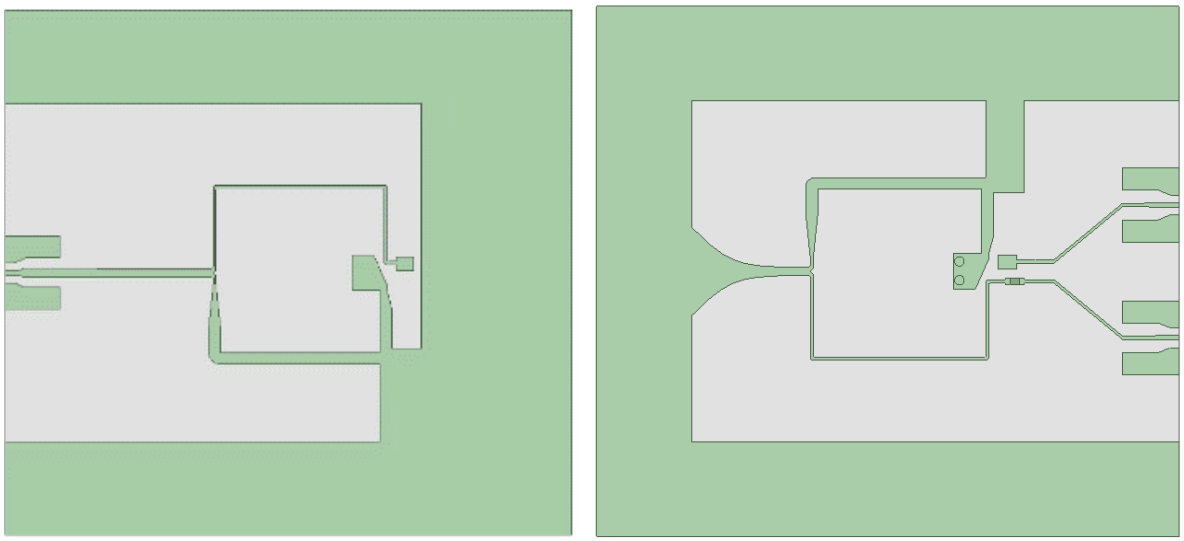

(a) (b)

Fig. 23: ANSYS HFSS model of Guanella balun. (a) Top view. (b) Bottom view. SMA connectors for connectorized test are included.

In order to have two single-ended outputs on the same layer, the Guanella balun must have a single layer transition. Including a via in only one signal path introduces an in-band phase imbalance peak and also degrades high frequency performance. From circuit-level simulation in ADS, any coupled line realization with finite even-mode impedance will have port 2 magnitude

dominance at all frequencies. Therefore, the required layer transition is added in the port 2 line to aid amplitude balance.

The PCB Guanella balun is manufactured below in Figure 24 using a 10-mil Taconic TLY-5 substrate.

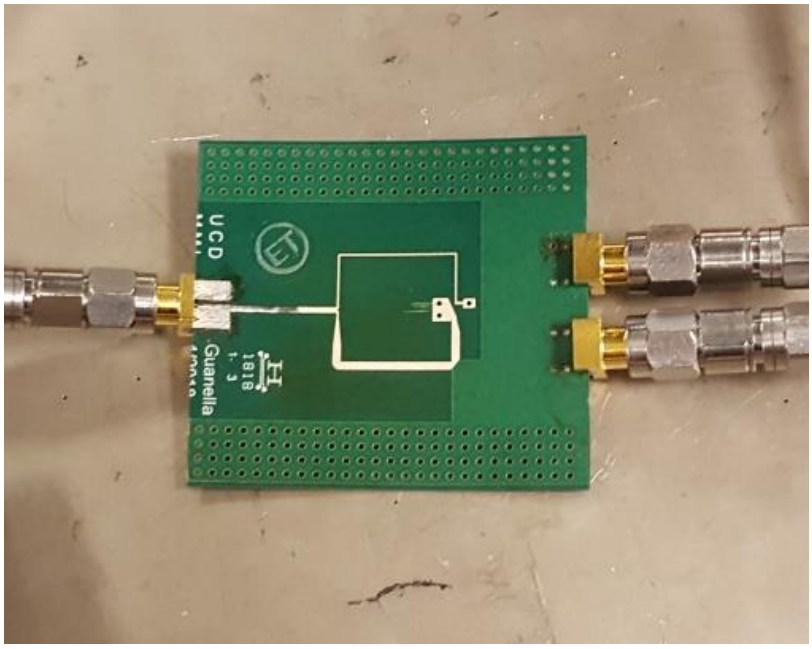

Fig. 24: Photograph of the manufactured balun in the measurement setup connected to the 4-port N5247 PNA-X.

The Guanella balun is tested using a 4 port N5247 PNA-X Network Analyzer with 50 Ω terminations. The vector S-parameters are de-embedded to the board edge and ports 2 and 3 are manually renormalized to 100 Ω terminating impedance. The input return loss S_{11} and differential transmission S_{dd21} are plotted in Figure 25.

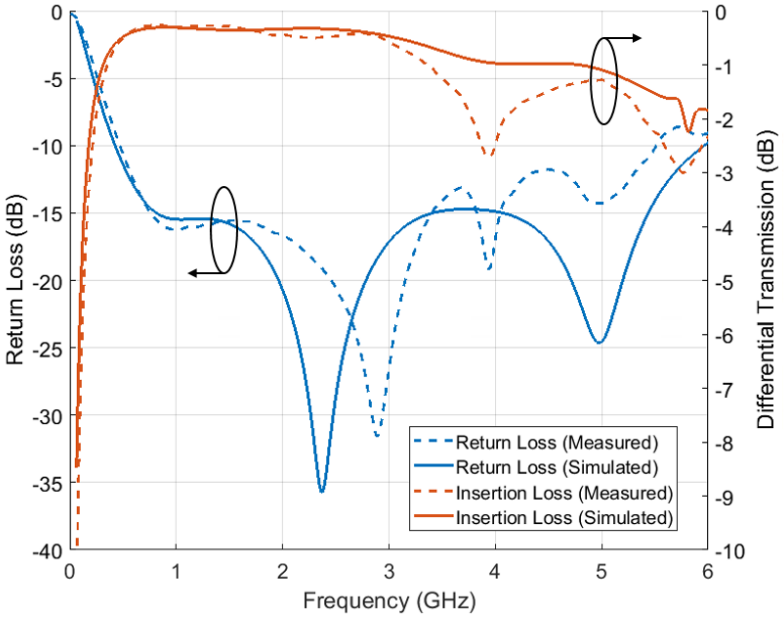

Fig. 25: Simulated versus measured differential transmission and input return loss plotted from 10 MHz to 6 GHz.

The Guanella balun has a 1 dB insertion loss band from 0.35 to 3.4 GHz. The unbalanced input port is matched under -10 dB from 0.49 to 5.5 GHz.

At 3.9 GHz, we see an unpredicted decrease in the transmission to -2.7 dB. At this frequency, there is a peak in common mode transmission to explain the decrease in differential transmission. This can be explained by poor grounding of the connectors, which mainly affects high frequency performance. In Figure 26, we also measure a peak in the phase imbalance of 12° at 2.6 GHz due to the layer transition.

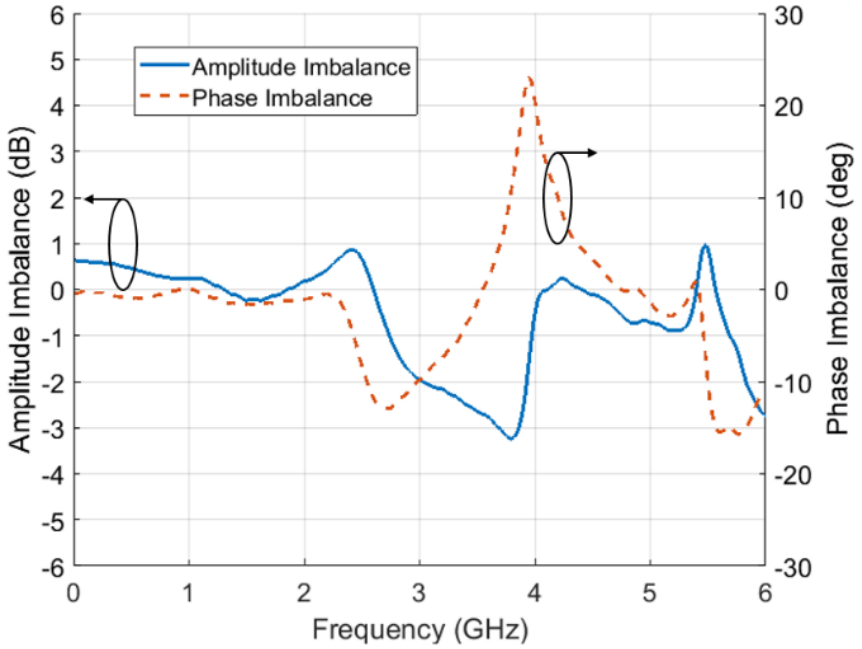

Fig. 26: Measured amplitude and phase imbalances of the Guanella balun plotted from 10 MHz to 6 GHz.

To test the pulsed response of this balun, we take the measured vector S-parameters and import them into ADS to test under an ideal pulse input. The input pulse is a Ricker wavelet described by the equation:

$$\psi(t) = \frac{-2}{\sqrt[4]{\pi}\sqrt{3\sigma}}\left[\frac{t^2}{\sigma^2} - 1\right]\left[e^{\frac{-t^2}{2\sigma^2}}\right] \tag{6}$$

and σ = 0.2 x 10^{-9}. The Ricker wavelet with σ = 0.2 x 10^{-9} has -3 dB frequencies of 700 MHz and 1.6 GHz.

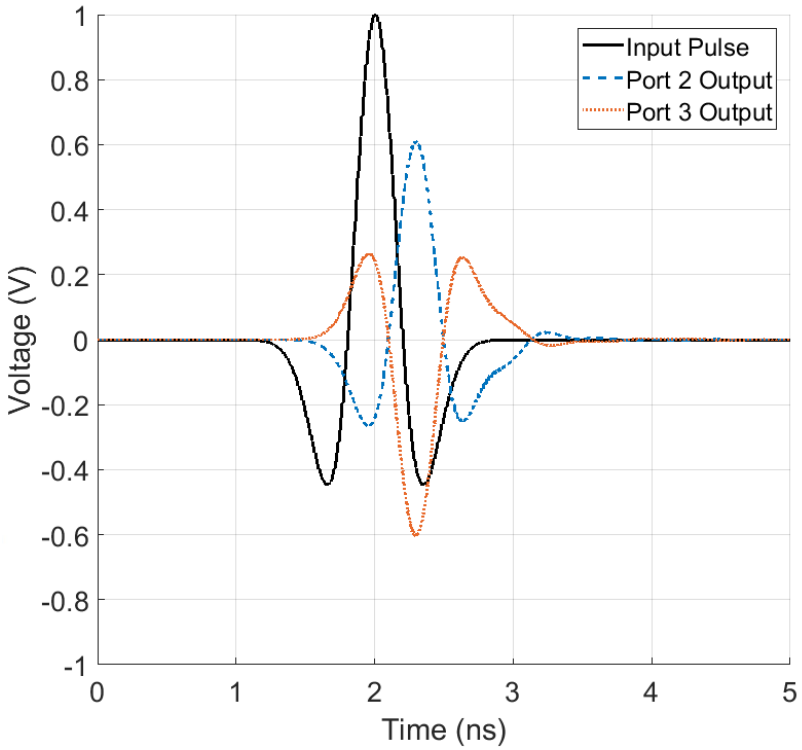

Fig. 27: Simulated Ricker wavelet response using measured vector S-parameters.

We can see that the balun transmits the pulse faithfully when looking at the balanced port. There is some distortion to be seen at 2.8 ns. This is caused by the in-band common mode resonance that can be seen in Figure 26.

In Table 4, we can see that this balun is the first published PCB balun to provide 50:200 Ω impedance transformation, while also providing the largest insertion loss bandwidth. Our Guanella balun is larger than the others, but has a small size of 0.0525λ x 0.04λ at its lowest operating frequency of 350 MHz.

Table 4: Summary of Published Guanella Baluns

Ref	Topology	Bandwidth (Sdd21 Loss)	Size (Excluding Connectors)
[39]	Thin-Film Guanella 50:200	1 dB: N/A 3 dB: 0.5 – 10.5 GHz	6.3 x 10.5 mm
[37]	PCB Guanella 12.5:50	1 dB: 0.45 - 1.1GHz , 1.2 - 2.2 GHz 3dB: 0.25 – 2.75 GHz	437.4 mm^2
This work	PCB Guanella 50:200	1 dB: 0.35 – 3.4 GHz 3 dB: 0.16 – 10.5 GHz	45 x 35 mm

2. GPR System-Level Effects and Specifications

A. Jitter

This section contains significant portions from [40], reprinted with permission. The preprocessing step of coupling removal is one of the most important algorithms for ground-penetrating radar (GPR) systems. Coupling removal is broadly performed with one of two simple methods: a background removal or a foreground calibration [41, 42]. Both background removal and calibration methods produce a reference signal to which the received coupling pulse is compared to and subtracted from. However, these methods of coupling removal are sensitive to changes in the coupling signal [31, 41]. Any change in the coupling signal will show up in the GPR scan as residue which can create false alarms when imaged. These changes could be deterministically caused by outside environmental factors [41] or random processes such as the jitter from a master system clock or high frequency mechanical vibrations [43]. Environmental factors can be calibrated out with external sensors [44], which leaves the jitter as a problem of interest. Onunkwo [45] has explored the issue of sampling jitter for UWB systems in general and proposes pulse shaping and averaging for reduction of sampling jitter. However, these two solutions may be unsatisfactory for GPR systems that run at high framerates or have high

bandwidth due to non-monotonicity. Hu [46] explored the issue of time-of-arrival jitter for through-wall radar. Several other schemes [45, 47] have been presented to reduce jitter but are hardware solutions or require prior knowledge of the shape of the signal to be effective. Furthermore, popular blind deconvolution methods have been developed to enhance resolution and accuracy of GPR systems [48, 49]. The deconvolution techniques have been shown to be generally sensitive to additive white noise and would likely suffer further reflectivity estimation degradation due to signal-dependent sampling jitter noise. What remains to be explored is the fundamental nature of the residue from jittered coupling removal algorithms and the residue's effect on the imaging performance of GPR systems.

We will first describe the experimentally observed problem and use simulation to introduce a mathematical model of jitter-induced coupling noise. We will examine how the residue affects image quality in the entire GPR system pipeline and demonstrate filtering methods. As filtering cannot remove all of the jitter-induced coupling noise, we propose two specifications called the linear slope and migrated probability specifications, respectively. The linear slope specification specifies the maximum slope a coupling signal may have such that residue is not visible in the raw background-removed B-scan. The migrated probability specification identifies problematic imaging depths for a given coupling signal in a jitter environment. Together, the two specifications allow for system designers to accurately determine how well a design can perform in a given jitter environment.

i. Sampling Jitter's Effect on GPR Scan Quality

Example Waveform Corrupted by Sampling Jitter

In this section, we describe the issue that arises from timing uncertainty in ground-penetrating radar. As direct RF sampling is neither a feasible nor economical choice for most systems which

operate above 2 GHz, high-frequency time-domain GPR systems employ equivalent-time receivers which sample once per waveform. Thus, any disturbance between waveform shots will realize itself as sampling jitter, a term which describes the uncertainty in sampling time. Sampling jitter is experimentally observed to be normally distributed with standard deviations of up to 100 ps [45, 46].

Fig. 28 shows an example of measured sampling jitter using a 28 GS/s equivalent-time receiver. The waveforms are 3000 sequentially recorded coupling pulses from a ground-penetrating radar array. Each pulse is different, and even some waveforms are jittered so much that the slopes at 1.25 and 1.75 ns appear non-monotonic. The main issue with the jittered traces in Fig. 28 is that background subtraction will not remove the entire coupling pulse. Residue or residuals (the terms are used interchangeably) will be created from the coupling signal which can rival the strength of a target return. For weaker targets, this residue, which we also refer to as jitter-induced coupling noise, can drown out the desired target return and decrease system performance.

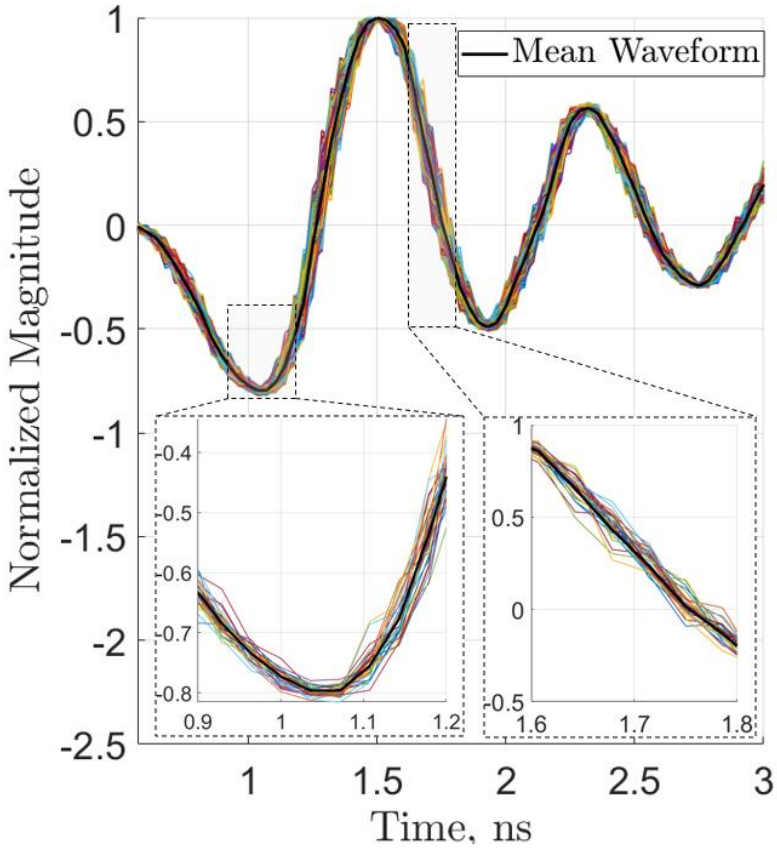

Fig. 28. Measured example of sampling jitter taken from an operational ground-penetrating radar array similar to that used in [1, 2]. Top plot shows 3000 sequentially taken coupling waveforms with a mean waveform (average) overlay. Inset plots show only 300 coupling waveforms for clarity. Y-axis is normalized to maximum of all traces.

We have found that using software to resample waveforms to simulate jitter results in nearly indistinguishable signals compared to measured jittered waveforms. Using software to jitter waveforms allows us to simulate and study jitter environments not easily recreated in laboratory conditions. For the remainder of this paper, we utilize both simulated and measured jitter waveforms. All simulated waveforms are based on a 0.3 - 3.0 GHz GPR system pictured below in Figure 29 using a real-time 20 GS/s oscilloscope. Some residue in Fig. 28 is caused by the addition of thermal noise. Thermal noise may be dominant near peaks or valleys of the signal as it is independent of the slope of the signal. However, as shown in the Fig. 28 insets, the signal variations due to jitter dominate where the first derivative of the signal is non-zero.

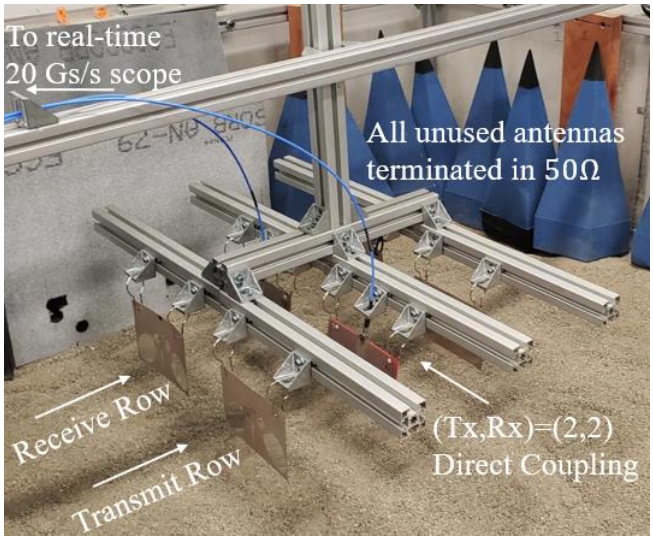

Fig. 29. Experimental setup showing the coupling measurement used as the basis for simulated jitter conditions. To take the coupling measurement, the array is moved to a height of 0.9m above the ground surface and the ground surface is covered with AN-79 absorber.

The setup consists of three transmit-receive pairs of elliptical resistively-loaded vee dipole antennas [28]. As direct coupling is generally the most problematic transmission path, we take the signal between a single transmit-receive pair as indicated in Fig. 29. The other two transmit-receive pairs are terminated in 50 Ω load to represent array conditions.

Jitter and Coupling Signal Models

To formalize a model, we denote our ground truth coupling signal of interest as $\phi(t)$. $\phi(t)$ is the direct antenna coupling signal in absence of any sampling jitter. We model the sampling jitter at time sample i of A-scan k as a normally (Gaussian) distributed random variable τ_{ik} where:

$$\tau_{ik} \sim \text{i.i.d. } N\left(0, \sigma_J^2\right) \tag{7}$$

In (7), the subscripts $i = 0, \ldots, N_i - 1$ and $k = 1, \ldots, N_k$. The term "i.i.d." means that each τ_{ik} is independent and identically distributed. The value σ_J is the standard deviation of the sampling

jitter, where higher σ_J implies more severe jitter. N_i and N_k are the number of time samples and A-scans in a 2-D B-scan, respectively.

We then model the sampled and digitized coupling signal corrupted by sampling jitter as $\phi_J[i,k]$ where the subscript "*J*" indicates jitter corruption. $\phi_J[i,k]$ is related to $\phi(t)$ as:

$$\phi_J[i,k] = \phi(iT_s + \tau_{ik}) \tag{8}$$

where T_s is the sampling period. Note that $\phi(t)$ is assumed to be independent with respect to A-scan index k. In other words, the ground truth coupling signal does not change over slow time.

We then perform background removal. Background removal may be performed by subtracting a reference mean signal $\bar{\phi}_J[i]$. $\bar{\phi}_J[i]$ is calculated as:

$$\bar{\phi}_J[i] = \frac{1}{N_k}\sum_{k=1}^{N_k}\phi_J[i,k] \tag{9}$$

Alternatively, a number other than N_k A-scans may be chosen to be averaged. In a jittered environment, the mean signal $\bar{\phi}_J[i]$ is not guaranteed to be equivalent to the ground truth coupling signal $\phi(iT_s)$. At high jitter values, signal peaks will be consistently underestimated. An approximate rule of thumb for when peak underestimation occurs is:

$$\sigma_J \geq \frac{FWHM}{7.2} \tag{10}$$

where $FWHM$ is the full-width at half-max of a peak in question. Equation (10) is derived by taking a peak with Gaussian roll-offs, resampling it many times with normally distributed jitter, and averaging the many jittered peaks such that the average underestimated peak value is 95% of the true peak value. As such, (10) may be interpreted as the cutoff between "high jitter" and "low

jitter" systems. We may also approximately replace $FWHM$ in (10) with $1/BW$ where BW is the 30-dB power bandwidth of the GPR system. For the signal in Fig. 28, the jitter standard deviation σ_J required for peak underestimation is calculated to be 41 ps. For high frequency systems, $FWHM$ will be correspondingly lower and the system will be more sensitive to jitter.

For systems with $\sigma_J < FWHM/7.2$, we can write the result of background subtraction as the residue signal $\phi_{JR}[i,k]$:

$$\phi_{JR}[i,k] = \phi_J[i,k] - \bar{\phi}_J[i] = \sum_{n=1}^{\infty} \frac{\phi^{(n)}(iT_s)\tau_{ik}^n}{n!} \tag{11}$$

The third term in (11) is the expansion of the Taylor series of $\phi(t)$ around iT_s. From (11), we can see a clear relationship between the derivatives of $\phi(t)$ and the residue. For reference, we examine the distributions of the first two terms of the infinite sum:

$$\phi'(iT_s)\tau_{ik} \sim N\left(0, \left(\phi'(iT_s)\sigma_J\right)^2\right) \tag{12}$$

$$\frac{1}{2}\phi''(iT_s)\tau_{ik}^2 \sim \mathrm{sgn}\left(\phi''(iT_s)\right)\Gamma\left(\frac{1}{2}, \sigma_J^2|\phi''(iT_s)|\right) \tag{13}$$

where $\mathrm{sgn}(\cdot)$ is the signum function. The sum of (12) and (13) provide very accurate estimations for the jitter for systems that obey (10). Equations (12) and (13) imply that the residue is mostly normally distributed in highly sloped areas where $\phi'(t)$ dominates, and mostly distributed as a Gamma random variable [50] near peaks and valleys where $\phi'(t) = 0$. Clearly, the problem of minimizing the residue $\phi_{JR}[i,k]$ is equivalent to reducing the derivatives of the coupling signal $\phi(t)$.

Effect on Residue on the Quality of Migrated GPR Images

In this section, we present a measured B-scan and its simulated jittered forms in Fig. 30. The system is imaging two metallic pipe-like targets buried at different depths in $\epsilon_r = 5.7$ dry sand. Fig. 30a shows the truth scan without any processing, and Figs. 30b and 30c show scans resampled with $\sigma_J = 10$ ps and $\sigma_J = 100$ ps, respectively. Figs. 30d, 30e, and 30f show the result of the B-scans after applying background removal (BKGR) as in (11). Figs. 30g, 30h, and 30i show the result of migrating the B-scans using the 2D time-domain Kirchhoff migration method [51, 52]. Each column represents a single processing pipeline, while each row is a step in the pipeline.

Each image in Figs 30g, 30h, and 30i are displayed such that the dark blue background is 10 dB below the yellow target maximum. The target images are not a single point because we are migrating a time-domain waveform similar to a Ricker wavelet with three peaks. In this case, the best possible image is Fig. 30g. All other returns in Figs. 30h and 30i are deemed additional noise. In Figs. 30e and 30f, we can clearly see a coupling residue in both the pre-ground bounce period and during the target return. Therefore, we expect to see noise in the migrated image near the surface. We do not see any additional significant false alarms in Fig. 30h where $\sigma_J = 10$ ps. This is because the process of migration presents a strong filter against high magnitude noise. While Fig. 30e contains high-magnitude noise compared to the target, the zero-mean random nature of the noise implies that summation through Kirchhoff migration regresses the absolute value of the magnitude of the noise image towards the zero. However, the analysis is not so simple: as migration includes weighting based on the effective angle and distance, a single pixel in the image is the result of a summation of dependent random variables with different distributions. Naturally, the resulting distribution of the pixel in absence of a target is depth-dependent and its distribution is not easily derived. The distribution of the magnitude of the noise will be explored later.

In the $\sigma_J = 100$ ps image, we see a distributed noise resulting from the residue $\phi_{JR}[i,k]$. In this case, $\phi_{JR}[i,k]$ has a distribution dependent on σ_J such that there is a high probability that its migrated image will have a magnitude similar to the target return. This noise is particularly problematic, as the image noise can drown out images, create false targets, and blur the edges of true targets. Critically, this migrated noise may limit the weakest detectable target.

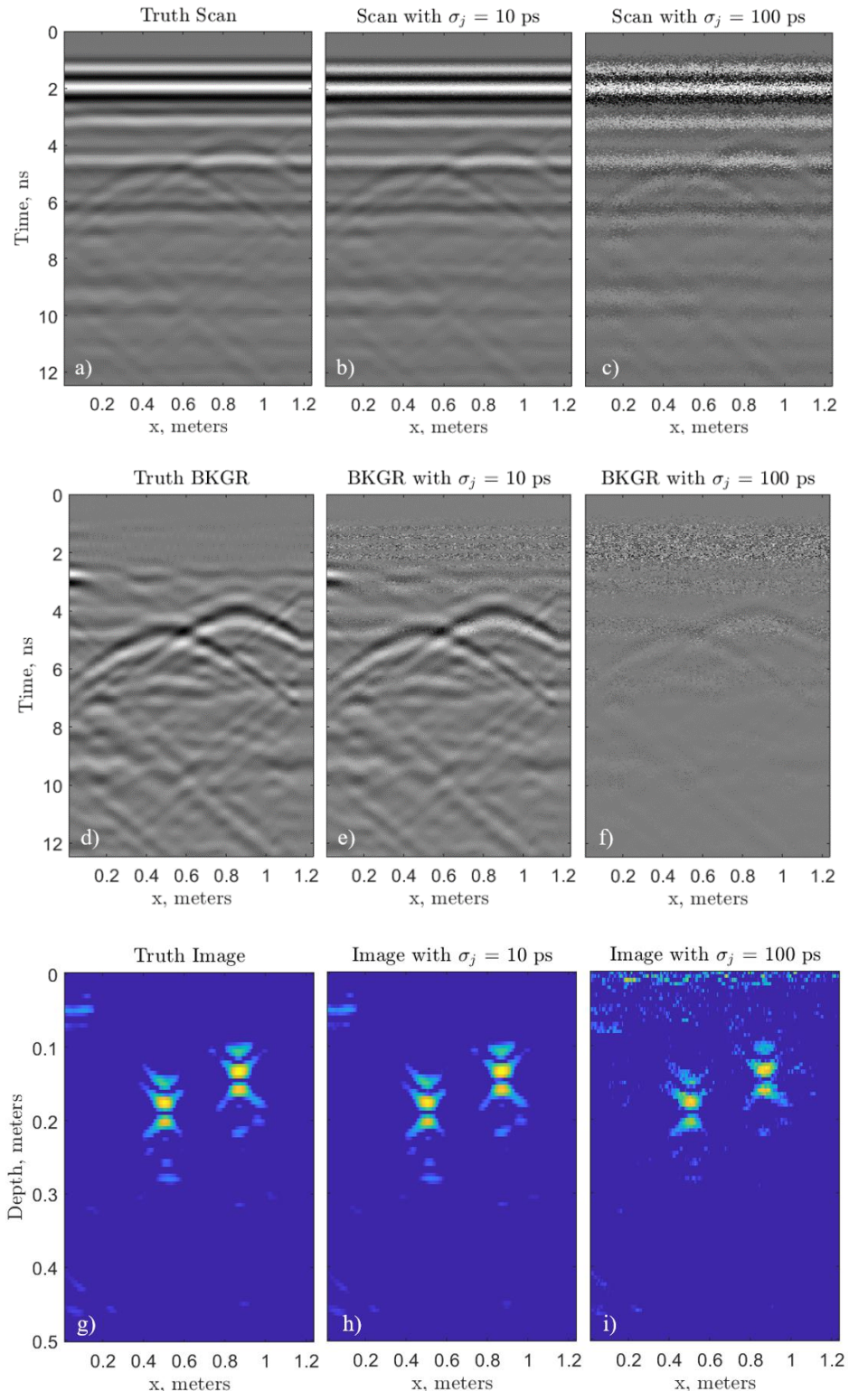

Fig. 30: a) Raw scan with no jitter, b) Raw scan with σ_J= 10 ps of sampling jitter, c) Raw scan with $\sigma_J = 100$ ps of sampling jitter, d) Background-removed scan with no jitter, e) Background-removed scan with σ_J=10 ps of sampling jitter, f) Background-removed scan with $\sigma_J = 100$ ps of sampling jitter, g) Image generated from d), h) Image generated from e), i) Image generated from f)

A coherent receiver operating characteristic (ROC) curve analysis in Table 5 using a signal-to-noise-ratio (SNR) based on the ratio of migrated target strength to background noise shows that the false alarm rate for Fig. 30g at 90% probability of detection is 1.05 false alarms (FA)/km. Fig. 30h with $\sigma_J = 10$ ps results in 1.06 FA/km. Fig. 30i with $\sigma_J = 100$ ps results in 3.1 FA/km, a near tripling of the false alarm rate.

Table 5: False Alarm Rate (FA/km) at 90% detection (P_d)

Image	FA/km at 90% P_d	FA/km at 95% P_d
Fig. 30g (no jitter)	1.05	3.92
Fig. 30h ($\sigma_J = 10$ ps)	1.06	3.95
Fig. 30i ($\sigma_J = 100$ ps)	3.10	9.87

ii. Noise Mitigation Via Post-Processing

In this section, we demonstrate a method for filtering out some of the sampling jitter noise. Unfortunately, we cannot apply a simple algorithm such as that proposed in [53] to correct for the coupling residue from jitter because there is no relationship between adjacent waveform points or a known truth waveform with which to compare. Examining Fig. 28, it is clear that a high-pass filter may be beneficial. Using (12) and (13), we generate simulated residuals for the example coupling waveform. We use these residuals to calculate the power spectral density versus frequency for the example signal at $\sigma_J = 10$ ps.

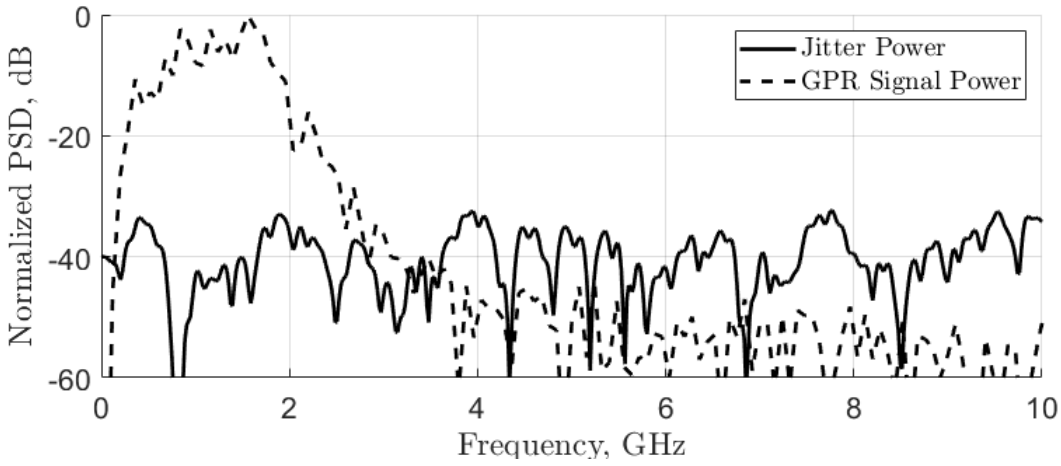

Fig. 31: Power spectral densities of the measured GPR signal (taken with target present) and simulated isolated $\sigma_J = 10$ ps jitter residue using (12) and (13).

Clearly, the GPR signal in Fig. 31 must be bandlimited at 3 GHz to minimize the contribution of jitter noise. Additionally, we may apply a spatial filter along the scan axis x to further mitigate the effects of sampling jitter. Creating a plot similar to Fig. 31 for the spatial dimension, we find a high-frequency cutoff of $k_x = 20\ \mathrm{m}^{-1}$ to be acceptable. In Fig. 32, three background-removed scans are displayed at different stages of filtering with $\sigma_J = 100$ ps.

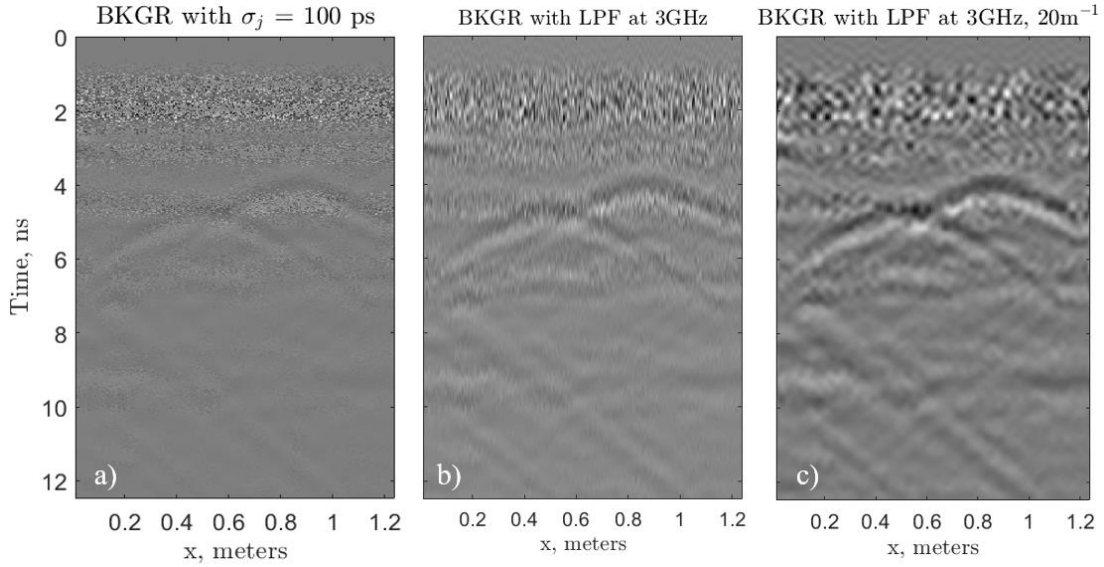

Fig. 32: Different B-scans with background removal (BKGR) and different filters. (a) Base BKGR B-scan with simulated $\sigma_J = 100$ ps and no filtering, (b) BKGR B-scan with a low-pass filter at 3 GHz, (c) BKGR B-scan with a low-pass filter at 3 GHz and at 20 m^{-1}.

For a means of comparison, we calculate the RMS value of the scan during the time band of 0.2 – 2.2 ns in Figs. 32a, 32b, and 32c and enumerate the results in Table 6. Ideally, the value would be extremely low, limited by thermal noise. We also calculate the value for the $\sigma_J = 10$ ps case similar to Fig. 30e.

Table 6: Resultant Coupling-Region RMS Noise of Fig. 32 scans

	No Filter	LPF at f = 3 GHz	LPF at f = 3 GHz and LPF at $k_x = 20$ m^{-1}
$\sigma_J = 10$ ps	-43.7 dB	-51.4 dB	-51.7 dB
$\sigma_J = 100$ ps	-26.1 dB	-34.4 dB	-40.2 dB

For the dramatically corrupted B-scans of $\sigma_J = 100$ ps, the two filters together achieve a 14.1 dB reduction in RMS noise in the coupling region. Some noise remains as is clear in Fig. 30e. A ROC curve analysis shows an improvement to 1.85 FA/km for 90% detection using the migrated version of Fig. 30e. However, filtering is unable to solve all errors. In particular, one possible error of concern is the added difficulty of ground-bounce removal in jittered environments. Because the ground bounce is generally of high magnitude, the possible residuals from ground-bounce removal may rival the coupling residuals. These residuals could additionally mute or obscure shallow targets, though the ground bounce is not the direct focus of this paper. In the next section, we examine carefully coupling signal design such that we minimize the additional false-alarms in jitter-prone environments.

iii. Noise Prevention Via Jitter-Hardened Coupling Signal Design

Because it is impossible to remove all jitter-induced noise from the random coupling residue, a system designer must design the coupling signal such that extra false alarms are minimized. However, no direct guideline in literature exists to design a coupling signal that is not problematic.

In this section, we present two guidelines to fulfill this purpose. As the coupling signal is generally the result of unwanted signal interactions, the process of coupling signal design is actually the multifaceted tuning of the antenna characteristics, array spacing, absorber placement, and mechanical design such that the coupling signal meets the desired specification. The only input to these methods is the time-domain coupling signal, which can be estimated either via full-wave simulations or measurements. In measurements, the simplest way to obtain the coupling signal is to point the radar towards the sky or absorbers instead of the ground and record the result.

Linear Slope Specification

This form of specification follows directly from (12) and is based on un-migrated data. As this specification is based on un-migrated data, the linear slope specification is ignorant of image magnitude and thus false alarms. This specification is intended to create a background removed B-scan with visually insignificant coupling residue based on the threshold parameter κ. Because we know the distribution of $\phi'[i,k]\tau_{ik}$ is Normal from (12), we can generate a two-sided confidence interval for the magnitude of the residual. The resulting linear slope specification format is as follows:

$$|\phi'(t)| = \left|\frac{d}{dt}\phi(t)\right| \leq \kappa \frac{s_{target}}{Z_{1-\frac{\alpha}{2}} \cdot \sigma_J} \tag{14}$$

where κ is a constant threshold parameter, typically 0.1 to represent -10 dB or 0.5 to represent -3 dB. s_{target} is the peak voltage of the target return, $Z_{1-\alpha/2}$ is the value such that $P\left(|Z| > Z_{1-\alpha/2}\right) = \alpha$, where Z is a standard normal variable. α is a probability parameter, typically 5% such that $Z_{1-\alpha/2} = 1.96$. A coupling signal $\phi(t)$ that obeys (10) will experience residues of at least κs_{target} magnitude with probability less than or equal to α.

For example, s_{target} can be estimated from theory or measured directly. In the case of Fig. 5d, $s_{target} = 26.8$ mV. Using $\kappa = 0.5$, $\alpha = 5\%$, and $\sigma_J = 10$ ps, we find that the coupling signal has a maximum allowable slope of 683 mV/ns. Fig. 8 plots the linear slope specification $\phi'(t)$ where the maximum allowable slopes of 638 mV/ns are indicated.

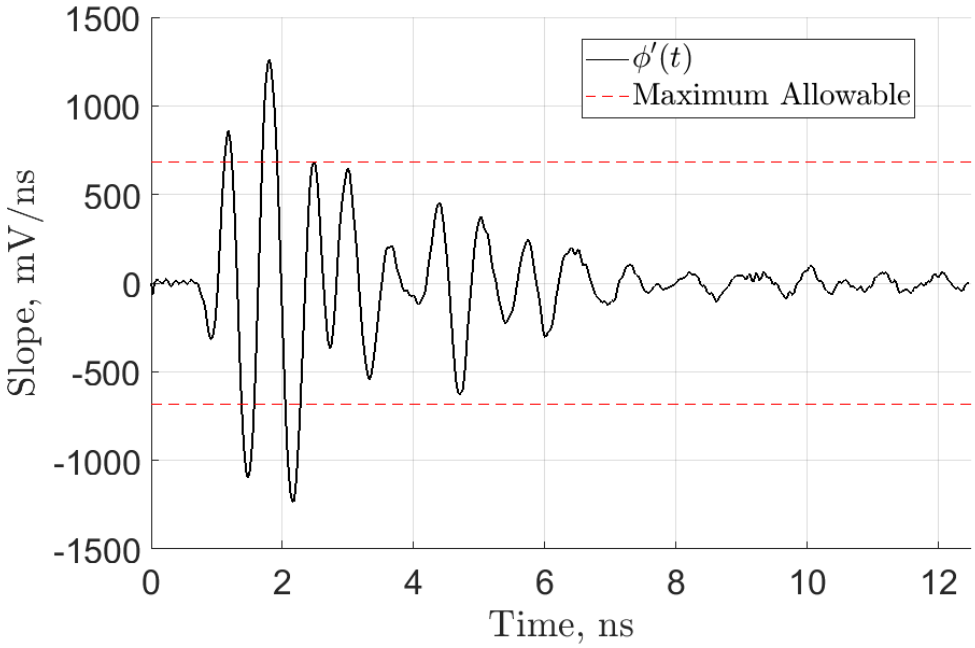

Fig. 33: Linear slope calculated from measured GPR coupling signal. Any slope above the red line is a violation.

The coupling shows several violation areas for the chosen parameters, and the time bins corresponding to the resulting violations contain visible residue as in Fig. 30e. Based on the results in Fig. 33, the system designer should consider whether the violations are problematic, and re-design the system to address the needs. Equation (14) is extremely useful and intuitive as a quick specification, but the result can be over-restrictive on the coupling slope because a high un-migrated residue magnitude does not necessarily create a false alarm further down the processing pipeline. The linear slope specification is based off of visually removing residue, and in the next section we will provide a more fundamental specification based on the probability that migrated noise creates a false alarm.

Migrated Probability Specification

In this section, we propose a framework method to generate a probability distribution for migrated jitter-induced coupling noise based on an antenna's coupling signal. The problem is much more obfuscated than the linear slope specification presented in the previous section, but results in a more accurate and lenient specification. For a reference, we reproduce the 2D Kirchhoff Migration formula here [51]:

$$I(x_q, z_q) = \int_{x \in X} \frac{\epsilon_r^{1/4} \cos\theta}{\sqrt{\pi c r}} \frac{\delta^{\frac{1}{2}}}{dt} E\left(x, t = \frac{2r\sqrt{\epsilon_r}}{c}\right) dx \tag{15}$$

The 2D Kirchhoff Migration may be interpreted as mapping an integration along a hyperbolic curve in the rectangular sample space (x, t) to the query space (x_q, z_q) where x_q is scan position and z_q is depth beneath ground. We are interested in the depth-dependent probability distribution of the migrated image of the residue $\phi_{JR}[i, k]$. In this case, we want to migrate the coupling only to find out how it will pass through the filter. Taking $E(x, t) = \phi_{JR}[i, k]$, the resulting image $I_{JR}[x_q, z_q]$ is formed by summing large numbers of dependent random variables with probability density functions similar to a weighted summation of (12) and (13). Due to the half-derivative, integration, and spectral weights in (15), the overall analytic probability density function of $I_{JR}[x_q, z_q]$ is complex and not attempted here. By extensively simulating migrated images using MATLAB, we have concluded that the absolute value of the migrated noise $I_{JR}[x_q, z_q]$ is best fit by a 3-parameter Weibull distribution [50], or:

$$\left|I_{JR}[x_q, z_q]\right| \sim \text{Weibull}(\alpha, \beta, \gamma) \tag{16}$$

where α, β, and γ are the scale, shape and location parameters, respectively. Each parameter is estimated by numerical maximum likelihood methods. Fig. 34 shows an example of the fit for a single time bin i's migrated coupling noise.

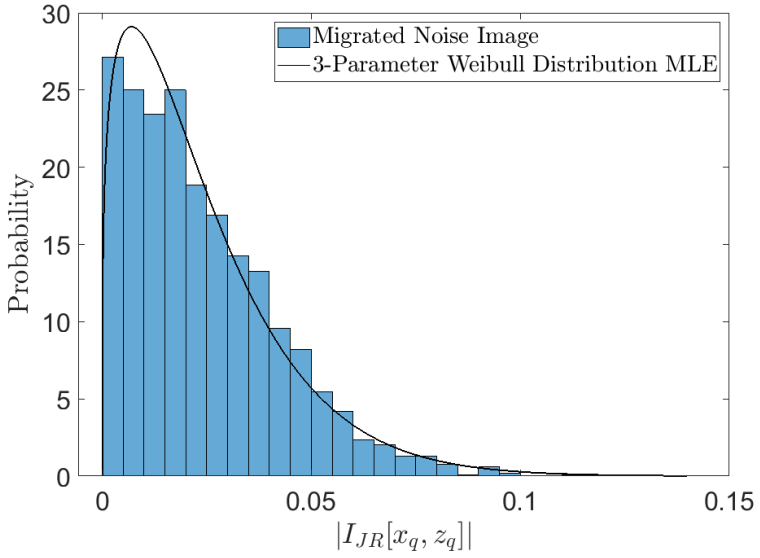

Fig. 34: Probability distribution of absolute value of migrated noise image for a single time bin with the three-parameter Weibull fit, estimated with maximum likelihood method. $\sigma_J = 40\ ps$.

The Weibull distribution is chosen because of its excellent adherence to the migrated coupling noise's tail distribution for each query depth z_q, which will be used to calculate the probability of false alarm. The fact that the Weibull's fit is poor at zero magnitude is inconsequential for the purposes presented here and only can create inaccuracies for very high probabilities of false alarms, above 50%. Calculation of the three Weibull parameters for each depth z_q results in a set of probability density functions (pdfs) $f_M(m; \alpha, \beta, \gamma)$ where m and M are dummy parameters representing the magnitude $\left|I_{JR}[x_q, z_q]\right|$. Finally, we construct a specification based on the probability of false alarm for each depth z_q by integrating each pdf as:

$$P\left(M > \kappa \middle| I_{target} \middle|\right) \leq P_{FA} \tag{17}$$

$$\int_{\kappa|I_{target}|}^{\infty} \frac{\beta}{\alpha}\left(\frac{m-\gamma}{\alpha}\right)^{\beta-1} e^{-\left(\frac{m-\gamma}{\alpha}\right)^{\beta}} dm \leq P_{FA} \tag{18}$$

where κ is again a constant thresholding parameter, typically 0.1 or 0.5, $|I_{target}|$ is the magnitude of the migrated target image known through either measurement or calculation, and P_{FA} is the probability that a given pixel contains a migrated image of magnitude greater than $\kappa|I_{target}|$, chosen to be 5%. For example, the rightmost target in Fig. 30h has a magnitude $|I_{target}| = 0.2239$. Using κ = 0.5, we calculate the probability that a noise peak will appear within -3dB of $|I_{target}|$ below in Fig. 35.

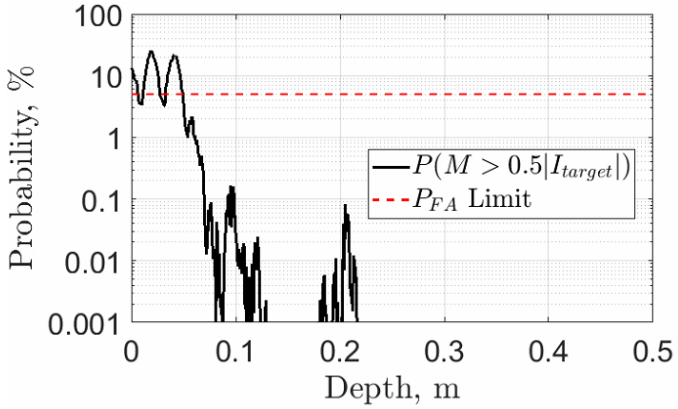

Fig. 35: Probability that migrated noise magnitude is greater than half of the expected target strength. Example calculated for $\sigma_J = 60$ ps. Violations appear near 0, 2, and 4 cm. Calculated with 2048 sample migrated waveforms.

The violations at 0, 2, and 4 cm deep in Fig. 35 imply that these depths are above 5% likely to have false alarms caused by jitter-induced coupling noise. The probability of a significant noise peak decreases extremely rapidly with respect to depth due to the exponential decay (lossy ringing) of the coupling signal.

Finally, we enumerate the steps to properly test if a coupling signal $\phi(t)$ is adequate for detecting a given target in a σ_J jitter environment.

1. Artificially resample $\phi(t)$ as $\phi_J[i]$ with sampling jitter $\tau_i \sim N\left(0, \sigma_J^2\right),\ i = 0, \dots, N_i - 1$.
2. Repeat step 1 for N_k waveforms to obtain $\phi_J[i,k],\ k = 1, \dots, N_k$. Choose $N_k \to \infty$ for consistent statistics.
3. Perform background removal (11) on the result of step 2 to obtain $\phi_{JR}[i,k]$. Any other processing (filtering, etc.) is done at this step.
4. Migrate the result of step 3 as (15) to obtain $I_{JR}\left[x_q, z_q\right]$.
5. For each z_q, fit a 3-parameter Weibull distribution to $\left|I_{JR}\left[x_q, z_q\right]\right|$ along the x_q dimension according to maximum likelihood estimates as in Fig. 34.
6. For each resultant 3-parameter Weibull distribution $f_{z_q}(m; \alpha, \beta, \gamma)$, calculate (18) to obtain probability of false alarm $P\left(M > \kappa \middle| I_{target}\right|)$ versus depth as in Fig. 35.
7. Determine P_{FA} to be used as the specification. Generally, $P_{FA} = 5\%$ results in small distributed false alarms. Sensitive systems should choose $P_{FA} \leq 1\%$.
8. Any depth with $P\left(M > \kappa \middle| I_{target}\right|) > P_{FA}$ in step 7 is a specification violation as the result of coupling. If violation is significant, the system designer should redesign the relevant components. This may be inclusion of absorbing material, spacing of antennas, choice of pulse, or even redesign of antenna components.

The proposed method results in an extremely powerful test for the robustness of a given coupling signal in a jitter environment. However, the migrated probability specification method has non-technical issues including computing time and lack of portability. For example, migrating $N_k \times N_i$ datapoints with high spatial resolution can take on the order of an hour. Because the migrated probability specification does not result in a scalar number similar to the linear slope specification,

it is less attractive for simple and portable calculations. Together, both form a set of specifications that are of aid to GPR system designers in order to more accurately characterize the severity of potential coupling residues.

B. Added Distortion and Clutter from Surrounding Structures

This section contains significant portions from [54], reprinted with permission. Ground-penetrating radar (GPR) is a class of radar that focuses on detecting subterranean objects. Due to the difficulty of accurate detection, GPR systems are inherently sensitive to clutter. Constant clutter is easily removed with signal processing techniques such as background removal but removal of non-deterministic clutter is unreliable [42, 55]. This non-deterministic clutter can come from outside interference, target-dependent reflections, and physical objects in the vicinity of detection. Oftentimes GPR systems are designed with a reflective backplate to mitigate outside interference and enhance structural integrity. However, adding a reflective backing will clearly increase target-dependent clutter. In this paper, we explore the severity of clutter contribution from the reflective backplate of a multi-static GPR array. Using images taken at the UC Davis sandbox, we take GPR images with and without the backplate to analyze the effect of the mechanical system construction. Ultimately we conclude image quality is significantly worsened with a reflective backplate, but can be slightly improved with the inclusion of absorbing materials. This result is important in the design of any high-accuracy GPR array.

i. Structural Contribution to Ringing

Description of Structural Geometry

First, we establish the geometry of the array. To maintain generality, the chosen shape is the "first conscious choice" design of a multi-static GPR array shown in Fig 37a. Mechanical necessity

dictates rigid metallic crossbeams for each antenna. Ten antennas in total are hung in a 2 x 5 matrix where the first row is receive and the second row is transmit. The distance between each column (transmit-transmit) is 20 cm. The distance between each row (transmit-receive) is 15 cm. The metallic back-plate is realized by placing aluminum sheets on top of the crossbeams.

ii. Key Clutter Contributions from Multi-Static Structures

The three main contributions that such a structure would have to the clutter are labelled A, B, and C below in Fig. 36.

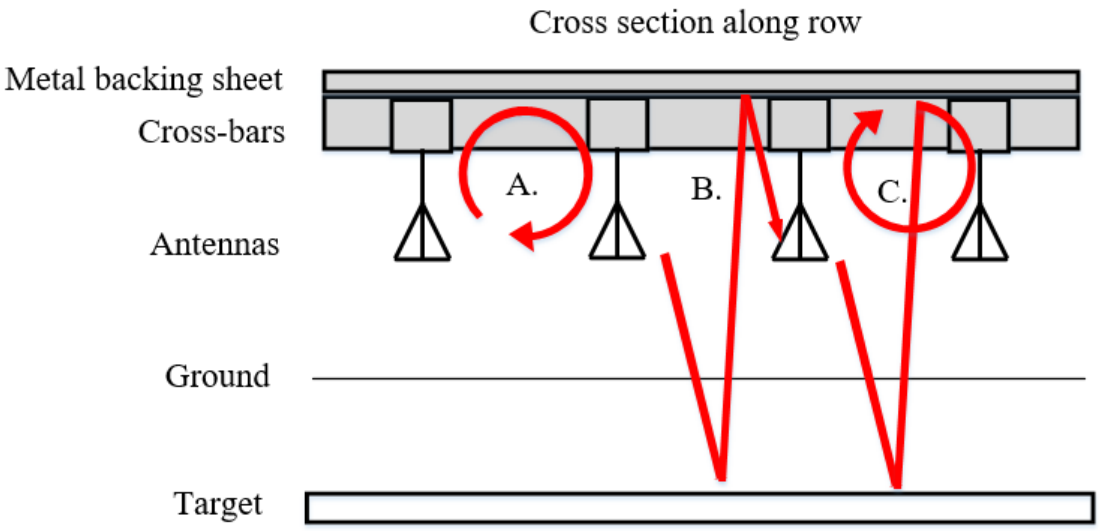

Fig. 36: Cross section across length of multi-static array setup showing additional clutter generated from inclusion of a supporting structure

1. First, the monostatic coupling between antennas is enhanced. An evanescent ringing cavity mode will also be excited in the volume consisting of the cross-bars and metal backing sheet. This contribution is deterministic.
2. Second, an additional multipath is created. This will occur with the ground return as well as any target return. This path can create a single ghost image placed close in time to the first image.

3. Finally, the structure bounce described in B can excited a ringing mode described in A. This will lead to target-specific ringing, and several ghost images close in time to the first image. This contribution, along with B, can be target dependent and difficult to compensate.

Clearly, the addition of a metal backing plate adds the potential for significant image distortion. The added ghost images from the multipath and ringing mode poses a significant issue for radars that aim to detect multiple collocated objects.

iii. Experimental Validation and Mitigation

In this section, we present three different GPR images. The antennas used are resistively loaded vee dipoles (RLVDs) [22] for their low boresight RCS. The UWB pulse is a Ricker centered at 1 GHz generated using an AWG and sampled with a 20 GS/s oscilloscope. The test target is a metal plate buried at 50 cm in sand with $\varepsilon_r = 5.8$. The sandbox dimensions are 1.8x2.4x1 meter, placed above ground. The crossbeams were left uncovered throughout all three experiments for an accurate assessment of the effect of the reflective backing. As the target is a plate and thicker than the skin depth, minimal hyperbolic returns are expected (only second-order edge diffraction), and

the main image should be straight. In Fig. 37d, we see a clear return with some minimal late-time ringing due to the antenna – this is the baseline which to compare Figs. 37e and 37f.

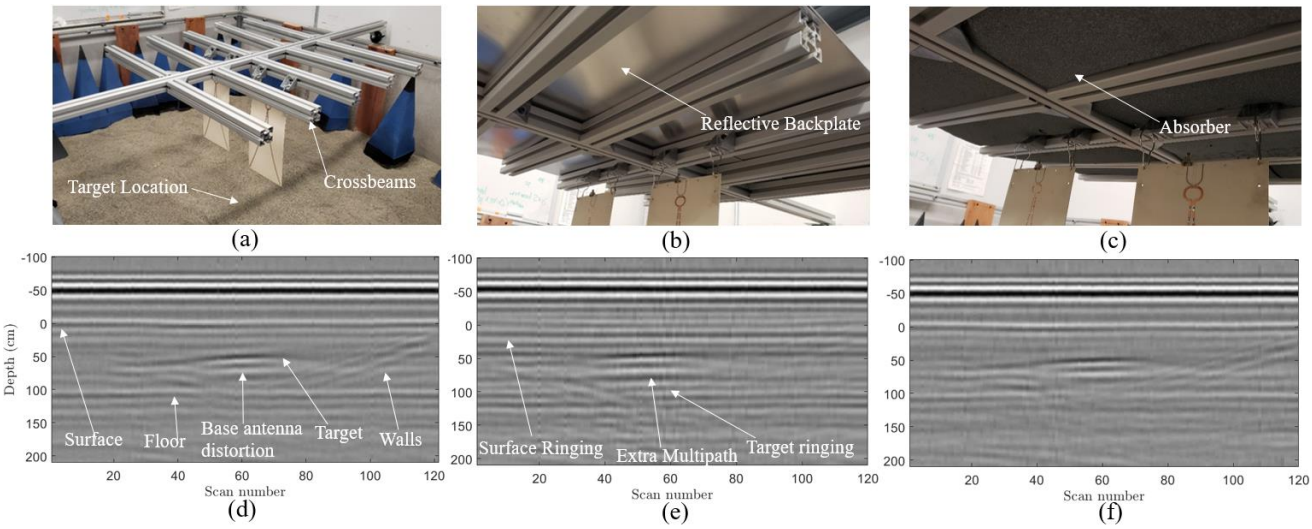

Fig. 37: a) System without backing (only two antennas pictured for clarity of structure) b) System with metal backing c) System with backing with AN-75 RAM covering reflective backplate d) Raw image taken without backing e) Raw image taken with metal backing f) Raw image taken with AN-75 covering reflective backplate

We can see in Fig. 37e, the metal-backed image, there is a significant ghost image on top of the antenna distortion. This is due to the multipath. Additionally, the ground line is much less well defined with the additional ringing caused by the volume between the aluminum backing and the crossbeams. This issue can clearly be seen in Fig. 38, where the reflective sheet backing trace has higher ringing magnitude after surface, target, and floor returns, burying the true image in clutter. The multipath is also quite clear in the target return.

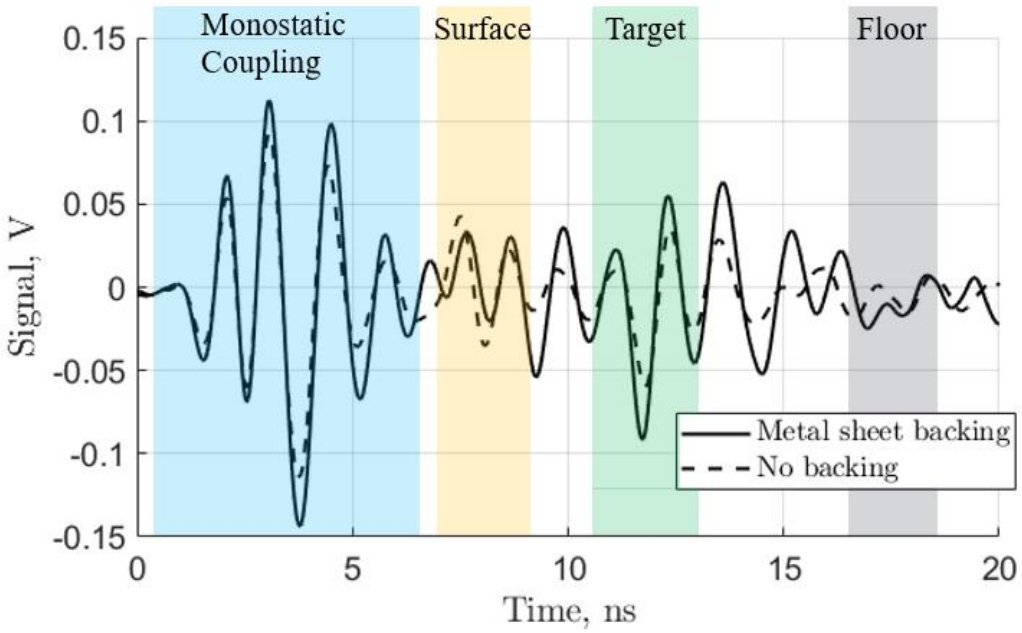

Fig. 38: A-scan from middle of target (scan 50) with both metal sheet backing and no backing traces

Finally, Fig. 37f is the image taken with the metal covered in AN-75 RAM absorbers. The image is of similar quality to Fig 37d, but with slightly less-defined features. This can be attributed to the proximity of the RAM to the antenna, resulting in a slight drop in boresight efficiency.

C. System-Based Antenna Specifications

Typical antenna design for ground penetrating radar (GPR) primarily focuses on the optimization of antenna gain and impedance bandwidth [56, 57]. For example, [58] uses a figure of merit based on gain, bandwidth, and size to compare a wide variety of antennas for GPR. Gain and bandwidth requirements are focused on because they relate to the most fundamental specifications given to a system designer: power, frequency, and link budget [59, 60]. However, an antenna which satisfies these generic requirements is not guaranteed to perform well in a GPR imaging scenario. For example, the antenna, despite having excellent gain and bandwidth, may significantly distort the transmitted signal [61], create unnecessary clutter reflections, have extremely loud cross-talk which smothers targets, or image with poor horizontal resolution [40, 54]. Several works, such as

[22, 28, 62-64] consider some of these phenomena, but never consider all at once. Lamensdorf [65] presented popular ways to quantify the performance of generic ultra-wideband antennas and extended the concept of pulse integrity. In GPR literature, however, there seems to be no consistent quantitative antenna specifications for the demanding application of GPR. Issues caused by these phenomena can be alleviated to some degree using signal processing algorithms. Logically, however, a higher quality radar signal will result in a better detection performance. To radiate a clean input signal, the antenna should consider the impact of each of the ancillary phenomena mentioned above. Though all aforementioned antennas may function well in a system (and many do), it is possible that the unconstrained phenomena could adversely impact system performance. By following quantitative specifications based upon the total system integration, a newly created GPR antenna is more likely to function well for a subsurface imaging application. Therefore, initial consideration of these antenna specifications can save time and money by avoiding expensive redesigns. In this paper, we explore several ancillary specifications for GPR antenna design. In separate sections, we estimate specifications on coupling signal shape, pulse distortion and ringing, gain and beamwidth for horizontal imaging resolution, radar cross section, and front-to-back ratio. Design equations and, where applicable, design plots, are provided. A final design table describes each specification, its severity, how to calculate each specification, and typical values. By verifying an antenna's performance against these specifications, an antenna engineer can avoid costly re-designs during the prototyping phase. An example MATLAB program for calculating all specifications is available [66]. For the first time, we have derived and compiled many new and useful secondary specifications for use in GPR antenna design.

i. Adverse Antenna Effects In a Real B-Scan

Two-dimensional (2-D) GPR data is presented in a B-scan format. The B-scan comprises a series of A-scans, where each A-scan is a transmitted-reflected pulse taken at a different scan position. Fig. 39 shows an experimental GPR B-Scan with labelled phenomena caused by potential antenna deficiencies.

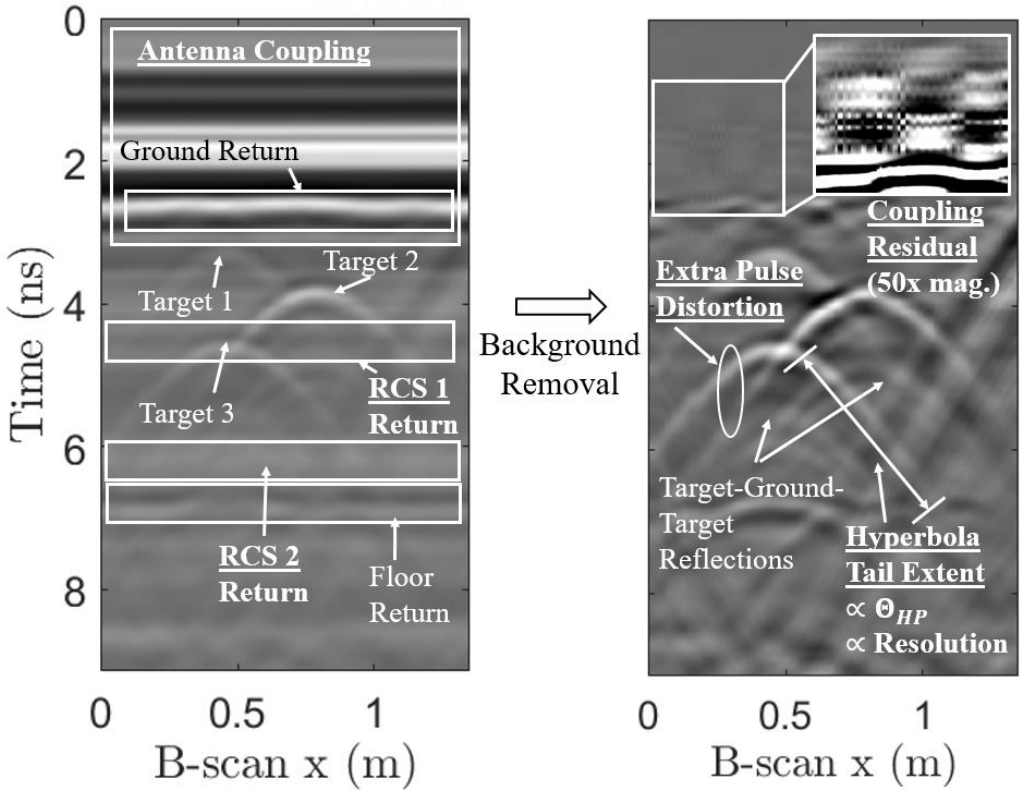

Fig. 39. Diagram showing an example GPR B-scan using real data. Bolded and underlined labels denote returns of issue to be explored. Data is taken with an indoor sandbox using a 0.5-4 GHz system, so floor and wall returns are present.

In order of Fig. 39 selection:

1. Antenna coupling is the direct signal from transmit to receive antenna. The coupling signal is typically of high magnitude with respect to the rest of the B-scan and can dominate targets.

2. Radar cross section (RCS) returns are multipath reflections which resonate in the antenna-ground surface-antenna loop. The multipath reflections typically appear during the target return, so they may interfere with background removal and cause false targets.
3. Coupling residual is the noise left over after the removal of the coupling signal. The residual noise is proportional to the slope of the coupling signal and can create a time-dependent noise floor.
4. Pulse distortion is the warping of the transmitted pulse from its ideal input shape. Typically, pulse distortion will cause ringing and elongate A-scan peaks which reduces the quality of imaging.
5. Hyperbola tail extent is the width of a point-target's hyperbola along the scan axis. This quantity is intimately related to the final image's horizontal resolution and is controlled by the antenna's beamwidth. A larger tail is better for imaging.

In addition, we will explore the impact of an antenna's front-to-back ratio. In order to create antenna specifications with respect to each topic, a designer must know several basic system parameters, listed in Table 7.

Table 7: Fundamental system parameters with common typical values for GHz GPR

Symbol	Name	Typical values
$V_{pp,t}$	Transmitted peak-to-peak voltage	1-10V
$[f_{low}, f_{high}]$	Upper and lower operation frequencies	0.3 – 3 GHz
λ_c	Wavelength at center frequency	0.6 m – 0.1 m
$x(t)$	System input pulse (or equivalent) that spans $[f_{low}, f_{high}]$	Ricker pulse with $\sigma =$ 100 ps
σ_J	System RMS jitter	10 – 40 ps
n	Number of dielectric layers	1 - 3
d_i	Thickness of i-th dielectric layer. $i = 0$ refers to the antenna layer (height), $i = n$ refers to the target layer	0 cm – 1m
G	Antenna gain at center frequency	0 dB – 10 dB
G_{amp}	Path gain from receive antenna to most compressible receiver component	10-15 dB

P_{1dB}	1-dB compression point of most compressible receiver component	10-20 dBm
Z_0	Characteristic impedance	50 Ω
$T(\theta)$	One-way power transmissivity through n layers for the ray path started by angle θ	Determined by (1) or simulation 0.1 - 1
$A(\theta)$	One-way power attenuation due to n layers for the ray path started by angle θ	Determined by (2) or simulation 0.1 - 1
σ	Expected target radar cross section (RCS)	-10: weak, 0: normal, 10: very strong (dBsm)
ϵ_i	Relative permittivity (real) of the i-th layer.	1 - 10
α_i	Attenuation constant the i-th layer	0.01 – 10 Np/m (dry – wet)
P_{int}	Maximum expected interferer power	26 dBm
$\hat{\Gamma}$	Radar enclosure electric field reflectivity	-1 – 0 (metal-air)

In the course of specification derivation, we acknowledge that any given GPR system is uniquely complex and involves many variables such that accurate prediction of how an antenna influences final performance is extremely difficult. Whenever possible, approximations are made in order to deduce "lower bound"-type specifications, where a violation of the specification may not ruin the radar system's integrity, but meeting the given specification most likely eliminates any problems associated with that phenomenon.

Application to Impulse, SFCW, and FMCW GPR Systems

Three common types of GPR systems are Impulse, SFCW (Stepped-Frequency Continuous Wave), and FMCW (Frequency-Modulated Continuous Wave) radars. Impulse radars operate in the time domain by sending and measuring an electromagnetic pulse. SFCW systems operate in the frequency domain by sending and receiving continuous-wave signals and measuring the complex reflection coefficient. FMCW systems operate by chirping a band of frequencies, mixing the received signal, and measuring the resultant beat frequencies. As all three types of systems fundamentally obey the radar range equation, they will obey the presented specifications derived from the radar range equation including coupling slope, gain-beamwidth, and antenna radar cross section specifications. Additionally, all three system types obey the presented coupling magnitude

and front-to-back ratio specifications, depending on the receiver compressing element. Impulse and SFCW radars are effectively interchangeable through a Fourier transform, so both follow the proposed distortion specifications. FMCW radars will not follow the discussed distortion specifications due to their transmitted waveform.

All specifications in this paper are presented with respect to impulse GPR. To transform an applicable specification to SFCW or FMCW GPR, convert transmitted and noise RMS voltage in the presented equations to an equivalent power as SFCW and FMCW typically operate in terms of power. To apply time-domain specifications to SFCW, take the inverse Fourier transform of the SFCW transfer function.

Notes on Multi-Layer and Inhomogeneous Media

As the overall application space of GPR systems is large, we attempt to include as many application cases as possible. Two popular applications are sensing in both multi-layer and inhomogeneous media. In the following sections, the proposed equations include generic terms for electromagnetic boundary transmissivity and loss which can be modified depending on the application.

In a multi-layer application, we are concerned with finding the correct value for $T(\theta)$, the θ −incident value for the total power transmissivity from the antenna layer to target layer, and A, the round-trip power attenuation from antenna-target-antenna. The choice of expression for T depends on the type of imaging algorithm the system implements. For migration-based algorithms such as F-K migration and Kirchhoff migration that specifically only consider the first target reflection and include no multipath effects, the correct value for T is the multiplicative combination of each layer's transmissivity:

$$T(\theta_0) = \prod_{i=0}^{n-1} T_i(\theta_i) \tag{19}$$

where $T_i(\theta)$ is the classical power transmissivity between the i and $(i+1)$ dielectric layers with an incident angle of θ_i in the i-th medium as in [67] or Appendix A. Appendix A contains expressions for the TE-polarized case, but (19) also works for a TM polarization. Irrespective of the sensing modality (impulse, SFCW, or FMCW), systems which use a migration based on the first target reflection (i.e., unknown layer properties), will use (19). Additionally, we approximate the total one-way dielectric power attenuation with simple addition as (20):

$$A(\theta_0) = \exp\left(-2\sum_{i=0}^{n} \alpha_i d_i \sec\theta_i\right) \tag{20}$$

Conversely, systems which use imaging algorithms that take into account the subsurface layer properties and depths, such as full inversion imaging based on the layered Green's function or migration including expected multipath, will not use (20), but rather use a full multilayer-reflection form of the power transmissivity. Though not reproduced here for brevity, the matrix method for transmission through n arbitrary dielectric layers is available in [67]. The reason that systems using inversion algorithms or expecting multipath can use the full n-layer transmission coefficient is that all multiply-reflected power will be useful.

In an inhomogeneous media sensing application, the concept of transmission and attenuation become difficult to quantify with simple equations. The reader is directed to [68, 69] to estimate inhomogeneous transmissivity T and attenuation A, or the result for T and A can be obtained through full-wave simulations of power transmissivity through the expected subsurface.

ii. GPR Antenna Coupling Specifications

In this section, we examine the coupling signal of a pair of antennas. Coupling affects GPR systems with transmit and receive antennas in close proximity (Δx small), shown in Fig. 40.

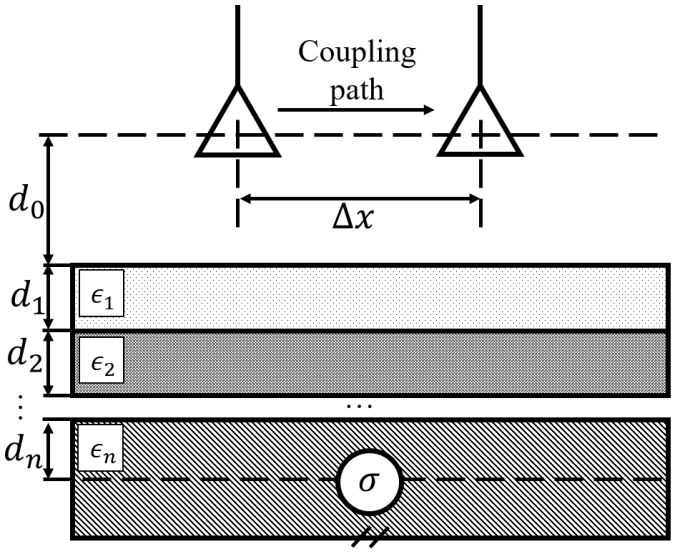

Fig. 40. Diagram showing coupling setup with operating height d_0, antenna separation Δx, sensing a target with RCS σ buried under n layers of $\epsilon_i, i \in 1 \ldots n$ permittivity.

Some energy radiated from the transmit antenna will be measured on the receive antenna. This energy is denoted as the coupling signal $c(t)$. If large in magnitude, the coupling signal will obfuscate the ground return and shallow target reflections. Typical removal methods include subtraction of a reference signal [40]. The coupling signal affects the radar scan in two ways that require constraint.

1. If the coupling signal is too large, receiver amplifiers will saturate. If amplifiers are compressed, the additional return from a buried target may be lost.
2. If the slope of the coupling signal is too large, coupling removal methods will create additional noise depending on the jitter of the system [40].

$c(t)$ is not easily predicted by antenna far-field parameters due to near-field proximity of the antennas. For this reason, we create specifications based only on $c(t)$ itself.

To address the coupling signal's magnitude, we approximate the large-magnitude sections of $c(t)$ as a sinusoid to estimate an equivalent power level. Consider a receiver containing a compressible element with antenna-to-component linear power gain G_{amp} and P_{1dB} in Watts. To maintain linearity, the coupling signal's peak-to-peak voltage V_{pp} should obey (21):

$$\max c(t) - \min c(t) = V_{pp} \leq 2\sqrt{2}\sqrt{\frac{P_{1dB}Z_0}{G_{amp}}} \tag{21}$$

where Z_0 is the system's characteristic impedance. For example, the HMC8412 low noise amplifier (LNA) has a P_{1dB} of 79.4 mW (19 dBm) with a gain of 14.5 dB. In a 50-Ohm system, the maximum coupling V_{pp} (21) is 1.06 V. This limit of 1.06 V implies that, if a coupling signal has an instantaneous V_{pp} higher than 1.06 V, the LNA will be compressed. If the LNA is compressed in a time period containing a target reflection, the target hyperbola will be visibly distorted even after coupling removal because the LNA is no longer linear. The engineer should design the antenna such that the coupling V_{pp} is less than 1.06 V. If the system does not have an LNA, then P_{1dB} may refer to the compression of the analog-to-digital converter (ADC) or a mixer – whichever is the most compressible element in the receiver chain. In this case, G_{amp} would be the total gain to and including the most compressible element.

The issue of coupling slope has been addressed directly in [40], where two different specifications are presented. Because the receiver samples the data randomly with some jitter or phase noise, the coupling signal $c(t)$ is not deterministic and cannot be completely removed. The incomplete removal is called coupling residual. To avoid any system-level impacts, we want to

specify the magnitude of the coupling residual after the removal algorithm to be smaller than our target reflection. Here, we expand upon equation (9) in [40] to obtain a single equation based upon basic far-field parameters as (22):

$$\left|\frac{d}{dt}c(t)\right| \leq \kappa_c \frac{V_{pp,t}}{2\sqrt{2}Z_{1-\frac{\alpha_c}{2}}\sigma_J}\left[\frac{G\lambda_c\sqrt{\sigma}T(0)A(0)}{(4\pi)^{3/2}\left(\sum_{i=0}^{n} d_i\right)^2}\right]u\left(t-\frac{2\sum_{i=0}^{n-1} d_i\sqrt{\epsilon_i}}{c}\right) \quad (22)$$

In (22), $T_n(0)$ refers to the expected perpendicular power transmissivity for an n-layer dielectric subsurface determined by (19) or simulation and A refers to the round-trip attenuation determined by (20) or simulation. The quantity in brackets in (22) is the square root of the well-known radar range equation in order to obtain the radar equation in terms of RMS voltage. All three terms together estimate the target reflection from a σ-strength target. For a detailed derivation, see Appendix A. The single-layer version of (22) is expanded in (23):

$$\left|\frac{d}{dt}c(t)\right| \leq \kappa_c \frac{V_{pp,t}}{Z_{1-\frac{\alpha_c}{2}}\sigma_J}\left[\frac{G\lambda_c\sqrt{\sigma}e^{-2\alpha_1 d_1}}{(4\pi)^{\frac{3}{2}}(d_0+d_1)^2}\right]\left[\frac{\sqrt{2\epsilon_1}}{(\sqrt{\epsilon_1}+1)^2}\right]u\left(t-\frac{2d_0}{c}\right) \quad (23)$$

In (22) and (23), $Z_{1-\alpha_c/2}$ is the parameter (Z-score) of a standard normal distribution that contains area $\alpha_c/2$ to the right of itself, α_c is the probability that the specification is violated, and κ_c is a threshold constant (coupling), typically 0.1 to 1. (22) and (23) are time-gated by the step function $u(t)$ which represents that coupling can be ignored before the final layer reflection. The

inclusion of the time-gate means that operating at a large height generally decreases sensitivity to coupling residual.

An antenna that satisfies (22) or (23) ensures that, once removed, the RMS voltage of the coupling residue has at most probability α_c to have greater than a κ_c-fraction of the reflected target signal's RMS voltage after the ground return. By ensuring a small coupling residue, the antenna's coupling signal will not interfere after removal. For example, a 500 MHz – 3 GHz system with $\sigma_J = 20$ ps detecting 0-dBsm targets a depth d_1 of 30 cm in a single layer ($n = 1$) of $\epsilon_1 = 5$ dry soil with $G = 4$ dB antennas at a height d_0 of 40 cm with a $V_{pp,t} = 1V$ has a coupling slope specification (22) of 160 mV/ns with $\kappa_c = 1$ and $Z_{1-\alpha_c/2}$=1.96 (for α_c = 0.05). Regions in the antenna's coupling signal after a time of 2.67 ns with a slope greater 160 mV/ns have above a 5% chance to have a residue on order of the magnitude of the approximate target reflection. Therefore, the engineer should take precaution to decrease the coupling slope at those regions in time.

To estimate $c(t)$, a designer should first simulate a pair of antennas in a coupling configuration to calculate the coupling voltage transfer function versus frequency. Then, the designer should calculate the output $c(t)$ after excitation with an equivalent GPR input pulse to verify (21) and (22).

iii. GPR Antenna Distortion Requirements

GPR systems typically operate over an ultra-wide bandwidth. Both frequency-domain and time-domain systems must be concerned about antenna distortion, a quality which is difficult to control over wide frequency ranges. Antenna distortion originates from many sources [61], some of which are labelled in Fig. 3. Pulse distortion is perhaps the most popular optimization subject other than gain and bandwidth in GPR literature. For example, [24, 28, 62, 64, 70, 71] all consider the radiated

waveform's integrity. [63] uses a metric called group delay flatness to describe the radiated pulse integrity. We desire to create a measurement that, above some threshold, the antenna's distortion is acceptable. If antenna distortion is too high, the distorted pulse can create misshapen targets and increase the overall clutter in the image.

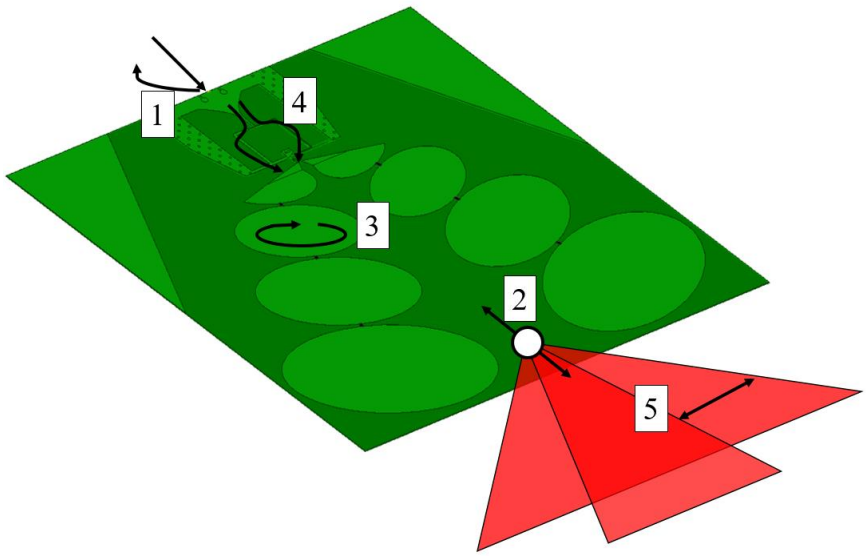

Fig. 41: Potential sources of distortion in an antenna: 1) Input reflection coefficient, 2) Phase center movement with respect to frequency, 3) Internal structural ringing, 4) Unequal magnitude/phase delay in baluns/feeding structures, and 5) Radiation pattern changes with respect to frequency.

Fig. 42 shows an experimental example of pulse distortion in a GPR scan. Using the same pair of antennas, we input both a clean pulse and a pulse with an exponential ringing profile in two different scans. By intentionally distorting the input pulse, we simulate an antenna with poor distortion properties in the form of ringing. In Fig. 42, the scan with increased pulse ringing has significantly worse ground removal, high target ringing, and worse clutter. The poor ground removal would entirely obscure a shallow target and the target ringing creates ghost images below the target upon imaging.

As the varied sources of distortion are complex, intertwined, and dependent on antenna structures, it is infeasible to attempt to create a specification based only on those fundamental sources. Rather, we examine the distortion on the output pulse when simulated going through a transmission system.

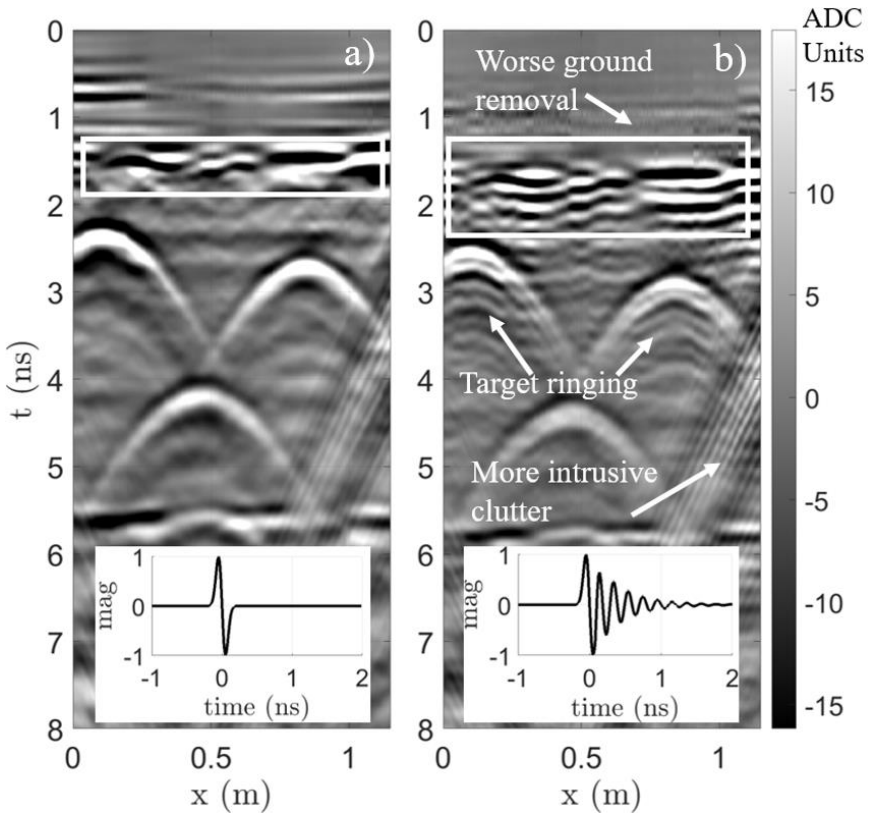

Fig. 42: Effects of poor pulse transmission on the quality of a background-removed GPR B-Scan. a) Reference scan with clean input pulse (inset a). b) Distorted scan with intentionally ringing pulse (inset b). Colorbar is ADC units, arbitrary units for voltage.

Pulse Integrity

We first employ the pulse integrity χ in (24), defined rigorously in [65]:

$$\chi = \max_{t}[|y(t) \star x(t)|] \geq \kappa_d \tag{24}$$

where $x(t)$ is the input pulse which spans the system's operating bandwidth, $y(t)$ is the output pulse given $x(t)$, $a \star b$ refers to the normalized cross-correlation between two vectors a and b

($|a \star b| \leq 1$), and κ_d is a threshold parameter (distortion), typically 0.9. Pulses with $\chi > 0.9$ tend to show negligible distortion. To find $y(t)$, first simulate or measure the voltage transfer function $H(f)$ between two antennas pointed towards each other at least twice the target distance apart. Then, apply an inverse Fourier transform to the product of $H(f)$ and the Fourier transform of $x(t), X(f)$, to find $y(t)$. An example of this simulation is shown below in Fig. 43. The transfer function $H(f)$ behind Fig. 43's output pulses is determined in 3-D electromagnetic simulation by determining the S_{21} of two antennas pointed at each other 1 meter apart.

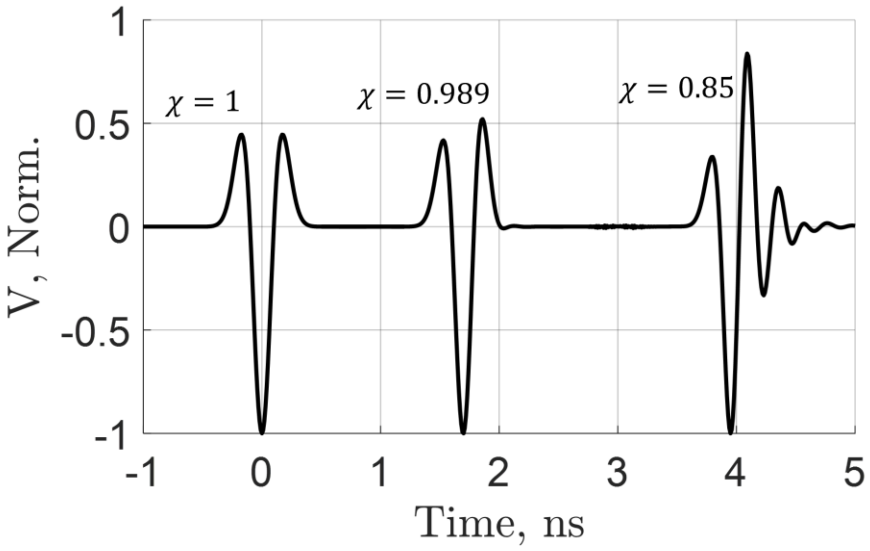

Fig. 43. Example showing three different values of pulse integrity χ

In Fig. 43 above, $\chi = 1$ represents the ideal input pulse, $\chi = 0.989$ represents an output pulse with very little distortion, and $\chi = 0.85$ represents an output pulse with noticeable ringing. For pulses used in GPR, $\chi \in (0.95,1]$ represents superb pulse reconstruction, $\chi \in [0.9, 0.95)$ has excellent pulse integrity, and $\chi < 0.9$ starts to show ringing. A pulse with $\chi \in [0.75, 0.9)$ can still be usable, but with degraded performance. If an antenna has a small χ, a designer should focus on smoothing group delay, flattening the voltage transfer function, and decreasing reflection

coefficient in the operation bandwidth. The limitation of using pulse integrity as a specification is that a low pulse integrity could come from the widening of a pulse, reshaping of a pulse, or ringing. Because a pulse integrity of $\chi = 0.9$ does not physically correspond to a certain quality of the radar scan, we will next directly examine the pulse's ringing.

Residual Ringing

We define another useful specification as the residual ringing in dB-scale after the initial pulse. An example of this plot is used in [72]. Residual ringing is more physically appealing as a specification because ringing is directly observable after target returns in both radar scans (Fig. 42) and focused images. We examine the quantity R in (25):

$$R = 20\log_{10}\left(\frac{|y(t)|}{\max_{t}|y(t)|}\right)u[t - t_0] \leq \kappa_r \tag{25}$$

The residual ringing R should be less than some threshold parameter κ_r for $t > t_0$. Typically, κ_r is equal to or less than -20 dB. Choosing this value for κ_r ensures that additional ringing will not be visible in radar imaging when displayed with a dynamic range of 10 dB. The parameter t_0 stands for the time at which a perfectly transmitted pulse with no ringing would end. Therefore, all energy after t_0 is considered distortion. A simple method to estimate t_0, assuming a time-symmetric input pulse, is given as (26):

$$t_0 = \underset{t}{\operatorname{argmax}}|y(t)| + \frac{\mathrm{FWTM}\{\mathrm{env}[x(t)]\}}{2} \tag{26}$$

where FWTM(x) is the full width in time at a tenth of the pulse's maximum value and is used as a representation of pulse width. The FWTM is taken on the envelope of $x(t)$, calculated using the

magnitude of $x(t)$'s analytical counterpart. Fig. 44 displays an example plot of (25). Violations of (25) due to the initial falling edge near $t - t_0 = 0$ are ignored due to the low-pass nature of a GPR system, which differentiates and widens the input.

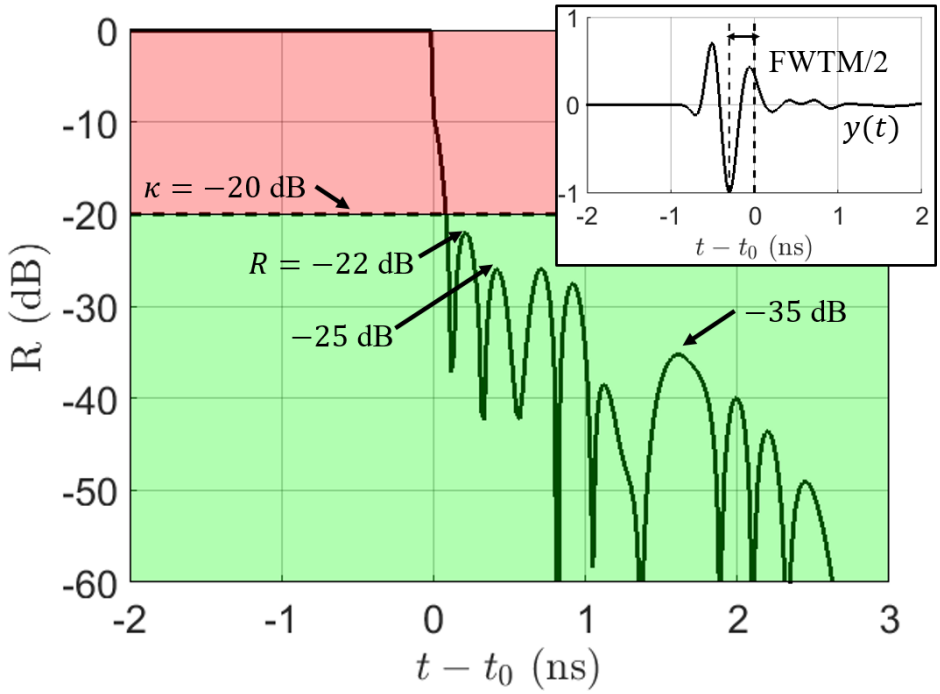

Fig. 44. Example residual ringing of a 0.5-3 GHz Ricker pulse going through a simulated antenna system with $\kappa_r = -20$ dB. This residual waveform passes specifications. The inset plot shows $y(t)$ in a linear y-axis for reference with the FWTM of $x(t)$ indicated by the dashed lines.

In the case of Fig. 44's waveform, the specification is met because the first ringing peak is -22 dB less than the maximum peak value. In the case of a violation, the designer should modify the antenna to decrease the ringing or else risk impacted imaging performance.

iv. GPR Antenna Gain, Beamwidth Considerations

An antenna which achieves the minimum required gain may still image poorly. As the vast majority of GPR systems operate using synthetic apertures, a better specification would keep the synthetic aperture in mind when specifying both the beamwidth and the gain.

With constant efficiency, an increase in gain will typically decrease an antenna's beamwidth. A decrease in beamwidth can in turn decrease the effective imaging aperture. The imaging aperture is inversely proportional to the resulting horizontal resolution, which should be small for accurate imaging. To estimate the horizontal resolution from imaging parameters, we use (27) [42]:

$$\text{Horizontal Resolution } HR \approx \frac{\lambda_c}{2\sqrt{\epsilon_n}\sin\theta_m} \tag{27}$$

where θ_m is the maximum view angle, indicated in Fig. 45. When selecting the antenna's beamwidth, denoted Θ_{HP} for half-power beamwidth, the engineer encounters a dilemma: given a constant antenna efficiency, a higher antenna gain implies both a higher target reflection and a lower beamwidth. Yet, a lower beamwidth implies a lower resolution after image focusing using the synthetic aperture. Then, what is the optimal beamwidth-gain configuration for a given system?

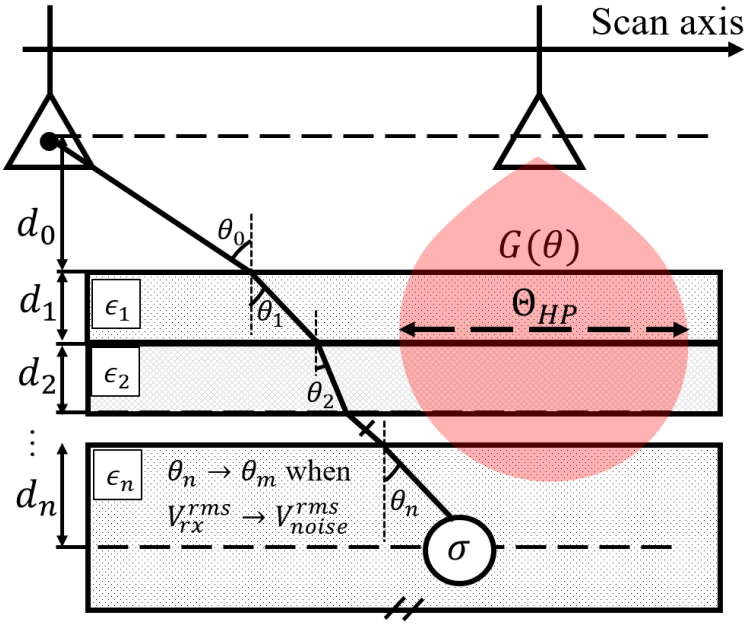

Fig. 45. Diagram showing the geometrical maximum view angle θ_m and half-power beamwidth Θ_{HP}.

To properly consider this question, we must constrain ourselves to a class of beamwidths. We select normalized antenna gain patterns $G_m(\theta)$ with power output centered at $\theta = 0$ which belong to a $\mathrm{sinc}(\theta)$ class (28):

$$G_m(\theta) = G_0 F_m(\theta) = \frac{G_0}{2\pi} \frac{|\mathrm{sinc}(m\theta)|}{\int_0^{\pi} |\mathrm{sinc}(m\theta)| \sin(\theta)\, d\theta} \tag{28}$$

By varying m in (28), we can alter the antenna's beamwidth Θ_{HP}. The $\mathrm{sinc}(\theta)$ shape of F_m is selected as the main lobe of a generic antenna pattern. We choose G_0=4 to simulate realistic antenna gains. We arrive at this number by comparing the maximum (peak gain) of $G_m(\theta)$ to the beamwidth of $G_m(\theta)$ for different G_0. G_0 implicitly contains the antenna's efficiency. For intrinsically inefficient antennas such as resistively loaded vee dipoles (RLVDs), then G_0 should be tuned to align with the proper gain-beamwidth relation.

Given a minimum RMS received voltage (noise level), we use $G_m(\theta)$ to simulate a simplified version of the GPR scan, and thus approximate the horizontal resolution for a given antenna gain pattern. To simulate the scan we again employ the well-known radar range equation, similar to the process shown in (22) and Appendix A:

$$V_{head}^{rms} \approx \frac{V_{pp,t}}{2\sqrt{2}} \left[\frac{G_0 F_m(\theta_0) T(\theta_0) \sqrt{\sigma} \lambda_c}{(4\pi)^{\frac{3}{2}} \left(\sum_{i=0}^{n} \frac{d_i}{\cos \theta_i} \right)^2} \right] A(\theta_0) - V_{noise}^{rms} \tag{29}$$

where now θ_i are the ray-based angles in the layered medium indicated in Fig. 45. In (29) all terms are defined in Table 7 or previously. The first term on the right side of (29) is the RMS received target-reflected voltage V_{rx}^{rms}, and the difference (headroom) between V_{rx}^{rms} and V_{noise}^{rms} is denoted V_{head}^{rms}. A positive value of V_{head}^{rms} indicates that the target is detected. A negative value of

V_{head}^{rms} indicates that the target is lost in noise. Only the main lobe of $G_m(\theta)$ is used in sensing. (29) is calculated at the center frequency, and we intentionally neglect the frequency-dependence and discussion of a point-spread function for sake of simplicity. To determine the best beamwidth, (29) is scanned by varying the antenna's-position along its scan axis. At each position, θ_g and θ_m are calculated using the path-of-least-time ray refraction angles (see Appendix A) and (29) is calculated for V_{head}^{rms}. To determine the maximum view angle θ_m, we observe when V_{head}^{rms} transitions from a positive to negative value, the target return disappears and we declare that $\theta_m = \theta_n$. A smaller θ_m implies a worse resolution in (27). The simulation of (29) will optimize for lowest horizontal resolution.

Fig. 46a – Fig. 46c demonstrate the nominal horizontal resolutions for various system archetypes versus beamwidth and gain. Ideally, the designer will select the antenna's gain and beamwidth for the minimum horizontal resolution.

Fig. 46a shows the horizontal resolutions for various target depths for a GPR system where the antennas are air-coupled at a height of d_0= 25 cm off the ground. Under these system parameters, Fig. 46a shows that it is generally favorable for the system to trade gain for beamwidth. In this case, the antenna designer should choose to aim for a beamwidth between 60 and 90 degrees, or a gain between 3 to 4 dB. There is no significant loss in resolution until approximately 30 degrees beamwidth.

Fig. 46b plots the horizontal resolutions on a drone-mounted GPR system operating at 1.5 meters off the ground. The additional height in a drone system causes increased path loss, which causes a smaller θ_m for a given set of a system parameters. The increased path loss of a UAV-based GPR system favors trading beamwidth for more gain. In the case of targets buried at 50 cm

deep, the antenna designer should aim for a beamwidth between 30 and 60 degrees, or a gain between 4 to 7 dB.

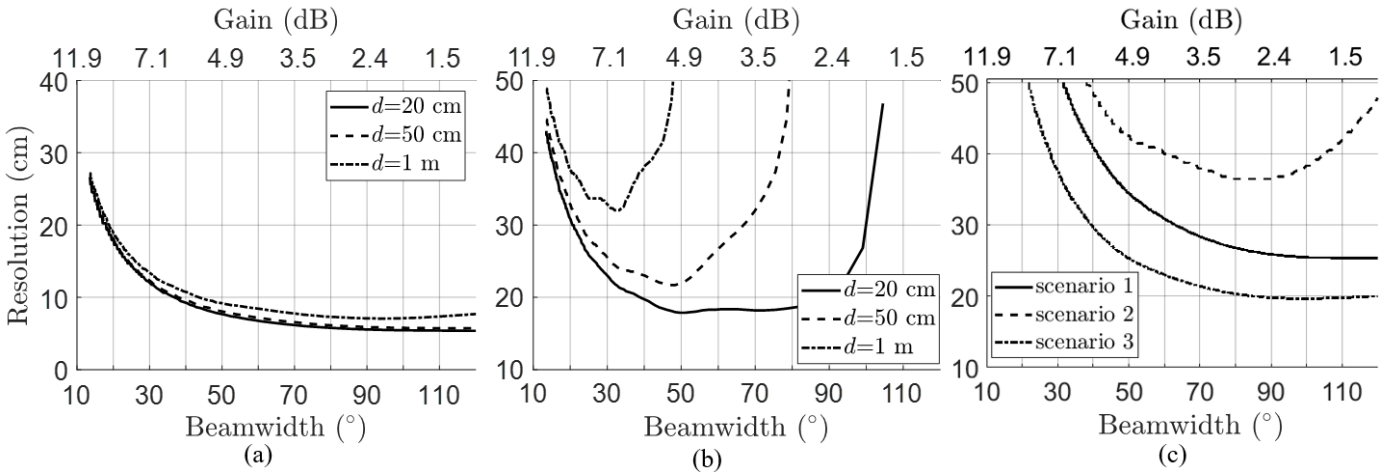

Fig. 46. Example beamwidth-resolution curves (29) for various GPR systems. Nominal parameters if not specified: $\alpha = 0.01$ dB/m, d_0=25cm, σ=0 dBsm, $G_0 = 4$, $\epsilon_r = 5$, $\lambda_c = 10$ cm, $V_{pp} = 1$V. Lower resolution is better. (a) Medium-height GPR system with d_0 = 25 cm. (b) Drone-mounted GPR system with $d_0 = 1.5$ m, $V_{pp} = 2$V. (c) Horizontal resolution for three multilayer scenarios ($\lambda_c = 30$ cm, V_{pp} =3V). Scenario 1: $d = (25, 10, 30)$ cm, $\epsilon = (1, 6, 4)$, $\alpha = (0, 3, 1)$ Np/m; Scenario 2: $d = (25, 30, 30)$ cm, $\epsilon = (1, 6, 4)$, $\alpha = (0, 3, 1)$ Np/m; Scenario 3: $d = (25,10,30)$ cm, $\epsilon = (1, 10, 2)$, $\alpha = (0, 3, 1)$ Np/m.

Fig. 46c shows the horizontal resolutions for three different three-layer detection scenarios, where each scenario is a different combination of three permittivities, depths, and electromagnetic attenuations. Scenario 1 is the base scenario from which scenarios 2 and 3 are derived. In scenario 1, the expected horizontal resolution curve implies that a low gain/high beamwidth antenna is best for sub-ground imaging with the particular parameters given in Fig. 46c. Scenario 2 has a thicker top-layer (30 cm) with a permittivity of 6. This combination of layers leads to interesting behavior in the resolution-beamwidth curve – for the given system settings, the resulting horizontal resolution is best when the antenna has a gain of 2 to 4 dB, and significantly worse when the antenna has lower or higher gain. Scenario 3 changes the permittivity values of bottom two layers. In this case, changing the last two permittivity values simply shifts the resolution-beamwidth curve down. From Fig. 46c, we can conclude that multi-layer applications have interesting gain-beamwidth behavior depending on the relative thicknesses and permittivities of their constituent layers.

In all previously considered situations, we have not yet discussed clutter. A larger beamwidth will include more clutter in the GPR image. Clutter, by nature, is random. Extra clutter in the imaging process will degrade the SNCR (signal to noise-and-clutter ratio) and increase false alarms. As these specifications give a qualitative range in which to design, it is best for the designer to err on the side of narrower beamwidths and higher gain, especially when operating at higher heights. Finally, we have performed additional simulations similar to Fig. 46 with lowering the target reflectivity and increasing soil loss. As in Fig. 46b, an increased difficulty of target sensing tends to favor higher gain antennas, from 6 to 9 dB. This and other results from this study are summarized in Table 8.

Table 8: Summary of qualitative specifications on antenna patterns for GPR antennas in various applications. System parameters in caption of Fig. 46. Beamwidth-gain conversions are based on (28).

Application/System	Gain Behavior	Beamwidth Behavior
Low-height GPR	3 - 4 dB	60° - 90°
Drone GPR	4 - 7 dB	30° - 60°
Weak Targets/Lossy Soil	6 - 9 dB	20° - 40°
High Clutter Environment	Higher gain	Lower beamwidth

v. GPR Antenna Radar Cross Section Specifications

The boresight radar cross section (RCS) of GPR antennas has been a long-considered parameter as in [24]. Antennas with a high RCS may introduce multiple clutter signals which can obscure or drown out target reflections. The studied clutter signal is the electromagnetic wave which bounces between the ground and antenna structure one or multiple times. Examples of RCS reflections are commonly found as horizontal striping in the B-scans of typically high RCS antennas, such as those in [62, 70, 73, 74].

The removal of these reflections can distort parts of the target hyperbola. If the ground profile is not flat, then removal of these multipath reflections will be difficult because the reflections will look extremely similar to targets. If the RCS reflections are poorly timed and arrive at the time-depth equivalent exactly equal to the target return, the top of the target hyperbola can be entirely smothered. These artifacts may collect errors

through the processing pipeline, leading to a decreased SNCR and increased false alarm rate. Fig. 47 shows an experiment to highlight the issues of a high antenna RCS.

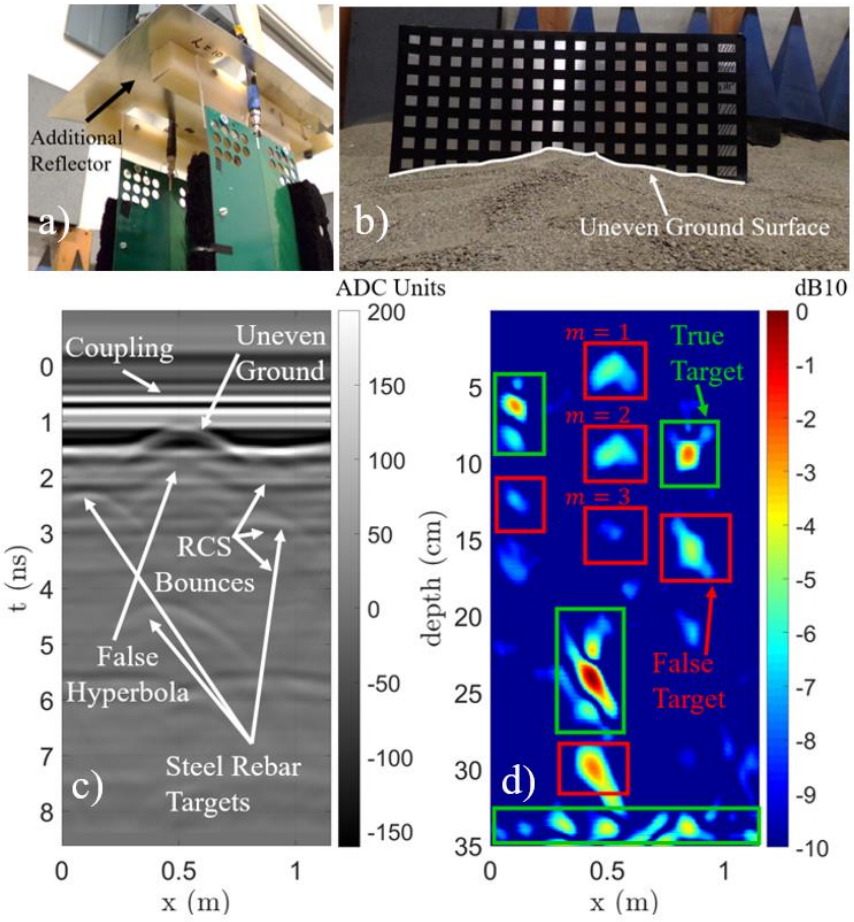

Fig. 47: Example of increased antenna RCS creating false targets. a) Photograph of metallic backing reflector to simulate increased antenna RCS. b) Uneven ground surface. Pictured grid reference is parallel to floor. c) Raw scan with coupling and RCS bounces labelled. d) Kirchhoff-migrated image with true and extra false targets shown.

In Fig. 47, we augment a pair of antennas with a metallic reflector to simulate increasing the antenna's RCS σ_{ant}. The antenna pair scans over a patch of uneven soil (Fig. 47b). In Fig. 47d, the first ($m = 1$) and second ($m = 2$) RCS reflections appear inside the target zone as a strong target (boxed in red). The combination of increased antenna RCS and an uneven ground surface entirely hallucinate these two targets. Additionally, true targets (boxed in green) have ghost followers (boxed in red) due to the antenna's RCS. The increased RCS has dramatically increased the radar's false alarm rate.

Though the idea of RCS as a far-field parameter becomes inaccurate when operating at medium-to-low heights, we use RCS as a first-order approximation of reflectivity due to its ready availability in full-wave simulation. Additionally, the RCS of an antenna is not the only source of reflection of up-going waves. The circuitry and mechanical holdings, generally placed above the antenna [54], have been shown to create additional reflections that can enhance or even dominate antenna-based reflections. The quantity σ_{ant} should ideally contain the contribution of both antenna and backing structure. This structural reflection is the principle behind Fig. 47.

A high antenna boresight RCS is only an issue when the time of arrival of the m-th coupling bounce ($m = 1, 2, \dots$) lies in the range of the time of arrival of expected targets. Otherwise, the multiply-reflected signals cannot affect target returns. By equating times of arrival in a boresight system condition, we derive that the m-th antenna RCS multipath reflection could potentially overlap a target detection when (30):

$$d_0\sqrt{\epsilon_0}(1+m) \geq \sum_{i=0}^{n} d_i\sqrt{\epsilon_i} \tag{30}$$

where the left hand side of the equation is related to the time-of-arrival of the m-th RCS bounce and the right hand side of the equation is related to the time-of-arrival of the target reflection at boresight. By itself, (30) is not a complete specification and does not make a claim about the magnitude of any RCS reflection.

(30) implies that there are three system applications in which a GPR system is insensitive to antenna RCS: drone-based systems operating at relatively large heights, low-to-medium height systems looking exclusively for deep targets, and ground-coupled GPR systems operating at $d_0 \ll \lambda_c$ where the concept of multipath bounces between antenna and ground due to RCS no longer holds. When (30) is true, we must constrain the expected magnitude of the multipath RCS reflections. We elect to constrain the expected RCS reflection magnitude against the expected target return.

In order to find an upper bound for the antenna RCS, we must estimate the reflectivity of the ground, $|R|$. After the ground reflectivity is estimated, we construct the specification by constraining the RMS voltage of the multipath RCS reflections. These reflections should be less than a scalar multiple κ_{rcs} of the expected RMS voltage of the target return. For generality, we assume an isotropic radiation pattern. In mathematical terms, we constrain the antenna's boresight RCS σ_{ant} as a function of received target RMS voltage V_{rx}^{rms} and other terms in Table 7 as (31):

$$\frac{V_{pp.t}}{2\sqrt{2}}\sigma_{ant}^{m/2}|R|^{m+1} \leq \kappa_{rcs}V_{rx}^{rms} \tag{31}$$

Equation (31) has the given form because the m-th RCS reflection is reflected by $\sqrt{\sigma_{ant}}$ m times and takes $m+1$ round-trip reflections between antenna and ground. In (31), V_{rx}^{rms} is here defined as the first term in (29) with $\theta_i = 0 \; \forall \; i$ and $G_0F_m(\theta) = 1$, explicitly defined in (32):

$$V_{rx}^{rms} = \frac{V_{pp,t}}{2\sqrt{2}}\left[\frac{\sqrt{\sigma}\lambda_c T(0)A(0)}{(4\pi)^{\frac{3}{2}}\left(\sum_{i=0}^{n} d_i\right)^2}\right] \tag{32}$$

In (32), R contains the reflectivity of the ground surface at an antenna height d_0, calculated as the reflection of a spherical wave emanated by and measured at a source point impinging on an infinite dielectric half-space [75, 76]. In estimating R, a proper treatment would calculate the Sommerfeld integral formulation [77], and this approach has been performed in literature [75]. However, we explicitly value simplicity over accuracy. Following the development of [75], the magnitude of reflection of a spherical wave from a planar boundary approaches the common Fresnel plane wave refraction coefficients. Then, we can make the intuitive approximation (33):

$$|R| \approx \frac{1}{8\pi d_0}\left|\frac{\sqrt{\epsilon_0}-\sqrt{\epsilon_1}}{\sqrt{\epsilon_0}+\sqrt{\epsilon_1}}\right| \tag{33}$$

(33) follows from Brekhovskikh's development [78] with a normal incidence angle with an approximation for kd_0 large (wavenumber k). The rightmost term in (33) is the normal-incident reflection coefficient of the ground while the left term accounts for geometric spreading with an equivalent image source height of $2d_0$.

Combining (33), (32), and (31) together and collecting constants, we obtain the final expression for an upper bound specification on the antenna RCS σ_{ant} (34):

$$\sigma_{ant}\ (\text{dBsm}) \leq -\frac{20(m+1)}{m}\log_{10}|R| + \frac{20}{m}\log_{10}\left[\frac{\kappa_{rcs}T(0)A(0)\lambda_c\sqrt{\sigma}}{\left(\sum_{i=0}^{n} d_i\right)^2}\right] - \frac{32.9}{m} \tag{34}$$

Again κ_{rcs} is a threshold parameter, typically in the range 0.1 to 2, chosen small for non-flat applications and large for flat applications. The value for m can be found by the first value which satisfies (30). An example calculation of (34) is shown below for a two-layer application ($n = 2$) in Fig. 48. In Fig. 48, an antenna which has an RCS higher than σ_{ant} for a given target depth curve and operating height will contend with multipath reflections due to antenna RCS on the order of the expected target return.

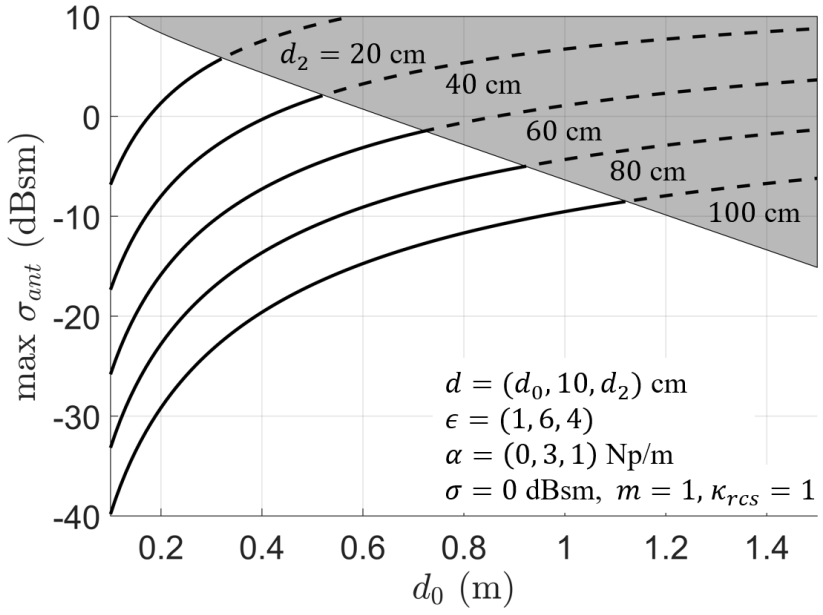

Fig. 48. Two-layer simulated maximum tolerable antenna RCS σ_{ant} versus operating height d_0 for various target depths d_2. In the shaded region, (30) is not satisfied and antenna RCS does not affect detection. Other system parameters not shown: $f_c =$ 1 GHz, $\alpha = 0.01$ Np/m.

In Fig. 48, there are several interesting trends worth elaborating upon. First, the general rule of thumb is – the more difficult an object is to detect, the lower the antenna RCS should be. Second – the valid RCS return time (non-shaded part of Fig. 48) generally sees the maximum allowable antenna RCS increase with height d_0.

At large d_0, however, the assumption that the ground reflection will scale as ${d_0}^{-1}$ will break down due to a finite antenna beamwidth. Similarly, at small d_0, both the implicit far-field assumption and plane-wave approximation of (33) become intolerable. Therefore, (34) is useful for d_0 in a medium range, from approximately 20 cm to 1 meter. When at the edges of applicability, (34) will tend to over-constrain the antenna RCS. However, (34) is still useful as a simple, portable tool to generate scalar values of RCS specification.

To verify (34), the antenna engineer should simulate the RCS in the boresight direction. Commonly used full-wave simulators have the option to calculate RCS. If an antenna violates (34), the antenna engineer should be careful to reduce the boresight RCS of the antenna. RCS reduction can be achieved in several ways,

the simplest being the introduction of absorbing material [79, 80], or physically modifying the antenna to present less physical cross-section when viewed from boresight.

vi. Front-to-Back Ratio Specification

Constraining an antenna's front-to-back ratio (FBR) is a common mode of specifying the antenna's radiation pattern. Bowtie and RLVD antennas such as [24, 81, 82] focus on or show improvements to front-to-back ratio. Designers typically view a higher FBR as better. Due to its interaction with the system's enclosure, FBR is innately related to the coupling signal $c(t)$ in (21) and (22), so some designers may use FBR as a proxy specification for decreased clutter from coupling. It would be useful to have a quantitative specification for FBR such that antennas with an FBR greater than a minimum are unlikely to suffer adverse effects related to low antenna FBR.

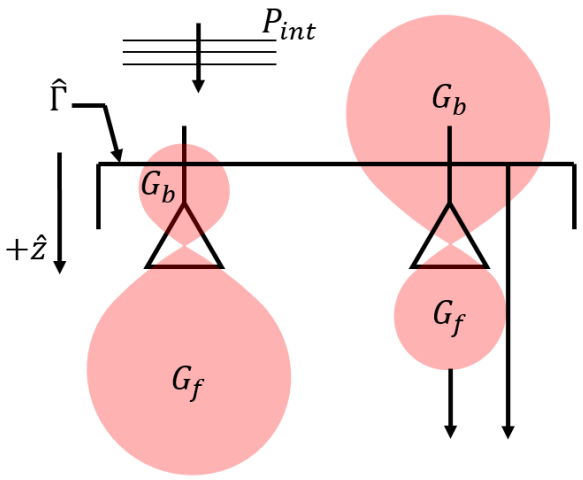

Fig. 49: Diagram showing (left) high-FBR and (right) low-FBR antennas in an enclosure with estimated reflectivity $\hat{\Gamma}$. $\hat{\Gamma}$ is assumed to be symmetric looking in $\pm\hat{z}$ and refers to reflected electric field.

Excluding coupling clutter, which has been constrained in (21) and (22), antennas with a low FBR can introduce two additional errors. We will examine specifications for both errors. First, a nearby interferer may transmit a signal with power P_{int} incident on the back of the radar as indicated in Fig. 49, where P_{int} is high enough to compress the receiver amplifiers. Second, the back-lobe's transmitted energy may reflect off the radar's enclosure [24, 54] and re-orient towards the ground (Fig. 49 right side), creating ghost images similar to those in Fig. 47d. To maintain generality, both specifications make use of the parameter $\hat{\Gamma}$. $\hat{\Gamma}$ estimates the

reflectivity of the enclosure and assumes the enclosure's shape is a z-symmetric thin sheet such that the enclosure's transmissivity is simply related to its reflectivity. These specifications also assume that the backward-reflected beam does not interfere with the forward beam.

Table 9: Table of secondary design specifications for GPR antennas

Goal Specifications					
Parameter (Equations)	Equation/Specification	Severity	Effects If Violated	Validity	Example Value
Beamwidth (29)	Simulate (29)	Hi	- Poor horizontal resolution - Poor imaging performance	Air-coupled GPR	30°-60°
Antenna boresight RCS σ_{ant} (33),(34)	σ_{ant} (dBsm) $\leq -\frac{20(m+1)}{m}\log_{10}\lvert R\rvert + \frac{20}{m}\log_{10}\left[\frac{\kappa_{rcs}T(0)A(0)\lambda_c\sqrt{\sigma}}{(\sum_{i=0}^{n} d_i)^2}\right] - \frac{32.9}{m}$	Low	- Distorted Target Hyperbolas - Poor ground removal	Medium d_0.	-6 dBsm $k_{rcs} = 1$
Front-to-Back Ratio (Interference) (35)	$\text{FBR} \geq G\left(1 - \lvert\hat{\Gamma}\rvert^2\right)\frac{P_{int}G_{amp}}{P_{1dB}}$	Low	- Receiver compression or damage - Distorted scans	Systems concerned with interference.	17.3 dB
Front-to-Back Ratio (Imaging) (36)	$\text{FBR} \geq \frac{\lvert\hat{\Gamma}^2\rvert}{\kappa_f}$	Med	- Ghost images below targets - Poor ground removal	Systems with reflective enclosures.	9.1 dB $\kappa_f = 0.1$
Verification Specifications					
Parameter	Equation/Specification	Severity	Effects If Violated	How to Simulate	Example Value
Coupling Magnitude V_{pp} (21)	$V_{pp} \leq 2\sqrt{2}\sqrt{\frac{P_{1dB}Z_0}{G_{amp}}}$	Low	- Receiver compression -Distorted target hyperbolas	– Two antennas in most severe coupling configuration - Two-port S-parameters - Input the system's pulse, measure $c(t)$ - Take maximum V_{pp} of consecutive peaks	1.06 V
Coupling Slope $\left\lvert\frac{d}{dt}c(t)\right\rvert$ (22)	$\left\lvert\frac{d}{dt}c(t)\right\rvert \leq \frac{\kappa_c V_{pp,t}}{2\sqrt{2}Z_{1-\frac{\alpha_c}{2}}\sigma_J}\left[\frac{G\lambda_c\sqrt{\sigma}T(0)A(0)}{(4\pi)^{3/2}(\sum_{i=0}^{n} d_i)^2}\right]\cdot u\left(t - \frac{2\sum_{i=0}^{n-1} d_i\sqrt{\epsilon_i}}{c}\right)$	Med	- Increased Noise - Poor coupling removal	– Same setup as above - Take derivative of output	160 mV/ns after 2.67 ns $\kappa_c = 1$
Distortion Pulse Integrity χ (24)	$\chi = \max_t[y(t) \star x(t)] \geq \kappa_d$	Med	- Poor focusing - Poor vertical resolution - Increased clutter	– Two antennas boresight, at least $2(\sum_i d_i)$ apart. - Two-port S-parameters - Input the system's equivalent pulse - Calculate ()	$\kappa_d = 0.9$
Residual Ringing R (25),(26)	$R = 20\log_{10}\left(\frac{y(t)}{\max_t y(t)}\right)u[t - t_0] \leq \kappa_r$	Hi	- Ghost images - Poor ground removal	- Same setup as above - Calculate ()	$\kappa_r = -20$ dB

FBR for Interferers

Low-magnitude interferers are easily removed in a radar's signal processing pipeline. SFCW and FMCW radars are insensitive to low-magnitude interferers because of their innate frequency-hopping operation. Equivalent-time GPR systems are insensitive to interferers because interferers are often not synchronized with the system's PRF. Therefore, the only significant worry is a high-magnitude interferer that can compress or damage the receiver's LNA. Using the same logic as (21), receiver compression can smother targets. The radar's received power from an incident interferer with power P_{int}, transmitted through an enclosure with reflectivity $\hat{\Gamma}$ will be equal to:

$$G_b \left(1 - \left|\hat{\Gamma}\right|^2\right) P_{int}$$

where G_b is the back-lobe's gain. If the enclosure is lossy, replace the quantity in parenthesis with the enclosure's insertion loss. To create a specification on $\text{FBR} = G/G_b$, we reference (21) to create (35):

$$\text{FBR} \geq G \left(1 - \left|\hat{\Gamma}\right|^2\right) \frac{P_{int} G_{amp}}{P_{1dB}} \tag{35}$$

(35) describes the minimum FBR for an antenna with forward gain G, enclosed in material with reflectivity $\hat{\Gamma}$, connected to a receiver with gain G_{amp} and most-compressible-component compression point P_{1dB}, and experiencing an interferer with power P_{int}. (35) can be calculated over all frequencies. For example, a system with an antenna gain of 6 dB, a P_{1dB} of 16 dBm, a G_{amp} of 14.5 dB, and reflectivity of 0.9 requires a minimum FBR of 17.3 dB to accept a 23 dBm incident interferer without receiver compression.

FBR for Imaging

An antenna with a low FBR can plausibly create a time-shifted version of the radar scan superimposed on the desired truth scan. The wave reflected from the enclosure can be thought of as a secondary source that transmits with a power of $\left|\hat{\Gamma}\right|^2$/FBR relative to the forward beam. If the FBR is low enough, the superimposed scan will impede background removal and create ghost targets beneath real targets. An intuitive specification arising from this system is constraining the reflected beam's relative power as in (36):

$$\text{FBR} \geq \frac{\left|\hat{\Gamma}^2\right|}{\kappa_f} \tag{36}$$

where κ_f is a thresholding parameter > 0 and describes the ratio between the forward and backward-reflected beam. Typically, $\kappa_f = 0.1$ such that the time-shifted superimposed scan is at least -10dB less than the transmitted scan. For example, a system with reflectivity $\left|\hat{\Gamma}\right|$ of 0.9 requires a minimum FBR of 9.1 dB to guarantee that the backward-reflected wave is less than -10 dB compared to the forward wave. Note that systems without an enclosure ($\hat{\Gamma} = 0$) can have any FBR with respect to imaging.

vii. Application of Specifications

Design Table

To use the proposed specifications, we have compiled a table. Table 9 is split into two sections: the goal specifications and the verification specifications. The antenna engineer should calculate the goal specifications before embarking on a design. Upon the first design revision, the antenna engineer should calculate the verification specifications. If the verification specifications are significantly violated, then the antenna engineer should enter a new design revision. Then, once

all goal and verification design specifications are met, the antenna engineer can then enter the prototype phase. In the prototype phase, it is still recommended to measure the post-design verification specifications because all three values may change in a real environment. However, by meeting all specifications, the designed antenna is much more likely to take excellent subsurface images compared to an antenna which violates one or many of these specifications.

Finally, we note that design of a GPR antenna is a multi-faceted problem, and it may be difficult or impossible to meet every specification in Table 9 for a given system. For that reason, we have included a "severity" column which denotes the qualitative importance of meeting each specification.

Discussion of Specification Interactions

This section contains a brief discussion on the interactions and trade-offs between gain, coupling, and other specifications. First, we examine the interaction between gain/beamwidth, coupling slope and magnitude, and front-to-back ratio. All three of these are fundamentally specifications on the spatial radiation profile of the antennas. An antenna with a wide beamwidth will likely have a low front-to-back ratio and high coupling slope and magnitude due to sideways-directed radiation. Conversely, high-gain antennas may have significant coupling if the gain is achieved with a large antenna size. Therefore, adjusting the antenna's gain to perfectly fit the imaging profile determined by simulation of (29) may cause the antenna's coupling and front-to-back specifications to fail. As all three are inter-related, this design difficulty extends to changing any single specification.

Another important specification relationship is that between boresight radar cross-section and antenna gain for non-endfire-radiating antennas. For this class of antennas, an increase in

antenna gain may lead to an increase in antenna size, which could impact the radar cross-section of the antenna and cause problems if it violates the specification (34).

viii. Conclusion

In conclusion, we have considered the context of GPR antenna deployment in a whole system to create a set of useful specifications. We have explored specifications on the antenna coupling signal, the transmitted pulse integrity, the transmitted pulse ringing, the beamwidth, the antenna's boresight RCS, and the antenna's front-to-back ratio. An example code to calculate specifications is available [15]. By calculating and considering these system-based specifications early in the design process, the antenna engineer can improve the antenna's chances of success in deployment.

ix. Appendix A

This appendix contains the concept behind the derivation of equations (22), (29), and (34). Consider the situation of Fig. 45 with $n = 1$, where an antenna radiates at an oblique angle with respect to the ground. We aim to calculate an expression for the received power P_r from a transmitted power P_t after refraction through ground and reflection from target. This derivation ignores near-field effects and has reduced accuracy at λ-small operating heights and depths.

Without the influence of ground, a transmit power P_t will induce (ignoring polarization losses), a receive power P_r of approximately (37):

$$P_r = P_t \sigma(\theta) G^2(\theta) \frac{\lambda^2}{(4\pi)^3 (d_0{}' + d_1{}')^4} \tag{37}$$

(37) is the radar range equation [83] for a σ-strength target at a radial distance of $d_0' + d_1{}'$ at an angle of θ. We consider that the transmit and receive antennas are identical and collocated with a gain at elevation angle $G(\theta)$. The inclusion of ground separates the in-ground and in-air angles,

adds dielectric loss, and creates a transmission coefficient at the dielectric interface. With the influence of a single dielectric ground, (37) becomes (38):

$$P_r = P_t \frac{\sigma(\theta_1) G^2(\theta_0) T^2(\theta_0)\, \lambda_c^2}{(4\pi)^3 \left(\frac{d_0}{\cos\theta_0} + \frac{d_1}{\cos\theta_1}\right)^4} e^{-\alpha \frac{4d_1}{\cos\theta_1}} \tag{38}$$

In (38), the exponential term contains the soil loss of the sole dielectric layer and $T(\theta)$ contains the power transmissivity through the dielectric interface. In the transition from (37) to (38), $d_i' = d_i \sec\theta_i$. θ_0 and θ_1 refer to the transmission angles in air and ground respectively for a single-layer case. With the addition of $n \geq 1$ horizontal dielectric layers beneath the antennas, (38) becomes (39):

$$P_r = P_t \frac{\sigma(\theta_n) G^2(\theta_0) \lambda_c^2 T^2(\theta_0)}{(4\pi)^3 \left(\sum_{i=0}^{n} \frac{d_i}{\cos\theta_i}\right)^4} A^2(\theta_0) \tag{39}$$

where now we have generalized the transmission $T(\theta_i)$ and attenuation $A(\theta_i)$ coefficients for n-layers. Substituting the values for $T(\theta_i)$ and $A(\theta_i)$ from (1) and (2) respectively, we arrive at a version of the radar range equation in (40) useful for GPR systems based on migration.

$$P_r = P_t \frac{\sigma(\theta_n) G^2(\theta_0) \lambda_c^2 \prod_{i=0}^{n-1} T_i^2(\theta_i)}{(4\pi)^3 \left(\sum_{i=0}^{n} \frac{d_i}{\cos\theta_i}\right)^4} e^{-\sum_{i=0}^{n} \frac{4\alpha_i d_i}{\cos\theta_i}} \tag{40}$$

In (40), the exponential term sums up the relative losses in each dielectric layer, the spherical spreading term adds the distance from each layer, and the power transmissivity term takes into account each layer's transmissivity. (40) reduces to (38) in the case of a single dielectric layer. The construct θ_i refers to the angle travelled in the i-th dielectric layer with respect to the normal. d_i refers to the either the depth of the ith dielectric layer or the target's depth in the last layer if $i = n$.

The angles θ_i can be solved for using an iterative approach as in [66]. Examining the Fresnel coefficients results in the simplified form of power transmissivity from layer i to layer $i+1$ in (41):

$$T_i(\theta_a) = \frac{4\sqrt{\epsilon_i \epsilon_{i+1}}\cos(\theta_i)\sqrt{1-\frac{\epsilon_i}{\epsilon_{i+1}}\sin^2\theta_i}}{\left[\sqrt{\epsilon_i}\cos(\theta_i)+\sqrt{\epsilon_{i+1}}\sqrt{1-\frac{\epsilon_i}{\epsilon_{i+1}}\sin^2\theta_i}\right]^2} \tag{41}$$

In (41), we assume the incident field is transverse electric (TE). Now, we derive (22) and (23). In (22), we are concerned with the received target-reflected RMS voltage V_{rms}^{rx} in a boresight sensing test, so we take the square root of (39) with $\theta_i = 0 \; \forall \; i$:

$$V_{rms}^{rx} = \frac{V_{pp,t}}{2\sqrt{2}} \frac{\sqrt{\sigma(0)}G(0)\lambda_c}{(4\pi)^{3/2}\left(\sum_{i=0}^{n} d_i\right)^2} T(0)A(0) \tag{42}$$

In the single-layer case, (42) is simplified in (43) using (40) and (41) with ϵ_0=1:

$$V_{rms}^{rx} = V_{pp,t}\left[\frac{G\lambda\sqrt{\sigma}}{(4\pi)^{\frac{3}{2}}(d_0+d_1)^2}\right]\left[\frac{\sqrt{2\epsilon_1}}{(\sqrt{\epsilon_1}+1)^2}\right]e^{-2\alpha d_1} \tag{43}$$

(A.7) is the main form of (23) and (42) is the main form of (22), excluding constraining parameters explained in Section II. Equations (29) and (34) are derived in a similar method. In particular, (29) uses the simulation of (39) for varying θ_0 to optimize the antenna's beamwidth by calculating the square root of (39), and (34) uses (42) directly.

3. DC-12 GHz, 100 GS/s Equivalent-Sampling Receiver

This section contains the design of an equivalent sampling radar receiver based on a Zynq-7000 FPGA. A programmable receiver is necessary to run the radar because it gives us ultimate control over the timing and overall operation of the system. For example, on top of its main receiving job, the receiver will control input pulse triggering, switch networks, scan start/stop, and associate scan metadata with the data itself. In this section, we first provide a block diagram for the receiver, then describe its main components and operation, describe how the FPGA was programmed to offload data, and talk about real-time radar visualization.

A. Overview/Block Diagram

The block diagram of the equivalent sampling receiver is shown below in Fig. 50, with subsystems highlighted. The receiver operates at an equivalent sampling rate of 100 GS/s with an input bandwidth of 12 GHz. This upper limit is a soft limit as it is determined by the RF balun's loss, which may permit higher-frequency signals to propagate into the system. Operationally, the bandwidth limit can be up to 18 GHz by bypassing or sourcing a better balun.

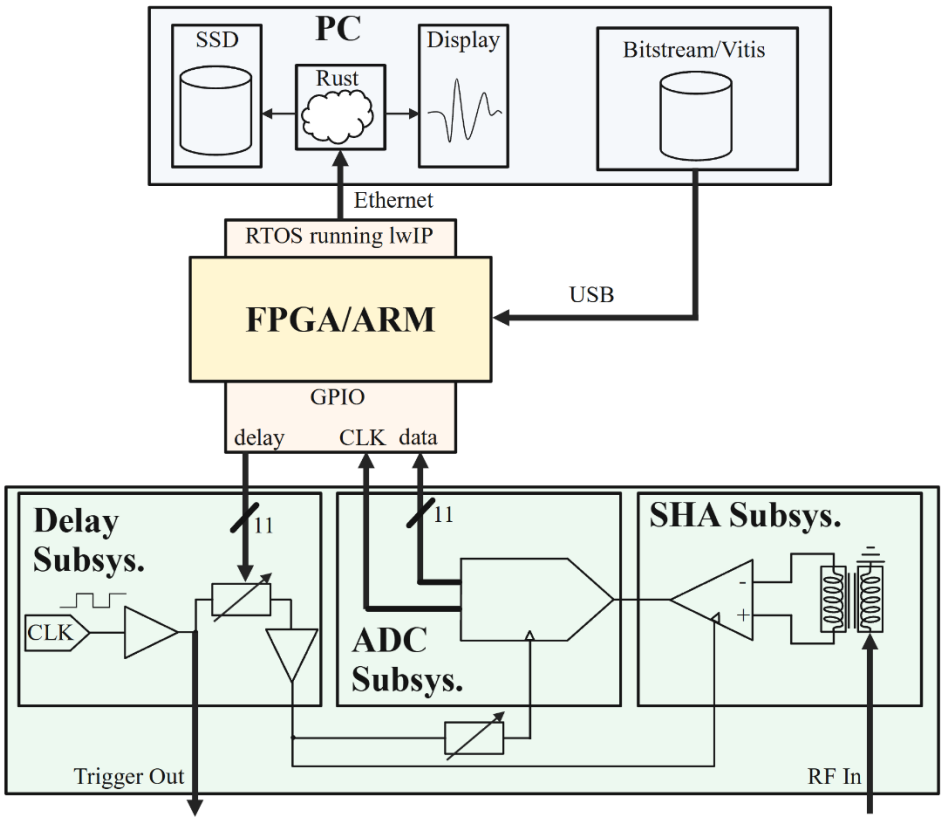

Fig. 50: Simplified equivalent-sampling receiver block diagram showing hardware, FPGA, and software.

The total receiver consists of three hardware subsystems, an FPGA, and a PC. The three hardware subsystems are indicated in Fig. 50 as Delay, ADC (Analog-Digital Converter), and SHA (Sample-Hold Amplifier) Subsystems. The Programmable Delay Board will take a clock input, copy it, and delay the copy relative to the original. The original clock is then output to trigger the transmitter to synchronize the TX and RX. The SHA subsystem uses the delayed clock to hold an incoming RF waveform in order for the slower ADC subsystem to sample it. The SHA has a typically much higher bandwidth than the ADC, allowing for the equivalent sampling of much higher frequency RF signals than the sampling rate of the ADC. The ADC will send data to the programmable logic (PL) of the FPGA, which queues the data and sends it to the programmable system (PS) ARM core. The ARM core is running runtime operating system (RTOS) with the open-source

lightweight IP (lwIP) [84] stack configured for TCP/IP operation. The PS sends the queued data over ethernet to the PC, which receives it using a TCP socket programmed in the Rust programming language. The program on the PC dequeues the data, performs basic pre-processing on the data, and provides a real-time waveform feedback to the radar operator. The full scan is saved to the internal SSD for later processing. In the next several sections, we explain all of these concepts in depth.

B. Equivalent Sampling & Hardware

First, we cover the principle of equivalent sampling and describe the hardware in the green-shaded part of Fig. 50. Equivalent sampling is a powerful technique used to extend the effective bandwidth of a digitizing receiver. The described receiver works on this principle. The operating principle is diagrammed in Fig. 51 below.

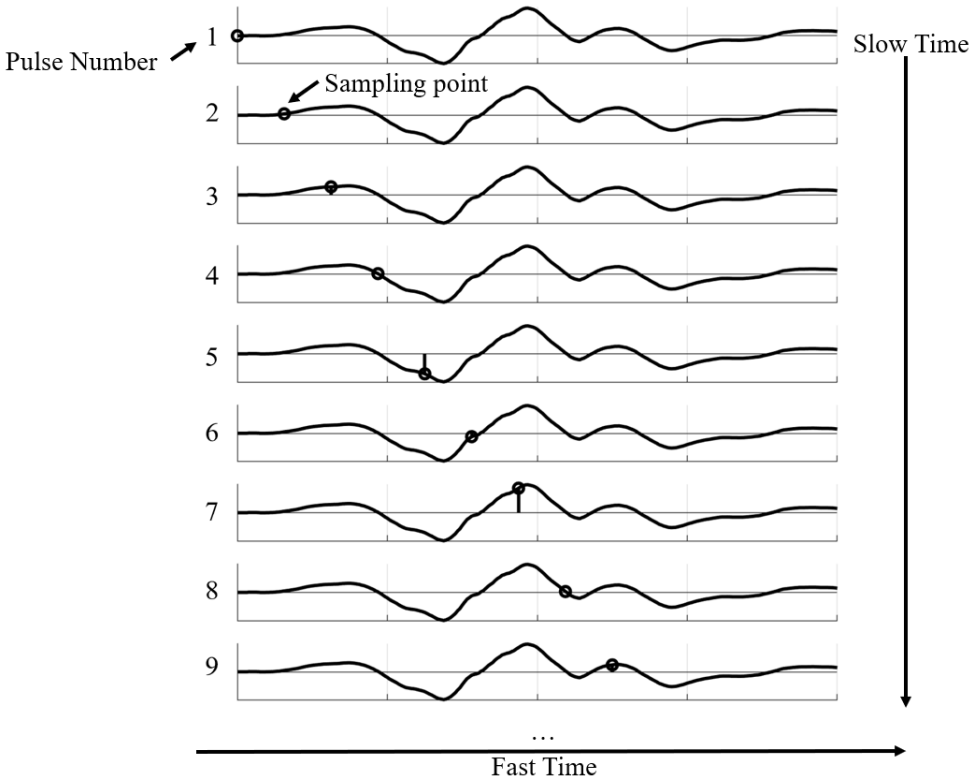

Fig. 51. Concept of equivalent-time sampling. In fast time, a single waveform occurs. Over slow time/pulse number, multiple waveforms occurs. One sample is taken per waveform, and re-combined after many transmissions to form a single waveform.

In Fig. 51 and this section, we use the term "slow time" to mean the time axis across different transmitted pulses and the term "fast time" to refer to the time axis within a single transmitted pulse. In a normal sampling application, an entire waveform would be digitized over fast-time – each slow-time point would create a new waveform. In our equivalent sampling application, however, the receiver digitizes only a single point per waveform. The simplest method would be to increment the sampling time (in fast time) for each slow time tick, as in Fig. 51 where the sampling point travels along the waveform versus slow time. Then, for example, if the waveform was to be digitized into N samples, the transmitter would have to transmit N waveforms in order for the receiver to complete one waveform. Naturally, we assume that the reflected signal does not change during a single waveform operation.

Though equivalent sampling operates more slowly than real-time sampling, it has several key advantages. First, the highest-speed current ADCs, typically pipeline ADCs such as the AD9213 are expensive, require complex output interfaces such as JESD204A/B, and still cannot attain the sampling rate required for alias-free direct RF sampling. For example, the AD9213 boasts a maximum direct sampling rate of 10.25 GS/s, for a Nyquist frequency of 5.1 GHz. But in radar operations, we prefer typically a 2.5x oversampling rate to increase SNR [85-87] and stability versus jitter. Therefore, the ideal usability of the 10.25 GS/s rate for high-accuracy radar would be approximately 2 GHz – which does not meet out bandwidth desires. Additionally, the high speed of direct RF sampling has dramatic considerations for the down-stream system. If we drive the AD9162, which has a 12-bit digital word output, at 10 GS/s, the data coming into the FPGA would be 120 Gb/s. Saving this data directly to a PC would be nearly impossible – running the radar for a minute would generate nearly 1 TB of data. Comparatively, an equivalent-sampling system operating at 10 MHz would generate nearly 1 GB of data in the same time – much more manageable from a pre-processing perspective.

Lastly, the key advantage of equivalent-time sampling is that a slower ADC can be used to perform the actual digitization – the only high bandwidth requirement is on the initial sample-holder amplifier (SHA). Therefore, an RF SHA which feeds an ADC can achieve equivalent sampling rates in the high GS/s and input bandwidths in the low tens of GHz.

To describe the SHA-ADC handoff, we perform an experiment to understand the output of the RF SHA. Fig. 52 below shows the input signal, sampled/held output signal, and input clock signal from an RF SHA.

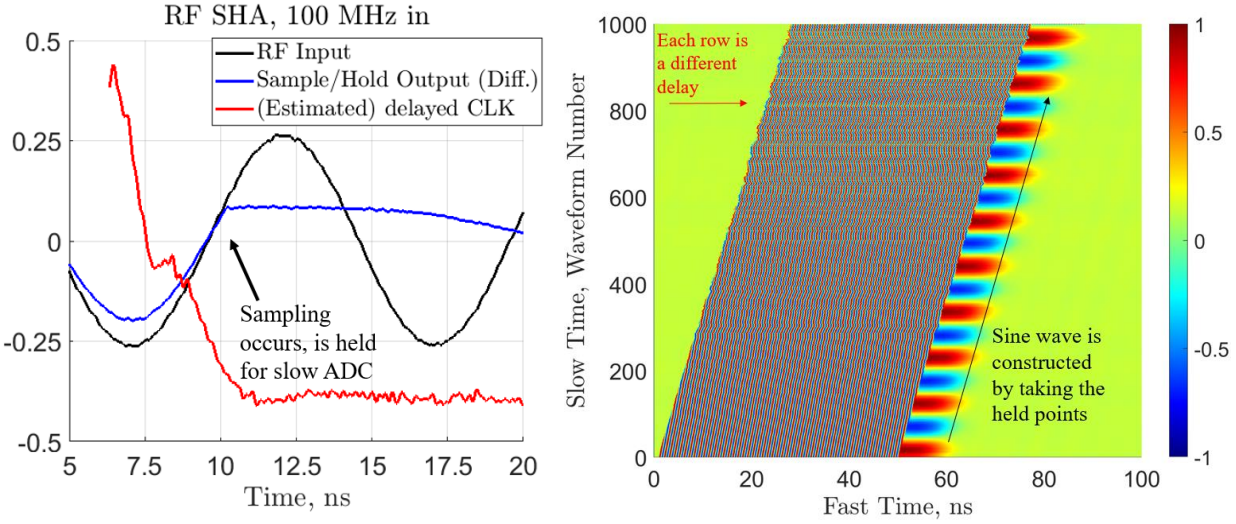

Fig. 52: (left/a) Measured waveform showing the concept of sampling/holding. Black waveform is the RF input. Blue waveform is the measured output from an SHA. Red waveform is estimated clock signal with sample/hold occurring at the negative edge crossing zero, with an unknown delay. (right/b) Showing the sampling of a 1 GHz sine wave. Each row (y-axis) is a different waveform along slow time as in Fig. 51.

In this test shown in Fig. 52a, we connected a 100 MHz sine wave output of an M8195 AWG to the input of an RF SHA (HMC661) fed by a DC-12 GHz balun. The negative output of the M8195 AWG is connected directly to an Agilent 86100A oscilloscope. A single end of the differential SHA output is connected to the Agilent 86100A oscilloscope, and we also measure the clock pulse that generates the sampling. The clock edge (shown in red) has a kink in it that was fixed in a future version – but the concept remains the same.

In Fig. 52a, the output (blue) tracks the input (black) with some loss. Once the clock edge crosses 0 on the falling slope, the input is held to a sample after some delay. The exact delay between clock edge and trigger sample is unknown due to delays in the board, but can be calibrated

out in the actual system. The blue waveform is acquired very quickly (less than 6 ps) and held at a near-constant value for approximately 5 ns. As the HMC661 SHA droops voltage approximately linearly proportional to time in this period (1.4%/ns from datasheet), it is good to select the ADC sampling point for less than 1 ns after the SHA sampling point by tuning the delay line in the bottom of Fig. 50 in the path of the ADC clock. In the final receiver, this delay is realized with a physical SMA cable with an electrical delay of an estimated 700 ps (short cable in Fig. 53).

Fig. 52b is the experimental extension of Fig. 52a with a sliding sampling point as in Fig. 51. Each point in slow-time (y-axis) is taken at a different point of a 1 GHz sine wave, with a delay generated by programming two chained SY89296U digital delay lines. The clock triggering the RF SHA is a 10 MHz square resulting in a period of 100 ns with a 50% duty cycle, so the 1 GHz signal is only visible for 50 ns. The fast ripple is the 1 GHz sine wave, and the slow fall-off for each slow-time sample is the ramping fall-off of the RF SHA after holding. The digitized sine wave is constructed by vectorizing each held point in slow time. In Fig. 52b, 1024 samples of the 1 GHz sine wave are taken at a 10ps/sample rate for an equivalent sampling rate of 100 GS/s.

To construct the receiver, we first prototyped each subsection in a separate PCB. Eventually, all subsections were integrated into a single board, as in Fig. 53 below.

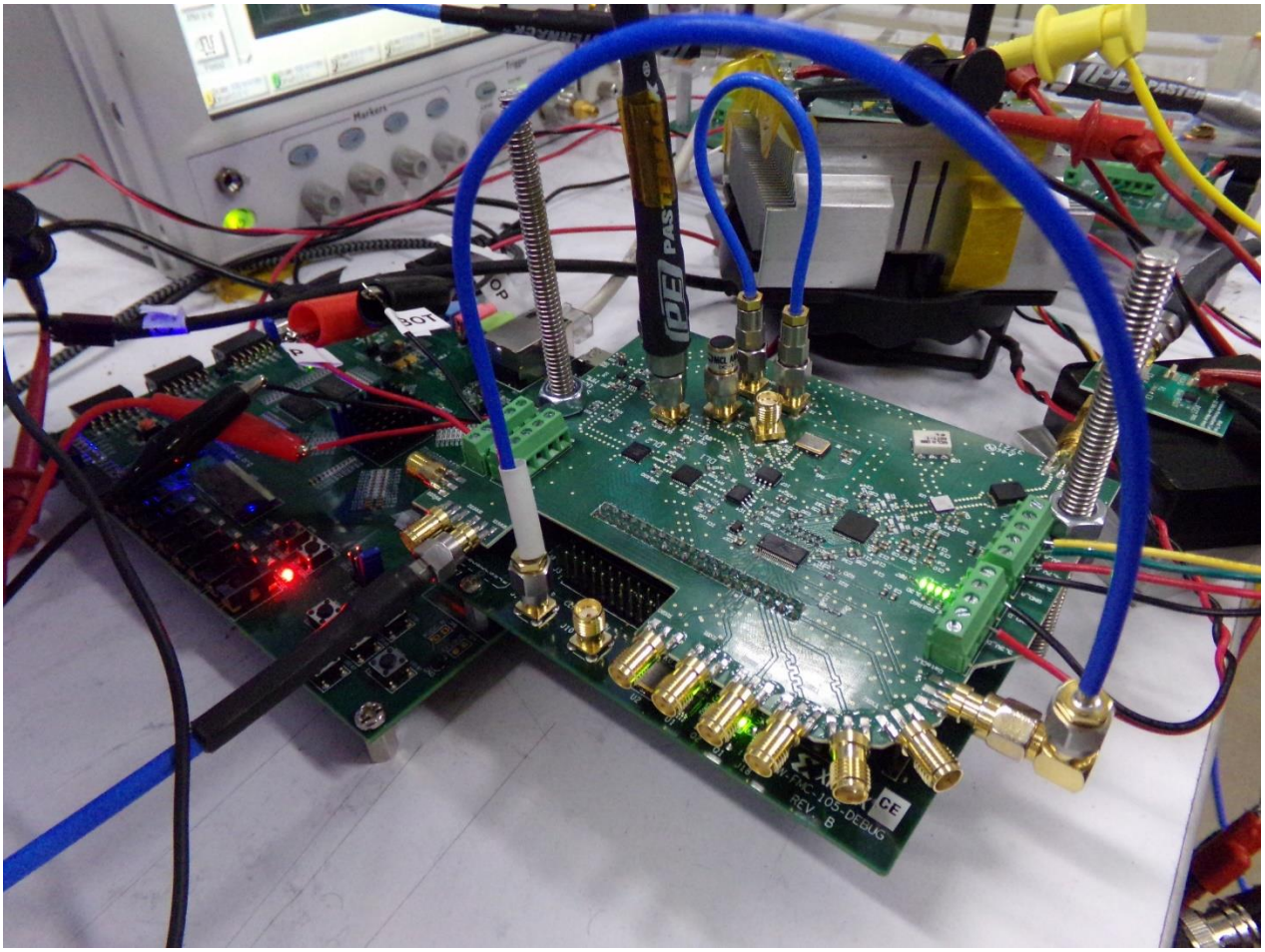

Fig. 53: Photograph of custom-build receiver showing the Zynq-7000 development board, FMC LPC expansion card, and PCB with hardware shown in Fig. 50.

The receiver is built onto a two-layer Rogers 4350 material with a 100-mil pitch header for direct plug-in for to the J1 connector bank of the XM105 LPC FMC. The XM105 plugs into the FMC adapter on a Zedboard [88] with a Zynq-7000 FPGA/ARM SoC. This adaptation method was found to provide acceptable but not ideal signal integrity as many lines on the J1 bank are not impedance controlled. The two delay lines used are Micrel SY89296U, the ADC is Texas Instruments ADC11C125, and the SHA is Analog Devices HMC661. The general specifications of the receiver are detailed in Table 10 below.

Table 10: RX specs

Specification	**Value**	**Specification**	**Value**
Equivalent Sampling Rate	100 GS/s	ADC Data Output Bits	11
Input bandwidth	12 GHz (Balun), 18 GHz (HMC661)	Output Data Rate	160 Mb/s (max)
Adjust delay range (sampling window)	approx. 18.4 ns (2048 tap)	Total BOM Cost	$1620
Power Draw	4.3W (PCB), ~5W (FPGA)	Extra GPIO	9
TX/RX Switch Interfaces	3 bits each – 8x8 array	Typical PRF	10 MHz
Total Waveform Acquisition Time	204.8 μs (typ)	Max Possible PRF	< 100 MHz

Extra GPIO pins allow the receiver to be interfaced with miscellaneous external devices such as motors, physical switches, and limit switches.

C. FPGA-Based Data Offloading

This section describes the programming to take the data from the ADC to the PC. The data is fed from the ADC into the Zynq-7000 FPGA in an 11-bit parallel-CMOS format (0-to-3.3V). The goal of the FPGA-based data offloading is to take the parallel-CMOS data from the ADC and package it up into TCP packets to be sent to the external PC for storage and postprocessing. The FPGA PL is programmed in VHDL using Xilinx Vivado 2020.1 and the FPGA PS is programmed in C using Xilinx Vitis 2020.1. The block diagram of the program is shown below in Fig. 54.

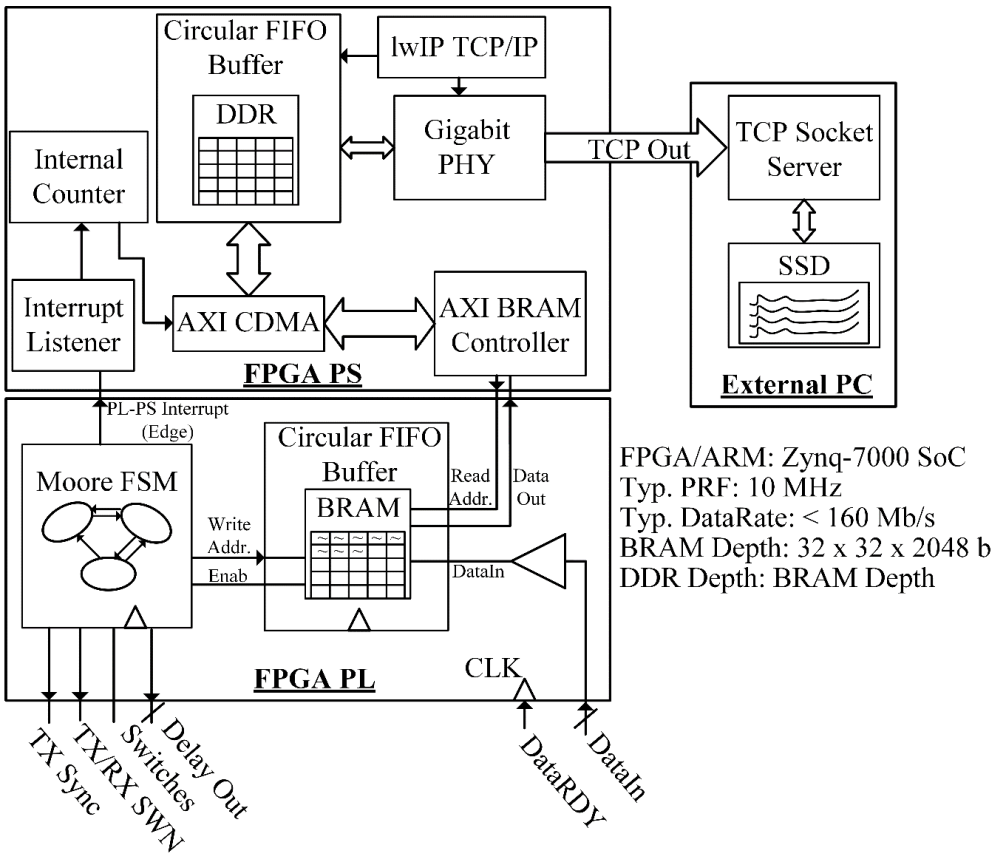

Fig. 54: Block diagram with more detail of FPGA program.

Once the receiver is started by pulling an asynchronous reset low, the parallel-CMOS data is registered in the FPGA PL. A finite state machine (FSM) has an internal counter of how many samples have been taken and writes the data to the correct address in the internal FPGA BRAM. Once the data is written, the FSM will update the delay word to the RX delay lines, and the next sample will come in. Each sample is packaged into a 32-bit word with another sample and some metadata, as in Fig. 55.

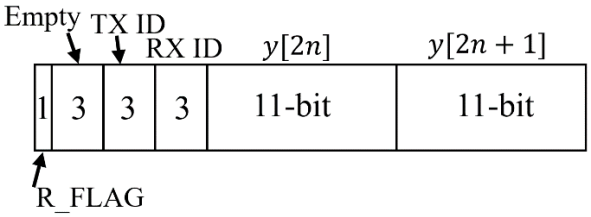

Fig. 55: Inner structure of each transmitted 32-bit word. Left is MSB, right is LSB.

The n-th 32-bit word will contain the $2n$-th and the $2n+1$-th sample store as in Fig. 55. If real-time averaging is enabled on the FPGA, then each sample will contain an averaged data point implemented by an accumulation buffer and a bit-shift divider. For 3-D and post-processing, the 32-bit word also contains the TX-RX pair that the waveform was taken with as well as an indicator flag as to whether or not the sample was taken on a sampling down-ramp or up-ramp.

Once all delays have been cycled through, a waveform is done and the PL sends an interrupt to the ARM core using a PL-PS interrupt. The PS has a synchronized internal counter and uses an AXI CDMA to transfer the waveform from the BRAM to DDR. Both BRAM and DDR are controlled as a circular FIFO (first-in first-out) buffer. The Zynq-7000 was only able to handle a BRAM depth of 32 waveforms (256 KB), so there is a possible data loss of 32 waveforms if the receiver runs too fast. The PS is running a modified version of lwIP echo server designed to send data from DDR to the external PC over ethernet using TCP/IP. Testing has shown that the Zedboard is able to reach at least 320 Mb/s over ethernet, possibly more.

For 2D scans, we do not use any switching methodology and can simply operate with a bistatic pair of antennas. For 3D scans, we operate the radar in full multistatic mode. In this mode, each TX will emit a pulse while each RX will listen for a pulse. We choose to cycle through all receivers for each transmitter, as in the top half of Fig. 56. For stability, every other waveform is taken by "down-ramping" the receiver delay lines. Down ramping refers to cycling the delay

backwards from 2047 to 0 (maximum to minimum) instead of “up-ramping” from 0 to 2047 (minimum to maximum) while sampling. Effectively, we record the waveform backwards. Down-ramping every other waveform ensures that there is no significant disturbance in the clock period in a sudden jump from delay = 2047 to delay = 0 as this can affect the FPGA’s timing and cause instability in the ADC. However, this scheme means that even TX-RX pairs are only taken as down-ramped samples. As down-ramping may have different sampling characteristics from up-ramping, even TX-RX pairs may have persistent inconsistencies. This potential bias is accounted for in the final switching configuration is as shown below in Fig. 56.

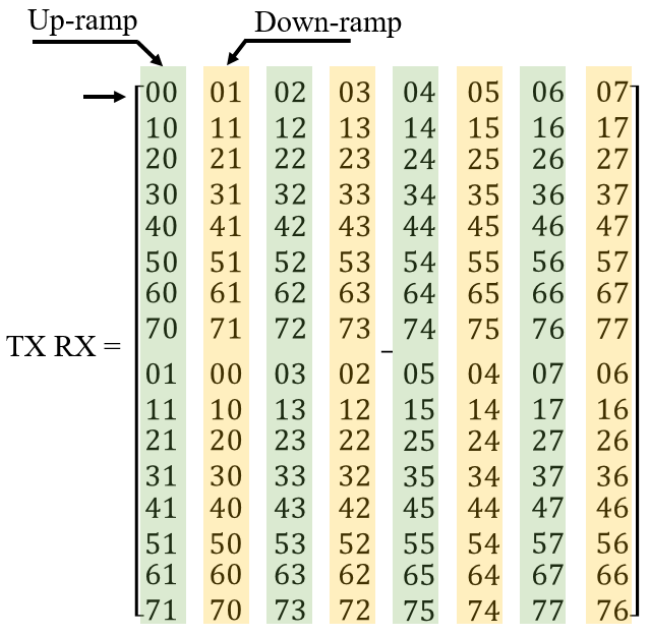

Fig. 56: Switching sequence for 3-D imaging. Traverse in row-major order (horizontal first).

After the scan is done, an external switch pulls an asynchronous reset high and the FPGA returns to its idle mode, with all internal counters intact in case another scan is initiated. The data, associated with its TX-RX pair, is de-interleaved in the next processing step on the external PC.

D. Real-time Visualization and Data Storage

In order to save the data stream to an external PC, we must create a program running on the external PC to handle, dequeue, and pre-process the data. For usability, we also use this program to display the real-time waveform output to the PC screen. The block diagram of the program is shown in Fig. 57 below.

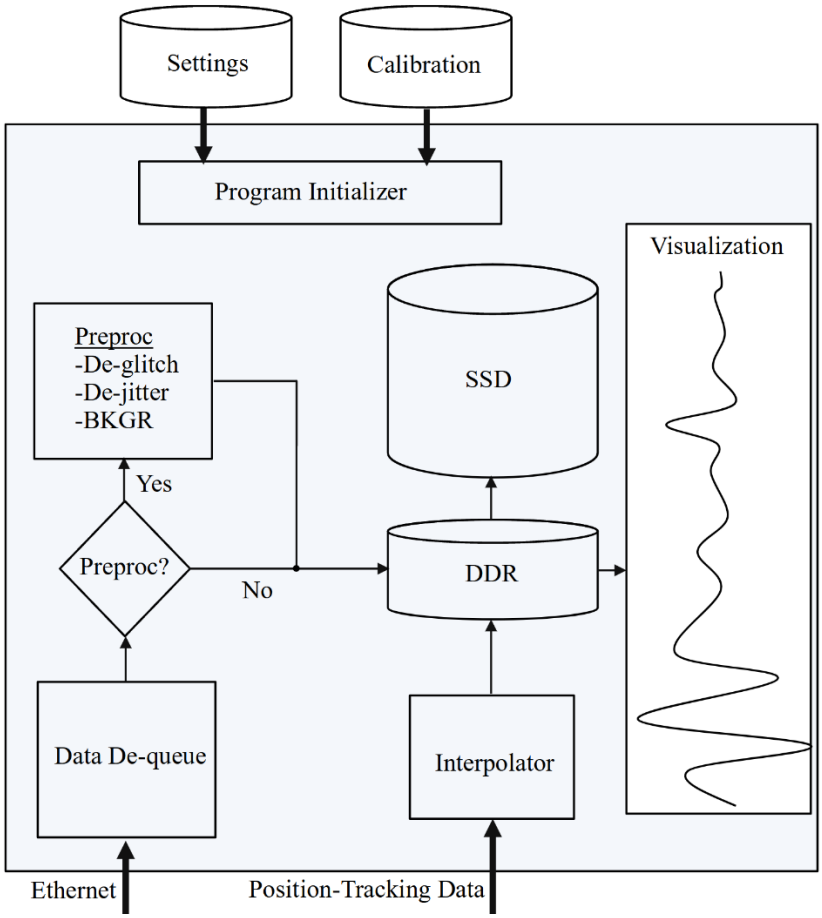

Fig. 57: Internal program structure of Rust-based real-time visualizer.

The program creates a TCP socket and listens on it for connections from the Zynq-7000. Once the link is established, it will parse all incoming 32-bit data words from the Zynq-7000 and form them into a 2-D array of waveforms. As TCP does not guarantee the number of bytes in an incoming packet, the program is made robust against the connection splitting both waveforms and words by

maintaining an overflow buffer to which unused bytes are written. Once a certain number of waveforms are written, a screen visualizer is updated with the latest taken waveform. The plot's refresh rate is limited to not slow down the main thread and drop any data from the receiver. An screencap of the real-time plot (during a scan playback) is shown in Fig. 58.

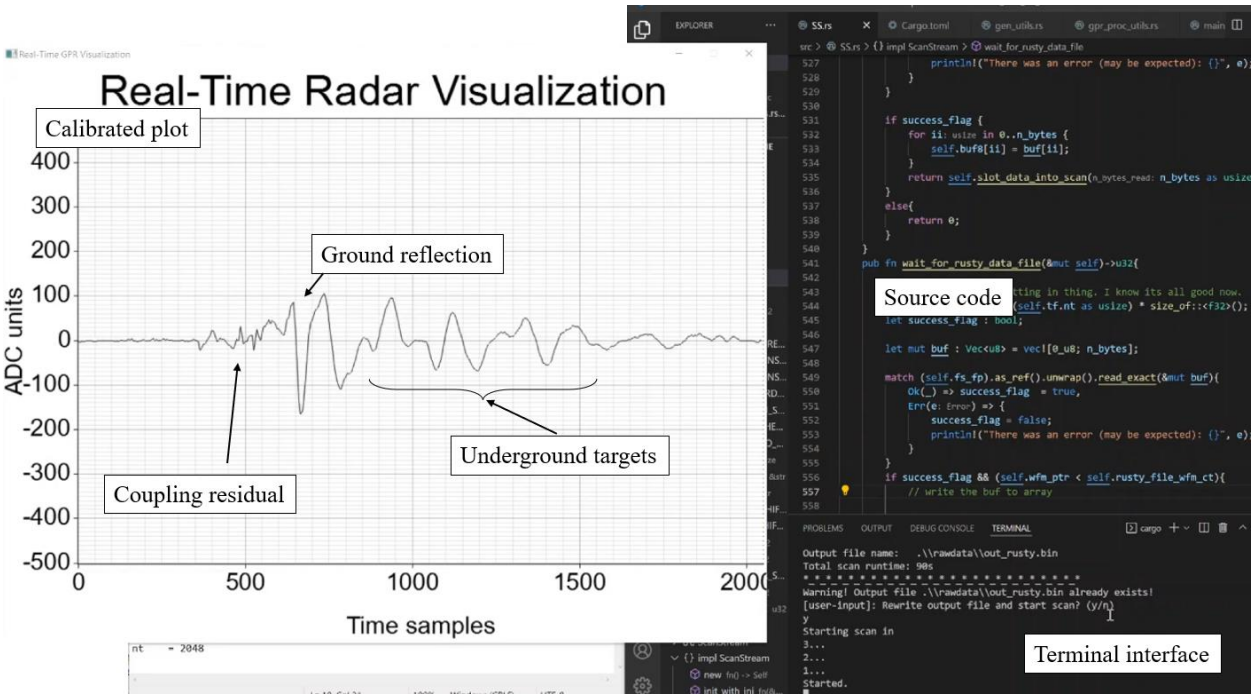

Fig. 58: Desktop screenshot of running the real-time radar visualization program. Waveform is read, processed, and stored in real time.

Additionally, the program takes a position-tracker as an input and interpolates its position to cover the timing of each waveform. Once the scan is over or DDR is nearing its capacity, data is written to the SSD. After the data is written, the program will exit and the data is ready to be processed.

4. GPR Scanning Systems (2D and 3D)

This section contains the system block diagrams and theories of operations of 2D and 3D GPR systems as well as pictures of the developed outside GPR cart.

A. 2D System Diagram

In a 2D application, the system uses one transmit and one receive channel. The two antennas operate in a bistatic constant-offset mode and are scanned along a linear direction across the scan area. The system block diagram of the 2D array is shown in Fig. 59.

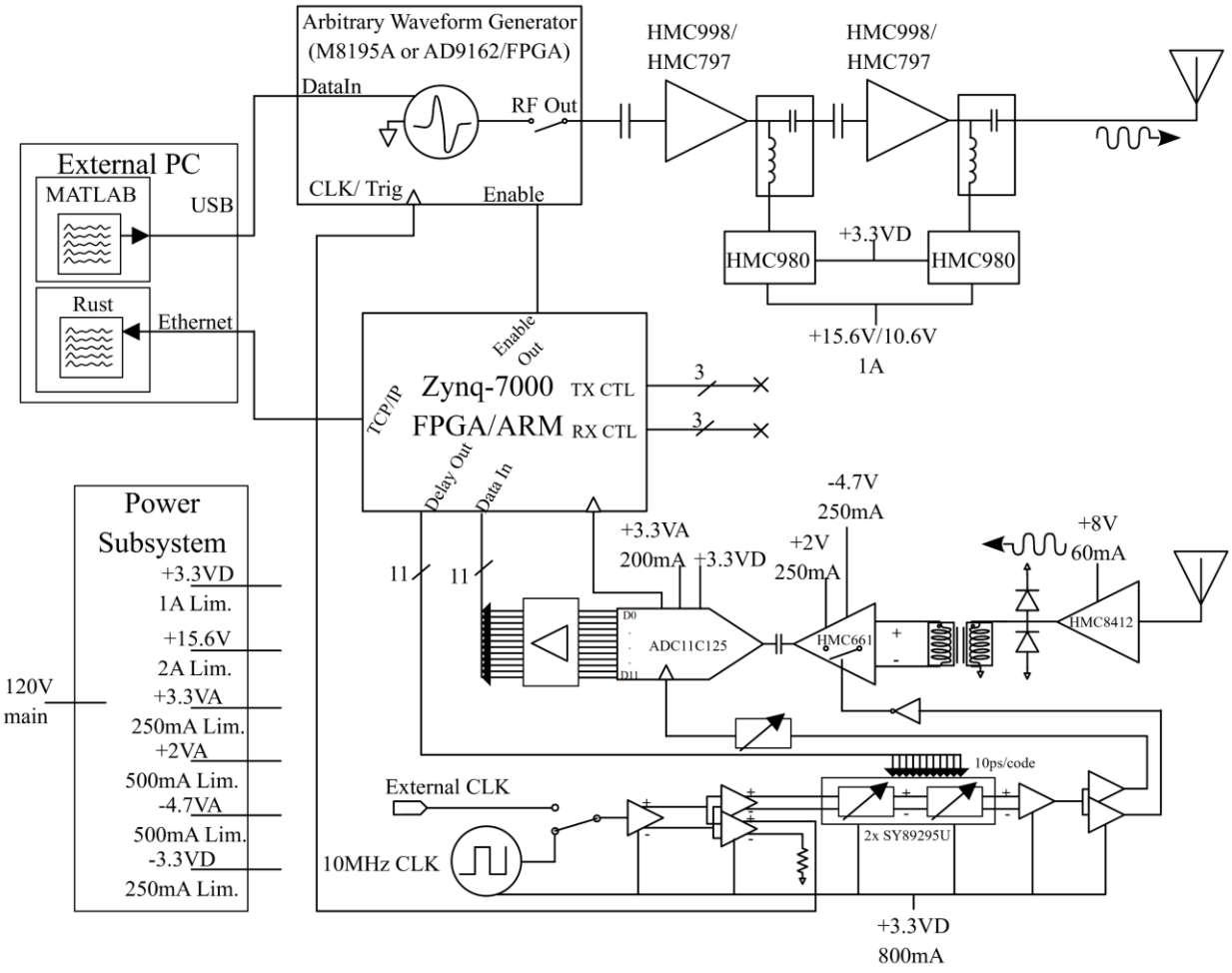

Fig. 59: System block diagram of the 2D GPR sensing system.

In Fig. 59, we introduce several components. On the transmitter, we use two chained HMC998 wideband GaAs distributed amplifiers to amplify the signal from the Keysight M8195 AWG to above 10 V_{p-p}. Occasionally, the HMC998 amplifiers are used interchangeably with an HMC797 GaAs PA, which has similar specifications but a lower output power. The amplifiers have time-stable currents controlled by an HMC980, which increases the quality and applicability of a radar calibration. The receiver is shown in greater detail than in Fig. 50, with all of the buffers, level translators, and miscellaneous circuitry shown. The receive path contains an HMC8412 LNA chained with an optional limiter designed to protect the HMC661 RF SHA. In the 2D case, TX and RX control bits from the FPGA are unconnected as there is no need to switch between antennas. Critically, this allows us to use the same exact system for both 2D and 3D scans.

B. 3D System Diagram

The 3D version of the GPR system is similar, but with a 1:8 switch network inserted on both TX and RX paths. Using a switch network allows us to create the system at a low cost – instead of using many transmitters or receivers, which would linearly scale the total cost with the sub-unit cost and number of antenna pairs, we can use one single transmitter and receiver. This reduction in complexity comes at the cost of radar frame rate. The system block diagram of the 3D GPR system is shown below in Figure 60.

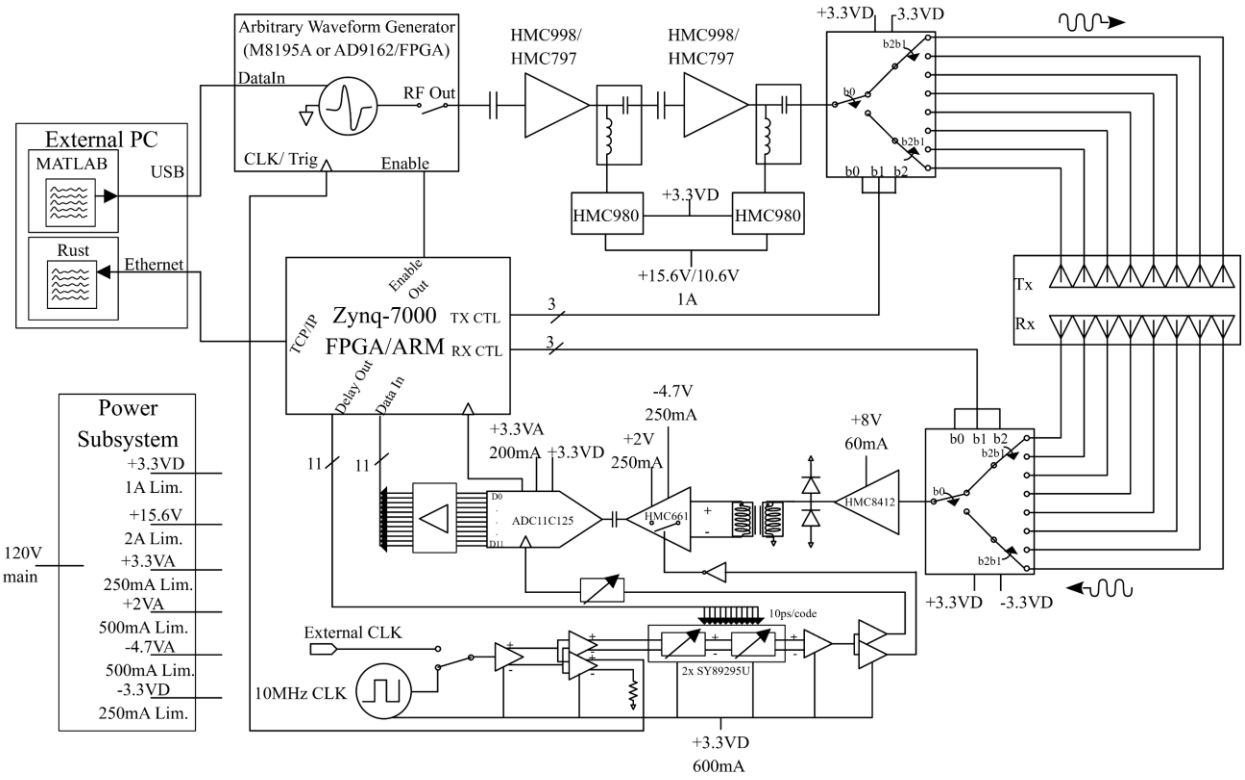

Fig. 60: System block diagram of the 3D GPR sensing system.

The 1:8 switches are constructed using a single 1:2 (ADRF5026) switch and two 1:4 (ADRF5044) switches. The TX and RX selection bits are controlled by internal state of the program running on the Zynq-7000 FPGA. This setup allows the receiver to correlate waveforms with what TX-RX pair they were taken with. Lastly, with this system diagram we can arrive at the ensemble fast-time axis shown below in Fig. 61.

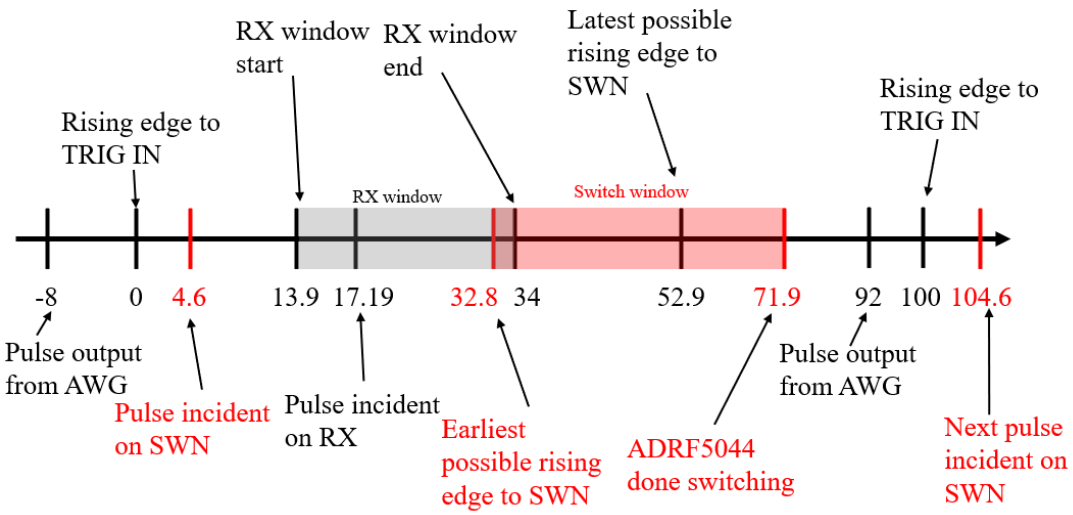

Fig. 61: Overall fast-time axis for GPR system with relevant windows and events indicated.

Here, we calculate the delays in the system based on PCB trace lengths, cable lengths, and digital delays in order to get a picture of the timing of a single waveform in the system. The system is running off a 10 MHz clock, so at 0 and 100 ns a rising edge is sent to the M8195 AWG to start a waveform playback. The M8195A AWG has a 628 ns delay from rising edge to waveform output, and the programmed waveform is intentionally delayed such that the pulse is output from the AWG at approximately 692 ns. In Fig. 61, this means that the AWG pulse is output at a time of -8 ns with respect to the clock input. At 4.6 ns, the pulse is incident on the switch network. This time is important to avoid “hot switching”, which can burn the switch network if a high-power RF pulse is incident on the pulse during the switching process. Based on IC and trace delays in the receiver, the receiver will start receiving at a time of 13.9 ns for a window of approximately 20 ns up to 32 ns. The radar-reflected pulse is incident on the receiver at 17.19 ns, so there is an effective receiving length of 16.8ns – we typically only look at 10 ns in applications. After a sample is taken in slow-time, it is possible that the receiver sends a switch command at either 13.9 ns or 34 ns, depending on whether the last waveform was taken with down- or up-ramp sampling. The delay

from command to switch operation is 18.9 ns, so the switch may start switching at 32.8 ns or 52.9 ns. Based on the ADRF5044's switch time of 19 ns, the last time that we may consider the switch operation to be active is 71.9 ns. At 92 ns, the next pulse is output and the situation occurs again.

Note that Fig. 61 is the ensemble of all possible fast-time axes and the exact numbers depend mostly on the electrical length of the cables. Indeed, TX-RX switching is only done after all slow-time points have been digitized and the waveform is complete. Fig. 61 implies that no hot-switching occurs in the system with a buffer of approximately +/- 30 ns, but we have found that potentially poor signal integrity on the switching lines makes this analysis questionable; future research is required to develop a fully-safe switch network for system implementation.

C. Sandbox System

We built the first iteration of the 2D system in an above-ground sandbox, pictured in Fig. 62.

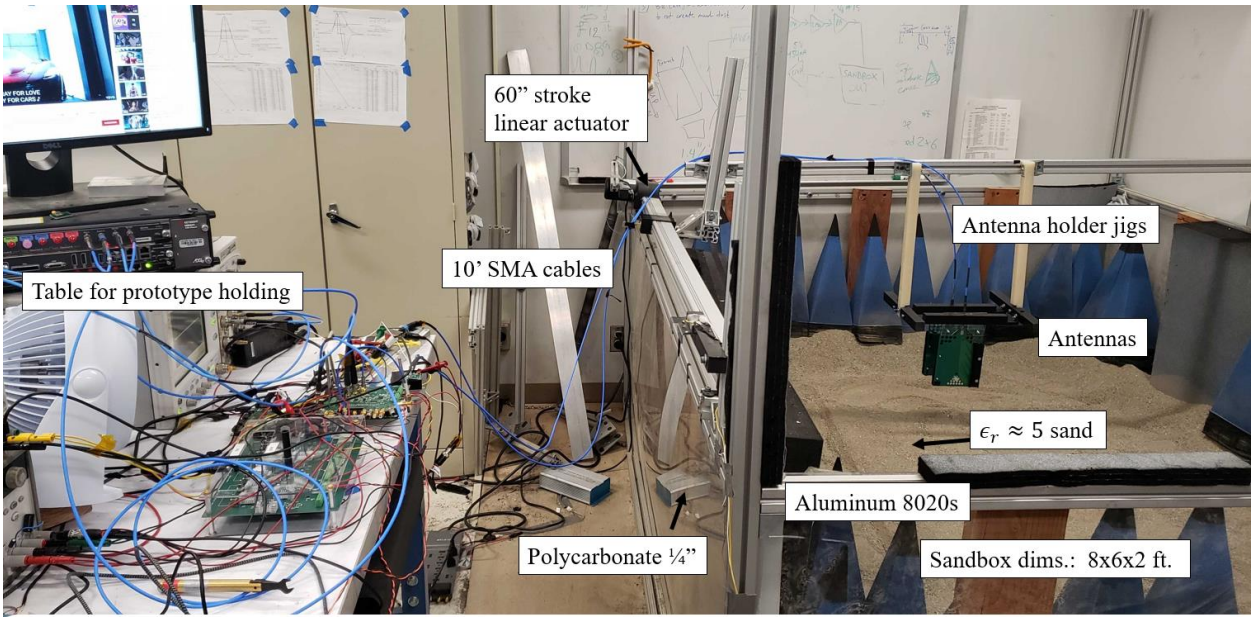

Fig. 62. Photograph of sandbox GPR system.

The sandbox is built using T-slot aluminum extrusion with dimensions of 6’ x 8’ (1.82 x 2.4 m) and a sand-depth of approximately 2’ (0.6 m). The coarse sand is purchased locally and has a measured relative permittivity (using the coaxial probe method [89]) in the range from 5 to 6 with a relatively low dielectric loss tangent for soils ($\tan\delta < 0.1$). The antennas are scanned along the sandbox length with a 60”-stroke linear actuator using a worm drive and threaded rod. The linear actuator is controlled by the Zynq-7000 FPGA with a custom motor relay. On each end of the sandbox, we have mounted limit switches fed into the FPGA receiver so the scan can progress autonomously.

In this system, we typically test for improvements in the system imaging quality by measuring SNR, clutter, and target-reflected waveform quality. Typical targets are pipe-like objects (1/4”-diameter rebar, wires, or spare aluminum extrusion) buried width-wise up to 20cm deep. An example of the radar circuitry is shown in Fig. 63, below.

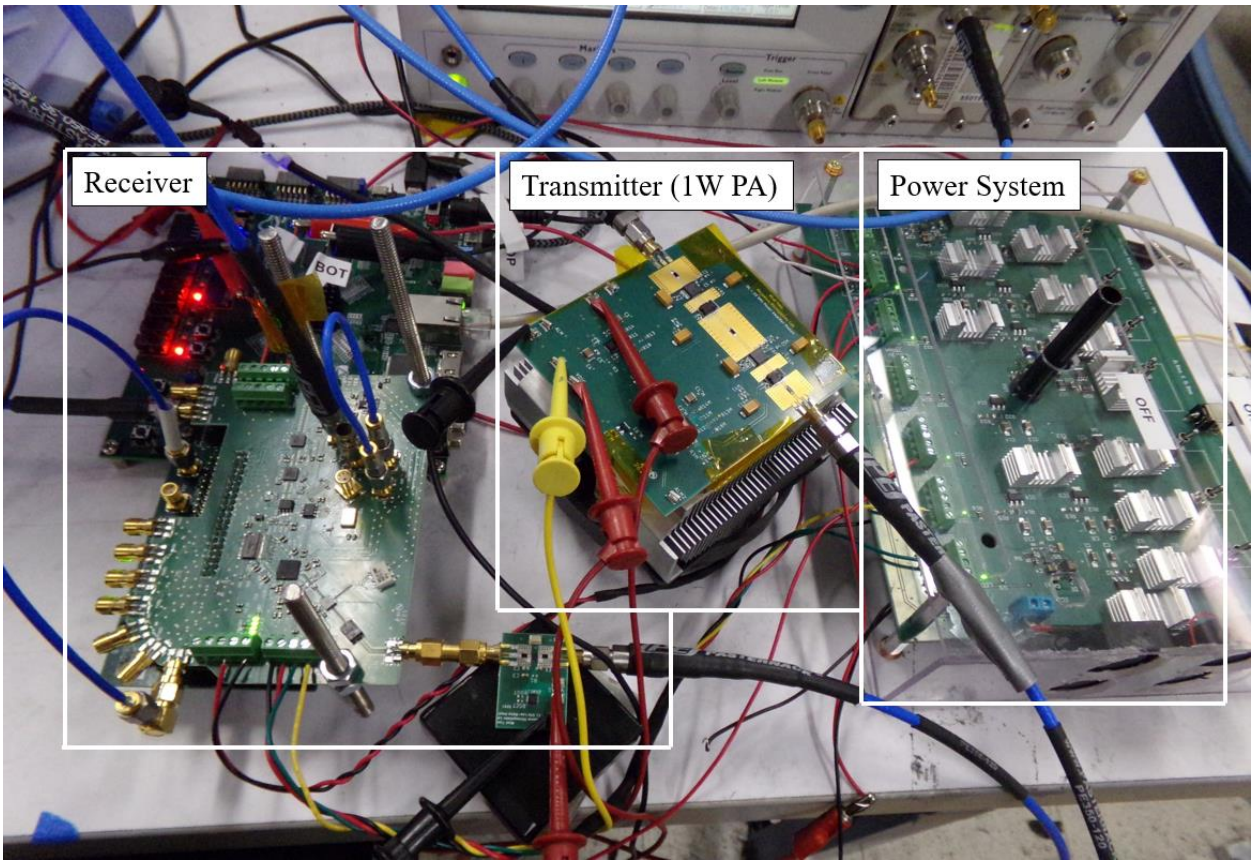

Fig. 63: Benchtop layout of radar circuitry. Left-to-right, receiver, transmitter, and power subsystems.

In the benchtop application, we line up the Receiver and Transmitter (using HMC797) with 10-foot (3m) flexible SMA cables going directly to the TX and RX antennas (2D). Here, the main challenges are:

- Maintaining the quality of the SMA cable connection, as scans taken in the sandbox are high-precision actions and an awkward bend in the SMA cable is visible in the resulting scan.
- Integration with other benchtop equipment – GPIB lanes and an extra Arduino are connected to the PC to provide extra information and controls to the scan.

Naturally, the logical conclusion of the benchtop system and Fig. 63 is to mount the system on an cart and take real-world scans with the best-performing system. Additionally, the sandbox is too small for a fully multistatic 3D scan. The next section details this effort.

D. Outside GPR Cart System

The final stage of a GPR application is scanning over unknown targets and environments to image, detect, and alarm. While we have developed the system based on the sandbox, to properly assess its capabilities for real-world applications, we must build a mechanical structure to hold the antenna array and radar circuitry. Figs. 64 through 66 show the build cart, circuitry holder, and 8x8 antenna array.

Fig. 64. Photograph of cart operating on dirt track (2D scan).

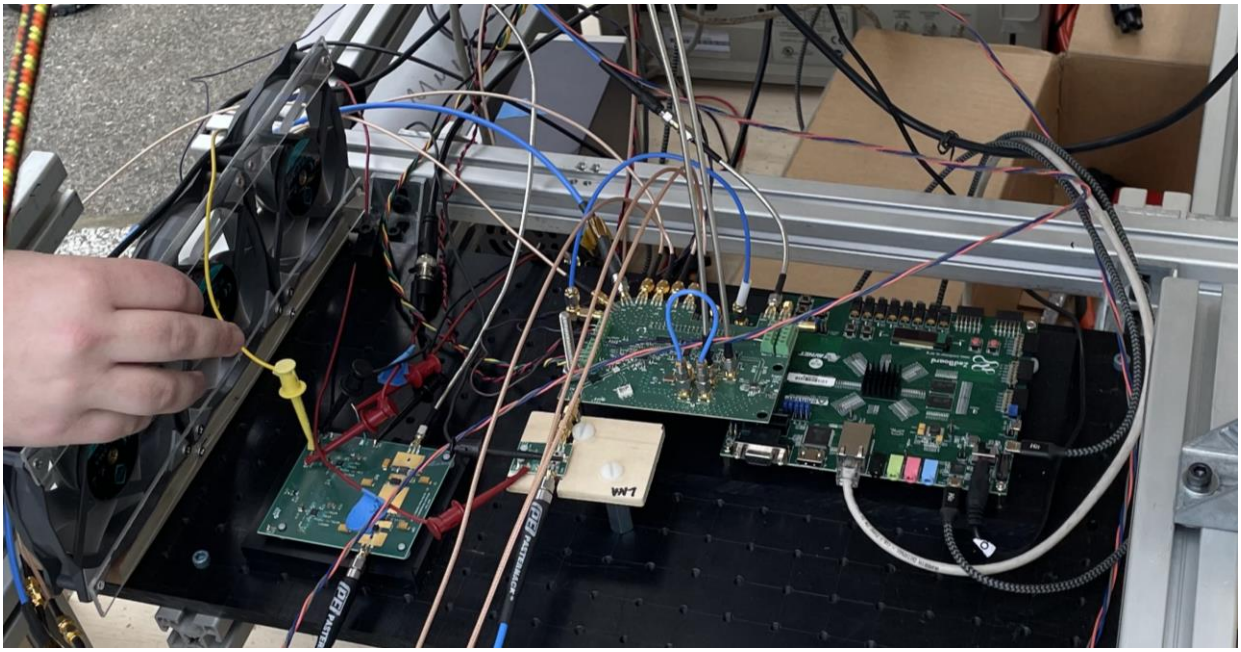

Fig. 65. Closeup zoom of cart circuitry. Bottom left: power amplifier. Center bottom: low-noise amplifier. Center top: FPGA-based receiver.

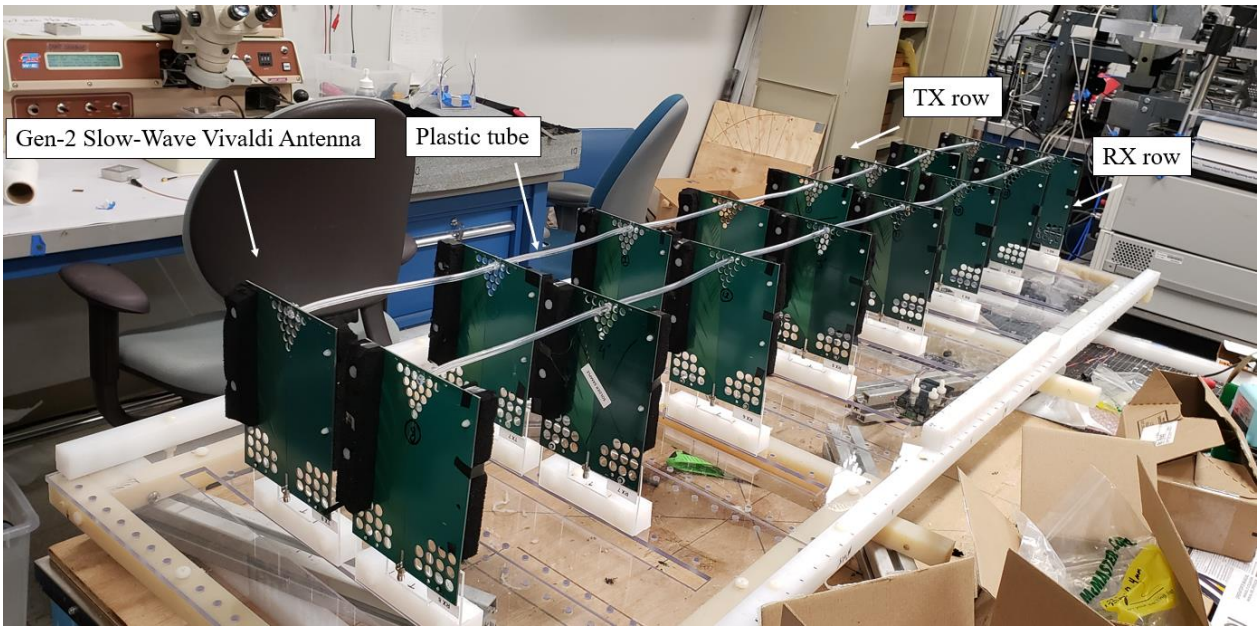

Fig. 66. 8x8 (Tx x Rx) antenna array of Vivaldi-type antennas

The cart, photographed in action in Fig. 64, is a custom two-deck wooden cart with extruded aluminum internal skeleton for mounting of the array. On the bottom level of the cart

visible near the pusher, a Jackery 1000 kWh power supply supplies 120VAC power to all circuits, PC, and power supplies. On a single charge, the system can run for three to four hours. A majority of the power is taken up by the M8195 AWG (mounted on top level) and HP power supply (for extra voltages – mounted on bottom level). Bungee cables and additional aluminum beams are used to stabilize the array during operation, but the array still does bounce during a scan, especially on non-flat ground.

The modular circuit holder is pictured in Fig. 65. The black holder is a custom 1" grid of 1/4"-20 holes so all circuits can be securely mounted onto the cart. On the left, three high-throughput CPU fans serve two purposes. First, the fans cool the PA and receiver. Second, as the holder is modular and designed to be open to the environment, the fans prevent foreign objects from settling on the circuits during operation. To the right of the fans is the 1-Watt PA (HMC797) which amplifies the pulse to above 10 $V_{p\text{-}p}$, depending on the M8195 AWG settings. At the right of the holder are the LNA and FPGA-based receiver, with ethernet, serial, and programming cables going through a hole in the upper deck to the PC. All power cables go to the top deck where a power control PCB is mounted.

Fig. 66 shows the assembled 8x8 (TX x RX) antenna array. The antennas are all slow-wave Vivaldi-type antennas which have impedance bandwidths from 350 MHz to above 50 GHz. The antennas transmit and receive differential (1^{st} derivative of Gaussian) pulses excellently (pulse integrity > 0.9) up to 3 GHz of instantaneous baseband bandwidth and acceptably (pulse integrity > 0.75) up to 14 GHz of instantaneous bandwidth. Each antenna is held in place by a thin sheet of acrylic with standardized mounting holes. The acrylic is attached to a UHMWPE plastic bar, which is then attached to a polycarbonate sheet with holes for mounting and a slot for SMA cable input.

This configuration allows for varying the distances between antennas and quick swapping of antennas. The polycarbonate sheets are attached with nylon screws to a combination of UHMWPE and nylon 1” bars. Care is taken to reduce the use of metallic reflectors in direct line-of-sight with the antennas. The inner two nylon bars in Fig. 66 have periodic series of screw assemblies which slide into the T-slot aluminum bars. Finally, each row is tied together using a plastic tube to reduce the total vibration of the array.

To operate the cart, we first must take a calibration scan which measures the coupling between the antennas. To perform this, the cart is positioned in the “Skyshot” configuration as in Fig. 67 below.

Fig. 67. Cart “skyshot” configuration – used to take calibration and coupling waveforms between each antenna pair.

After the calibration has been measured, the array can be put down and scanned. For 2D scans, the Rust receiver program will automatically perform the background subtraction. For 3D scans, the calibration must be applied in the processing pipeline in MATLAB. The next section describes a processing pipeline for 2D and 3D scans.

5. GPR Processing Pipeline

This section describes common techniques used in the processing of GPR data that we have developed or modified. As the proposed systems have three forms (2D sandbox, 2D cart, 3D cart), special consideration will be taken when a specific processing step is altered for a system. When applicable or feasible, MATLAB code will be written in-line. This section, though not technically complex, is intended to be a useful reference of the methods used in this dissertation.

A. Preprocessing

First, let us consider the following 2D sandbox environment, shown in Fig. 68 and Fig. 69. Three targets (1/4”-diameter steel rebar) are buried in varying depths.

Fig. 68: Sandbox with half-buried rebar targets. Targets are fully buried later to depths of Fig. 69.

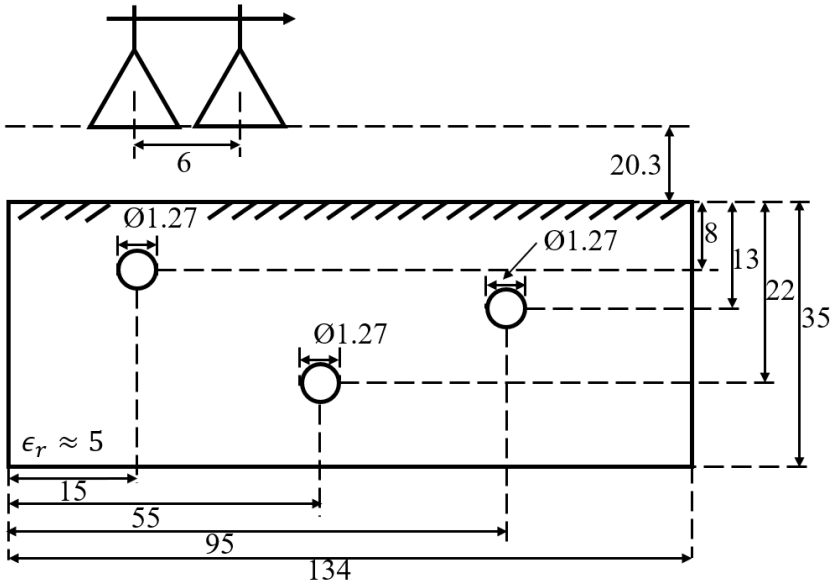

Fig. 69: Dimensions of buried rebar targets in sandbox.

Two antennas are scanned over the sandbox and collect the reflected pulses. A single transmit-reflected pulse is called an A-scan. A collection of A-scans (stacked in the column dimension) is called a B-scan. For 2D GPR processing, the B-scan is the fundamental unit on which to process. A collection of B-scans taken in the same spatial location can be called a C-scan, the fundamental unit for 3D GPR processing. An example of an A-scan and B-scan are shown below in Fig. 70 and Fig. 71.

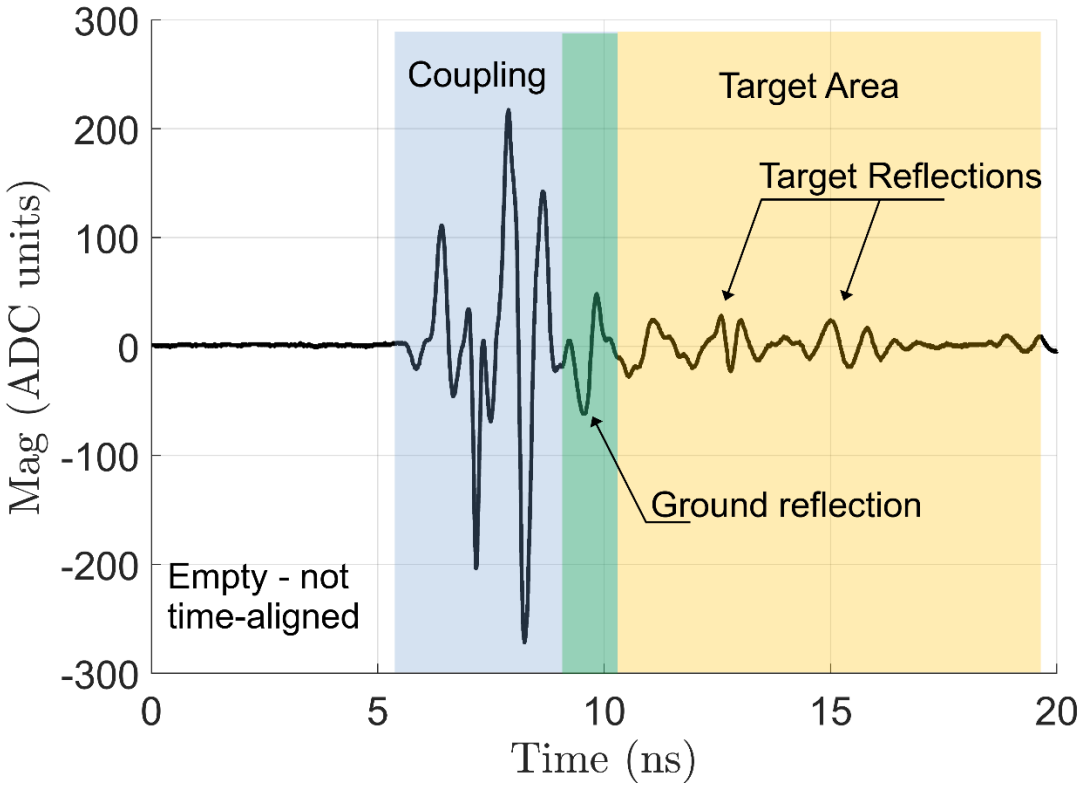

Fig. 70: Example GPR A-scan with coupling, ground reflection, and targets highlighted.

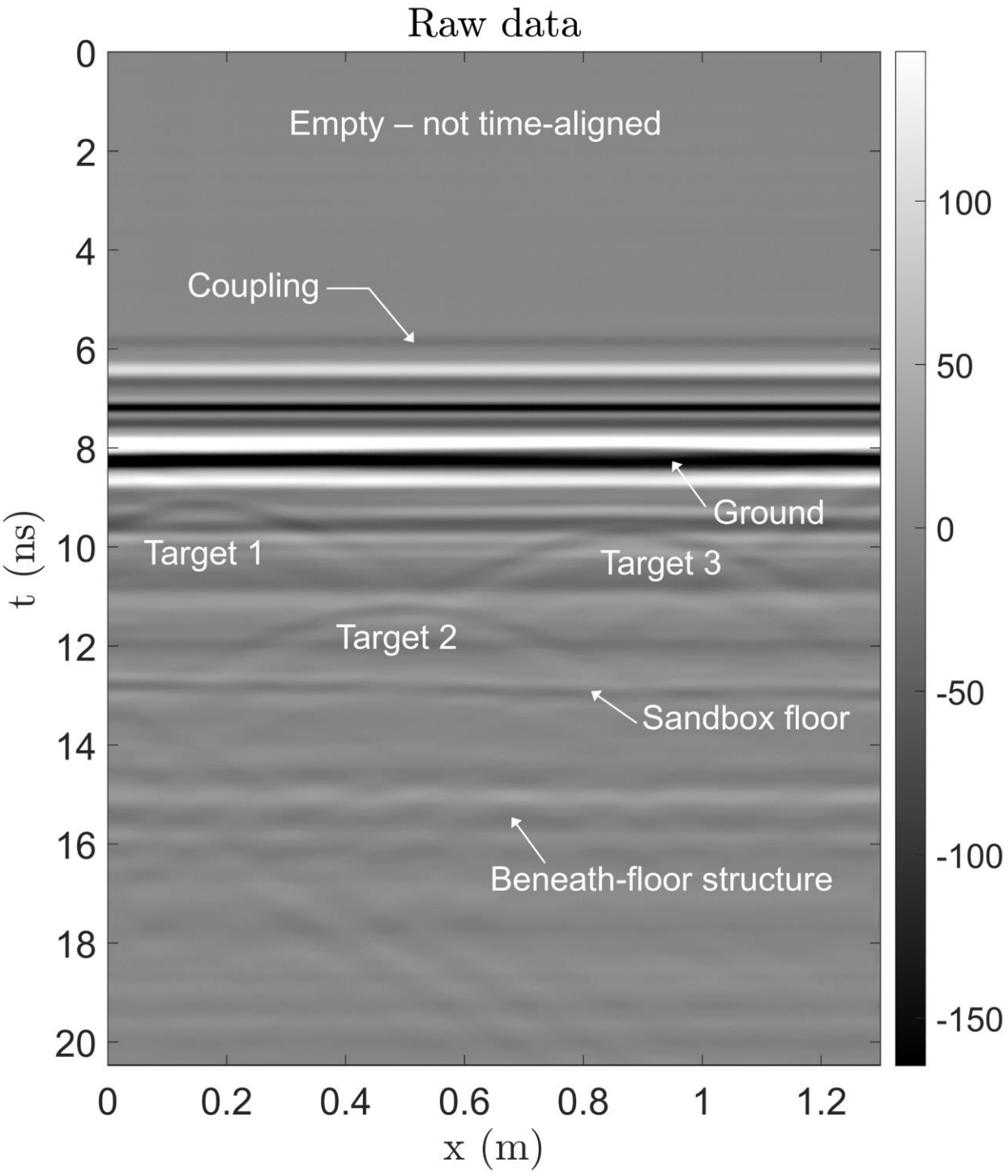

Fig. 71. Example GPR B-scan with coupling, ground, and targets highlighted.

The A-scan has magnitude of ADC units (corresponding to approximately 1 mV) and contains antenna coupling, ground reflection, and target reflections. Note that the time axis in Fig. 70 is not

aligned for t = 0. The B-scan is a collection of A-scans over slow-time and shows how the reflection profile changes throughout the scan. GPR B-scans are traditionally displayed in grayscale and the color of a single pixel maps directly to magnitude/voltage. Typically, a strong white color is a strong positive magnitude and a deep black color is a strong negative value. The B-scan displayed in Fig. 71 is raw – the most un-processed version of the B-scan data. The goal of the pre-processing pipeline is to apply corrective algorithms to the raw data in order to prepare the B-scan for an imaging algorithm. This section contains several helpful algorithms to clean the data; some are specific to the receiver presented in Section 3 and some are applicable in general. First, we examine de-glitching.

i. Glitch Removal

De-glitching is typically the first step in pre-processing because the presence of glitches can impact the performance of any other step. Here, we defined glitches as an unexpected occurrence in the data – from interference, receiver stability/numerical errors, or any other strange phenomena that makes the received waveform spike unnaturally. Here, we consider two types of errors – edge glitches and full-waveform glitches. The first type, an edge-glitch, is shown below in Fig. 72.

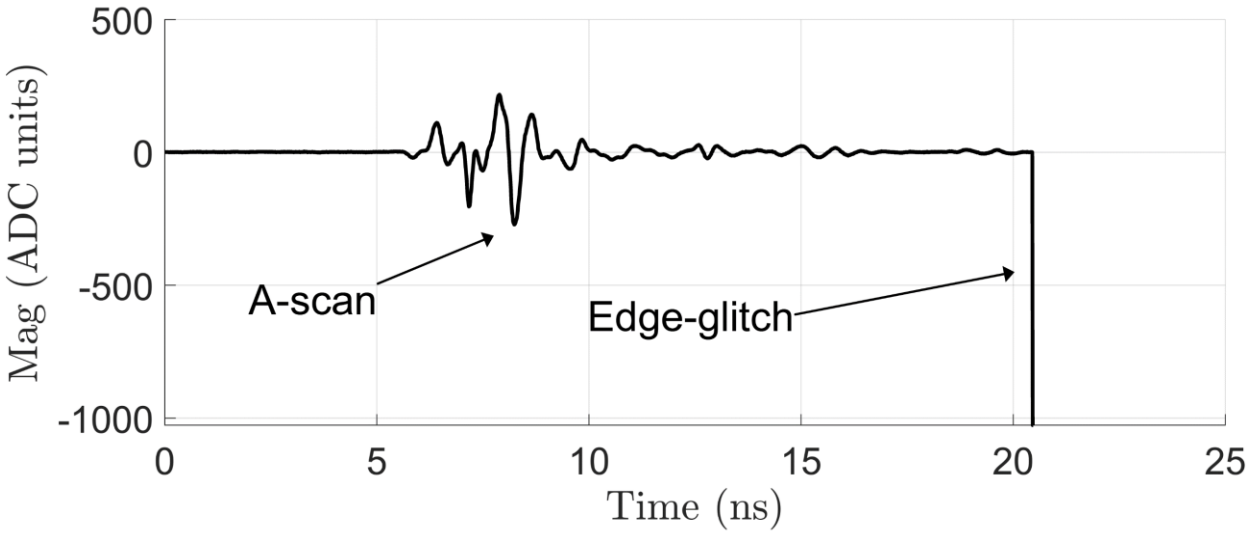

Fig. 72: Example of an edge glitch.

The edge-glitch is typically caused by numerical errors or bugs in the custom receiver or in the Rust pre-processing. Due to their potential magnitude, they must be removed. Luckily, edge-glitches are simple to fix in post-processing by simply zeroing the edges of the B-scan and are not computationally expensive to remove. This works under the assumption that the start and end of the GPR scan will be low magnitude. An example code to perform this task in MATLAB is below.

```
function D = remove_edge_glitches(D)
    % inputs.
    %   D - 2D array (N_t x N_x) of raw B-scan data
    % outputs.
    %   D - 2D array (N_t x N_x) of raw B-scan data, de-glitched

    N_SAMPLES_TO_REMOVE = 5; % how many samples from start and end to remove
                             % typically defined in calling script

    % set the potential glitch samples to zero.
    D(1:N_SAMPLES_TO_REMOVE,:)             = 0;
    D(end - N_SAMPLES_TO_REMOVE + 1:end,:) = 0;
end
```

Fig. 73. Code to remove edge glitches.

Now, we can examine the other type of glitch to be removed in this step, dubbed the A-scan glitch. An A-scan glitch is a glitch in an entire waveform that causes the waveform to behave dramatically

different compared to its neighbors. Fig. 74 shows an example of a single A-scan glitch in measured data.

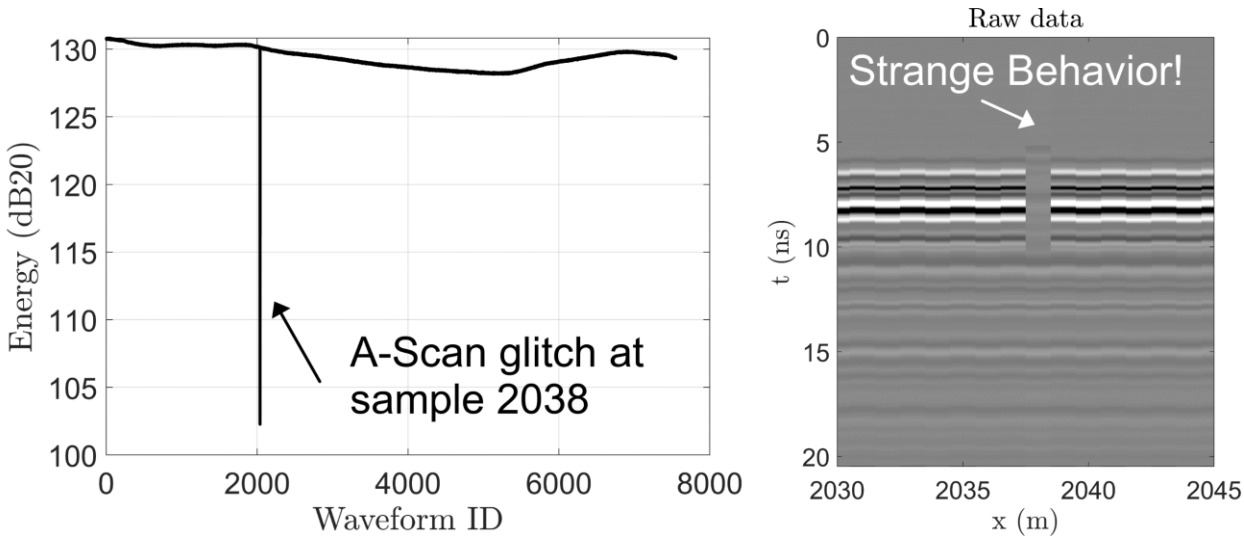

Fig. 74: A-scan glitch (energy-based detection method)

We choose to measure how "different" an A-scan is from its neighbors by examining its energy integrated over time. This type of measure will catch waveforms which have interferes or trouble sampling. As the scan has changing energies over time, we must compare the energy of a scan to is neighborhood.

```
function D = remove_Ascan_glitches(D)
    % inputs.
    %   D - 2D array (N_t x N_x) of raw B-scan data
    % outputs.
    %   D - 2D array (N_t x N_x) of raw B-scan data, de-glitched
    [~, N_x] = size(D);

    % algorithm parameters
    energy_threshold_dB = 10; % define "tolerance" to throw out an A-scan
    window_size         = 32; % define local "window" to compare a scan

    % integrate each A-scan to get Energies (1xN_x)
    Energies = 10.*log10(trapz(D.^2, 1));

    % calculate vector of center points for windows
    window_centers = (round(window_size/2) + 1):window_size:N_x;
    Nwindows       = numel(window_centers);

    % loop over each window
    for ii = 1:Nwindows
        % calculate the window left, right, and center.
        window_center = window_centers(ii);
        window_left   = max(1,   window_center - round(window_size/2));
        window_right  = min(N_x, window_center + round(window_size/2) - 1);

        % window the energies
        Energy_window = Energies(window_left:window_right);
        Energy_median = median(Energy_window);

        % determine if any glitches exist in the current window.
        is_Ascan_glitch = abs(Energy_window - Energy_median) > energy_threshold_dB;

        if(sum(is_Ascan_glitch) > 0) %there is a glitch
            % replace the glitches with this "median" waveform.
            [~,ind_median] = min(abs(Energy_window - Energy_median));
            median_wfm     = D(:,ind_median + window_left - 1);

            for jj = find(is_Ascan_glitch)
                D(:,jj + window_left - 1) = median_wfm;
            end
        end
    end
end
```

Fig. 75: Code to remove A-scan energy-based glitches.

The code in Fig. 75 will use a median-based filtering technique to compare the energy of a single A-scan to its local window. If the energy of an A-scan is greater or less than 10 dB with respect to its neighborhood, then we label it a glitch and replace it with a median. This algorithm will replace the glitch at sample 2038 in Fig. 74. The aggressiveness of this de-glitching algorithm can be tuned by reducing the energy threshold (10 dB in Fig. 75) and window size. From experience, 10 dB is

a fair comparison threshold which will not unnecessarily throw out A-scans as glitched. Due to its structure, this algorithm is moderately computationally inexpensive, running on a 2048x7551 single-precision data matrix in only 189 ms. To apply this to a 3-D scan, the de-glitching algorithm should be ran on each TX-RX pair's B-scan independently as comparing energies between TX-RX pairs will lead to unstable behavior.

ii. ToA Jitter Removal

Consider the plot of two consecutive A-scans below in Fig. 76.

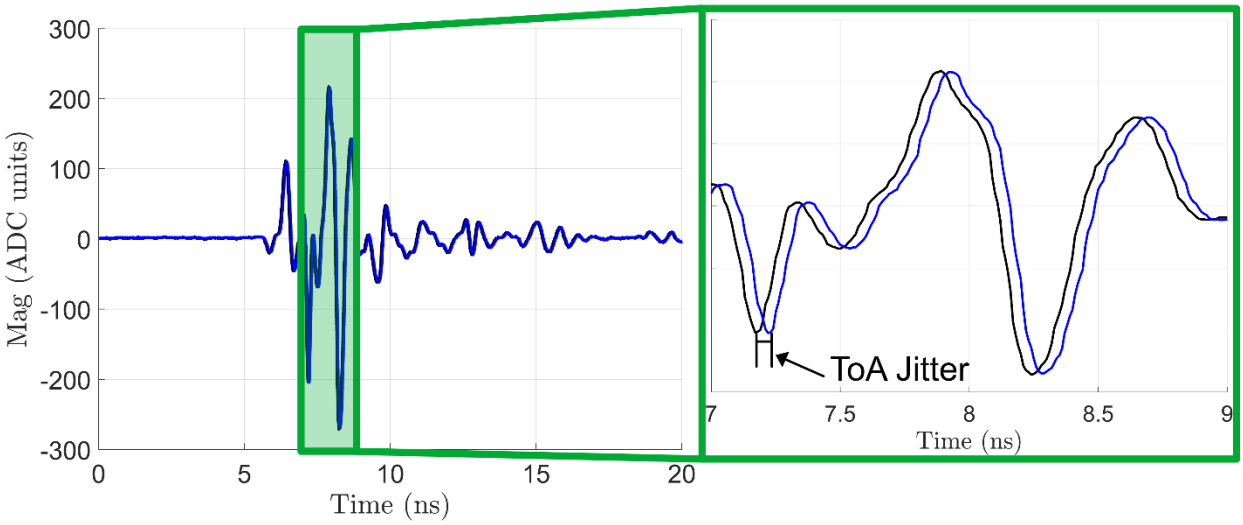

Fig. 76: Example time-of-arrival jitter in GPR A-scans.

The two A-scans are displaced in fast time with respect to each-other. This is an example of time-of-arrival (ToA) jitter, discussed briefly in Section 2.A. In the receiver presented in Section 3, ToA jitter can manifest somewhat randomly due to the discrepancy between up-sampling and down-sampling. This means that the down-sampled waveforms are sometimes delayed with respect to the up-sampled waveforms. In a generic real-time (not equivalent-time) receiver, ToA jitter manifests properly in the B-scan due to uncertainty in the trigger waveform. Notably, we have observed significant ToA jitter when using a real-time TDS6604 20 GS/s oscilloscope. ToA jitter

must be dealt with at this stage because any further background removal or any operation along the x-dimension on the scan will fail due to any ToA jitter. Fig. 77 below displays an algorithm to center the times based on cross-correlation with a reference waveform.

```
function D = remove_GPR_Bscan_jitter(D, is_interp_enable, interp_ratio)
    % inputs.
    %   D - an N_t x N_x matrix of singles or doubles
    %   is_interp_enable - interpolate D(:,) for better accuracy?
    %   interp_multiple  - the ratio of interpolated points to normal points
    % outputs.
    %   D - the B-scan without ToA jitter.

    % interpolate the B-scan along dimension 1
    if(~is_interp_enable)
        interp_ratio = 1;
    end
    maxlag      = 200*interp_ratio;
    N_frames    = size(D,2);

    % interpolate the 2-D matrix by interp_ratio
    % custom function - not explained - simple linear interp.
    D = linear_interpolate(D, 1, interp_ratio);

    % use the median envelope time-of-arrival to create `ref_wfm`
    env_max_inds = zeros(N_frames, 1);
    for kk = 1:N_frames
        [~,env_max_inds(kk)] = max(abs(hilbert(D(:,kk))));
    end
    [~, refwfm_frame_ind] = min(abs(env_max_inds - median(env_max_inds)));
    ref_wfm = D(:, refwfm_frame_ind);

    % iterate through A-scans and cross-correlate each A-scan with ref_wfm
    for kk = 1:N_frames
        %cross-corr `ref_wfm` with the kk-th A-scan
        wfm           = D(:,kk);
        [xC, lags]    = xcorr(ref_wfm, wfm, maxlag);
        [~,max_xc_ind]= max(xC);
        D(:,kk)       = circshift(wfm, lags(max_xc_ind));
    end

    D = D(1:interp_ratio:end,:);
end
```

Fig. 77: Code to remove time-of-arrival jitter.

This ToA-jitter removal algorithm iterates through each A-scan and compares it to a reference waveform using cross-correlation. The index of that maximum cross correlation is used to shift the waveform back to align with the reference waveform. In the extreme case of every-other

waveform being jittered as is the case for certain run configurations of the presented custom receiver, the scan will be un-jittered as in Fig. 78 below.

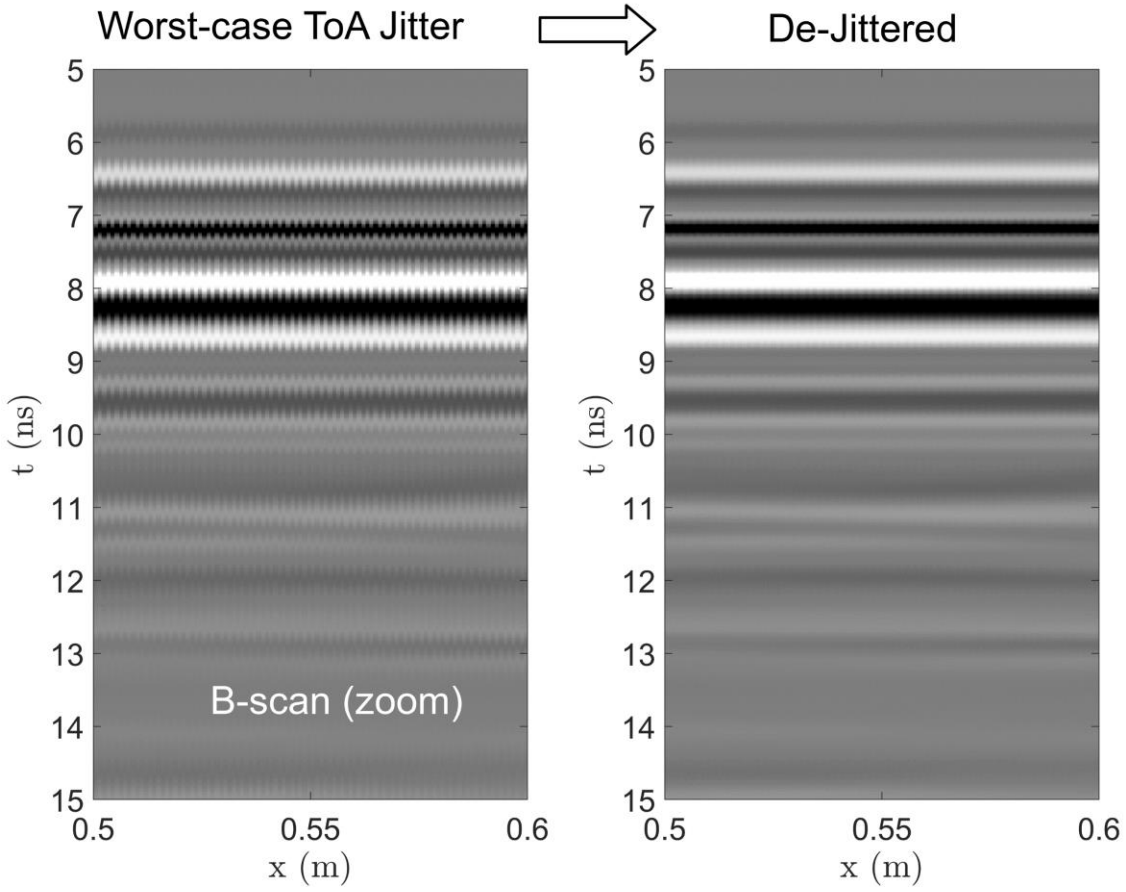

Fig. 78: Performance of de-jittering on a worst-case time-of-arrival jitter GPR B-scan.

In Fig. 78, the benefit of de-jittering is clear – the processed B-scan is much more smooth. With the B-scan de-jittered, we can now go on to more complex algorithms to improve the quality and ready the scan for imaging. For 2D and 3D outside imaging, the reference waveform used to de-jitter the scan (*ref_wfm* in Fig. 76) is the coupling-calibration waveform. For 3D scans, each TX-RX pair is de-jittered independently, with variations of the same presented algorithm.

iii. Moving Average

Now that the scan is de-jittered, we want to perform a moving average along the slow time (x) axis. Typically, a moving average along slow time implies some function f: $\mathbb{R}^{N\times M} \rightarrow \mathbb{R}^{N\times M}$ in which the m-th column of the moving-averaged matrix is the mean of the local columns near m. Alternatively, we use this time to down-sample the matrix from M to M' columns where M' follows some ideal sampling rate. We would like to down-sample in slow-time in order to reduce the computational burden of the background removal, filtering, and imaging steps. Then, we design an algorithm that transforms $\mathbb{R}^{N\times M} \rightarrow \mathbb{R}^{N\times M'}$ where:

$$M' = \left\lceil \frac{\delta x}{\delta x'} M \right\rceil \tag{44}$$

In (44), M' is the new number of A-scans, $\delta x'$ is the desired spatial sampling rate, δx is the current (linearized) spatial sampling rate, and M is the number of A-scans. The code to perform the down-sampling moving average is shown in Fig. 79.

```
function [Dp, xp] = moving_average(D, x, dxp)
    % inputs.
    %   D - N_t x N_x (M) B-scan
    %   x - (N_x x 1) x-vector (d/dtslow must be constant!)
    %   dxp - ideal spatial sampling period (m)

    % determine M prime, approx. number of samples
    M              = size(D,2);     % # old A-scans
    dx             = x(2)-x(1);     % old spatial sampl.
    Mp             = ceil(dx/dxp*M);% ideal # A-scans
    desample_rate  = round(M/Mp);   % closest desampling rate

    % create windows. overlap windows to avoid "staircasing" in
    % moving average.
    window_centers = (round(desample_rate/2) + 1):desample_rate:M;
    window_overlap = floor(desample_rate/4);  % how much to overlap.
    Nwindows       = numel(window_centers);

    % loop through windows to populate `Dp`, new averaged scan
    Dp = zeros(size(D,1),Nwindows,'single');
    for ii = 1:Nwindows
        window_center = window_centers(ii);
        window_left   = max(1, window_center - round(desample_rate/2) - window_overlap);
        window_right  = min(M, window_center + round(desample_rate/2) + window_overlap);
        Dp(:,ii)      = mean(D(:,window_left:window_right),2);
    end
    % create `xp`, new averaged x-vector
    xp = x(window_centers);
end
```

Fig. 79: Code to perform windowed moving average.

The moving average is useful for decreasing the size of the data without drastically harming quality or outright throwing away information. For example, the scan in Fig. 78 is size 2048×7551 with a δx of 0.17 mm. After running through the moving average algorithm (computation time of 90 ms), the data matrix is size 2048×260 with a δx of 0.5cm, which is significantly less than the radar's horizontal resolution and shouldn't affect imaging quality. The moving average also reduces any one-time glitches that appear in the middle of the scan because they are averaged out. If necessary, 3D averaging is done independently for each TX-RX pair.

iv. Time-Zero Alignment

In order to image correctly, we must define $t = 0$. $t = 0$ refers to the time at which the transmitted pulse reaches the phase center of the transmitting antenna. The inherent modularity in the defined

system (changing out amplifiers, cables, and pulse definitions) means that keeping track of the exact delays in the system is painful. Indeed, it is more useful to create an algorithm to define the "start" of the pulse and assign. There are many methods to perform time-zero alignment; two are used in this work – coupling-based time-zero estimation and ground-based time-zero estimation. In data generated from the sandbox, the coupling cannot be independently removed from the ground and we must use coupling-based time-zero estimation. In data generated from a skyshot or calibration scan, there is no ground reflection and again we must use coupling-based time-zero estimation. For all other data collection modes, it is significantly more powerful to measure the height between antenna phase center and ground and use that to estimate time-zero. The code for a coupling-based time-zero estimation is shown below in Fig. 80.

```
function [Dp, tp] = align_t0_from_coupling(D, t, tx_rx_dist, ant_len)
    % inputs.
    %   D - N_t x N_x B-scan
    %   t - N_t x 1 time vector
    %   tx_rx_dist - distance between tx+rx antenna
    %   ant_len  - antenna length
    % outputs
    %   Dp - t0-aligned B-scan
    %   tp - t0-aligned time vector

    % get mean waveform energy (normalized)
    d_dt_energy = mean(D,2).^2;
    d_dt_energy = d_dt_energy ./ max(d_dt_energy);

    % find the first "significant" peak of the waveform
    min_pk_significance = 0.005;
    has_neg_slope       = gradient(d_dt_energy)<0;
    is_significant      = d_dt_energy >= min_pk_significance;
    first_sig_point     = find(is_significant,1,'first');
    pk_ind              = find((1:size(D,1))' >= first_sig_point & has_neg_slope,1,'first')-1;
    pk_ind              = min(max(1,pk_ind),size(D,1));
    pk_val              = d_dt_energy(pk_ind);

    % from that peak, find its FWHM
    left  = d_dt_energy(1:pk_ind);
    fwhm2_left  = find(left < pk_val/2, 1,'last');
    fwhm2_sec = (pk_ind - fwhm2_left) .* (t(2)-t(1));

    % define t=0 as the first coupling peak - fwhm/2 - coupling distance + antenna length.
    t0     = t(pk_ind) - fwhm2_sec - tx_rx_dist/3e8 + ant_len/3e8;
    t0_ind = min(max(1, round(t0/(t(2)-t(1)))),size(D,1));

    % shift Bscan and time vector
    Dp = D(t0_ind:end,:);
    tp = t(1:(end-t0_ind+1));
end
```

Fig. 80: Code to automatically correct t=0 errors in a GPR B-scan.

The algorithm works by assuming a certain “smoothness” of the first coupling peaks and estimating the $t = 0$ point based on the first coupling peak. The accuracy of this coupling-based method depends on the length of the antenna – for long antennas, this method may under-correct the time axis because the distance between excitation point and phase center may bias the estimate to a lower time. At this point, we may examine the average A-scan as shown below in Fig. 81.

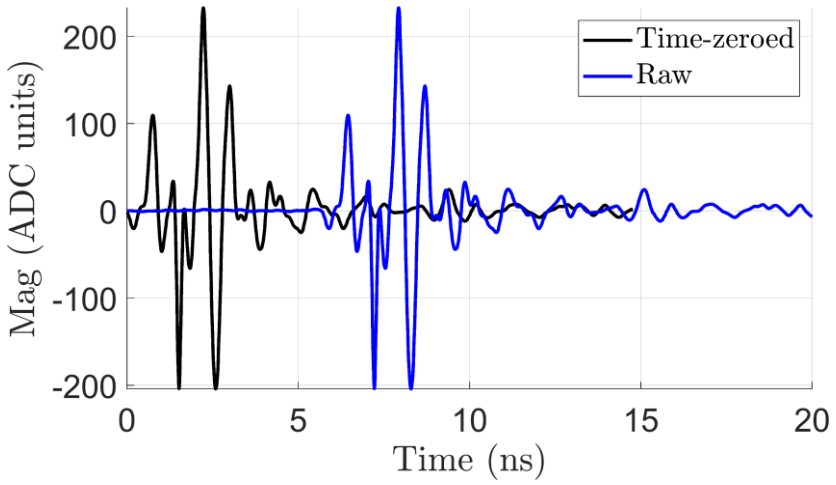

Fig. 81: Example time-zeroed A-scan.

We see that the time-zeroed A-scan (black) has been shifted to a more appropriate spot in the fast-time axis, according to the coupling pulse and geometry of the problem. Additionally, the useful A-scan time now only lasts for approximately 15 ns as compared to 20 ns with the non-time-zeroed (raw) A-scan. The above coupling method is appropriate for scans with no calibration waveform. For 2D and 3D scans with a calibration waveform, a more powerful method is to instead estimate the ground height in the scan and zero to that in a method similar to Fig. 80. An example of the time-zeroed scan is also shown in Fig. 83.

v. Background Removal

Background removal (BKGR) is one of the most important steps in the pre-processing pipeline. It is also most dependent on the experimental setup. For scans where the coupling cannot be disentangled from the ground response, only one BKGR step is needed. In these situations, we develop an algorithm to remove horizontal lines from the B-scan. For scans where the coupling between antennas is calibrated, two BKGR steps are used. In these situations, we first remove the coupling (line up the coupling and subtract it) and then optionally remove the ground bounce by

removing horizontal lines. Here, we only show the method to use horizontal lines called Principle Component Analysis (PCA), in Fig. 82.

```
function D_BKGR = BKGR_PCA(D, L)
    % inputs.
    %   D - N_t x N_x B-scan, pre-processed
    %   L - number ( > 1) of singular values to remove
    % outputs.
    %   D_BKGR - Background-Removed B-scan

    [U, S, V] = svd(D, 'econ');
    o = diag(S);
    D_BKGR = U * diag([zeros(L,1); o(L+1:end)]) * V';
end
```

Fig. 82: Code to perform B-scan background removal with PCA.

This method will use the singular value decomposition to decompose the data matrix into its singular vectors. Singular vectors with large singular values correspond to horizontal stripes in the scan. We sometimes wish to remove horizontal stripes in the scan because they are typically either coupling or ground returns. The number of singular values to remove is also important. For low-bandwidth pulses, generally only the first singular value is removed. For high-bandwidth pulses, we remove two singular values. The process to determine the number of singular values to remove can also be based on thresholding the singular value's magnitude itself. An example of background removal on the sample data is shown below in Fig. 83.

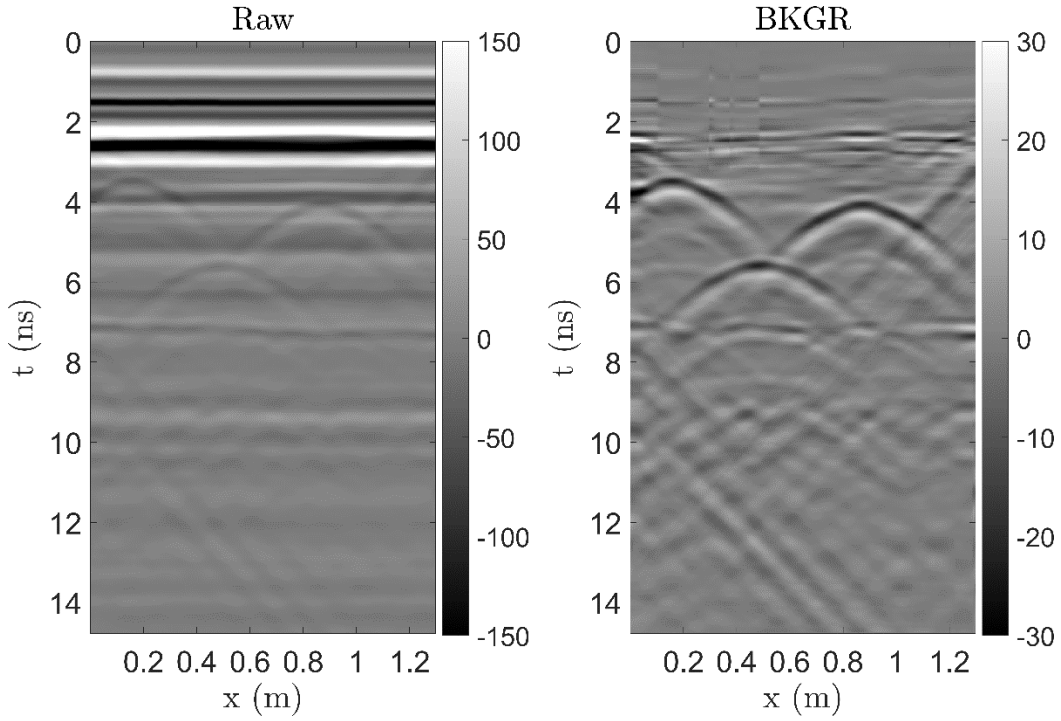

Fig. 83: Comparison of raw and background-removed GPR B-scan data.

Fig. 83 shows PCA removal with L = 2. In this case, L=2 is aggressive because the top (flats) of the target hyperbolas are disturbed by the removal. The three buried rebar targets are now clearly visible after background removal. Around 2 ns in the scan, some residual is clearly visible. Some of this residual is impossible to clear up; however, certain parts of the residual can be fixed by filtering. Next, we examine common filtering routines.

vi. Filtering

To clean up the scan, we use FIR filters in both t and x dimensions, as below in Fig. 84:

```
function D = filter_2D(D, t, x, flims, kx_max, N_f, N_kx)
    % inputs.
    %   D      - N_t x N_x data matrix to be filtered
    %   t      - time vector
    %   x      - spatial sample vector
    %   flims  - [f_low f_high] for bandpass F filter
    %   kx_max - corner for lowpass X filter
    %   N_f    - order of FIR filter in frequency
    %   N_x    - order of FIR filter in x
    % outputs.
    %   D - filtered N_t x N_x data matrix

    [N_t, N_x] = size(D);

    % create time frequency vector
    Ts = t(2)-t(1);
    Fs = 1/Ts;
    f  = linspace(-Fs/2,Fs/2,N_t);

    % create spatial frequency vector
    dx = x(2)-x(1);
    Kx = 1/dx;
    kx = linspace(-Kx/2,Kx/2,N_x);

    % FFT to f-x representation
    D_f    = fftshift(fft(D,[],1),1);

    % create bandpass FIR filter with order N_f
    fir_b = fir1(N_f, flims./(Fs/2));
    TF_f  = freqz(fir_b, 1, f, Fs).';

    % apply the filter
    D_f   = D_f.*repmat(TF_f,1,N_x);
    D     = real(ifft(ifftshift(D_f,1),[],1));
    D     = circshift(D, -N_f/2, 1);

    % FFT to t-kx representation
    D_kx   = fftshift(fft(D,[],2),2);

    % create lowpass FIR filter with order N_kx
    fir_b = fir1(N_kx, kx_max./(Kx/2));
    TF_x  = freqz(fir_b, 1, kx, Kx);

    % apply the filter
    D_kx  = D_kx.*repmat(TF_x,N_t,1);
    D     = real(ifft(ifftshift(D_kx,2),[],2));
    D     = circshift(D, -N_kx/2, 2);
end
```

Fig. 84: Code to filter B-scans in frequency and space.

While the above code is standard, it is worth reproducing for clarity. An example of a filtering process on the data in Fig. 83 using a 60-order frequency bandpass filter from 300 MHz to 5 GHz and a 60-order lowpass spatial filter with a cutoff of 10 m^{-1} is shown in Fig. 85.

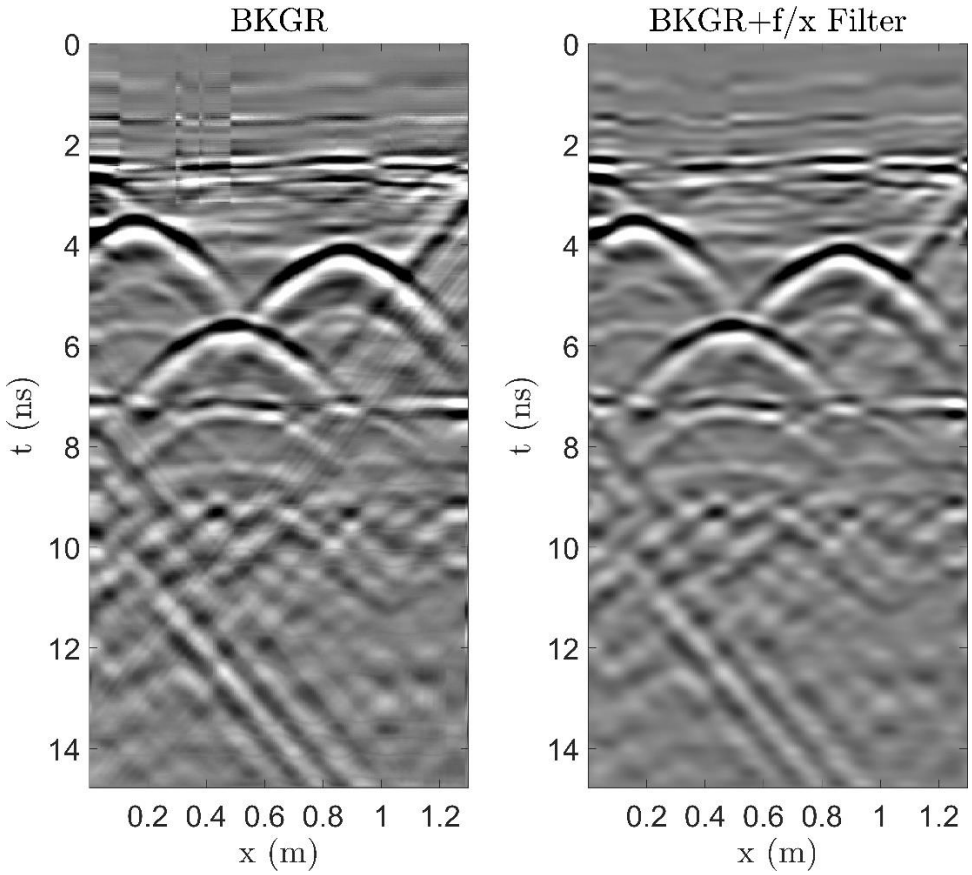

Fig. 85: Comparison of filtered and un-filtered GPR B-scans.

Filtering removes two major components still present in the scan – residual errors from background-removal and the diagonal-moving clutter from the sandbox walls.

vii. Matched-Filtering

After background removal, the data is ready for migration. Migration at this point, however, would result in an undesirable target image. This is because the target reflection in the B-scan contains multiple peaks which will all appear in the migrated image. In the case of Fig. 85, the target reflection waveform is white-black-white or up-down-up, which will create three "hotspots" upon imaging. Matched filtering is a cross-correlation with the expected target waveform that can be

used to compress the pulse into a single peak with comparable vertical resolution. The code used to do this is below in Fig. 86.

```
function D_MF = matched_filter(D, matched_wfm)
    % inputs.
    %   D - N_t x N_x B-scan
    %   matched_wfm - waveform to filter D with, taken at same sample rate
    % outputs.
    %   D_MF - N_t x N_x matched-filtered B-scan

    % flip matched_wfm and ensure column vec.
    matched_wfm = flip(matched_wfm(:));

    % 2D convolution
    D = conv2(D, matched_wfm,'same');

    % (optional) unset wrong-sign pixels
    if(max(D_MF,[],'all') > 0)
        D_MF(D_MF<0) = 0;
    else
        D_MF(D_MF>0) = 0;
    end
end
```

Fig. 86: Code to perform a matched filter on a GPR B-scan.

Applying the matched-filter to Fig. 85 results in the changes of Fig. 87.

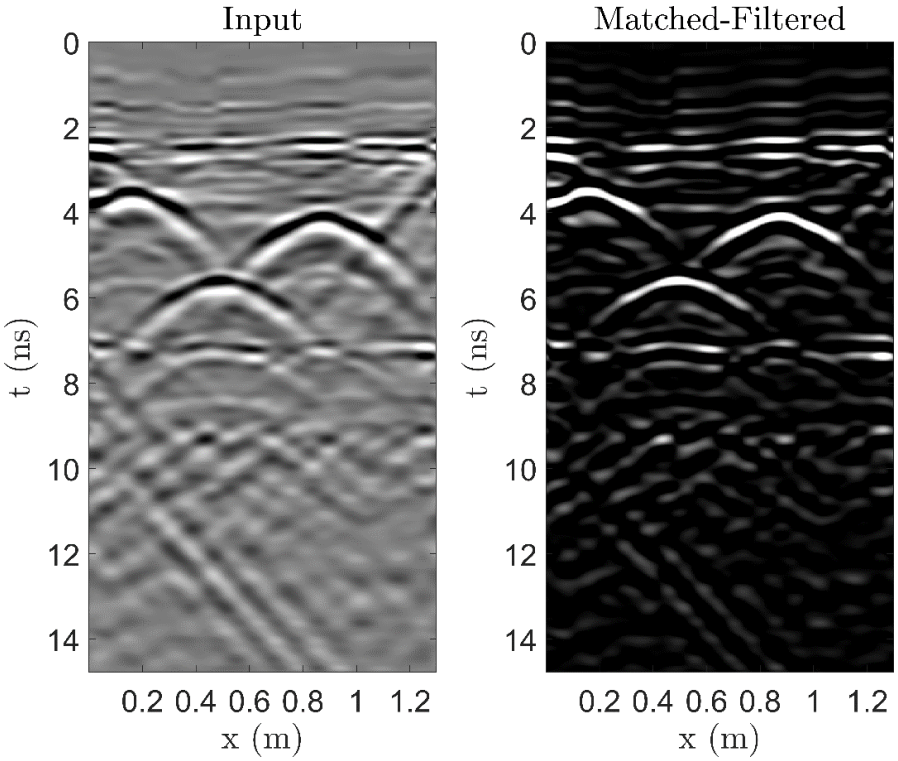

Fig. 87: Comparison of filtered and matched-filtered GPR B-scans.

To perform the matched-filter, we must input the expected target-reflected waveform to convolve with the B-scan. Determining the waveform may be done in two ways. One option is to extract the waveform from the B-scan itself. Another option is to use a standardized waveform and accept slight errors. In controlled conditions like the sandbox, we prefer the second method. As a rule of thumb, the system will either be inverting or non-inverting and take at least one derivative of the input pulse. In Fig. 87, the original scan was taken with a $\sigma = 100$ps differential (1st derivative of Gaussian) up-down pulse. Therefore, the matched filter is performed using a $\sigma = 100$ ps Ricker wavelet (up-down-up) and pixels which contain negative values of the convolution are set to zero as in Fig. 86. From the scan in the right-hand-side of Fig. 87, we can see that each target-reflected hyperbola is dominated by a single peak, which implies that the migrated image will also have a single peak. At this point, the B-scan is ready to be imaged.

B. Imaging

In this work, we use Kirchhoff Migration as the imaging algorithm. Kirchhoff migration is a time-domain range-migration algorithm which approximates the inverse scattering problem. The equation for 2D scattering is reproduced from (15) below in (45):

$$I(x_q, z_q) = \int_{-\infty}^{\infty} \frac{\epsilon_r^{1/4} \cos\theta}{\sqrt{c|\vec{r}\,|}} \frac{\delta^{\frac{1}{2}}}{\delta t^{\frac{1}{2}}} E(x_a, t = t_{exp}) dx_a \tag{45}$$

where I refers to the resulting image energy at pixel (x_q, z_q), θ refers to the angle between the antenna at point $(x_a, -h)$ and pixel (x_q, z_q), x_a is the scan axis, $\vec{r}$ is the vector pointing from antenna to pixel, $E(x_a, t)$ is the measured electric field (B-scan pixel) at antenna position x_a at time t, and t_{exp} is the "expected" time at which a target at (x_q, z_q) would appear in an A-scan taken from antenna position $(x_a, -h)$.

The parameter t_{exp} traces out a hyperbola when plotted versus x_a, and is thus the factor that transforms the target-reflected hyperbolas into imaged point targets. For a two-layer problem, t_{exp} can be expanded as (46):

$$t_{exp} = \frac{2h}{c} \sec\theta_a + \frac{2z_q\sqrt{\epsilon_r}}{c} \sec\theta_g \tag{46}$$

Where h is the antenna height, c is the speed of light, θ_a is the ray-based angle in air, θ_g is the ray-based angle in ground, z_q is the target depth in soil, and ϵ_r is the real part of the soil permittivity. (?) extends naturally for multilayer systems by adding additional delay terms. The new unknowns in (?) are the ray-based angles θ_a and θ_g, which can be solved using a least-squares approximation or using the routine detailed in Section II.C. Once the ray-based angles are obtained, we can

perform the migration. To avoid the expensive integration and speed up computational times, the approximation to (45) used is (47), below:

$$I(x_q, z_q) = \sum_{|x_q - x_a| < \tau_x} E(x_a, t_{exp}) \tag{47}$$

In (47), we skip the calculation of $\cos\theta$, $\vec{r}$, and the half-derivative of E. Though technically correct to use, these factors were found to only consume computation time and either harm or not dramatically affect the quality of the resulting migrated image. In addition, (47) also limits the summation boundary by limiting $|x_q - x_a| < \tau_x$. The physical meaning of this limitation is that we do not expect scans taken greater than some distance τ_x from the target position to have a significant contribution. For shallow scans, $\tau_x = 0.5\text{m}$ is appropriate. This limitation also dramatically speeds up computation.

An example of 2D Kirchhoff Migration is shown below in Fig. 88.

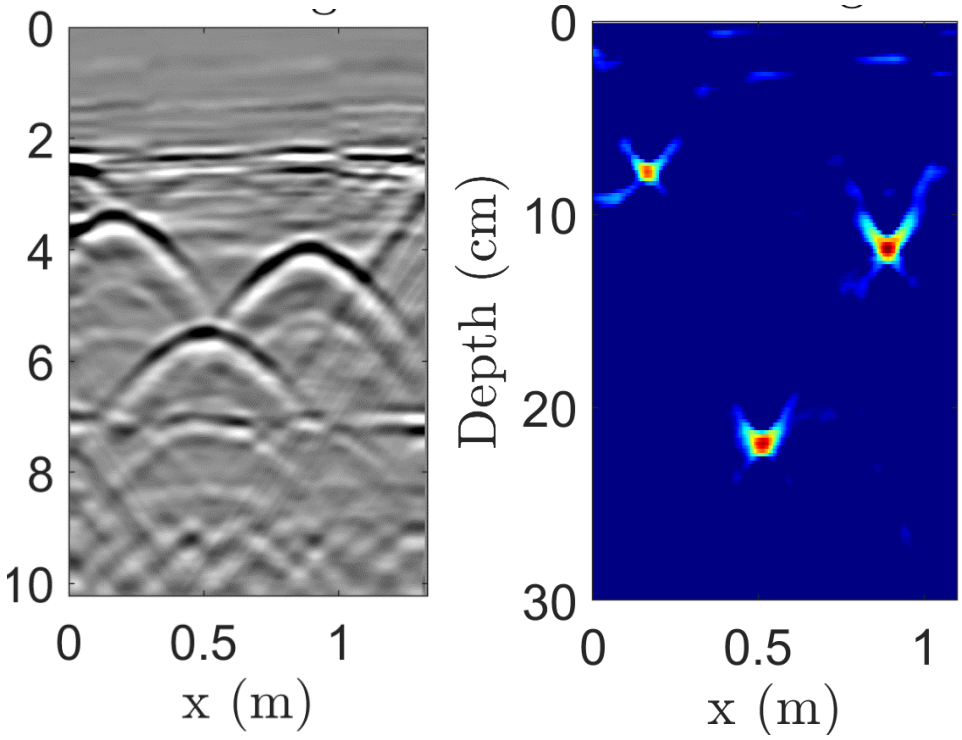

Fig. 88: Comparison of BKGR GPR B-scan and migrated 2D image.

On the left is the pre-processed scan before matched filtering. On the right is the migrated, matched-filtered image. The three buried targets are clearly visible as point targets.

In the same vein as (?), we can write a simplified approximate 3-D migration formula as (48):

$$I(x_q, y_q, z_q) = \sum_{\Omega_x} \sum_{\Omega_y} E(x_a, y_a, t_{exp}) \tag{48}$$

Where now t_{exp} follows the same equation (?), but now θ_a and θ_g are calculated from $(x_a, y_a, -h)$ to (x_q, y_q, z_q) and creates a hyperboloid in $x_a - y_a - t$ space. In (48), we use the forms $\Omega_{x,y}$ to refer to the limits over which x_a and y_a are considered, similar to (47) and stated in (49):

$$\Omega_x = \{x_a : |x_a - x_q| < \tau_x\} \tag{49}$$

Note that (?) is not a proper solution to the inverse scattering problem and is merely a barebones numerical tool to approximate the result. The proper formula for 3D Kirchhoff migration is derived in [42]. For simple images with pre-determined setups such as the three-rebar sandbox, we can now determine qualities of the scan such as signal-to-noise ratio (SNR), target width, and target height. These image qualities can be used to compare system configurations against each-other.

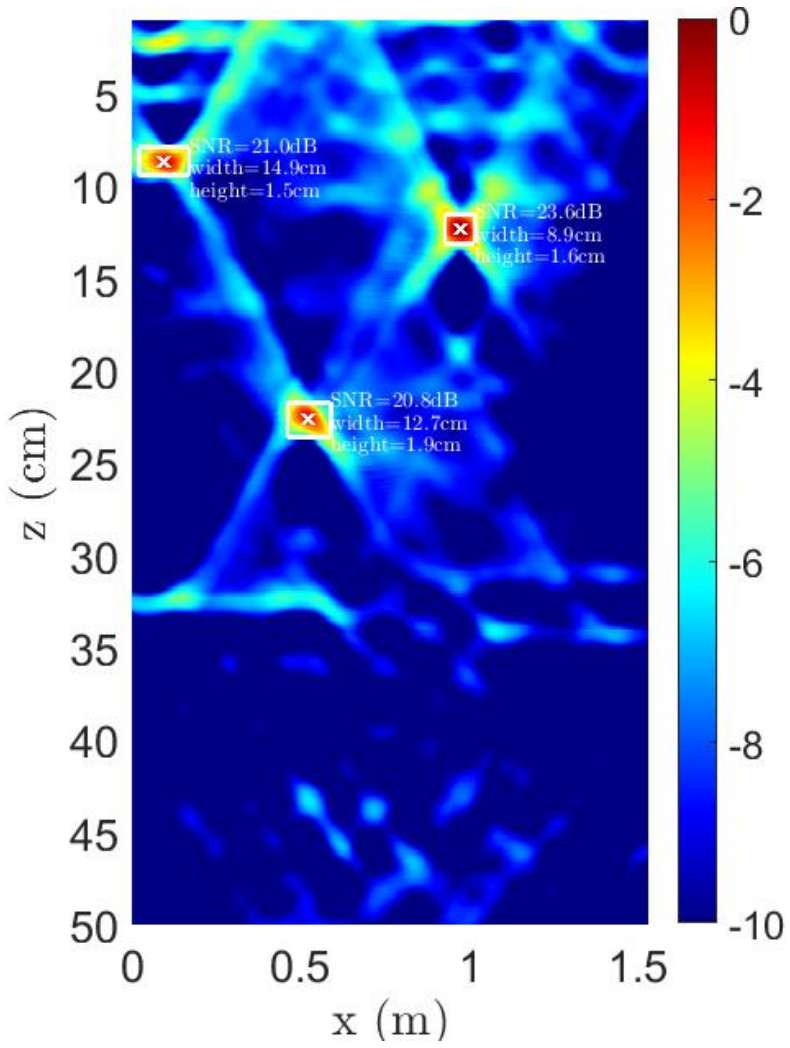

Fig. 89: Annotated 2-D GPR image.

An example of SNR automatically calculated on the migrated image is shown in Fig. 89. Clearly, the rightmost target (target 3) is the strongest return with 23.6 dB of SNR and a horizontal

resolution of 8.9 cm. The bottom target has poorer SNR and resolution because of its added depth. The leftmost target has poorer SNR and resolution because the full hyperbola is not in the scan – the sandbox is too short to fit the leftmost target response as in Fig. 89.

6. 2D GPR Scan and Image Results

This section contains interesting or important results from 2-dimensional GPR scans taken in the sandbox and outside.

A. Buried Wire

This section contains significant portions from [11], reprinted with permission. Ground penetrating radar (GPR) is one of the leading technologies for non-destructive characterization of subsurface environments and buried hazard detection. Many possible targets including pressure plates include small wires (diameter < 1mm) buried near the surface used to electronically trigger the hazard. Thus, it is of critical interest to be able to detect a small wire in order to accurately detect and classify a target using GPR. [90] demonstrates detection of 16-mm diameter buried fiber-optic cables using GPR. However, the specific problem of near-surface extremely small wires has not been demonstrated in literature. There are two distinct problems with detection of near-surface wires: the removal of ground-bounce and surface clutter, and the small magnitude of the reflected pulse from the wire due to the wire's small size with respect to the interrogation wavelength. The former problem may be remedied (but not entirely removed) with more high-powered surface removal algorithms like PCA or RPCA [91], however, the latter problem is a fundamental physical limit. To overcome the small size of the wire, we operate our GPR system at a higher bandwidth of up to 7.75 GHz, much higher than the bandwidth of typical GPR systems. In this paper, we will demonstrate for the first time that a GPR system with these specifications can successfully detect

wires with diameters less than 1mm. The ability to detect these small wires will lead to increased imaging capability and classification performance for the detection of buried hazards.

i. Radar System Specifications and Wire Reflections

The experimental system is a time-domain ground-penetrating radar setup with a single transmit and receive antenna pair in an air-coupled bi-static arrangement with a constant offset of 5cm at a height of 20 cm, shown in Fig. 90.

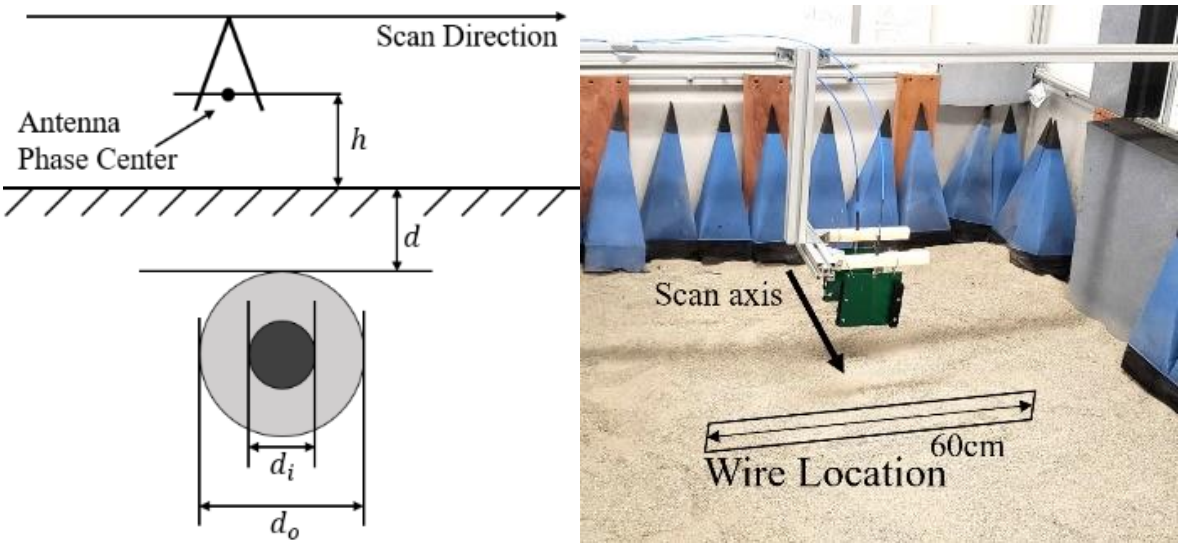

Fig. 90: System and experimental diagram for detecting sub-surface wires with all relevant dimensions labelled, not to scale.

The transmitter is a Keysight M8195A 65 GS/s Arbitrary Waveform Generator. The output pulse is amplified using two HMC998 amplifiers to achieve a total peak-to-peak voltage of 9.32 V. The receiver is a benchtop Agilent 86100A sampling oscilloscope with an HP 54752A 50-GHz receiver module. Both transmit and receive antennas are customized compact Vivaldi antennas with above 5 dB of flat-band gain. The wires have an internal copper core with diameter d_i with a dielectric jacket for a total diameter d_0 as in Fig. 90. The relevant parameters are shown in Table 11 below.

Table 11: Critical Operating Parameters of Experimental System

System Parameter	**Value**
20-dB Pulse Bandwidth	0.25 – 7.75 GHz
Pulse Type/Shape	Gaussian ($\sigma = 50$ ps) Monocycle
Pulse peak-to-peak voltage	9.32 V
Wire buried depth d	Approximately 2 cm
Inner copper wire diameter range d_i	0.16 to 2.05 mm (AWG 34 to 12)
Total wire diameter range d_o	0.37 to 3.03 mm

To approximate the reflectivity of the wire, we examine its canonical radar cross section (RCS). We reproduce the approximate monostatic TM-incident RCS σ here in (50) [92]:

$$\sigma \approx \frac{4\ell^2}{\pi}\left|\sum_{n=-\infty}^{\infty}\frac{J_n(k_s a)}{H_n^{(2)}(k_s a)}\right|^2 \tag{50}$$

In (50), ℓ is the length of the wire, k_s is the wavenumber in soil, a is the wire radius, J_n is the Bessel function of the first kind with order n, and $H_n^{(2)}$ is the Hankel function of the second kind with order n. (50) ignores near-field and resonant effects.

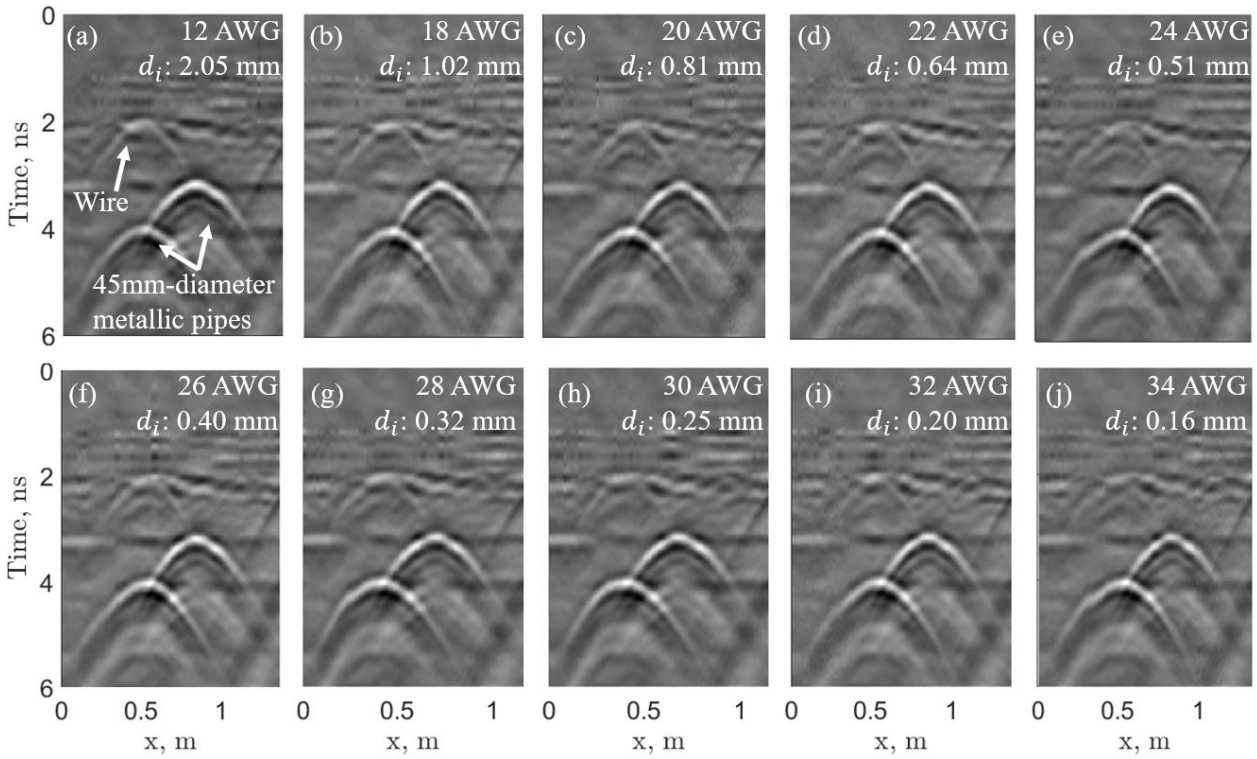

Fig. 91: Ground-penetrating radar B-Scan data for wires of varying diameter. The ground is removed by PCA with the two largest singular values removed.

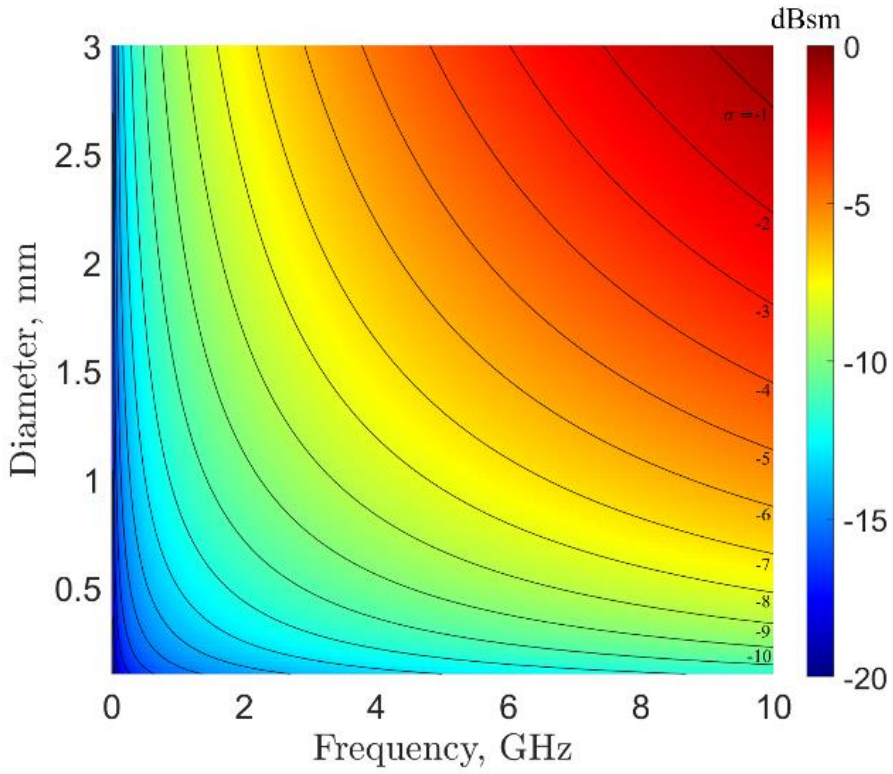

Fig. 92: RCS of a 60-cm cylindrical wire (in $\epsilon_r = 5$ soil) versus diameter and frequency. Contours are of a constant RCS.

The plot of (50) versus wire diameter and frequency is shown in Fig. 92. From Fig. 92, higher frequencies than a "typical" pulsed GPR's bandwidth of 2 to 3 GHz are required to sense useful reflections. For this reason, we have chosen to extend the experimental system's bandwidth up to 7.75 GHz to allow the detection of smaller wires.

ii. Experimental B-Scan Results

Each diameter wire is buried at 3-cm deep in the same x-location and scanned using the setup in Fig. 90. The collected B-scan results are in Fig. 91. For reference, two metallic pipes are also buried at depths of 15 and 20 cm. After each experiment, the sand above the wire is compacted to a similar density of its surroundings to ensure reflections come from the wire alone. From 12 AWG to 34 AWG, the hyperbola return is quite clear and crisp, which indicates that each wire has clear returns. However, wire diameters less than 18 AWG tend to contain only higher frequency content

and have similar magnitude to ground clutter. At 34 AWG, the hyperbola is only visible because of the long tails which extend into a time without surface clutter, implying that the relatively low directivity of the antennas is critical in the visual detection of small wires. We note that the typical electronics wire gauge is in the 20- to 24-gauge range, and the system clearly detects these wires.

iii. Conclusion

We present experimental data showing detection of small wires using GPR. Wires, while being an important part of several buried hazards, have not yet been shown in literature to be directly detectable by GPR. By employing a high-bandwidth system of up to 7.75 GHz, we show the reliable detection of 12 AWG down to 34 AWG wires. The ability of a system to detect wires can drastically impact its detection and classification abilities.

B. Sandbox GPR Scans - Rebar

In the following section, we present select data from imaging rebar in the sandbox using the 2D system as shown in Fig. 62. The targets are three 1/4”-diameter steel rebar as shown in Figs. 68 and 69. In five separate scans, we input five different instantaneous pulse bandwidths: 25ps, 50ps, 75ps, 100ps, and 200ps. These numbers refer to the parameter σ of a Differential pulse. A lower σ value implies higher bandwidth. The numerical results of the scan are shown below in Table 12.

Table 12: Results of sandbox rebar scans using different pulse widths.

Scan Type (σ/BW) / Spec.	25ps/18 GHz	50ps/9 GHz	75ps/6 GHz	100ps/4 GHz	200ps/2 GHz
Target 1 Position (x, depth) (cm)	(11, 5)	(10, 5)	(9, 5)	(11, 6)	(10, 6)
Target 2 Position (x, depth) (cm)	(48, 18)	(47, 19)	(44, 19)	(48, 19)	(47, 19)
Target 3 Position (x, depth) (cm)	(87, 9)	(86, 9)	(82, 9)	(87, 9)	(86, 10)
Target 1 SNR (dB)	14.5	12.8	12.8	12.2	7.0
Target 2 SNR (dB)	8.1	11.3	12.1	13.4	11.2
Target 3 SNR (dB)	9.4	13.7	14.9	16.5	12.5
Target 1 (cm) Dimensions (h x w)	0.6 x 8.9	1.2 x 9.9	1.6 x 12.0	2.1 x 12.1	5.1 x 20.1
Target 2 (cm) Dimensions (h x w)	1.9 x 13.6	1.3 x 9.5	1.4 x 10.4	1.5 x 11.0	2.6 x 16.2
Target 3 (cm) Dimensions (h x w)	1.6 x 14.2	1.1 x 9.9	1.4 x 11.5	1.6 x 11.0	3.2 x 17.8

These results come from Figs. 93 and 94, shown below. We note that though the claimed bandwidth of this GPR system is 12 GHz, we still input a pulse with an 18 GHz bandwidth in order to see what happens. The 18 GHz bandwidth is limited by the receiver balun (12 GHz), which has an upper frequency limit which rolls off somewhat slowly.

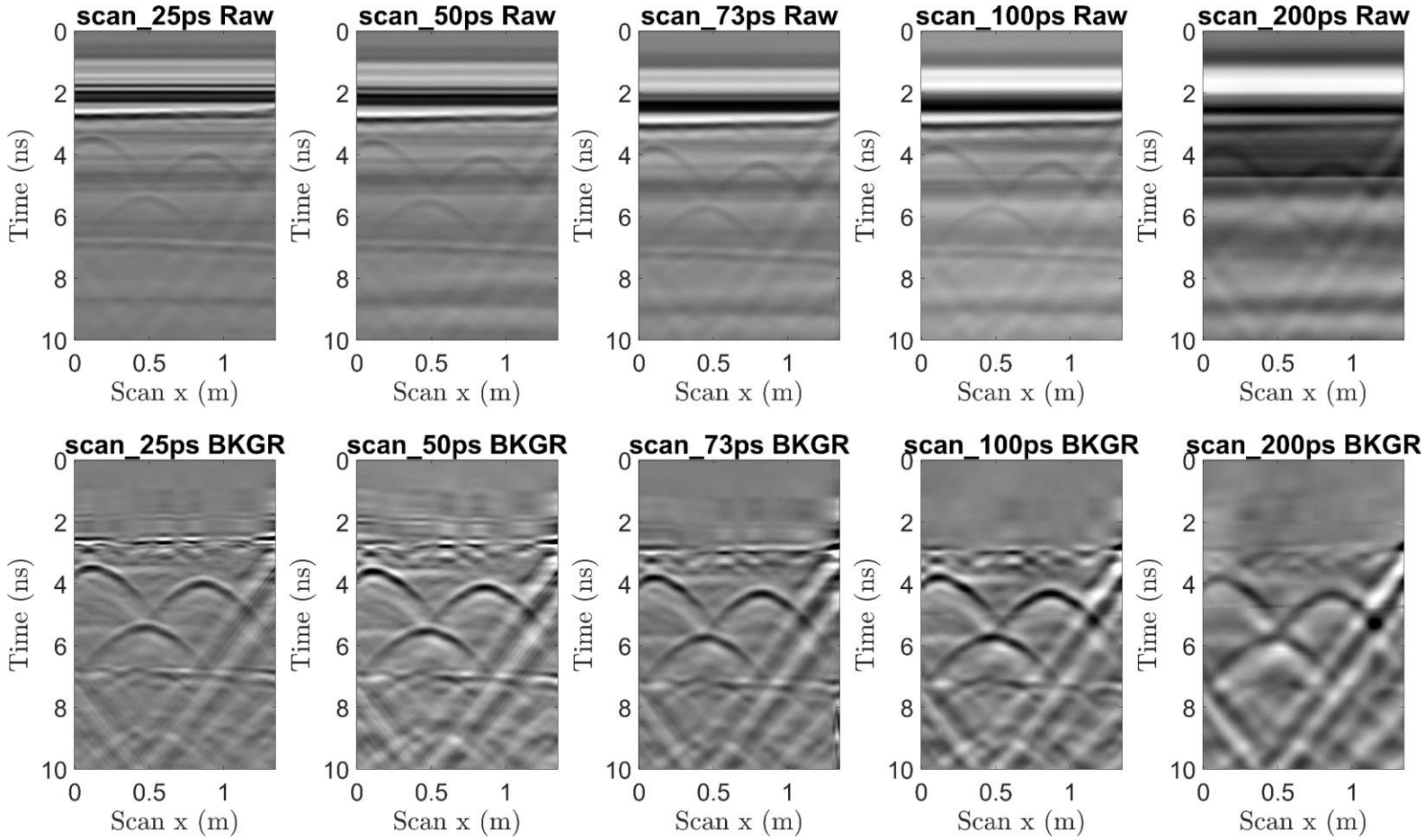

Fig. 93: Raw (top) and pre-processed (bottom) GPR B-scans of three rebar targets using pulses of different bandwidths.

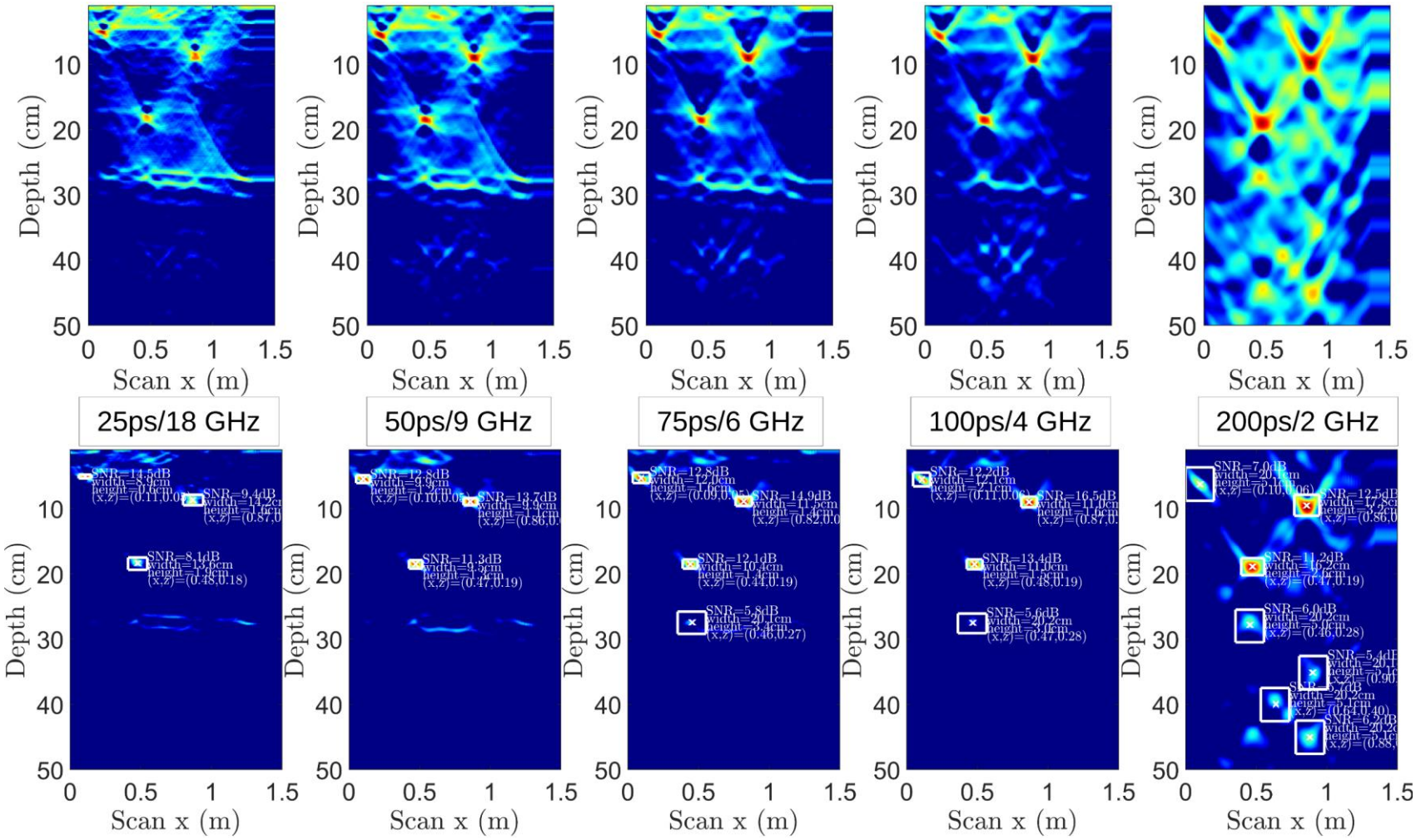

Fig. 94. Migrated images of Fig. 93. (top) Image displayed with 10 dB of dynamic range. (bottom) Image displayed with 6 dB of dynamic range and annotated targets. All targets are found using a 2-D peaksearch, SNR and shape-based discrimination, and outlined with a white box denoting its 3-dB area. The horizontal and vertical resolutions of each target are taken to be the 3-dB with of these boxes.

Fig. 93 shows the Raw (upper row) and Pre-processed (lower row) GPR B-scans of the three-target buried sandbox. Five scans are shown per row, with the nearest integer GHz bandwidth – 25ps (18 GHz), 50 ps (9 GHz), 75 ps (6 GHz), 100 ps (4 GHz), and 200 ps (2 GHz). In all five scans, the three targets are clearly visible. Examining the quality of each B-scan response, we can draw the following conclusions:

- As bandwidth decreases, the scans become "fuzzier" – this is the vertical resolution of the radar degrading (increasing in magnitude).
- As bandwidth increases, the hyperbolas have shorter tails and less relative magnitude in the tails. This phenomenon is likely due to a narrower radiation pattern and radar power budget at high frequencies, and impacts the achieved horizontal resolution as compared to the theoretical horizontal resolution.
- Though not directly indicated in Fig. 93, the target response magnitude generally increases with decreasing bandwidth. Target 3's BKGR peak has maximum values: 25ps, 5 mV; 50 ps, 17 mV; 75 ps, 30 mV; 100 ps, 44 mV; 200 ps, 43 mV. This increase is likely due to increased system loss (cables, soil, spherical spreading) and decreased amplifier gain at high frequencies. Additionally, the 200ps target return does not increase in magnitude due to low-frequency portion of the antenna's gain slope.
- The amount of visual clutter also tends to increase with decreasing bandwidth. This phenomenon is likely due to a wider radiation pattern at low frequencies.

To properly assess these scan qualities, we put each scan through a matched filter and image them with Kirchhoff migration as described in Section 5. The results are shown in Fig. 94.

In Fig. 94 we see two rows of images. The upper row is the migrated image plotted with 10 dB of dynamic range. The bottom row of images are the exact same plots but with 6 dB of dynamic range and automatically-recognized targets labelled. The white box surrounding each target on the bottom row is the smallest rectangle that fits the -3dB width of each target. To quantify the relative performance of each pulse, we track the SNR, total area, and horizontal/vertical width in Table 11. These values are plotted for each target in Fig. 95 below.

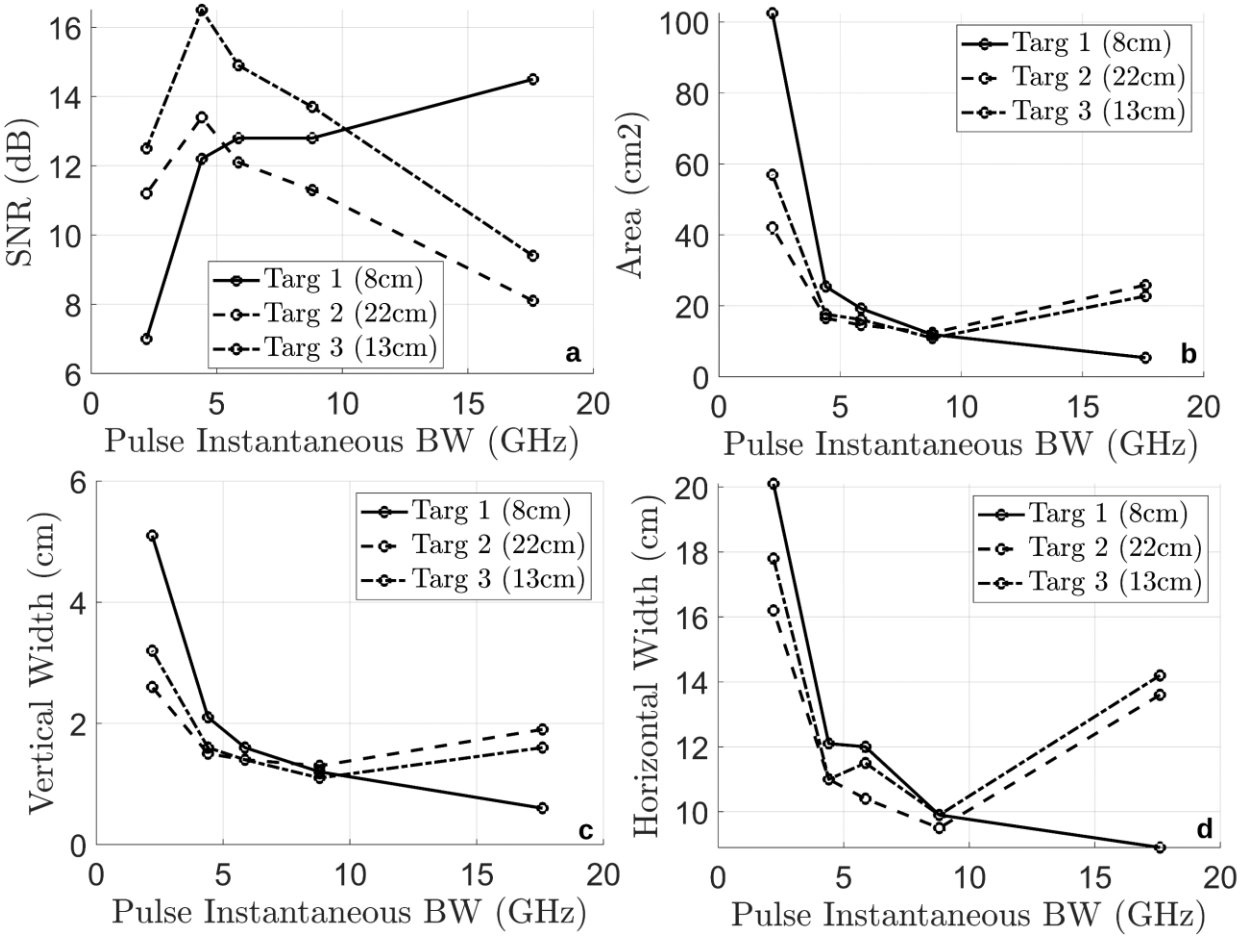

Fig. 95: SNR and target horizontal/vertical resolutions versus pulse bandwidth.

From Fig. 95 we can identify clear trends in the imaging properties of the created GPR system, enumerated below. Because the targets used are very small and metallic, we can use the reconstructed width and height as proxies for horizontal and vertical resolutions, respectively.

In Fig. 95a, As bandwidth increases, Targets 2 and 3 decrease in SNR and Target 1 increases in SNR. The 200ps pulse (2.2 GHz) has a lower SNR for all targets. These behaviors are consistent with clutter-limiting at low pulse bandwidths and power-limiting at high pulse bandwidths. Target 2 (22 cm deep) has a consistently lower SNR than Target 3 (13 cm deep), likely due to the increased distance travelled in soil. Target 1 is a special target because of its position close to the surface. Likely, Target 1 is sensed better by high-bandwidth pulses because the high-bandwidth pulse leads to a sharper and easier-to-remove ground with less clutter.

In Fig. 95b, the area decreases sharply with increasing bandwidth. This area is the area of the square that contains the 3-dB (half-power) zone around each target. Ideally, the target area varies proportional to the inverse of the bandwidth squared. The 25-ps/18 GHz pulse sees an uptick in target area for Targets 2 and 3 due to a decreased SNR. As the area is the product of the vertical and horizontal widths, we examine each independently.

The vertical width of each target (Fig. 95c) tends to decrease with increasing bandwidth. Ideally, the target vertical width varies proportional to the inverse of the bandwidth. From the Target 1 response curve, we find that the vertical resolution (VR) varies with respect to bandwidth (BW) as:

$$\mathrm{VR} \propto \frac{1}{\mathrm{BW}^{1.0061}}$$

which is a very good agreement with the theoretical result of an inverse scaling with exponent 1.0. The scaling exponent for deeper targets, however, is significantly worse as the deeper targets endure a more severe spatial low-pass filter. Targets 2 and 3 have least-square fit exponents of 0.51 and 0.77 respectively when neglecting the 25ps scan. The 25 ps/18 GHz pulse shows a

degradation in vertical resolution for the deeper targets. This decrease is consistent with a lowpass system transfer function – arising from antenna gain, amplifier gain, cable loss, and soil loss. The shallow target shows little deviation from the inverse-bandwidth curve, likely due to the higher relative power returned from the shallow target. This higher power is evident in a small peak near the top of the Target 1 hyperbola in Fig. 93 compared to the Target 2 and 3 hyperbolas.

In Fig. 95d, the horizontal width of each target also tends to decrease with increasing bandwidth. Ideally, the target horizontal width varies proportional to the inverse of the bandwidth. However, as the horizontal width depends on the specifics of the synthetic aperture imaging environment as in (27), the exact relationship is complex and can degrade based on the frequency-dependence and spatial-dependence of the system transfer function. From a least-squares fit of the Target 1 horizontal resolution (HR) response curve in Fig. 95d we measure approximately:

$$\mathrm{HR} \propto \frac{1}{\mathrm{BW}^{0.3814}}$$

which highlights the effect of variation in the combined spatial-frequency transfer function. The horizontal width of a migrated point-target depends on the maximum view angle in-ground and bandwidth. Because the antenna has a frequency-dependent radiation pattern and the target depth leads to longer paths and path loss at higher view angles, the combined spatial-frequency transfer function dictates that the tails of the target hyperbolas will contain mostly low-frequency content. Therefore, the maximum view-angle in ground is also weakly frequency-dependent and decreases the benefit of additional bandwidth. An ideal system design would not have this limitation because its power budget would allow for a consistent maximum angle of view versus frequency, and we would see a higher exponent-of-variation with respect to bandwidth. The 25 ps shows this idea

well – as most of its power spectral density is concentrated in higher frequencies, the maximum view angle is actually lower than the lower-bandwidth pulses.

Lastly, Fig. 95 demonstrates the differences between shallow and deep targets and the reason that radar flexibility is so useful. Consider the problem of detecting the shallow target "Target 1". Not only is the target's SNR dramatically higher when detected with a 25 ps/18 GHz pulse, but the vertical and horizontal resolutions are the smallest. The resolutions are excellent because the radar power budget for shallow targets can produce useful reflections near the maximum view angle with relatively low incident power spectral density. The SNR is better because the clutter in the surrounding area is reduced. The clutter for shallow targets tends to be from uneven ground removal. Imaging the ground with a sharper pulse leads to a crisper ground reflection which is more easily removed, producing less clutter compared to imaging with a broader, lower-bandwidth pulse. From this analysis, we can conclude that, out of the pulses tested, the 25ps pulse is the best pulse to use when detecting shallow targets. Conversely, examination of the SNR of deeper targets reveals that lower-bandwidth pulses are better for the imaging of deeper targets. From Fig. 95, we see that a 75ps (6 GHz) or 50 ps (8 GHz) pulse has the best tradeoff of image quality for SNR for the given GPR setup. Note that these results are based on a dry sandbox, and the choices would skew for even lower bandwidth pulses when imaging in moisture-rich soils.

Overall, we proved that the described GPR system can take reliable images in a laboratory setup. By varying the pulse width, we explored the possible design space of different instantaneous bandwidths and their tradeoffs with imaging performance. When imaging shallow and relatively deep targets, we concluded that higher-bandwidth pulses inherently image shallower targets better

than lower-bandwidth pulses. When imaging deep targets, we found that lower-bandwidth pulses are preferred.

C. Outside GPR Scans

This section contains 2D GPR scans around Kemper Hall at UC Davis. The exact underground structure is unknown; rather, these scans are just to test whether or not the radar is capable of imaging targets outside of a sandbox. First, we examine the south side of Kemper Hall in Fig. 96.

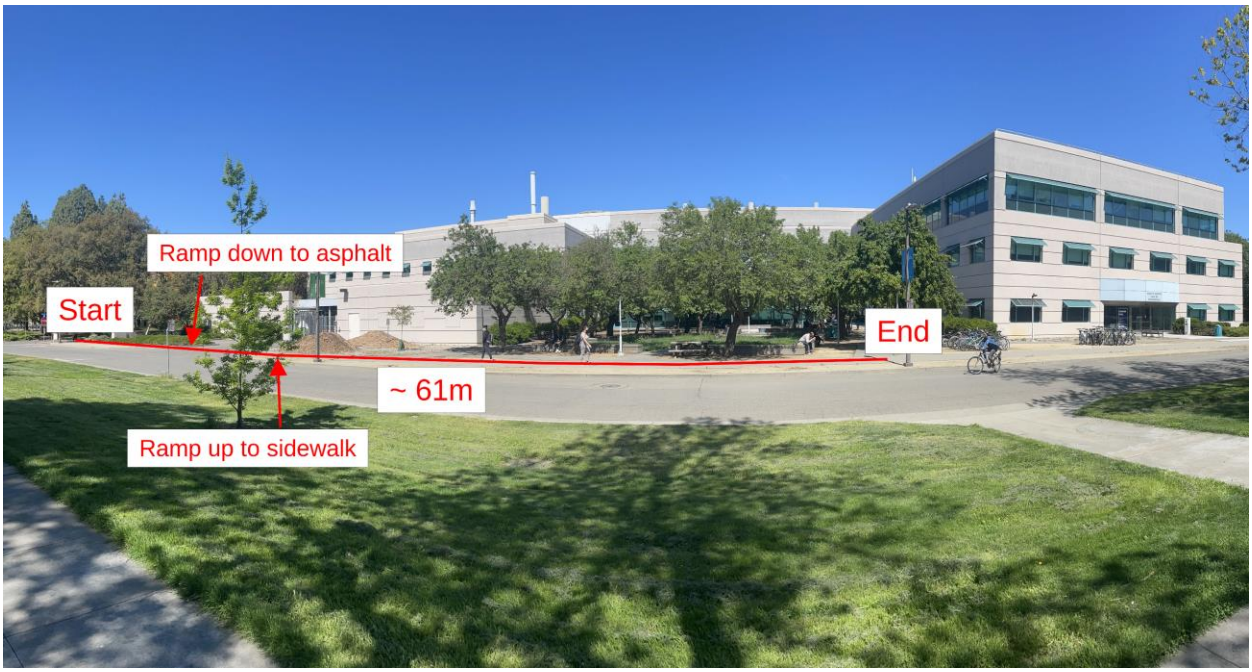

Fig. 96: Photograph of sidewalk scan south of Kemper Hall.

In this scan, we use a 100ps (4 GHz) differential pulse. The track is approximately 61m long and consists of three parts: sidewalk, asphalt, and sidewalk. The transition between sidewalk and asphalt is a wheelchair-accessible ramp with a bumpy surface. The ground-flattened coupling-removed B-scan, the ground-removed pre-processed scan, and the migrated image is shown in Fig. 97.

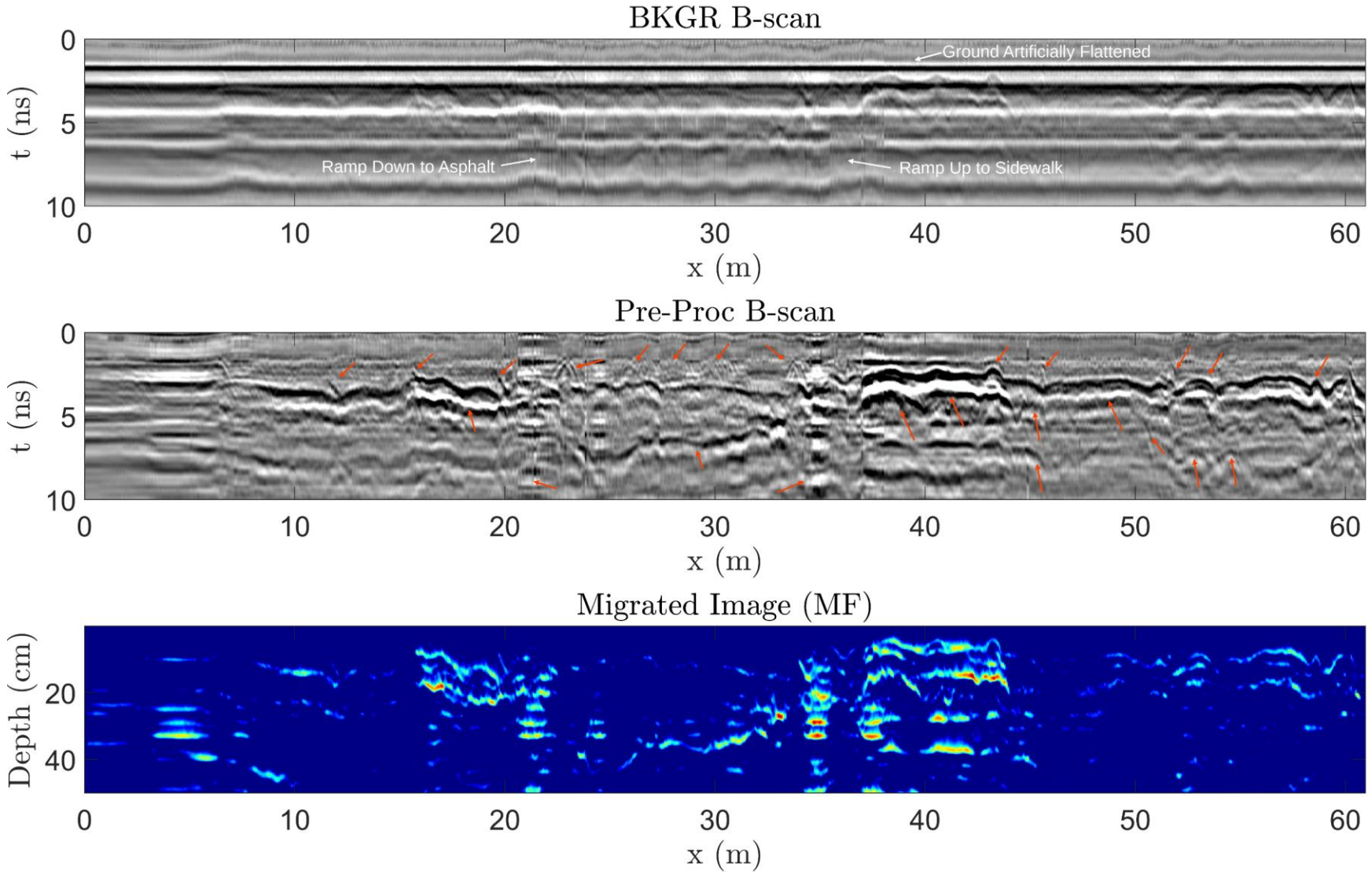

Fig. 97: 2D GPR scan of sidewalk south of Kemper Hall. (top) Raw data with ground flattened artificially and coupling already removed. (middle) Background-removed (BKGR) data with red arrows pointing to areas of interest. (bottom) Migrated image.

In Fig. 97, the ramps up and down are indicated in the top Figure. In the middle Figure, red arrows point out targets of interest. In the underground scan, the radar is able to see many pipe-like and horizontal targets. As we do not know the exact subsurface behavior, it is difficult to ascribe a certain target return to a certain feature. One interesting phenomenon is the large amount of false alarms created by the ramp up and ramp down of the sidewalk. Likely, the slight slope evades background removal and the ground reflections and multipath bleed into the scan. These ramp artifacts persist even into the migrated image around 20 and 35 meters. In these points, we see a vertical stacking of targets that is unlikely to be sensed in reality. Another thing to note is that the sidewalk portion is much more stable than the asphalt portion – this can be seen in the relatively poor removal of the surface reflection between 25 and 35 meters, indicated by arrows.

Another track of interest is the eastern side of Kemper Hall shown in Fig. 98.

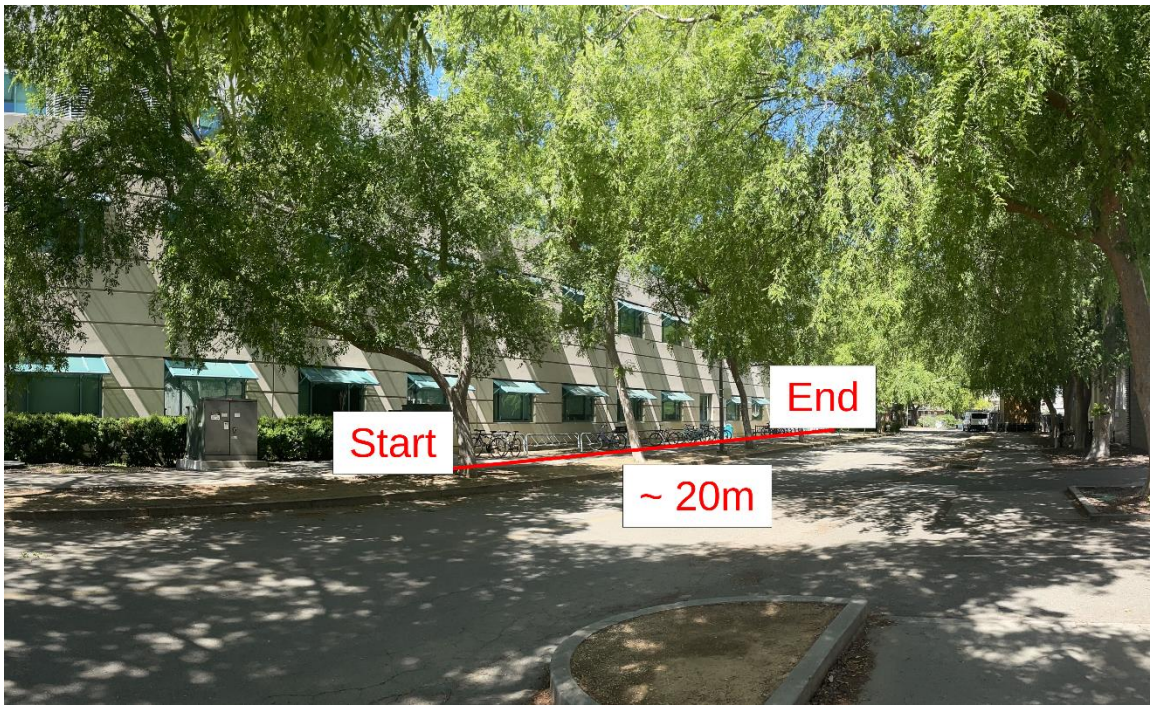

Fig. 98: Photograph of sidewalk scan to the east of Kemper Hall.

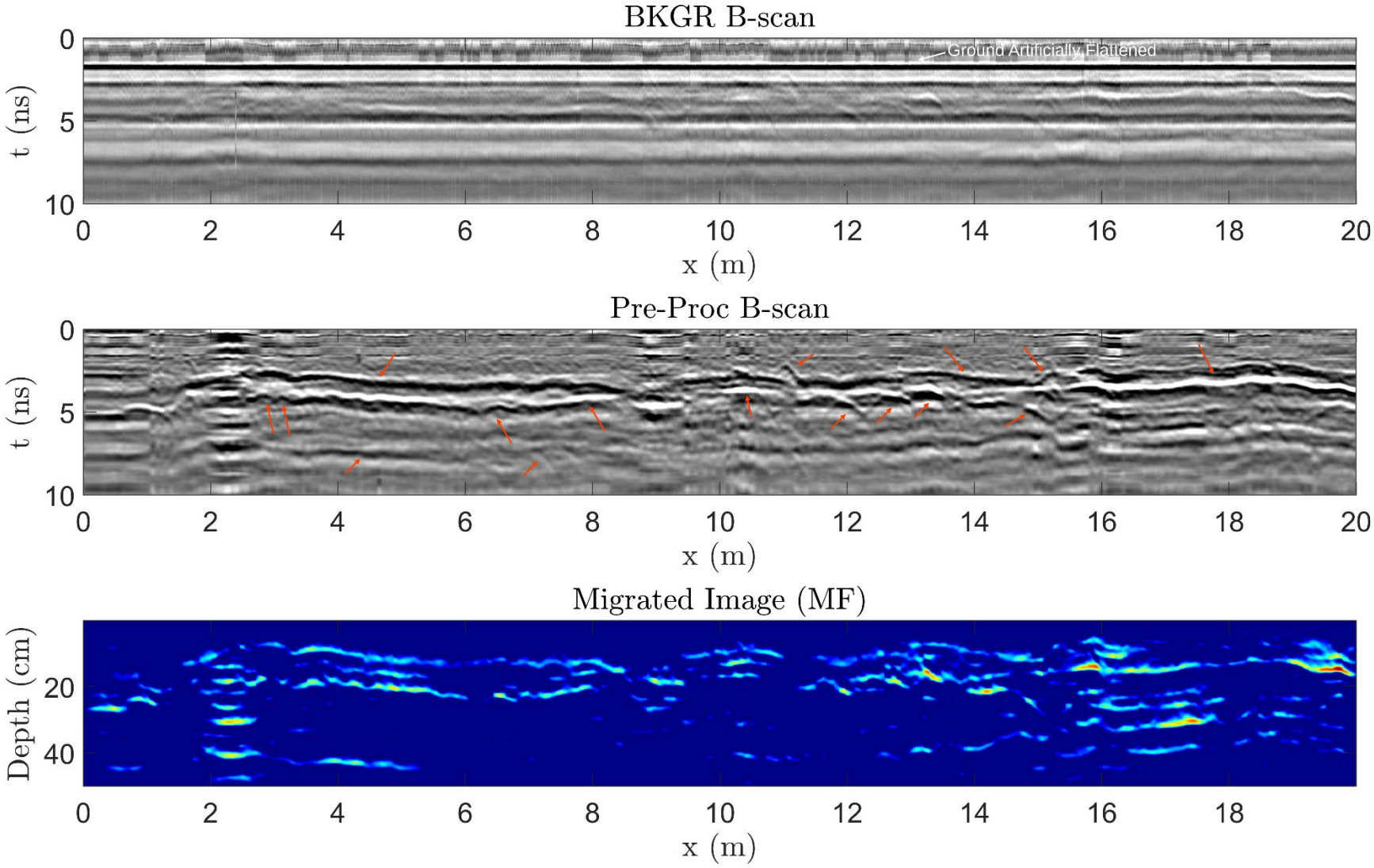

Fig. 99: 2D GPR scan of sidewalk east of Kemper Hall. (top) Raw data with ground flattened artificially and coupling already removed. (middle) Background-removed (BKGR) data with red arrows pointing to areas of interest. (bottom) Migrated image.

The scan shown in Fig. 99 is taken entirely on a sidewalk and lasts for approximately 20 meters. In Fig. 99, there are three particular items of interest. First, the area from 2 to 8 meters appears to be a slanted plastic pipe, potentially a sewage pipe. We can tell the pipe is slanted because we see the first reflection (wall) increase in depth from about 10 cm to 20 cm over several meters. The measured slope is approximately 3cm/meter, and a typical drain pipe slope is 2.1 cm/meter. Accounting for potential error in the soil relative permittivity (Fig. 99 was created with a relative permittivity of 4 – likely an under-estimate), we can see that the imaged slope of the pipe is within reasonable bounds for typical drain pipe slopes. Another interesting visible phenomena are the three pipes visible from 12 to 13.5 meters into the scan. Each pipe is clearly migrated into a point target, and the pipes are offset from each-other in the soil. These pipes could be utility pipes. Additionally, there is a row of weak target hyperbolas in the range of 4 to 8 meters at a time of approximately 2.5 ns, just above the horizontal stripe. These small targets are consistent with high- a high-density of small plastic pipes running horizontal to the scan axis such as sprinkler pipes at a depth of approximately 7 cm. The last interesting phenomenon is a periodic "shake" in the scan. These shakes come from bevels between sidewalk concrete panels. The wheel dips down and shakes the radar electronics, creating unexpected behavior. The presence of shakes indicate that the radar is sensitive to vibrations. In the next several scans, this idea will be clear.

For the last four scans, we consider an un-groomed dirt track with unknown targets. The scan of interest is shown below, in Fig. 100.

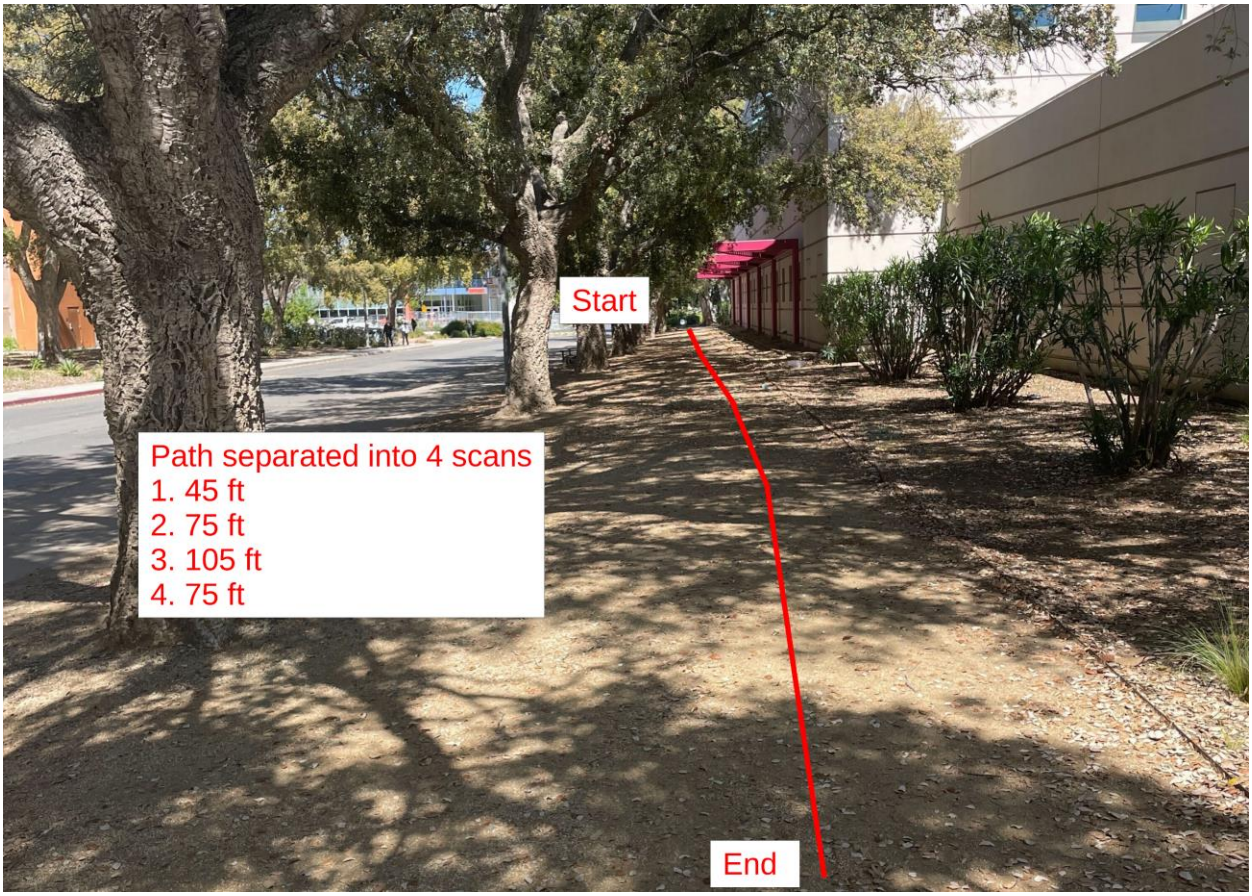

Fig. 100: Photograph of dirt scan to the west of Kemper Hall.

This dirt track is the west side of Kemper Hall at UC Davis. No targets are buried, so all imaging is of unknown targets. The scan is cut into four scans of lengths 45 ft (13.7 m), 75 ft (22.8 m), 105 ft (32 m), and 75 ft (22.8 m) approximately. In each scan, we see horizontal layers, pipe-like objects, and significant shaking. The pulse used is a 100 ps/4 GHz pulse with the same 2D setup as in Fig. 93. Figs 101-104 show the four scans along the length of the dirt track. It is necessary to note that these scans were taken in the winter season only days after rainfall. The soil was not wet to the touch, but not completely dry.

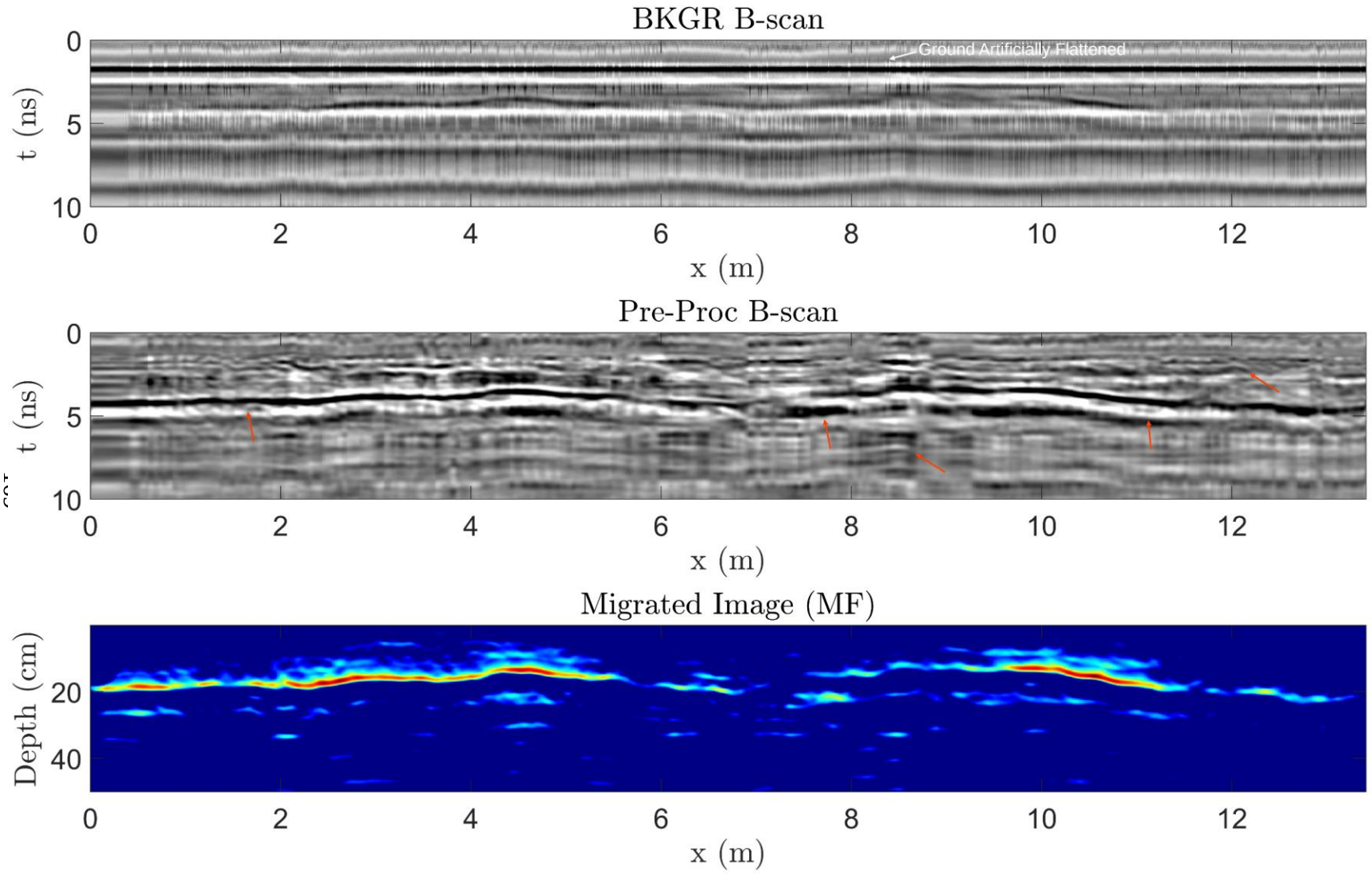

Fig. 101: 2D GPR scan of dirt section 1 west of Kemper Hall. (top) Raw data with ground flattened artificially and coupling already removed. (middle) Background-removed (BKGR) data with red arrows pointing to areas of interest. (bottom) Migrated image.

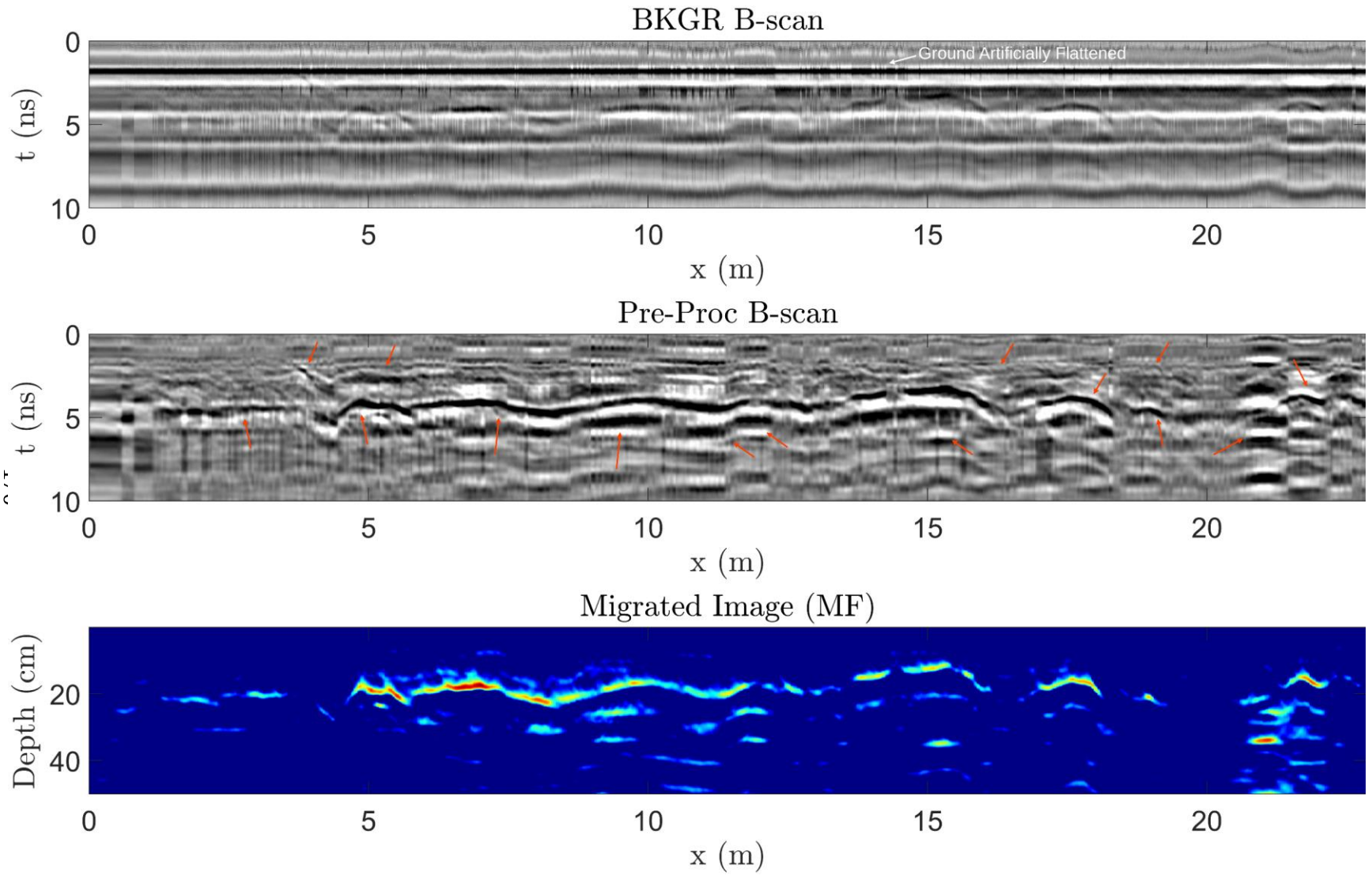

Fig. 102: 2D GPR scan of dirt section 2 west of Kemper Hall. (top) Raw data with ground flattened artificially and coupling already removed. (middle) Background-removed (BKGR) data with red arrows pointing to areas of interest. (bottom) Migrated image.

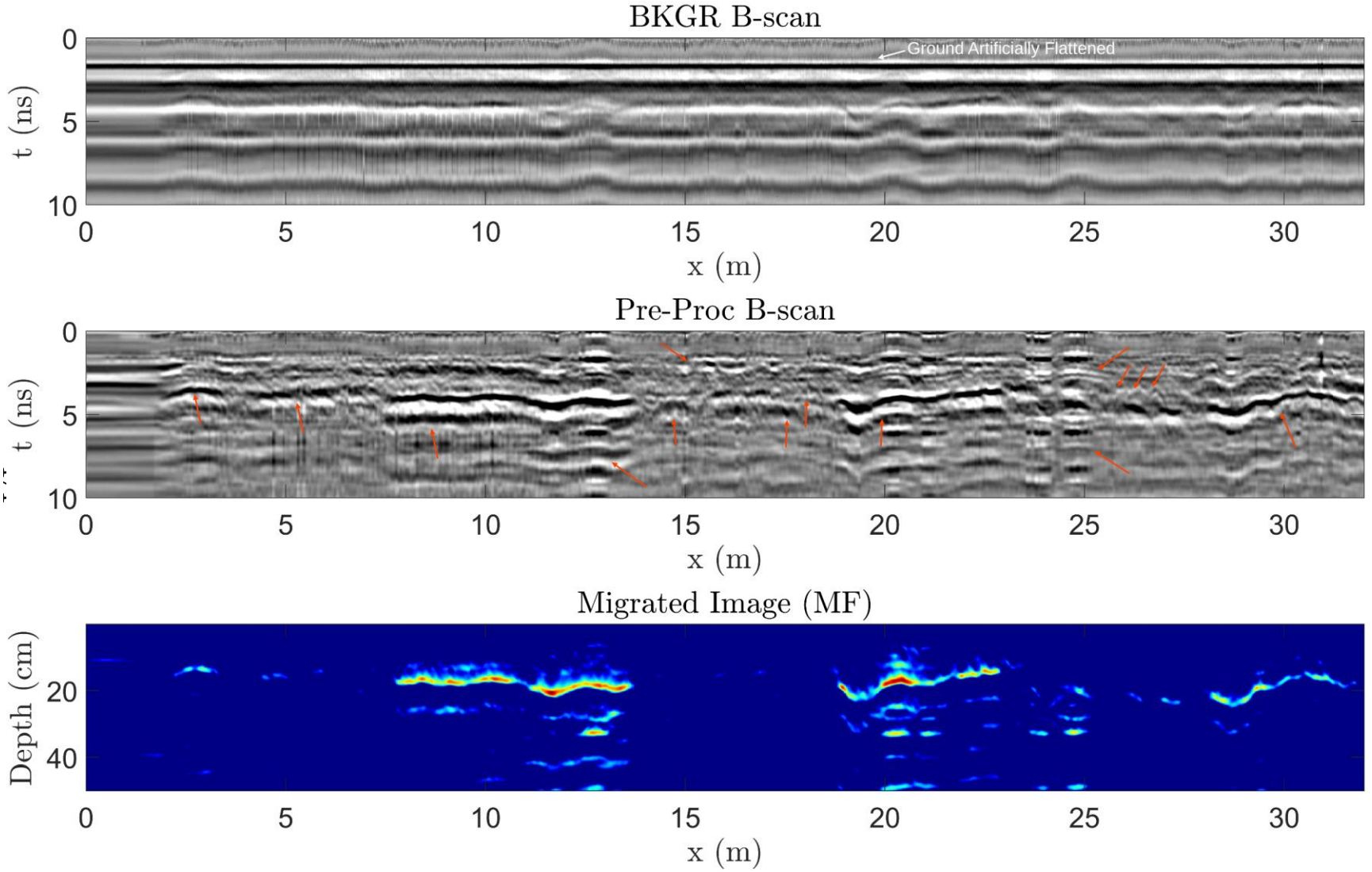

Fig. 103: 2D GPR scan of dirt section 3 west of Kemper Hall. (top) Raw data with ground flattened artificially and coupling already removed. (middle) Background-removed (BKGR) data with red arrows pointing to areas of interest. (bottom) Migrated image.

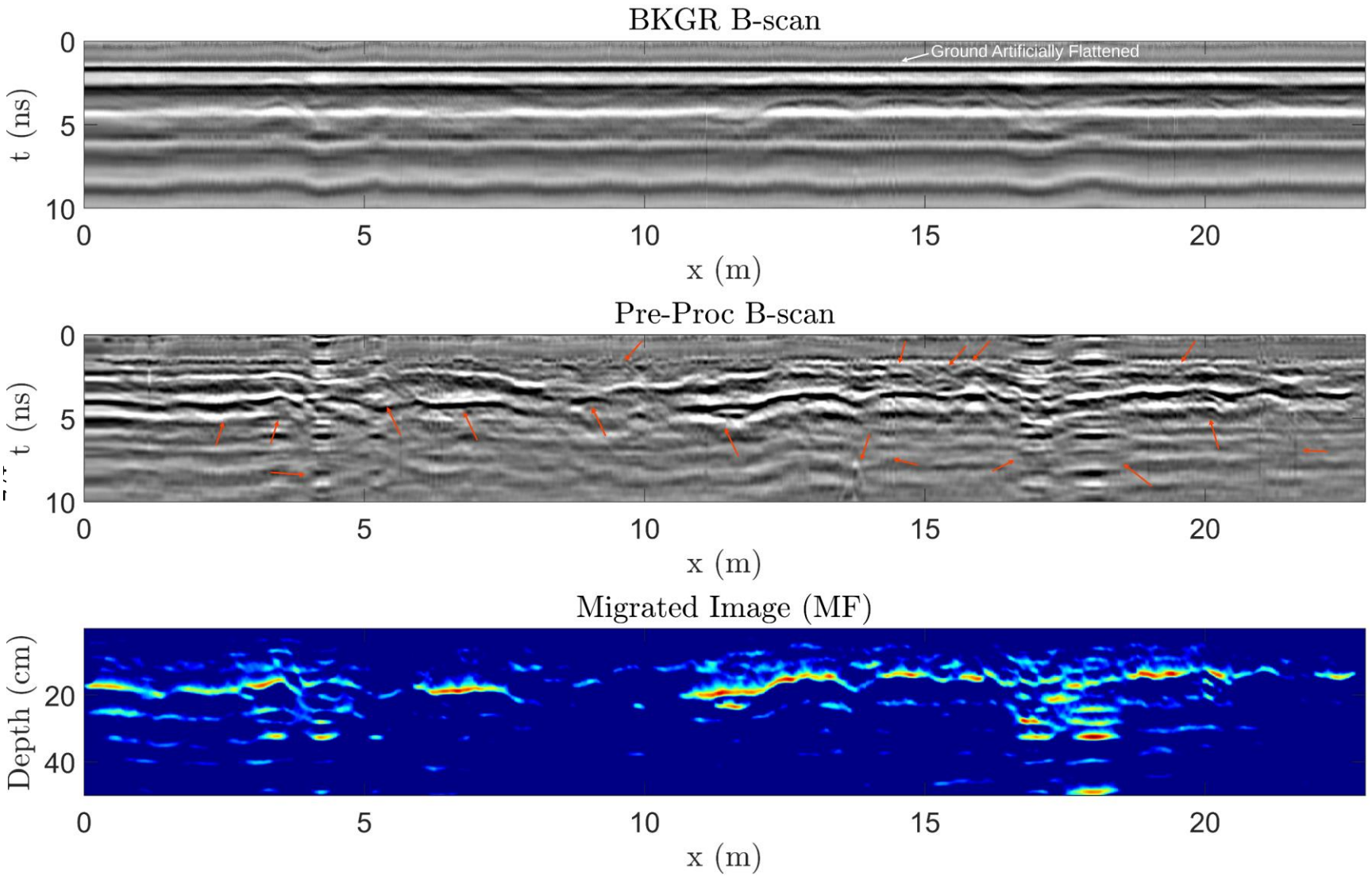

Fig. 104: 2D GPR scan of dirt section 4 west of Kemper Hall. (top) Raw data with ground flattened artificially and coupling already removed. (middle) Background-removed (BKGR) data with red arrows pointing to areas of interest. (bottom) Migrated image.

Fig. 101-104 show the scans with the described lengths coming towards the camera in Fig. 100. In general, we see a significant amount of more instability due to the uneven ground. In the first two scans - Fig. 101 and 102 – the raw B-scan shows "jitteriness" – where the A-scans are not consistent with respect to the x axis. However, these scans are not actually glitches, and do not get caught by the glitch-detection algorithm. These scans come from driving over uneven ground, where the vibration between antennas and the vibration of the SMA cables are great enough to affect the system's transfer function enough to create that jitter-like distortion. More work must be done to minimize this distortion, as the distortion decreases scan quality. Another type of distortion is the vertical-column-like responses that come from uneven ground, visible in 4.5 m and 17 m of Fig. 104, 13m, 20m, and 25m of Fig. 103, 11m and 21m of Fig. 102, and 8.5m of Fig. 101. These vertical column responses are consistent with the wheels of the cart travelling over a wheel-sized hole, which would aim the antennas at a different angle and cause background subtraction to fail. This uneven ground is also compounded by the artificial ground flattening in the processing pipeline, which could potentially create false targets. Overall, we can clearly see the difficulties of scanning over uneven ground, especially with small wheels.

In terms of targets seen, the major discovery is a layer approximately 20 cm below the ground that runs through most of the scans but is not consistent across space. This layer can be seen in the migrated images and the background-removed images. Given the intensity and multiple-peaked nature of this reflection, this reflection could either be many plastic pipes, gopher tunnels, or a true layered ground. Visual inspection of the scan site has verified that there are many gopher holes and utility boxes, so the truth is likely a combination of these explanations. Additionally, we see many pipe-like targets, especially in Fig. 103 which seems to contain the

most easily-detectable buried objects. Overall, we have proved that the GPR system is capable of imaging targets outside in soil.

We can identify four issues in the scans that can be fixed in future research. First and foremost is the physical stability of the cart when travelling over the uneven ground. An ideal system would hold a flat or known height over the mean ground surface over the entire scan, and maintain constant antenna pointing angle. This type of physical behavior can be achieved with a UAV, but work remains to make the system lightweight enough to mount on a UAV. Second, the processing does not know beforehand the relative permittivity of the medium. All images were taken with an assumed relative permittivity of 4, which is likely an underestimate and leads to inaccuracies in the depth axis. True inverse scattering imaging can pull out the relative permittivity of the medium, but this algorithm was not implemented with success in the real-world scenario. Third, the presence of a non-flat ground, even when measured from a static height, significantly increases the clutter in the B-scan and false targets in the migrated image. To remedy the problems caused by uneven ground, we believe that sensor fusion with a dedicated height sensor may be used as an input to an imaging algorithm to reduce these errors; however, this project requires significant future research. Fourth and finally, these scans were performed using single, static pulses with an unknown soil loss. We believe that future research will allow us to fully utilize the flexibility of our developed radar system and switch pulses during a scan in order to obtain ideal response. Future research should periodically estimate the soil loss and adjust the pulse in order to match.

Conclusion

In conclusion, we have developed methods, software, and hardware necessary to perform underground imaging using a ground-penetrating radar system. First, we have presented two baluns and resistively-loaded antennas. The first resistively-loaded vee dipole (RLVD) was designed to have an extremely low coupling signal in a band of 0.5-1.5 GHz. The second antenna, an elliptical RLVD (ERLVD) shows excellent gain and bandwidth for a resistive dipole when fed by a designed Guanella balun. Next, we describe the developed set of specifications for designing GPR antennas. We have found a gap in the literature where GPR antennas are typically designed to satisfy only gain, bandwidth, and another specification, typically radar cross-section or pulse integrity. By considering the whole system including jitter, soil type, bandwidth, and target response, we have derived a set of specifications that should prove useful to the GPR antenna community at large and increase success rate in new antenna designs. Next, we describe a developed 100 GS/s equivalent-sampling receiver based on a Zynq-7000 FPGA development board. The hardware, software, and FPGA code required to perform real-time sensing is shown. Then, we showed the block diagrams of 2D and 3D GPR systems. The GPR system is built in a sandbox and in a cart for outside scanning. In the GPR sandbox, we managed to perform excellent quality 2D imaging of buried steel rebar and proved that it was possible to image small shallow wires using high-bandwidth radar pulses. Using the outside GPR cart, we are able to take 2D images of the subsurface around the campus of UC Davis on sidewalks and dirt tracks detecting pipes, layers, and other buried objects. In future work, we emphasize the utilization of the full 3D capabilities of the array, sensor fusion for height detection and mitigation of uneven ground effects, and the full programming of the software-defined radar to take advantage of its inherent flexibility.

References

[1] J. B. Brooks, "Applications of GPR Technology to Humanitarian Demining Operations in Cambodia: Some Lessons Learned," in *Proc. Third International Symposium on Technology and the Mine Problem*, Naval Postgraduate School Monterey, CA, 1998, pp. 6-9.

[2] M. Sato, K. Kikuta, and R. B. Miller, "Evaluation of ALIS GPR for Humanitarian Demining in Colombia and Cambodia," in *2018 International Conference on Electromagnetics in Advanced Applications (ICEAA)*, 10-14 Sept. 2018 2018, pp. 114-117, doi: 10.1109/ICEAA.2018.8520518.

[3] D. H. N. Marpaung and Y. L. Lu, "A study of polarimetrie UWB GPR imaging for utility mapping survey application," in *2016 16th International Conference on Ground Penetrating Radar (GPR)*, 13-16 June 2016 2016, pp. 1-5, doi: 10.1109/ICGPR.2016.7572657.

[4] D. Pasculli, F. Giannino, A. Simi, and G. Manacorda, "High-density dual-polarized GPR array for underground asset mapping," in *2017 9th International Workshop on Advanced Ground Penetrating Radar (IWAGPR)*, 28-30 June 2017 2017, pp. 1-5, doi: 10.1109/IWAGPR.2017.7996080

[5] A. Zarkhidze and E. Lemenager, "Case study - use of 3D GPR technologies for utility mapping in paris," in *Proceedings of the Tenth International Conference on Grounds Penetrating Radar, 2004. GPR 2004.*, 21-24 June 2004 2004, vol. 1, pp. 375-378.

[6] L. B. Ciampoli, N. Economout, and R. Santarelli, "Prospecting an archaeological site by GPR: the case study of the buried necropolis Laurentina," in *2020 43rd International Conference on Telecommunications and Signal Processing (TSP)*, 7-9 July 2020 2020, pp. 329-332, doi: 10.1109/TSP49548.2020.9163454

[7] M. M. Thakur and A. Prashant, "GPR investigation at two sites of archaeological interest in Vadnagar, India," in *2016 16th International Conference on Ground Penetrating Radar (GPR)*, 13-16 June 2016 2016, pp. 16, doi:10.1109/ICGPR.2016.7572617.

[8] L. C. Chan, D. L. Moffatt, and L. Peters, "A characterization of subsurface radar targets," *Proceedings of the IEEE*, vol. 67, no. 7, pp. 991-1000, 1979, doi: 10.1109/PROC.1979.11380.

[9] A. L. Broome and D. M. Schroeder, "A Radiometrically Precise Multi-Frequency Ice-Penetrating Radar Architecture," *IEEE Transactions on Geoscience and Remote Sensing*, vol. 60, pp. 1-15, 2022, doi: 10.1109/TGRS.2021.3099801.

[10] W. Wenpeng, Z. Bo, L. Xiaojun, Y. Jian, and F. Guangyou, "High-resolution penetrating radar for ice thickness measurement," in *2012 14th International Conference on Ground Penetrating Radar (GPR)*, 4-8 June 2012 2012, pp. 115-118, doi: 10.1109/ICGPR.2012.6254844.

[11] S. Wagner, S. Pancrazio, A. Hossain, and A. V. Pham, "Experimental Detection of Buried Sub-mm Diameter Wires Using Microwave Ground-Penetrating Radar," in *2021 IEEE USNC-URSI Radio Science Meeting (Joint with AP-S Symposium)*, 4-10 Dec. 2021 2021, pp. 37-38, doi: 10.23919/USNC-URSI51813.2021.9703496. © 2021 IEEE

[12] D. Brown, "Electromagnetic Attenuation Properties of Clay and Gravel Soils," AIR FORCE WEAPONS LAB KIRTLAND AFB NM, 1975.

[13] L. Liu and G. Fang, "A Novel UWB Sampling Receiver and Its Applications for Impulse GPR Systems," *IEEE Geoscience and Remote Sensing Letters*, vol. 7, no. 4, pp. 690-693, 2010, doi: 10.1109/LGRS.2010.2045632.

[14] A. Omurzakov, A. K. Keskin, and A. S. Turk, "Avalanche transistor short pulse generator trials for GPR," in *2016 8th International Conference on Ultrawideband and Ultrashort Impulse Signals (UWBUSIS)*, 5-11 Sept. 2016 2016, pp. 201-204, doi: 10.1109/UWBUSIS.2016.7724188.

[15] J. Wang, Y. Su, C. Huang, M. Lu, and Y. Li, "Design of bow-tie antenna with high radiating efficiency for impulse GPR," in *2012 IEEE International Geoscience and Remote Sensing Symposium*, 22-27 July 2012 2012, pp. 594-597, doi: 10.1109/IGARSS.2012.6351524.

[16] A. Langman, S. P. Dimaio, B. E. Burns, and M. R. Inggs, "Development of a low cost SFCW ground penetrating radar," in *IGARSS '96. 1996 International Geoscience and Remote Sensing Symposium*, 31-31 May 1996 1996, vol. 4, pp. 2020-2022 vol.4, doi: 10.1109/IGARSS.1996.516875.

[17] A. B. Suksmono, E. Bharata, A. A. Lestari, A. G. Yarovoy, and L. P. Ligthart, "Compressive Stepped-Frequency Continuous-Wave Ground-Penetrating Radar," *IEEE Geoscience and Remote Sensing Letters*, vol. 7, no. 4, pp. 665-669, 2010, doi: 10.1109/LGRS.2010.2045340.

[18] G. Tronca, I. Tsalicoalou, S. Lehner, and G. Catanzariti, "Comparison of pulsed and stepped frequency continuous wave (SFCW) GPR systems," in *2018 17th International Conference on Ground Penetrating Radar (GPR)*, 18-21 June 2018 2018, pp. 1-4, doi: 10.1109/ICGPR.2018.8441654.

[19] R. Burr, M. Schartel, W. Mayer, T. Walter, and C. Waldschmidt, "A broadband UAV-Based FMCW GPR and the Influence of Vegetation," in *2019 12th German Microwave Conference (GeMiC)*, 25-27 March 2019 2019, pp. 210-213, doi: 10.23919/GEMIC.2019.8698145.

[20] R. Burr, M. Schartel, P. Schmidt, W. Mayer, T. Walter, and C. Waldschmidt, "Design and Implementation of a FMCW GPR for UAV-based Mine Detection," in *2018 IEEE MTT-S International Conference on Microwaves for Intelligent Mobility (ICMIM)*, 15-17 April 2018 2018, pp. 1-4, doi: 10.1109/ICMIM.2018.8443526.

[21] M. A. Yarlequé, S. Alvarez, H. J. Martínez, and A. C. Canelo, "FMCW GPR radar for archaeological applications: First analytical and measurement results," in *2017 XXXIInd General Assembly and Scientific Symposium of the International Union of Radio Science (URSI GASS)*, 19-26 Aug. 2017 2017, pp. 1-3, doi: 10.23919/URSIGASS.2017.8105225.

[22] S. Wagner, A. V. Pham, S. Bond, and J. Jeon, "Design of a Wideband Resistively Loaded Vee Dipole Fed by an Even-Mode Matched Marchand Balun," in *2018 IEEE International Symposium on Antennas and Propagation & USNC/URSI National Radio Science Meeting*, 8-13 July 2018 2018, pp. 1353-1354, doi: 10.1109/APUSNCURSINRSM.2018.8608889. © 2018 IEEE

[23] T. Wu and R. King, "The cylindrical antenna with nonreflecting resistive loading," *IEEE Transactions on Antennas and Propagation,* vol. 13, no. 3, pp. 369-373, 1965/05 1965, doi: 10.1109/tap.1965.1138429.

[24] K. Kangwook and W. R. Scott, "Design of a resistively loaded vee dipole for ultrawide-band ground-penetrating Radar applications," *IEEE Transactions on Antennas and Propagation,* vol. 53, no. 8, pp. 2525-2532, 2005/08 2005, doi: 10.1109/tap.2005.852292.

[25] H. Yang and K. Kim, "Ultra-Wideband Impedance Matching Technique for Resistively Loaded Vee Dipole Antenna," *IEEE Transactions on Antennas and Propagation,* vol. 61, no. 11, pp. 5788-5792, 2013/11 2013, doi: 10.1109/tap.2013.2275981.

[26] A. C. Chen, P. Anh-Vu, and R. E. Leoni, "A Novel Broadband Even-Mode Matching Network for Marchand Baluns," *IEEE Transactions on Microwave Theory and Techniques,* vol. 57, no. 12, pp. 2973-2980, 2009/12 2009, doi: 10.1109/tmtt.2009.2034220.

[27] A. C. Chen, P. Anh-Vu, and R. E. Leoni, "Development of low-loss broad-band planar baluns using multilayered organic thin films," *IEEE Transactions on Microwave Theory and Techniques,* vol. 53, no. 11, pp. 3648-3655, 2005/11 2005, doi: 10.1109/tmtt.2005.857102.

[28] S. Wagner and A. Pham, "The Ultrawideband Elliptical Resistively Loaded Vee Dipole," *IEEE Transactions on Antennas and Propagation,* vol. 68, no. 4, pp. 2523-2530, 2020, doi: 10.1109/TAP.2019.2949680. © 2020 IEEE

[29] K. Kangwook and W. R. Scott, "Improved resistively-loaded vee dipole for ground-penetrating radar applications," presented at the IEEE Antennas and Propagation Society Symposium, 2004., 2004.

[30] T. P. Montoya and G. S. Smith, "Land mine detection using a ground-penetrating radar based on resistively loaded Vee dipoles," *IEEE Transactions on Antennas and Propagation,* vol. 47, no. 12, pp. 1795-1806, 1999, doi: 10.1109/8.817655.

[31] D. W. Paglieroni, D. H. Chambers, J. E. Mast, S. W. Bond, and N. Reginald Beer, "Imaging Modes for Ground Penetrating Radar and Their Relation to Detection Performance," *IEEE Journal of Selected Topics in Applied Earth Observations and Remote Sensing,* vol. 8, no. 3, pp. 1132-1144, 2015/03 2015, doi: 10.1109/jstars.2014.2357718.

[32] C. A. Balanis, "Antenna Theory: Analysis and Design," 3 ed. New York, NY, USA: Wiley, 2005, pp. 562-563.

[33] C. H. See, R. A. Abd-Alhameed, S. W. J. Chung, D. Zhou, H. Al-Ahmad, and P. S. Excell, "The Design of a Resistively Loaded Bowtie Antenna for Applications in Breast Cancer Detection Systems," *IEEE Transactions on Antennas and Propagation,* vol. 60, no. 5, pp. 2526-2530, 2012/05 2012, doi: 10.1109/tap.2012.2189730.

[34] S. Wagner, G. Le, and A.-V. Pham, "Ultrawideband Compact 50:200 Ohm Guanella Balun Using Asymmetric Broadside-Coupled Lines," presented at the 2018 Asia-Pacific Microwave Conference (APMC), 2018/11, 2018. © 2018 IEEE

[35] A. C. Chen, M. J. Chen, and A.-V. Pham, "Design and Fabrication of Ultra-Wideband Baluns Embedded in Multilayer Liquid Crystal Polymer Flex," *IEEE Transactions on Advanced Packaging,* vol. 30, no. 3, pp. 533-540, 2007/08 2007, doi: 10.1109/tadvp.2007.901577.

[36] G. Guanella, "New Method of impedance matching in radio frequency circuits," *Brown Boveri Rev,* vol. 31, p. 327, 1944.

[37] T. Nakatani, J. Rode, D. F. Kimball, L. E. Larson, and P. M. Asbeck, "Digitally-Controlled Polar Transmitter Using a Watt-Class Current-Mode Class-D CMOS Power Amplifier and Guanella Reverse Balun for Handset Applications," *IEEE Journal of Solid-State Circuits,* vol. 47, no. 5, pp. 1104-1112, 2012/05 2012, doi: 10.1109/jssc.2012.2185554.

[38] Z. Zhang and G. Boeck, "Ultra broadband planar transmission line transformers with ferrite based bandwidth extension," presented at the 2016 46th European Microwave Conference (EuMC), 2016/10, 2016.

[39] F. H. W. S. T. v. H. R. K. a. E. Quandt, "3D thin film Guanella-balun," in *The 7th German Microwave Conference*, 2012, pp. 1-4.

[40] S. Wagner, B. M. Worthmann, and A. V. Pham, "Minimizing Timing Jitter's Impact on Ground-Penetrating Radar Array Coupling Signals," *IEEE Transactions on Geoscience and Remote Sensing,* vol. 59, no. 6, pp. 4717-4724, 2021, doi: 10.1109/TGRS.2020.3019976. © 2021 IEEE

[41] D. Chambers, D. Paglieroni, J. Mast, and N. Beer, "Real-Time Vehicle-Mounted Multistatic Ground Penetrating Radar Imaging System for Buried Object Detection," Office of Scientific and Technical Information (OSTI), 2013/01/15 2013.

[42] R. Persico, "Introduction to Ground Penetrating Radar," ed: John Wiley & Sons, Inc, 2014.

[43] H. Liu *et al.*, "Quantitative Stability Analysis of Ground Penetrating Radar Systems," *IEEE Geoscience and Remote Sensing Letters,* vol. 15, no. 4, pp. 522-526, 2018/04 2018, doi: 10.1109/lgrs.2018.2801827.

[44] S. Mann *et al.*, "High-Precision Interferometric Radar for Sheet Thickness Monitoring," *IEEE Transactions on Microwave Theory and Techniques,* vol. 66, no. 6, pp. 3153-3166, 2018/06 2018, doi: 10.1109/tmtt.2018.2825328.

[45] U. A. Onunkwo, "Timing jitter in ultra-wideband (UWB) systems," Doctor of Philosophy, Georgia Institute of Technology, Atlanta, GA, 2006.

[46] J. Hu, Z. Yuan, G. Zhu, and Z. Zhou, "Robust Detection of Moving Human Target Behind Wall via Impulse through-Wall Radar," *Defence Science Journal,* vol. 63, no. 6, pp. 636-642, 2013/12/18 2013, doi: 10.14429/dsj.63.5766.

[47] G. A. Keeler, B. E. Nelson, D. Agarwal, and D. A. B. Miller, "Skew and jitter removal using short optical pulses for optical interconnection," *IEEE Photonics Technology Letters,* vol. 12, no. 6, pp. 714-716, 2000/06 2000, doi: 10.1109/68.849094.

[48] S. Jazayeri, N. Kazemi, and S. Kruse, "Sparse Blind Deconvolution of Ground Penetrating Radar Data," *IEEE Transactions on Geoscience and Remote Sensing,* vol. 57, no. 6, pp. 3703-3712, 2019/06 2019, doi: 10.1109/tgrs.2018.2886741.

[49] L. Lianlin, "Sparsity-Promoted Blind Deconvolution of Ground-Penetrating Radar (GPR) Data," *IEEE Geoscience and Remote Sensing Letters,* vol. 11, no. 8, pp. 1330-1334, 2014/08 2014, doi: 10.1109/lgrs.2013.2292955.

[50] G. Casella and R. L. Berger, "Statistical Inference," *Biometrics,* vol. 49, no. 1, p. 320, 1993/03 1993, doi: 10.2307/2532634.

[51] J. Gazdag and P. Sguazzero, "Migration of seismic data," *Proceedings of the IEEE,* vol. 72, no. 10, pp. 1302-1315, 1984, doi: 10.1109/proc.1984.13019.

[52] C. Özdemir, Ş. Demirci, E. Yiğit, and B. Yilmaz, "A Review on Migration Methods in B-Scan Ground Penetrating Radar Imaging," *Mathematical Problems in Engineering,* vol. 2014, pp. 1-16, 2014, doi: 10.1155/2014/280738.

[53] C. Chen, S. Wu, S. Meng, J. Chen, G. Fang, and H. Yin, "Application of Equivalent-Time Sampling Combined with Real-Time Sampling in UWB Through-Wall Imaging Radar," presented at the 2011 First International Conference on Instrumentation, Measurement, Computer, Communication and Control, 2011/10, 2011.

[54] S. Wagner and A. V. Pham, "Structural Effect on Image Quality Degradation in Ground-Penetrating Radar Array," in *2019 IEEE International Symposium on Antennas and Propagation and USNC-URSI Radio Science Meeting*, 7-12 July 2019 2019, pp. 1631-1632, doi: 10.1109/APUSNCURSINRSM.2019.8889120. © 2019 IEEE

[55] R. Solimene, A. Cuccaro, A. DellAversano, I. Catapano, and F. Soldovieri, "Ground Clutter Removal in GPR Surveys," *IEEE Journal of Selected Topics in Applied Earth Observations and Remote Sensing*, vol. 7, no. 3, pp. 792-798, 2014/03 2014, doi: 10.1109/jstars.2013.2287016.
[56] I. Hertl and M. Strycek, "UWB antennas for ground penetrating radar application," presented at the 2007 19th International Conference on Applied Electromagnetics and Communications, 2007.
[57] X. L. Travassos, S. L. Avila, R. L. d. S. Adriano, and N. Ida, "A Review of Ground Penetrating Radar Antenna Design and Optimization," *Journal of Microwaves, Optoelectronics and Electromagnetic Applications*, vol. 17, no. 3, pp. 385-402, 2018/09 2018, doi: 10.1590/2179-10742018v17i31321.
[58] W. Coburn and S. McCormick, "Ultra-wideband antenna performance comparison," presented at the 2018 International Applied Computational Electromagnetics Society Symposium (ACES), 2018/03, 2018.
[59] S. I. Keceli, T. Ozbey, O. Ari, and O. Sutcuoglu, "Link Budget Analysis &verifications for system design of GPR," presented at the 2015 16th International Radar Symposium (IRS), 2015/06, 2015.
[60] T. P. Wibowo and F. Y. Zulkifli, "Analysis of Concrete Inspection Radar Equations to Obtain Radar System Specifications," presented at the 2019 16th International Conference on Quality in Research (QIR): International Symposium on Electrical and Computer Engineering, 2019/07, 2019.
[61] W. Sörgel and W. Wiesbeck, "Influence of the Antennas on the Ultra-Wideband Transmission," *EURASIP Journal on Advances in Signal Processing*, vol. 2005, no. 3, 2005/03/17 2005, doi: 10.1155/asp.2005.296.
[62] G. Chen and R. C. Liu, "Design of a shielded antenna system for ground penetrating radar applications," presented at the 2009 IEEE Antennas and Propagation Society International Symposium, 2009/06, 2009.
[63] J.-F. Hofinghoff and L. Overmeyer, "Resistive Loaded Antenna for Ground Penetrating Radar Inside a Bottom Hole Assembly," *IEEE Transactions on Antennas and Propagation*, vol. 61, no. 12, pp. 6201-6205, 2013/12 2013, doi: 10.1109/tap.2013.2283604.
[64] A. A. Lestari, E. Bharata, A. B. Suksmono, A. Kurniawan, A. G. Yarovoy, and L. P. Ligthart, "A Modified Bow-Tie Antenna for Improved Pulse Radiation," *IEEE Transactions on Antennas and Propagation*, vol. 58, no. 7, pp. 2184-2192, 2010/07 2010, doi: 10.1109/tap.2010.2048853.
[65] D. Lamensdorf and L. Susman, "Baseband-pulse-antenna techniques," *IEEE Antennas and Propagation Magazine*, vol. 36, no. 1, pp. 20-30, 1994/02 1994, doi: 10.1109/74.262629.
[66] *Ground Penetrating Radar Antenna Design Specs Generator*. (2020). Github Repository, Online. [Online]. Available:https://github.com/Samuel-Wagner/Ground-Penetrating-Radar-Antenna-Design-Specs-Generator
[67] S. J. Orfanidis, *Electromagnetic Waves and Antennas*. Online, 2016.
[68] W. A. Bereuter and D. C. Chang, "Electromagnetic remote sensing of inhomogeneous media," National Bureau of Standards, 1977.
[69] S. Habib Mazharimousavi, A. Roozbeh, and M. Halilsoy, "Electromagnetic wave propagation through inhomogeneous material layers," *Journal of Electromagnetic Waves and Applications*, vol. 27, no. 16, pp. 2065-2074, 2013/09/05 2013, doi: 10.1080/09205071.2013.831741.
[70] S. Jinjin, F. Guangyou, F. Jingjing, J. YiCai, and Y. Hejun, "TEM Horn Antenna Loaded With Absorbing Material for GPR Applications," *IEEE Antennas and Wireless Propagation Letters*, vol. 13, pp. 523-527, 2014, doi: 10.1109/lawp.2014.2311436.
[71] M. Li, R. Birken, N. X. Sun, and M. L. Wang, "Compact Slot Antenna With Low Dispersion for Ground Penetrating Radar Application," *IEEE Antennas and Wireless Propagation Letters*, vol. 15, pp. 638-641, 2016, doi: 10.1109/lawp.2015.2465854.
[72] A. A. Lestari, A. G. Yarovoy, and L. P. Ligthart, "RC-Loaded Bow-Tie Antenna for Improved Pulse Radiation," *IEEE Transactions on Antennas and Propagation*, vol. 52, no. 10, pp. 2555-2563, 2004/10 2004, doi: 10.1109/tap.2004.834444.
[73] A. Ahmed, Y. Zhang, D. Burns, D. Huston, and T. Xia, "Design of UWB Antenna for Air-Coupled Impulse Ground-Penetrating Radar," *IEEE Geoscience and Remote Sensing Letters*, vol. 13, no. 1, pp. 92-96, 2016/01 2016, doi: 10.1109/lgrs.2015.2498404.
[74] A. A. Jamali and R. Marklein, "Design and optimization of ultra-wideband TEM horn antennas for GPR applications," presented at the 2011 XXXth URSI General Assembly and Scientific Symposium, 2011/08, 2011.
[75] J. Li, S. Wang, Y. Tao, C. Dong, and G. Tang, "A novel expression of the spherical-wave reflection coefficient at a plane interface," *Geophysical Journal International*, vol. 211, no. 2, pp. 700-717, 2017/07/26 2017, doi: 10.1093/gji/ggx308.

[76] J. Li, S. Wang, J. Wang, C. Dong, and S. Yuan, "Frequency-Dependent Spherical-Wave Reflection in Acoustic Media: Analysis and Inversion," *Pure and Applied Geophysics*, vol. 174, no. 4, pp. 1759-1778, 2017/02/16 2017, doi: 10.1007/s00024-017-1489-y.
[77] C. Tie Jun and C. Weng Cho, "Fast evaluation of Sommerfeld integrals for EM scattering and radiation by three-dimensional buried objects," *IEEE Transactions on Geoscience and Remote Sensing*, vol. 37, no. 2, pp. 887-900, 1999/03 1999, doi: 10.1109/36.752208.
[78] L. M. Brekhovskikh, "Reflection and Refraction of Spherical Waves," in *Waves in Layered Media*, ed: Elsevier, 1980, pp. 225-298.
[79] Y. Liu, Y. Hao, H. Wang, K. Li, and S. Gong, "Low RCS Microstrip Patch Antenna Using Frequency-Selective Surface and Microstrip Resonator," *IEEE Antennas and Wireless Propagation Letters*, vol. 14, pp. 1290-1293, 2015, doi: 10.1109/lawp.2015.2402292.
[80] W. Zhang, Y. Liu, S. Gong, J. Wang, and Y. Jiang, "Wideband RCS Reduction of a Slot Array Antenna Using Phase Gradient Metasurface," *IEEE Antennas and Wireless Propagation Letters*, vol. 17, no. 12, pp. 2193-2197, 2018/12 2018, doi: 10.1109/lawp.2018.2870863.
[81] K. K. Ajith and A. Bhattacharya, "Improved ultra-wide bandwidth bow-tie antenna with metamaterial lens for GPR applications," presented at the Proceedings of the 15th International Conference on Ground Penetrating Radar, 2014/06, 2014.
[82] Y. Li and J. Chen, "Design of Miniaturized High Gain Bow-Tie Antenna," *IEEE Transactions on Antennas and Propagation*, vol. 70, no. 1, pp. 738-743, 2022/01 2022, doi: 10.1109/tap.2021.3098595.
[83] C. A. Balanis, *Antenna Theory: Analysis and Design*, 3 ed. John Wiley & Sons, 2005.
[84] "lwIP - A Lightweight TCP/IP stack." https://savannah.nongnu.org/projects/lwip/ (accessed April 7, 2022).
[85] A. Abumurad and K. Choi, "Increasing the ADC precision with oversampling in a flash ADC," in *2012 IEEE 11th International Conference on Solid-State and Integrated Circuit Technology*, 29 Oct.-1 Nov. 2012 2012, pp. 1-4, doi: 10.1109/ICSICT.2012.6467786.
[86] I. J. Dedic, "A 16X oversampling CMOS ADC with 100 kHz bandwidth and 90dB SNR," in *1994 Second International Conference on Advanced A-D and D-A Conversion Techniques and their Applications*, 6-8 July 1994 1994, pp. 82-89, doi: 10.1049/cp:19940548.
[87] K. Nguyen, R. Adams, and K. Sweetland, "A 113 dB SNR oversampling sigma-delta DAC for CD/DVD application," *IEEE Transactions on Consumer Electronics*, vol. 44, no. 3, pp. 1019-1023, 1998, doi: 10.1109/30.713228.
[88] Avnet. "ZedBoard Development Kit." https://www.avnet.com/wps/portal/us/products/avnet-boards/avnet-board-families/zedboard/ (accessed.
[89] D. L. Gershon, J. P. Calame, Y. Carmel, T. M. Antonsen, and R. M. Hutcheon, "Open-ended coaxial probe for high-temperature and broad-band dielectric measurements," *IEEE Transactions on Microwave Theory and Techniques*, vol. 47, no. 9, pp. 1640-1648, 1999, doi: 10.1109/22.788604.
[90] V. Utsi, "Detection of Fibre Optic cables using GPR," presented at the Proceedings of the 15th International Conference on Ground Penetrating Radar, 2014/06, 2014.
[91] X. Song, D. Xiang, K. Zhou, and Y. Su, "Improving RPCA-Based Clutter Suppression in GPR Detection of Antipersonnel Mines," *IEEE Geoscience and Remote Sensing Letters*, vol. 14, no. 8, pp. 1338-1342, 2017/08 2017, doi: 10.1109/lgrs.2017.2711251.
[92] C. A. Balanis, *Advanced Engineering Electromagnetics*. Hoboken, NJ: John Wiley & Sons, 2012.